This electronic thesis or dissertation has been downloaded from Explore Bristol Research, http://research-information.bristol.ac.uk

Author:
Hinchliff, Janna

Title:
Nuclear spin control and manipulation in self-assembled quantum dots

General rights
Access to the thesis is subject to the Creative Commons Attribution - NonCommercial-No Derivatives 4.0 International Public License. A copy of this may be found at https://creativecommons.org/licenses/by-nc-nd/4.0/legalcode This license sets out your rights and the restrictions that apply to your access to the thesis so it is important you read this before proceeding.

Take down policy
Some pages of this thesis may have been removed for copyright restrictions prior to having it been deposited in Explore Bristol Research. However, if you have discovered material within the thesis that you consider to be unlawful e.g. breaches of copyright (either yours or that of a third party) or any other law, including but not limited to those relating to patent, trademark, confidentiality, data protection, obscenity, defamation, libel, then please contact collections-metadata@bristol.ac.uk and include the following information in your message:

- Your contact details
- Bibliographic details for the item, including a URL
- An outline nature of the complaint

Your claim will be investigated and, where appropriate, the item in question will be removed from public view as soon as possible.

Nuclear spin control and manipulation in self-assembled quantum dots

By

Janna Hinchliff

Department of Physics
University of Bristol

A dissertation submitted to the University of Bristol in accordance with the requirements of the degree of Doctor of Philosophy in the Faculty of Sciences.

December 2018

Word count: 42966

ABSTRACT

Quantum dots come in many shapes and sizes, with a huge variety of material and optical properties. The subject of this thesis will be to examine the environment of self-assembled InGaAs quantum dots for applications in quantum information processing. Quantum dots are made up of many atoms, each of which has a spin and it is the dynamics of these nuclear spins and their effect on an electron spin confined in the quantum dot that we will discuss. There are numerous applications for quantum dots in the field of quantum information processing, many of which exploit their atom-like optical properties using light-matter interactions. The application that will be the focus of this thesis is the nuclear spin quantum memory - a device that is able to store quantum states on long timescales.

We will show both theoretical and experimental results that indicate ways in which we can gain control of the nuclear spin dynamics. We demonstrate this by designing an optical setup capable of measuring the precession frequency of an electron spin and show how we can induce changes in this precession frequency by controlling the configuration of the nuclear spin bath. We also discuss how we can manipulate this system to create a nuclear spin quantum memory - storing the initial state of the electron spin in a single nucleus. We also discuss how we can exploit the nuclei within the quantum dot as qubits to expand this protocol into a full-scale quantum computing model.

ACKNOWLEDGEMENTS

I would like to thank all of the people that have helped me throughout the four years of my PhD. Firstly, my supervisors, Ruth Oulton and John Rarity for all their help and support. They have given my lots of opportunities to progress with my work and to attend conferences in the field, where I have learnt valuable skills. I would also like to thanks the quantum dot research group at the University of Bristol. I have worked closely with all of them over the last four years and have had lots of useful discussions. Particular thanks go to Petros Androvitsaneas, who has helped a great deal with the supervision of my research, as well as staying around with me for lots of late nights in the lab and making me read Greek parables! Thanks also go to Dara McCutcheon and Thomas Nutz for their help and discussion on the theoretical side of my research and to Andrew Young, Edmund Harbord and Adetunmise Dada for their help in the lab. I am also very grateful for the help of Janet Anders from the University of Exeter, for her insights and discussion.

Thanks also go to the other PhD students that I have worked with during my time at Bristol. In the quantum dot office, Ben Lang, Joe Lennon and Matthew Parker and also my colleagues on the quantum engineering CDT, and the CDT staff - Pete Turner, Chris Erven, Andrea Watkins and Lin Burden. We have shared lots of good times, both academically and socially. Finally, I would like to thank my family, particularly my parents, John and Julie Hinchliff for their support over the last four years and for driving all the way to Bristol to visit me!

AUTHOR'S DECLARATION

I declare that the work in this dissertation was carried out in accordance with the requirements of the University's Regulations and Code of Practice for Research Degree Programmes and that it has not been submitted for any other academic award. Except where indicated by specific reference in the text, the work is the candidate's own work. Work done in collaboration with, or with the assistance of, others, is indicated as such. Any views expressed in the dissertation are those of the author.

SIGNED: .... DATE: ....

TABLE OF CONTENTS

Page

LIST OF FIGURES

PUBLICATIONS

P. Androvitsaneas, A.B. Young, J.M. Lennon, C Schneider, S Maier, J.J. Hinchliff, G Atkinson, M Kamp, S Höfling, J.G. Rarity and R. Oulton. "An efficient quantum photonic phase shift in a low Q-factor regime". *ACS Photonics,* 2019, 6, 2, 429-435

Chapter 1

Introduction

This thesis will examine the prospects of spin-based quantum information processing and quantum computation in self-assembled InGaAs quantum dots (QDs), with a focus on nuclear spin effects. We will explore several theoretical concepts in relation to control and manipulation of the nuclear spin environment of the QD and exploitation of the naturally-occurring spin effects. We combine these studies into a theoretical protocol for a nuclear spin quantum memory using an In atom contained in a QD. In the experimental section of this thesis, we discuss the implementation of aspects of the nuclear spin quantum memory protocol - more specifically, controlling the behaviour of the full nuclear spin bath to enhance spin qubit coherence times. We present results showing that the precession of an electron spin within a QD can be controlled to some extent through application of carefully chosen laser pulses and magnetic fields acting to "calm" the evolving state of the nuclear spins within the QD environment. A detailed thesis structure is outlined below.

1.1 Thesis Overview

Chapter 1 is a background theory chapter, beginning with a brief introduction to the key concepts used in the following chapters. We will introduce the concept of an open quantum system, which can be used as a theoretical description of a semiconductor QD. We will then discuss the finer details of the fabrication of the self-assembled QDs studied in this thesis and their optical properties. Next,we outline the motivation for studying these QD systems, including applications in quantum information processing, quantum computation and quantum key distribution.

Chapter 2 will discuss the environment of a semiconductor QD, focusing specifically on the dynamics of the nuclear spins and how they affect the coherence of an electron spin qubit within the QD. This is a theoretical chapter and incorporates background information on an existing model for a nuclear spin bath with a novel extension of this model, making it applicable to an experimental setting. We give details of a theoretical protocol known as nuclear frequency focusing (NFF), which outlines a method for suppressing these nuclear spin effects, leaving the electron spin free to precess coherently. We adjust and expand on ideas in the original model to create an experimentally applicable proposal for this process. The original model was developed by Sophia Economou, but rewritten independently and adapter by the author.

Chapter 3 will focus on single nuclear spin isolation and manipulation in the QD environment, assuming that the techniques outlined in Chapter 2 can be successfully implemented. This is a theoretical chapter, comprising predominantly novel material. The models used in this section were developed by the author. For this, we analyse the strain profile of a typical InGaAs QD and show that it is possible to find a nuclear spin that is isolated in frequency from the rest of the nuclear spin bath such that it can be addressed individually by a radiofrequency (RF) pulse. We discuss the effect of this RF pulse on the remainder of the nuclear spin bath, showing that the system should retain coherence on sufficiently long time scales. We give details of how we can use the manipulation of single nuclear spins to create a two-qubit system of the electron and a target nuclear spin that will periodically evolve into a maximally entangled state.

Chapter 4 will consider how we can transform the two-qubit system described in Chapter 3 into a nuclear spin quantum memory protocol. This is the final theoretical chapter and is made up entirely of novel material. The models described in this section were developed by the author. We outline a method for reading out the stored nuclear spin state via entanglement and readout of an ancilla photon. We then look into the effect of additional nuclei in the spin bath on the entanglement of the electron and nucleus, showing that under certain conditions this effect will be sufficiently small for the protocol to be successful. Finally, we discuss the prospect of using the system as a platform for a full quantum computation scheme and give preliminary simulation data motivating this area of research.

Chapter 5 will focus on the characterisation of QD samples. This is the first of two experimental chapters and is predominantly an experimental methods and characterisation chapter. The novelty in the chapter is the design of the interferometer used to measure the precession of an electron spin in a QD. The author was involved to a large extent in the design and building of the experimental setups described. We will give details of the sample that we analyse and describe the optical setup used for photoluminescence (PL) and resonant scattering measurements on QD samples. We will then show how this setup can be used to characterise the behaviour of single QDs, including the dependence of the wavelength of the QD on its temperature, and the intensity of the emission from the QD on the linewidth and laser power. We will show how these techniques can be used to infer properties of particular QDs, and show how we can use them to differentiate between excitons and biexcitons.

Chapter 6 will show the experimental outcomes of our implementation of the NFF protocol. This is an experimental results chapter, showing novel results using the interferometer described in the previous chapter. The results in this chapter were taken by the author. We design a setup that allows to measure the precession of an electron spin in a negatively-charged QD using interferometry. We attempt an implementation of the NFF protocol described in Chapter 2, and measure the change in electron spin precession due to different pulse sequences and as a function of external field. We relate this to our theoretical predictions and comment on the outcomes.

Chapter 7 gives a short conclusion and summary of all of the results discussed. We outline ideas for further research in the field and how this would complement the results already found.

1.2 Quantum Systems

This section will discuss both open and closed quantum systems and the types of platform that each of these systems represents.

1.2.1 Closed quantum systems

A closed quantum system is defined as a system that is isolated from its environment [1]. This means that there will be no mixing of the states of the system with the unknown state of the system's environment. As a result of this, we are able to describe the time evolution of the system by a unitary operator. If we label the time-dependent state vector of our system as $|\psi(t)\rangle$ and define some unitary operator $U(t,t_0)$, where $t-t_0$ is the evolution time period we are considering, we can describe the state after some time, t, as

$$|\psi(t)\rangle \quad = \quad U(t,t_0)|\psi(t_0)\rangle \,. \tag{1.1}$$

Substituting this into the Schrödinger equation and solving for a time-independent (closed) system gives

$$U(t,t_0) \quad = \quad e^{-iH(t-t_0)} \tag{1.2}$$

for some Hamiltonian, H, describing the dynamics of the physical system such that $U(t_0,t_0) = \mathbb{1}$. This is sufficient to describe the dynamics of any closed system, however, such closed systems are used to give idealised representations of systems and do not include the more complex processes a particular platform might experience, as we are usually unable to keep our system sufficiently isolated from its environment. In general, systems will be susceptible to some decoherence processes from the surrounding environment. This leads to a non-unitary time evolution of the system, meaning we cannot model the evolution according to $U(t,t_0)$. Such systems are known as open quantum systems and will be introduced below.

1.2.2 Open quantum systems

Open quantum systems are much more complex and difficult to model than closed quantum systems as in general we do not know the full state of the environment acting on the system

[1, 2]. The interaction between our system and our environment introduces some uncertainty in the dynamics of the system. In this case, we represent the system by a density operator, $\rho(t)$ rather than a state vector, $|\psi\rangle$ which represents an ensemble of i possible states, each of which has some probability, p_i and is defined as

$$\rho(t) = \sum_i p_i |\psi_i(t)\rangle \langle\psi_i(t)|. \tag{1.3}$$

Then if we know our state with certainty, we have $i = 1$ and $p_i = 1$ and we call this a pure state. For any state with $p_i \neq 1$ for any i, we have more than one possible state and therefore we call this a mixed state. As p_i are a set of probabilities we have the condition

$$\mathrm{Tr}(\rho(t)) = 1 \tag{1.4}$$

and we can therefore determine whether a state is pure or mixed using the conditions

$$\mathrm{Tr}(\rho^2) = 1 \tag{1.5}$$

for a pure state and

$$\mathrm{Tr}(\rho^2) < 1 \tag{1.6}$$

for a mixed state. The evolution of these states is given by

$$\rho(t) = \sum_i p_i U(t,t_0)|\psi_i(t_0)\rangle \langle\psi_i(t_0)|U^\dagger(t,t_0). \tag{1.7}$$

In general, we will approximate a system interacting with its environment as some density operator

$$\rho = \rho_s \otimes \rho_e \tag{1.8}$$

where ρ_s represents the density operator of the system and ρ_e represents the density operator of the environment, which will usually contain some approximations and assumptions about how the system behaves. We can then construct an equation of motion for this by taking the time derivative,

$$\frac{d\rho(t)}{dt} = -i[H(t),\rho(t)]. \tag{1.9}$$

This open quantum system representation can accurately represent the behaviour of a range of platforms, and in particular is the representation we will use in this thesis to accurately model the range of effects present in a semiconductor QD.

1.3 Motivation and applications

This section will motivate the research discussed in this thesis, and give examples of the potential applications of the systems. We will first introduce the concept of quantum computation, defining the important theoretical aspects. We will then move on to consider quantum key distribution, which is currently one of the most advanced applications in the field of quantum information processing and discuss how our research is applicable to this field.

1.3.1 Quantum Computation

1.3.1.1 Theoretical Description

Quantum computation (QC) is an incredibly powerful process that takes a new approach to processing information, based on the laws of quantum mechanics [3, 4]. Whereas a classical computer will encode its information in bits, a quantum computer will use qubits, which operate according to two key principles of quantum physics: superposition and entanglement. A qubit is a quantum mechanical system that has two possible states. A classical bit exists in one of two states, 0 or 1, however a qubit can exist in a superposition of these states, i.e. it has some probability of being in either one of the two states, essentially allowing a large degree of parallelisation in computing processes. For example, a classical bit may be in the state 0, or it may be in the state 1. The bit can be represented as some column vector where a 0 bit is defined as $\begin{pmatrix}1\\0\end{pmatrix}$ and a 1 bit is defined as $\begin{pmatrix}0\\1\end{pmatrix}$. Then the equivalent qubit may be defined as the vector $\begin{pmatrix}\alpha\\\beta\end{pmatrix}$, subject to the normalisation condition $|\alpha|^2 + |\beta|^2 = 1$. A qubit is said to be in a superposition if both α and β are non-zero, however, this can only be the case before any measurements are performed on the system. Any measurement of a qubit in the computational basis $\{\begin{pmatrix}1\\0\end{pmatrix}, \begin{pmatrix}0\\1\end{pmatrix}\}$ will project the system into the state $\begin{pmatrix}1\\0\end{pmatrix}$ with probability $|\alpha|^2$ or $\begin{pmatrix}0\\1\end{pmatrix}$ with probability $|\beta|^2$, i.e. although the qubit state can be any combination of the computational basis states, measurement projects the system into one of two possible states [5].

Quantum information processing will usually consist of some form of quantum gate or measurement being performed on a qubit or qubits. A quantum gate is a linear transformation of a qubit into some new state that preserves the condition $|\alpha|^2 + |\beta|^2 = 1$ and can be described by a unitary matrix [5]. Then, if we consider the scenario where we have two classical bits, we can have one of the four states $\{00, 01, 10, 11\}$ at any one time, meaning that a classical computer must analyse each state one by one to get a result. In a quantum computer, we have the same four possible states, however, any operation performed on a qubit can provide results for the 0 and 1 simultaneously. Then we can see that as we add more qubits, the power the quantum computer possesses increases exponentially, i.e., we can analyse 2^n states with n qubits at any one time, whereas in classical computing we can analyse only n states with n qubits at one time.

Excluding entanglement, it is possible to simulate the action of a qubit on a classical computer, and if n is the number of qubits we want to simulate, we require only $2n$ bits to do this. When we include entanglement, we allow the effect of a quantum operation on a particle to be mapped onto any particle(s) it may be entangled to. Then, where we stated above that superposition means that the state of a particle is not in a single state, but a set of states each with some probability of occurring and that this means we can perform computations in parallel, we find that entanglement is the implementation of this parallelisation between multiple qubits. Creating large entangled states is one of the big challenges in QC currently, as loss of one qubit in a large group of entangled qubits can destroy any chances of completing an operation on any of the qubits in the entangled state if the entangled state is not chosen and prepared in the correct way [6, 7].

To successfully use qubits for quantum computation, there are five important conditions that must be satisfied, known as the DiVincenzo criteria [4]. These criteria are as follows:

Criterion 1: Well-defined qubits A qubit can be described as a two-level system with an energy gap between the two states. We require that the system remains (within some small error) in the subspace of these two energy levels to be well-defined. Creating one such qubit is quickly becoming standard practice in the quantum computing world, however the difficulty comes in extending this to larger and larger numbers of well-defined qubits all confined within the same system. For many platforms, the problem facing scientists is the scaling of the experimental setups required to accommodate large numbers of qubits.

Criterion 2: Qubit initialisation Any quantum computing model is based on performing operations on a qubit state. To read out the result of these operations, a measurement must be performed. To determine whether the operation has been successful, the measured state must be compared to the initial state of the qubit and so the initial state must be known. One particularly common way to initialise a state is simply to wait until it has relaxed into its ground state, providing the timescale of this process is known. Another way to initialise a state is through some form of optical pumping of the state, and this can give shorter initialisation times and higher fidelity states.

Criterion 3: Universal set of quantum gates In order to implement a particular quantum algorithm, we need a particular set of quantum gates. Different models of QC require different gate sets to create a universal quantum computer, i.e. a computer that can perform any operation.

Criterion 4: Qubit specific measurements Measurement of the system we have prepared is essential in determining the outcome of the computation. If a particular measurement technique is not 100% efficient, it is often possible to correct for this by repeating the computation several times, however this can quickly become time-expensive. Detection often involves single photon counting and many detectors have now reached the required level of reliability needed to count the number of photons passing through with the desired level of accuracy.

Criterion 5: Long coherence times Decoherence of a quantum system is often the result of an interaction between the quantum system and its environment, which causes loss of quantum behaviour. Superposition and entanglement are destroyed when a system decoheres, meaning that the required quantum operations are no longer possible. This

> means that we must construct systems with decoherence times much longer than the average gate implementation time. Then the small amount of decoherence the system will still experience can be overcome with error correction protocols. However, a system that utilises strong interactions and therefore has short gate implementation times will usually experience decoherence on a shorter timescale due to these strong interactions and vice versa with a system with weaker interactions. This criterion is of particular relevance in this thesis, as the QD experiences particularly strong environmental effects which limit the coherence time and this is an issue that will be addressed directly in subsequent chapters.

Satisfying one or even several of these criteria is well within the capability of many physical platforms, however, finding a platform that has the ability to satisfy all five has proven to be a huge challenge [3]. In QDs, the biggest sticking point is Criterion 5 - the coherence time of the qubit [8, 9]. The QD has a very well-defined qubit, and it has been possible to construct theoretical protocols for initialisation, manipulation and measurement of qubit operations [10]. However, despite significant progress being made [11], the coherence time of the qubits confined within QDs is still a difficult issue facing the community. This thesis focuses on how we can address this problem, by suggesting a protocol to effectively decouple the electron spin from its environment, thus lengthening its coherence time.

We should note here that these criteria were established when the field of QC was in its infancy and as such, it may be necessary to make some adjustments to the criteria for newer applications. For example, in Chapter 3, we discuss a method of QC known as ancilla-driven quantum computation. For this, we can, to some extent, relax criterion 4. In this case, we do not require the register qubit storing the information to be measured to retrieve its state - we instead measure an ancilla qubit that is entangled to this register qubit. This does not completely remove the need to make measurements on qubits, but does mean we reduce the number of measurements, and instead perform them on an ancilla qubit, adding a extra degree of protection for the register qubit. Similarly, several photonic QC schemes do not require criterion 1 to be satisfied to the extent that was originally anticipated and in some cases error correcting schemes can be applied to overcome the photon error and loss [12, 13].

1.3.1.2 Experimental implementations and limitations of QC

Experimentally, the field of QC is huge. There are many platforms other than QDs with which scientists propose and attempt to implement QC, including solid state systems (for example, nitrogen vacancy centres in diamond, p-doped silicon and a wide range of 2-D materials [14–17]), trapped ions [18, 19], superconducting circuits [20] and linear optics [21]. One of the major difficulties with QC is that some of the basic criteria we require have conflicting needs. An example of this is the need to interact with our chosen system to perform processes such as measurement or error correction, but a need to protect the system from any external processes to preserve the coherence of the quantum states.

Currently, the more successful implementations of QC are those that use platforms that are more easily assembled, for example, linear optical quantum computing, which requires use of only standard linear optical devices, but that may suffer from other difficulties, such as scalability, as they use probabilistic computation schemes [22]. One of the more scalable platforms is superconducting circuits. This seems to be the platform of choice for creating machines with competitively large numbers of qubits, with Intel, IBM and Google creating 49, 50 and 72 qubit devices respectively, although these are much bulkier systems and require mK temperatures [23–26]. While most of these systems are fabricated using a "bottom-up" approach, i.e., beginning with a single qubit and scaling up, we should also draw attention to D-Wave Systems, who have fabricated a device that is claimed to contain 2000 qubits, using the "top-down" approach of including a huge number of potential qubits in the system, and constructing a graph state structure that allows for some specific processes to be implemented even with loss of some of these potential qubits. However, this is not a universal quantum computer and there has been significant controversy on its legitimacy as a quantum processor [27].

Although QDs are not currently competing with these sophisticated schemes, it is important to realise that the main difficulties facing QDs as an experimental platform are found in the understanding and control of the structure itself. Designing a system containing qubits with a long enough coherence time to perform significant computations, although challenging, is showing significant progress [28]. QDs, unlike many other systems, provide a deterministic platform for QC, which will be useful in avoiding some of the scaling difficulties found in other platforms. We should note here, however, that QDs currently have their own difficulties in scaling due to the random growth process (discussed in Section 1.4.1). We can also consider other quantum information processing applications for QDs, rather than full universal QC. For example, there is a lot of promise for QDs as a source of single photons [29], quantum memories [30] or as a photon switching device [31], due to their deterministic nature and potential to be integrated on chip. These devices also have the potential to be combined with other architectures, forming some kind of hybrid quantum computation platform [32–35].

We should note here that a quantum computer will not always provide an exponential speedup over its classical counterpart, despite being inherently faster at searching through data sets, due to the superposition property described above. Many quantum algorithms require additional processing power not needed in the classical equivalent, for example, storage of quantum states is computationally expensive, meaning that the speedup provided by the qubits themselves is negated in many cases [36]. Despite this, there are some applications in which QC is particularly effective. One of these is its ability to study interactions between atoms and molecules with much greater precision than classical computers will ever be capable of on reasonable timescales. This will have extensive applications in drug discovery and potentially creating new materials such as room temperature superconducters [37, 38]. Other potential applications which QC is particularly suited to include quantum machine learning, optimisation problems and financial modeling [39–42].

1.3.2 Quantum Key Distribution

This section will introduce the key concepts of quantum key distribution (QKD) and the current state of research in the field. The motivation for this section is the need for a long-lived quantum memory, an essential component of any long distance quantum communications protocol.

1.3.2.1 Theoretical description

QKD is one of the most advanced fields of quantum information processing in terms of applications. It is a method of transferring information securely between two parties, the quantum mechanical equivalent of public key cryptography [43–46]. In 1994, the world of cyber security faced a new type of threat - a quantum computing algorithm that allowed the reversal of the one-way functions that form the basis of public key cryptography [47, 48]. Although this algorithm came with the caveat that it required a quantum computer, it still had a huge impact on the field of classical cryptography, as its application would render many of the current classical protocols insecure. This led to research in the area of quantum cryptography and QKD quickly became established. QKD has the intrinsic advantage that its security relies not on the limits of today's computing power, but on the fundamental laws of physics. There are many different QKD protocols, and importantly, they all involve detection of any third party, or eavesdropper, who may be trying to intercept a message whilst it is being transferred between parties [49–56]. The fundamental concept used in all QKD protocols is that once a quantum state has been observed, it is irreparably changed. Then, if an eavesdropper were to intercept a message, translate it and then send it on to the receiver, hoping to remain undetected, it should in fact be possible to infer that the message has been read. This can be verified if we consider the errors induced in the message due to the eavesdropper.

The first QKD protocol to be developed, BB84 [49], uses the classical concept of encoding a signal in a light pulse, but with the significant difference that this light pulse contains only a single photon. This means that it is not possible for an eavesdropper to measure the information encoded in just part of each pulse and must instead observe the photon, destroying its state. It is possible for the eavesdropper to simply create a new qubit that is identical to the state they have observed, and send this state on to the receiver, however, the BB84 protocol details a method of encoding such that this is still detectable to the sender and receiver. This encoding method involves polarisation of single photon states that will then be transferred between the sender and receiver. Similarly to the classical case, the protocol will encode a 0 qubit and a 1 qubit. The condition that a 0 qubit must be encoded as either a horizontal state or a $-45°$ diagonal state, whereas a 1 qubit must be either a vertical state or a $+45°$ state is introduced. The sender will prepare these states randomly and the receiver will then choose at random to measure in either the horizontal-vertical basis or the diagonal ($\pm45°$) basis. Each qubit state will then be detected either in the correct basis with 50% accuracy or in the incorrect basis with 50% accuracy dependent on whether the receiver's choice of basis matches the sender's choice of basis. If the receiver chooses correctly, the qubit state they measure will be correct 100% of the time (assuming a perfect system). If the receiver chooses incorrectly, the qubit state they measure will be correct 50% of the time, i.e. the qubit state will be projected into either of the states in the chosen basis with equal probability. This gives an overall success probability for the receiver of 75%, excluding all errors. The receiver can then communicate with the sender over a classical channel, where they reveal the basis they used to measure the photon, but not the actual state of the photon. The sender will then tell the receiver which of their basis choices are correct and they both discard any photons where the receiver has chosen incorrectly, leaving them with a secure key which should be approximately half of the length of the original sequence.

Now, if we consider the introduction of an eavesdropper into this system, we find that this eavesdropper can also recover 75% of the information correctly by performing these random chosen basis measurements. However, they will not be able to compare measurement bases with the sender, and the quantum state that they have intercepted will be destroyed. They will then have to create a new quantum state, but will not be aware whether they have chosen the basis correctly or not, meaning that they will also not know whether the quantum state they have collected is correct. Then, if they want to send on a quantum key to the receiver, they will have to guess which of their states are correct and which are incorrect. This induces an error rate into the system. The sender and receiver can easily detect the presence of this error rate by simply selecting a small sample of their results and comparing the qubit state the receiver has detected (rather than just comparing the basis measured) with the state the sender encoded. Errors in this comparison confirm the presence of an eavesdropper and hence this key can be destroyed before it is used to transfer any quantum information.

1.3.2.2 Experimental implementations and limitations of QKD

Today, we have had many experimental implementations of QKD. The first of these was performed on a prototype device in 1989 by Bennett and Brassard [57, 58]. Since then, there have been many advancements, using various protocols and over various distances [59–62]. In addition to this progress, several countries are now building quantum networks, such that quantum information can be transferred over distances of a few hundred kilometres (the current record is 421km using ultra low-loss fibre [63] and 144km in free space [64]). However, performing QKD protocols over longer distances than this is difficult, due to the scaling of the error probability with the length of the channel, such that the photon count rate at the detectors is not sufficient to be reliably measured. To overcome this problem, the concept of a quantum repeater was introduced [65, 66]. A quantum repeater is a device that allows us to transfer a quantum state over longer distances by renewing the quantum state. However, unlike in the classical case, the quantum states cannot be detected or amplified without destroying the state. Instead, a quantum repeater is made up of two sources of entangled particles and a quantum measurement device. One of each of the two entangled pairs is measured using the quantum measurement device, thus projecting the other two particles into an entangled state. If the particles that are not measured have each moved some equal distance, d, in opposite directions from the source, then the entanglement distance is extended to a distance of $2d$, increasing the distance we could achieve entanglement over from a single source of entangled particles.

To extend this over even longer distances, multiple quantum repeaters can be used to reinforce the entangled state [67–69]. Then it becomes possible to excite the repeaters using a strong laser pulse to interfere photons from two neighbouring repeaters and entangle their excited states, extending the entanglement distance further still. However, this process does not have a 100% success rate and requires large cluster states. This suggests a need for a quantum state storage, known as a quantum memory, which encodes the quantum information in an excited state of matter [70, 71]. Proposals for such a quantum memory usually involve some solid state system, for example, an atom such as sodium or rubidium that possesses very strong optical transitions [72, 73], or rare-earth atoms that have transitions that are weak but much narrower [74]. These atomic memories are desirable because they possess naturally long coherence times, allowing for quantum states to be stored on long timescales. This application of quantum memories is the motivation for the work outlined in this thesis. In later chapters, we will discuss how we can use an Indium nuclear spin within a QD as a quantum memory, for applications in QKD and QC.

1.4 Semiconductor quantum dots

This section will discuss many of the properties of semiconductor quantum dots (QDs), motivating research that utilises this system as a platform for quantum information processing and quantum computation (QC), a concept first introduced in the late 1990s [10, 11, 75, 76]. We will study the solid state environment of QDs, including their status as effective two-level systems, fabrication of self-assembled QDs and their optical properties [77–80].

A QD is a semiconductor of typically $5-50$nm in size and containing around 10000-100000 atoms; small enough to exhibit quantum properties [81]. The development of QDs arose from the need for complete quantum confinement of light. The dimensionality of a semiconductor affects its density of states, such that as the dimensions are restricted, discrete energy levels for motion in the restricted plane are created. For example, the quantum well is a semiconductor that consists of a high bandgap semiconductor (the substrate) with a layer of low bandgap semiconductor, just a few nm thick, inside it. Then the carriers in this quantum well will have discrete energy levels in the normal direction of the plane of the well. As the dimensionality is restricted further, the discrete energies are found in all directions. A quantum well is 2-D, a quantum wire 1-D and the QD is found when we reach zero dimensions (see Fig. 1.1). The confinement of an electron within the QD is possible because the conduction band electrons in the low bandgap semiconductor have

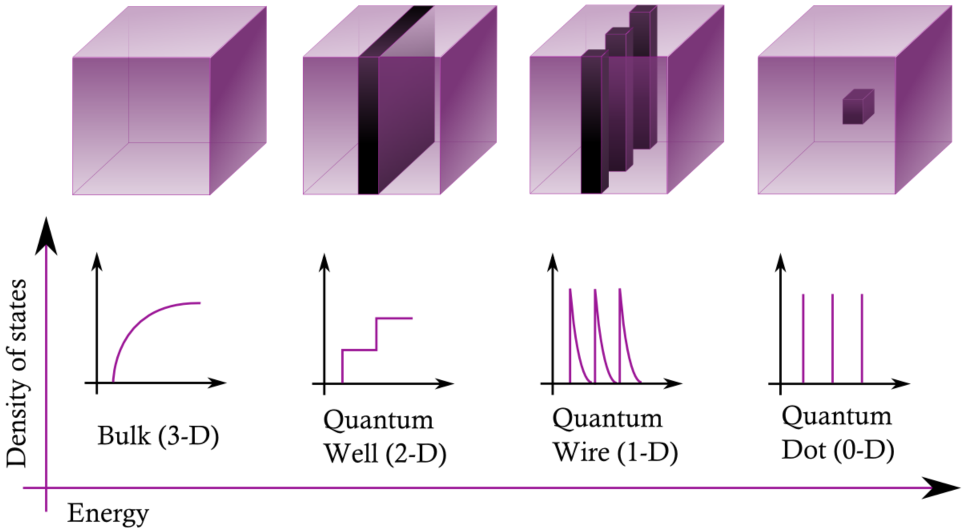

Figure 1.1: Visual representation of the effect of quantum confinement on the density of states of the excitonic states in bulk (3-D), quantum wells (2-D), quantum wires (1-D) and quantum dots (0-D).

a lower potential energy than those in the high bandgap material, which provides the confining potential. Similarly, the valence band of the low bandgap material is higher than that of the high bandgap material and so holes are also confined. Full quantisation of energy levels, as found in a QD, is a feature of atomic orbitals. This is the reason why a QD is often referred to as an artificial atom, and shares many of its behaviours.

1.4.1 Fabrication of self-assembled quantum dots

There are several conditions one wants to satisfy when fabricating a QD. Quantisation in all spatial dimensions is required with a level spacing on the order of tens of meV. We also require that one electron-hole pair remains bound, and these two conditions limit the size of the QD to a few nm. The fabrication method of the QDs we consider in this thesis is the Stranski-Krastanow growth technique [78, 82], a technique which uses molecular beam epitaxy (MBE). MBE allows for the deposition of monolayers of semiconductor materials on top of each other, allowing, initially, for the growth of quantum wells [83]. To extend this technique to QDs, we need to deposit two materials with differing lattice constants on top of one another.

The materials used for the QDs in this thesis are GaAs (high bandgap) and InGaAs (low bandgap). The QDs themselves will be formed from the InGaAs layer when it is deposited onto the GaAs. When depositing the InGaAs onto the GaAs, there will be an initial uniform layer known as the wetting layer. Then, as the thickness of the InGaAs layer increases, the strain induced by the lattice mismatch causes a preference for the InGaAs to grow into 3 dimensions, such that small islands are formed. These islands are the QDs, which are then capped with another layer of GaAs before they begin to break apart. A natural asymmetry will occur in the growth process, with the QD being smaller in the z direction than the x and y directions respectively (i.e. it will be wider than it is tall), leading to a greater confinement in the z direction. InGaAs QDs in a GaAs substrate will typically emit light at wavelengths of 850-1000nm and the particular QD samples we consider emit light at around 890nm, the near-infrared regime.

When using semiconductor QDs as a platform for quantum information processing, we would usually consider an excess electron spin confined within the QD as a spin qubit. For this electron spin to be present in the material, it is possible to dope InGaAs QDs with silicon such that they become ionised [84]. This is possible because of the tetrahedral structure of GaAs. Two silicon atoms each donate each of the four electrons in their outer shells to one of the four sp^3 hybrid bonds, allowing the material to form the diamond type lattice. Substitution of a silicon atom into a group III or V element produces a mobile hole or electron and an immobile ion. In the case of InGaAs, the group V element (As), must donate an electron to the group III element (Ga or In) to allow the formation of the sp^3 orbitals. This process can be controlled such that we can grow charged QDs with just one excess charge. Here we use silicon to created a negatively doped material, but we can choose to create an excess charge which is either positive or negative, depending on the nature of the ionising atoms we inject. The attraction of charged QDs is that the electron spins possess some very useful transition properties, which will be discussed below. The samples used in this thesis are produced using this method by the University of Würzburg.

1.4.2 Optical properties of quantum dots

Treating the QD as an artificial atom has many implications. We can assume that, as in an atom, excitons will recombine to produce photons, and furthermore, the energies of these photons will be well-defined. We find that the smaller the QD, the better the confinement, i.e., the larger the spacing of the energies between the levels. This large spacing leads to a high degree of isolation from the environment. However, the QD is, predominantly, a semiconductor, meaning that it has both advantageous and disadvantageous properties an atom does not. Optically, semiconductors are hugely flexible, as their size and shape are tunable [85]. QDs are also a useful tool in quantum optics as they are able to both absorb and emit photons. The absorption of a photon at the correct wavelength leads to a single electron residing in the valence band (VB) of the QD to gain sufficient energy to move to the conduction band (CB). This leaves a hole in the VB which will then be paired with the electron, forming an exciton, due to the Coulomb force between the two [86]. Due to the lower bandgap of the QD layer, the energy of the photon needed to excite an electron in this layer is lower than in the GaAs substrate. Because of this, the substrate is effectively transparent to the photons we use, and we are able to successfully excite an electron in the InGaAs QD layer only [87]. Recombination of the electron and hole will occur, provided that the total angular momentum of the electron and hole is equal to the possible values for the angular momentum of a photon (0 or ± 1). Similarly, optical excitation of a singly negatively charged QD leads to the

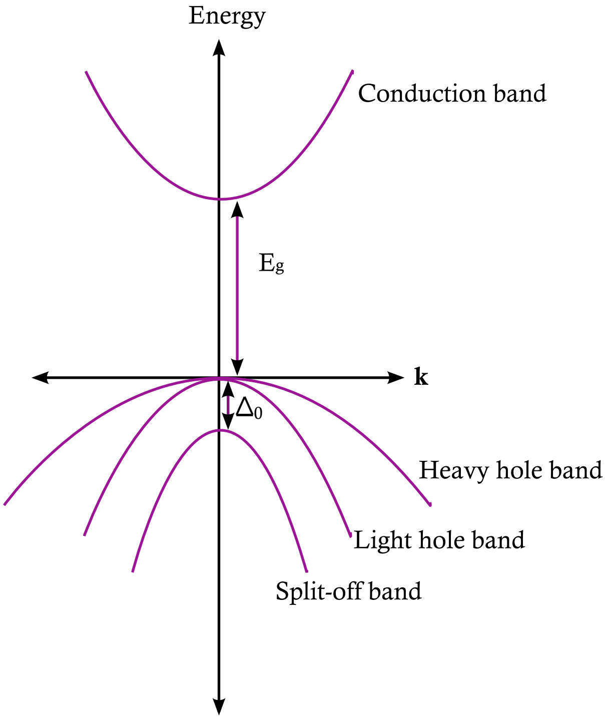

Figure 1.2: Bandstructure of a bulk direct bandgap semiconductor showing the allowed energy bands as a function of crystal momentum **k**. E_g is the bandgap energy and Δ_0 is the energy difference between the heavy and light hole bands and the split-off band. The conduction and split-off bands have total angular momentum $j = \frac{1}{2}$ and $j_z = \pm\frac{1}{2}$ whereas the heavy and light hole bands have $j = \frac{3}{2}$ with the heavy hole having $j_z = \pm\frac{3}{2}$ and the light hole $j_z = \pm\frac{1}{2}$

.

creation of a negatively charged exciton (trion) - a combination of two electrons and a single hole [88].

The bandstructure of a solid state system arises from both the intrinsic spin of the electrons within it and the atomic orbitals of the material itself (in this case InGaAs). GaAs and InAs are bulk direct bandgap semiconductors and have a band structure as shown in Fig. 1.2. In general, the CB will be filled with electrons and the VB filled with holes. The VB of the GaAs substrate is actually made up of three bands, each of which comes from the same p-shell, with orbital angular momentum $l = 1$. The CB comes from the s-shell and therefore has a single band which has a spin degeneracy of 2 and an orbital angular momentum of 0. As the electrons in the CB have a spin of $\frac{1}{2}$, the total angular momentum of the CB is $\mathbf{j} = \frac{1}{2}$. In the VB, as $l = 1$ we have $\mathbf{j} = \frac{3}{2}$. Then the CB has just one possible eigenvalue, corresponding to the single line we see in Fig. 1.2 [89, 90]. The VB has two possible eigenvalues, $j = \frac{1}{2}, \frac{3}{2}$. $j = \frac{1}{2}$ corresponds to the split-off band which has a large energy separation from the $j = \frac{3}{2}$ bands and can be neglected. The $j = \frac{3}{2}$ state then has $j_z = \frac{\pm 1}{2}, \frac{\pm 3}{2}$. The $\frac{\pm 3}{2}$ band has a larger effective mass and so is called the heavy hole (HH) band and the $\frac{\pm 1}{2}$ band is called the light hole (LH) band. The angular momentum of the HH is 1 and

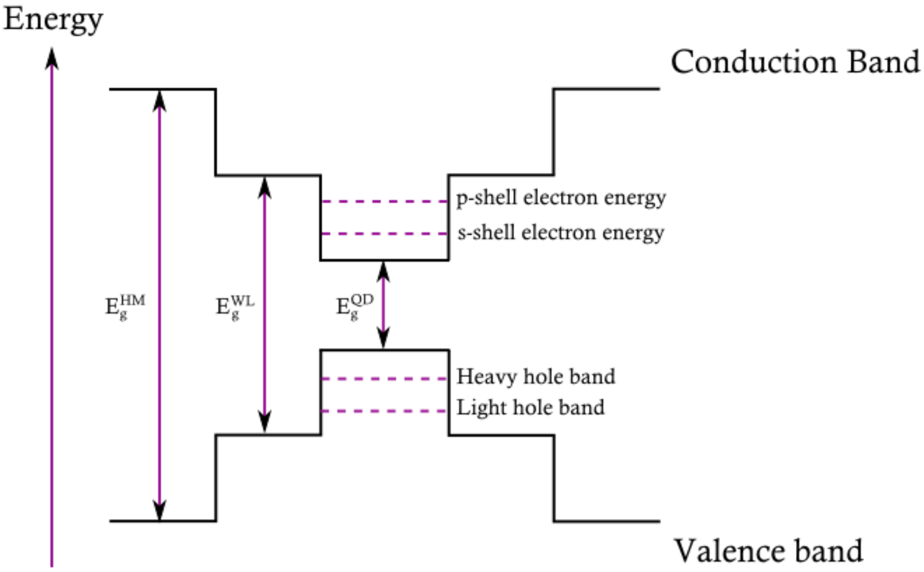

Figure 1.3: Bandstructure of a semiconductor QD. E_g^{HM} is the bandgap of the host material (GaAs). E_g^{WL} is the bandgap of the wetting layer - the interface between the GaAs and the QD. E_g^{QD} is the bandgap of the QD. Here there is a sub-band structure, containing, for the CB, the *s*- and *p*-shell transitions and, for the VB, we have the HH and LH bands. In contrast to the bulk semiconductor, these have an energy splitting.

the LH has an angular momentum of 0.

To extend this to QDs rather than bulk semiconductors we must consider the effects of confinement and strain [85]. In a bulk semiconductor, we expect to see mixing of the HH and LH. In the CB, we find that the electron can occupy one of two energy states, the lower energy *s*-shell and the higher energy *p*-shell. In the VB of a QD, the confinement potential and in-plane strain cause the degeneracy of the LH and HH bands to break and we find an energy separation between the two (see Fig. 1.3). This energy separation is small and the energies of the HH and LH still remain the closest of any of the dot states, meaning that there will still be some mixing of the energy levels. This causes the polarisation selection rules to become slightly elliptical, however, this isn't a large effect and can usually be ignored. The HH band is shifted less than the LH band and so is closer to the CB, which means that it is the more likely of the two to couple to the transition. We will assume that this is the prominent band and neglect the presence of the LH band. As HHs have angular momentum $m = \pm 1$ and spin quantum number $\pm\frac{1}{2}$, their possible states can be $\pm\frac{3}{2}$ and $\pm\frac{1}{2}$. However, the $\pm\frac{1}{2}$ states occur when the spin and angular momenta are anti-aligned (rather than aligned as in the $\pm\frac{3}{2}$ case) and this leads to these states being energy shifted far from the transition energy, meaning that we can neglect them and consider the $\pm\frac{3}{2}$ states only.

It is also necessary to define the wavefunction of the electron (or similarly the hole). This is

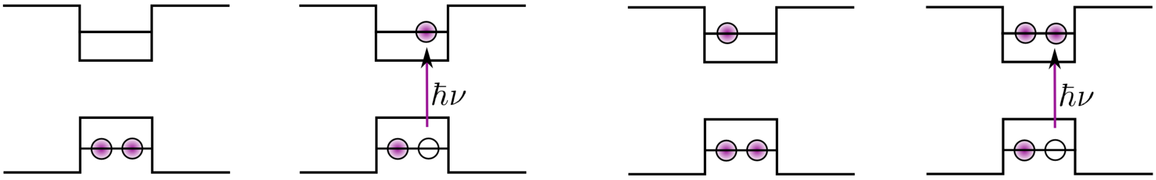

(a) Neutral QD

(b) Negatively charged QD

Figure 1.4: Diagram showing the occupied bands for (a) a neutral QD in the ground and excited state and (b) a charged QD in the ground and excited state. $\hbar\nu$ is the energy of the photon that excites the system.

delocalised over the envelope wavefunction describing the carriers and the total wavefunction is represented by the product of the Bloch wavefunction and the envelope wavefunction:

$$\Psi = u_k \phi(z). \tag{1.10}$$

Here, u_k represents the Bloch wavefunction part and $\phi(z)$ represents the envelope wavefunction part. We can think of the envelope part of the wavefunction in terms of homogeneity of the materials in the semiconductor. The confinement then follows from the difference in the CB and VB energies of the InGaAs and GaAs parts. The lowest energy state of the envelope wavefunction will have a Gaussian profile. When considering the Bloch part of the wavefunction, it is important to note the difference between an electron (or hole) in free space and in a semiconductor. In free space, the wavefunction of the electron will be given by a superposition of all possible locations of the electron. However, in a semiconductor, we instead define the wavefunction as a superposition of all atomic orbitals of each atom. Because, the crystalline structure of a QD is periodic, there is a coherent superposition over all available Bloch wavefunctions found on each ionic centre in the crystal. This means that the electron and hole wavefunction is delocalised, represented by the envelope wavefunction, which defines the exciton. This then gives an excited state that is a collective state and thus has a higher dipole strength than each individual part, giving a stronger light matter interaction than most atomic systems [79].

Considering the HH band as the only component of the VB, we can construct a simple diagram of the ground and excited states of the QD, as shown in Fig. 1.4. In Fig. 1.4(a) (the neutral QD), we start with the VB containing all of the electrons, one of which is excited to the CB upon introduction of a photon, leaving a HH behind in the VB. In Fig. 1.7(b) (the negatively charged QD), there is an excess electron in the CB before the state is excited, such that after the excitation there are two electrons in the CB and a hole in the VB. In the case of the neutral QD, the electron in the CB is bound to the hole it has left behind in the VB due to the Coulomb interaction, whereas in the charged QD, we have two electrons bound to one hole.

The energy level structure of a neutral QD is shown in Fig. 1.5. This takes into account the fine structure splitting that a non-symmetric neutral QD will experience. The structure will instead be as shown in Fig. 1.5 [91]. A neutral QD will have an empty ground state. There are

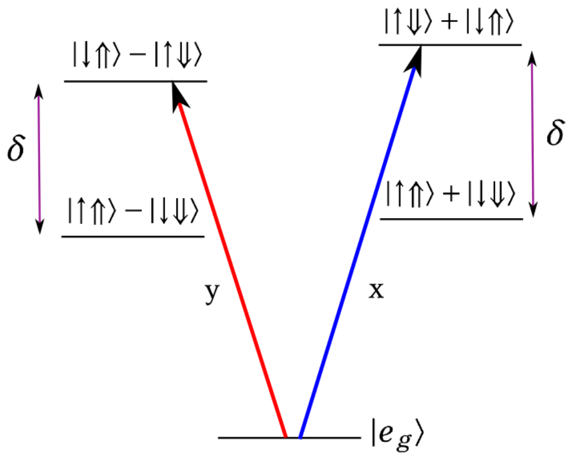

Figure 1.5: Spin selection rules of a neutral QD including the effects of fine structure splitting. The transitions are linear and there are four doublet states. δ is the energy splitting between the doublet states.

four exciton states, which will be arranged in doublets, with the possible electron-hole pairs being $|\uparrow\Uparrow\rangle$, $|\downarrow\Downarrow\rangle$, $|\uparrow\Downarrow\rangle$ and $|\downarrow\Uparrow\rangle$. The energy difference, δ, between the doublets is a result of the electron-hole exchange interaction and is affected by the strain acting on the system and its asymmetry. The higher energy doublets correspond to a bright transition and these have angular momentum of $m = \pm1$. The lower energy doublets have angular momentum $m = \pm2$ and are dark in general but may become bright when acted on by an external field with a component that is perpendicular to the optical axis, leading to a mixing of the two exciton transitions. This mixing leads to the transitions becoming linearly polarised with some energy splitting, which we call the fine structure splitting. This varies considerably between QDs, and is dependent on the geometry and crystalline structure of the QD.

We will now consider how the excess electron in a charged QD can be used as a spin qubit. If we consider the two spin states of this exciton, we find that due to the Pauli exclusion principle, which states that we cannot have two or more electrons or holes in the same state, the spin states of the two electrons are restricted such that we have either $|\uparrow\downarrow\rangle$ or $|\downarrow\uparrow\rangle$ where the arrows refer to the up and down spin states of each electron. In addition to this, formation of the charged exciton induces a change in angular momentum that leads to the polarisation sensitive transitions shown in Fig. 1.6. This means that for each electron spin state there is one possible trion state only, and this is what allows us to consider the electron spin as a qubit. First, consider the case of a charged QD in zero field, where the spin states of the system will be as shown in Fig. 1.7. We will consider excitation of the system via σ^+ (σ^-) photons, as these add (subtract) an angular momentum of 1 to the system.

We call the system a spin-up (-down) system if the electron in the CB is in the spin-up (-down) state and denote this electron spin state as $|\uparrow\rangle$ ($|\downarrow\rangle$). This state corresponds to the $\frac{+1}{2}$ ($\frac{-1}{2}$)

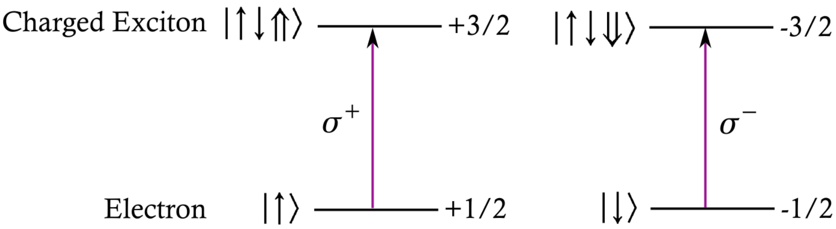

Figure 1.6: Allowed transition states of a charged QD subject to σ^+ and σ^- circularly polarised light.

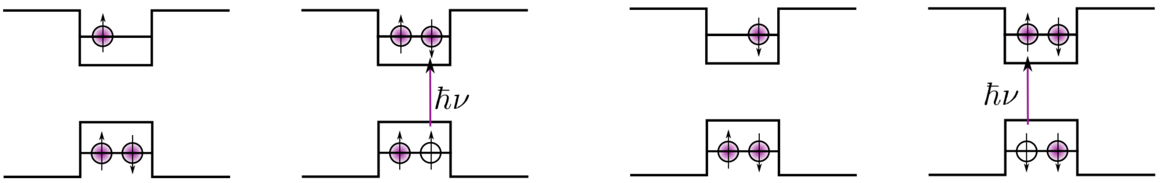

(a) Charged QD σ^+ excitation

(b) Charged σ^- excitation

Figure 1.7: Ground and excited spin states of a charged QD excited by (a) a σ^+ pulse and (b) a σ^- pulse along the optical axis.

angular momentum state. The promotion of a VB electron to the CB leaves a HH in the VB with angular momentum of $\frac{+3}{2}$ ($\frac{-3}{2}$) for the spin-up (-down) state. Thus, for angular momentum to be conserved we cannot have a transition between the two ground states of the system, leading us to consider the application of a magnetic field. The system we will consider in this thesis focuses on a magnetic field in the plane of the QD, perpendicular to the optical axis (Voigt geometry). We can define a Hamiltonian for the system of an electron-hole pair acted on by a Voigt field as [92]

$$H_B = \mu_B B_{ext}(g_e\hat{S}_e + g_h\hat{S}_h) \tag{1.11}$$

where g_e (g_h) is the g-factor of the electron (hole). We should note that the g-factor is different along the x axis to the z axis - the values of these vary quite considerably but reasonable values are around $g_{ex} \approx 0.5$ and $g_{ez} \approx 0.25$ [93, 94]. This difference in g factor is a result of the strain the system experiences during growth and the more highly strained the system, the greater the difference in these values. μ_B is the Bohr magneton and $\hat{S}_e$ ($\hat{S}_h$) is the spin operator for the electron (hole) where

$$\hat{S}_e = \frac{\hbar}{2}(\sigma_x + \sigma_y + \sigma_z) \tag{1.12}$$

and $\hat{S}_h$ is the corresponding term for a HH. σ_i are the Pauli matrices, which we will define as

$$\begin{aligned} \sigma_x &= \begin{pmatrix} 1 & 0 \\ 0 & -1 \end{pmatrix}, \\ \sigma_y &= \begin{pmatrix} 0 & -i \\ i & 0 \end{pmatrix}, \\ \sigma_z &= \begin{pmatrix} 0 & 1 \\ 1 & 0 \end{pmatrix}. \end{aligned} \tag{1.13}$$

We should note here that the σ_x and σ_z expressions are swapped with respect to the standard definition. This is due to the model we will introduce in Chapter 2 and will be explained in that section. Here, we will outline the process for an external field in both the Faraday and Voigt geometries.

For an external field in the Faraday geometry, we have

$$H_{BFar} = (g_{ex} + g_{hx})\frac{\mu_B B_x}{2}\sigma_x. \tag{1.14}$$

The Zeeman splitting of the spin states due to the external field is found by calculating the eigenstates of the system. The eigenstates of the ground state are

$$\begin{aligned} |e_{g1}\rangle &= |\uparrow\rangle \\ |e_{g2}\rangle &= |\downarrow\rangle \end{aligned} \tag{1.15}$$

with eigenvalues

$$\lambda^g_{1,2} = \frac{g_{ex}\mu_B B_x}{2}. \tag{1.16}$$

The eigenstates of the trion states are given by

$$\begin{aligned} |e_{t1}\rangle &= \frac{1}{\sqrt{2}}(|\uparrow\downarrow\rangle - |\downarrow\uparrow\rangle)|\Downarrow\rangle \\ |e_{t2}\rangle &= \frac{1}{\sqrt{2}}(|\uparrow\downarrow\rangle - |\downarrow\uparrow\rangle)|\Uparrow\rangle \end{aligned} \tag{1.17}$$

with eigenvalues

$$\lambda^t_{1,2} = \hbar\nu \mp \frac{g_{hx}\mu_B B_x}{2}. \tag{1.18}$$

This leaves the eigenstates of the system being along the z axis, which is also the energy eigenbasis.

For B_{ext} in the Voigt geometry we have

$$H_B = (g_{ez} + g_{hz})\frac{\mu_B B_z}{2}\sigma_z. \tag{1.19}$$

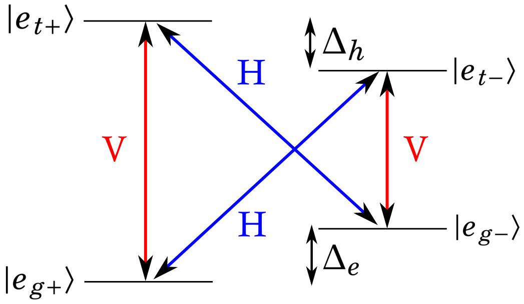

Figure 1.8: Diagram showing the optical transitions of a negatively-charged QD linearly polarised light in a Voigt field. The red lines are vertically polarised (y) transitions and the blue lines are the horizontally polarised (z) transitions. Δ_e (Δ_h) is the Zeeman energy splitting of the ground (trion) states.

By calculating the eigenstates of this system, we can find the Zeeman splitting of the spin states due to the magnetic field. We find that the eigenstates of the ground state are

$$|e_{g\pm}\rangle = \frac{1}{\sqrt{2}}(|\uparrow\rangle \pm |\downarrow\rangle) \tag{1.20}$$

with eigenvalues

$$\lambda^g_{0,1} = \pm\frac{g_{ez}\mu_B B_z}{2} \tag{1.21}$$

which represent the energy of the $|\uparrow\rangle$ ($|\downarrow\rangle$) state. The eigenstates of the trion states are dependent on the splitting of the LH and HH [95]. In practice, these are likely to be of the form

$$|e_{t\pm}\rangle = (a|\Uparrow\rangle \pm b|\Downarrow\rangle)|\uparrow\downarrow\rangle \tag{1.22}$$

where $|\Uparrow\rangle$ ($|\Downarrow\rangle$) is the spin-up (-down) state of the hole. Then the values of a and b are dependent on the amount of splitting between the LHs and HHs and if the splitting is large, the state approaches the case in which $a = b = \frac{1}{\sqrt{2}}$. This is because population can only move between the two HH states if it moves through the intermediate LH spin states. These are energetically separated by the LH/HH splitting. The exact eigenstate of the HH may actually involve all four possible hole states, whose weighting are determined by the relative power of the applied magnetic field, the g-factor and the HH/LH splitting. The eigenenergies that correspond to these eigenvalues are

$$\lambda^t_{0,1} = \hbar\nu \mp \frac{g_{hz}\mu_B B_z}{2}. \tag{1.23}$$

Thus, for B_{ext} in the plane of the QD, the eigenstates of the system will be along the z axis (although this is not the energy eigenbasis) and the size of B_{ext} determines the size of the energy splitting between the ground states of the electron. This leads to the optical transitions shown in

Fig. 1.8 for a negatively charged QD exposed to linearly polarised light, assuming no mixing of the trion states. The Zeeman splittings are given by

$$\begin{aligned} \Delta_e &= g_{ez}\mu_B B_z \\ \Delta_h &= g_{hz}\mu_B B_z \end{aligned} \tag{1.24}$$

for the ground and trion states respectively.

We can use these optical properties to control and define spin-based qubits within QDs. Protocols can be constructed that exploit these effects in a variety of ways for applications in quantum information processing, QC and QKD. In this thesis, our focus will be on nuclear spin quantum memories in QDs, and we will use the optical properties discussed above to lay out a realistic protocol for implementing a quantum memory scheme.

CHAPTER 2

NUCLEAR FREQUENCY FOCUSING IN A CHARGED QUANTUM DOT

This chapter will discuss the environment of a QD system, in particular, the dynamics of the nuclear spins in the host materials and how these nuclei affect the dynamics of the electron spin. This is a purely experimental chapter and begins with a summary of an existing model of the nuclear spin bath of a QD, leading on to a novel extension of the model, where we find parameters applicable to an experimental setting. We find that the nuclei act as a decoherence mechanism for the electron spin, such that its spin precession is perturbed and its coherence time shortened. We will consider potential solutions to this problem which involve creating a stable configuration for the nuclear spin using a train of laser pulses in conjunction with an external magnetic field in the plane of the QD. We then give details of how we will implement this experimentally and discuss parameters for the system that will allow this implementation to be successful.

2.1 Nuclear spin environment

2.1.1 Decoherence processes in quantum dots

As discussed in Chapter 1, a QD is a semiconductor made up of a large number of atoms. The QDs we consider are singly negatively charged InGaAs QDs in a GaAs substrate. Each of the atoms in the QD has a spin, with quantum numbers of up to 3/2 for Ga and As and 9/2 for In [96]. We will discuss how this nuclear spin bath affects the precession of a single electron spin qubit. We define the spin up and spin down states to be along the optical axis. To perform any quantum computation using this qubit, we need to fulfill the DiVicenzo criteria listed in Chapter 1. However, Criterion 5 states that the qubit needs to have sufficient isolation from its environment to limit the decoherence. The existence of the spin bath in a QD makes this qubit

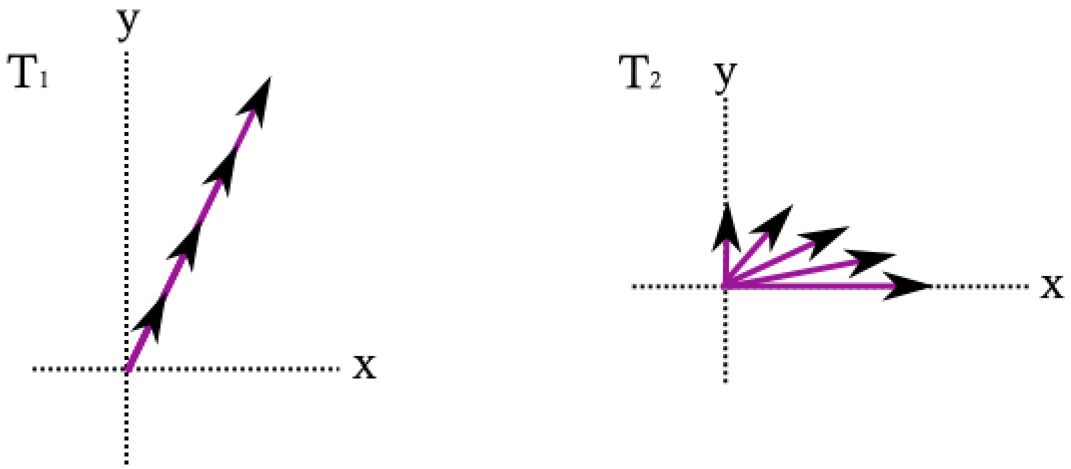

Figure 2.1: Here we see the decay of a spin particle in terms of the T_1 (left) and T_2 (right) timescales. The T_1 relaxation time is the time taken for the polarisation along the quantisation axis to decay, whereas the T_2 time is a transverse decay and as such, there is no polarisation decay, simply a loss of the phase information of the spin. In both cases, the arrow on the surface of the Bloch sphere shows the initial state, and this state becomes further from the original as the timescale increases.

isolation very difficult to achieve and it has therefore become the subject of interesting research in the field of QDs [97–99]. There are two possible ways in which a qubit state can experience decoherence, one of which can be characterised by the spin relaxation timescale T_1 and the other by the decoherence timescale T_2 (see Fig. 2.1) [100, 101]. The T_1 time characterises the likelihood of a spin-flip along the quantisation axis. The T_2 time describes the timescale on which the interactions between the spin and the environment change the phase of the spin precession about the quantisation axis [102]. An ensemble setting can refer either to multiple QDs or to multiple measurements on the same QD and describes the timescale over which the initial polarisation of a system decays back to its equilibrium value. The T_2^* time is the ensemble dephasing. When considering the ensemble dephasing time, there are additional factors to take into consideration, for example, variations in the local precession frequency of each spin can lead to a much faster ensemble dephasing. In addition to this, each QD has its own unique environment and these environmental configurations can vary dramatically between QDs, particularly in self-assembled samples, which will also play a role when we are considering the ensemble to be many QDs. The ensemble dephasing time in either form is labeled the T_2^* time and will obey the relation $T_2^* \leq T_2$ [103, 104].

In QDs, the decoherence and relaxation are mainly due to the hyperfine interaction and the spin-orbit interaction respectively. In general, the most significant component of the T_1 relaxation occurs as a result of spin-orbit interactions, most of which are suppressed in QDs due to the strong confinement of the wavefunction of the electron [105]. The electron-nuclear hyperfine flip-flop interaction can also play a role in the spin relaxation but this is suppressed in the presence of large external fields, where phonon-assisted relaxation dominates, giving typical T_1 times of the order of $10-100\mu$s without preparation of the electron spin [106], due to the size of the nuclear Zeeman splitting being considerably smaller than that of the electron (this is approximately three orders of magnitude smaller) [107]. However, preparation of the electron spin can lead to T_1 times on the order of ms [108]. In the low field limit ($B \lesssim 0.3T$), the hyperfine-induced relaxation will be the dominant term, and T_1 times can be on the order of seconds [109]. In contrast, the T_2 decoherence time is in general limited by pure dephasing mechanisms [106, 110]. T_2 can additionally be limited by spin-flip processes and can be much smaller than T_1, however it obeys the relation $T_2 \leq 2T_1$ [111], where $T_2 = 2T_1$ is the fundamental limit at which the spin relaxation is the only dephasing process. The T_2 time of electrons in InGaAs QDs has been shown to be of the order of up to μs, an unusually long decoherence time for electron spin qubits [112–114]. The T_2 time in the systems we consider is predominantly dictated by the hyperfine interaction, which we will describe in Section 3.1.1, and it is this that we will focus on controlling throughout this chapter.

2.1.2 Hyperfine interaction

The main source of decoherence in a low temperature QD is the hyperfine interaction: a dephasing of the electron spin induced by the presence of the nuclear spins. We will model the effect of this interaction and show that it is possible to suppress the effect of the spin bath on the electron spin using polarisation techniques discussed in detail below. First, we discuss the structure of the QD and how the atoms within it create such a noisy system. The QD itself is made of InGaAs, in a GaAs substrate. This tells us that we have many atoms of each of these materials within our system. In such a strained semiconductor, each of these atoms possesses a fermionic spin, as does the electron spin. This gives the electron and each of the nuclei a magnetic dipole moment, defined as

$$\mu = \frac{gq}{2m}\mathbf{S} \tag{2.1}$$

where g is the g-factor of the particle, q is the charge, m is the mass and $\mathbf{S}$ is the spin angular momentum (we will later define $\mathbf{S}$ to be the spin angular momentum of the electron and $\mathbf{I}$ to be the spin angular momentum of a nucleus). This value $\mathbf{S}$ is defined along any direction as

$$S_i = \hbar s_i, \; s_i \in \{-s, -(s-1), \cdots, s-1, s\} \tag{2.2}$$

where $i = x, y, z$, s is the spin quantum number and s_i are the eigenvalues of the system. Then each of the s_z, for example, has $2s+1$ possible values (the number is also the dimension of the Hilbert space of the system). For a spin-$\frac{1}{2}$ system this means that we have just two possible values of s_z, which are

$$s_z = \pm\frac{1}{2} \tag{2.3}$$

such that the spins are pointing in the $+z$ and $-z$ directions respectively. These states are then the spin up and spin down states along the z axis, a two-dimensional Hilbert space. These spin states will form a qubit along the quantisation axis. As this quantum number increases, we get more and more possible values of s_z. This defines the spin species of the atom. In terms of our QDs, Ga and As have nuclei of up to spin 3/2 and In has nuclei of up to spin 9/2. We can use this to model how the spin precession is affected by the presence of some external field, B_{ext}. First, consider the precession of an electron spin in the absence of a nuclear spin bath. In the absence of an external field, an electron spin will be randomly oriented with two degenerate energy levels. Applying some external field vector, $\mathbf{B}_{ext}$ causes these two energy levels to split as the spin projection must be oriented in one of two states either parallel or anti-parallel to $\mathbf{B}_{ext}$. This system comprising of a single electron spin in a field $\mathbf{B}_{ext}$ will then be described by the Hamiltonian

$$H_{elec} = \frac{g_e \mu_B}{2} \mathbf{S} \otimes \mathbf{B}_{ext} \tag{2.4}$$

where g_e is the g-factor of the electron, μ_B is the Bohr magneton and $\mathbf{S}$ is the spin vector of the electron. The energy of each of the two spin states can then be found by calculating the eigenvalues of H_{elec} as shown in Chapter 1.

This is the full Hamiltonian of an electron precessing according to an external field only, however, this Hamiltonian is not a reasonable description of an InGaAs QD system as we must also consider the nuclei found in the InGaAs material. This leads to two more terms in the system - a term describing the effect of the external field on each of the nuclei in the spin bath, given by

$$H_{nuc} = \frac{\mu_N}{2} \sum_{i=1}^{n} \mathbf{I}_i \otimes \mathbf{B}_{ext} \tag{2.5}$$

where μ_N is the magnetic moment of the nuclei, n is the total number of nuclei and $\mathbf{I}$ is the nuclear spin operator, and a hyperfine coupling term between the electron spin and each of these nuclei, defined as

$$H_{int} = \sum_i A_i \mathbf{S} \otimes \mathbf{I}_i \tag{2.6}$$

which will be derived below (A_i represents the coupling between the electron and each nucleus). It is this hyperfine coupling and its effect on the precession of the electron spin that will be the focus of the chapter. There is currently no conclusively accurate theoretical description of the electron and nuclear spin bath in a QD that sufficiently represents the complexity of the QD environment. Because the wavefunction of the excess electron overlaps with that of each nucleus within the QD, the magnetic moment of the electron will interact with the magnetic moment of each of these nuclei. This causes a shift in the energy levels of the electron and defines its hyperfine structure. This induces a coupling between the electron and nuclei, which is determined by their relative positions within the QD. This manifests as a change in the effective magnetic field applied to the electron spin (the effective field is defined as the external field plus the nuclear field), as the precession of each nucleus will cause perturbation of the effective field acting on the electron by some amount dependent on the strength of the coupling between them. We also find that as each nucleus has its own individual strain-dependent hyperfine splitting and therefore precession frequency, there is not only an effective field induced by the nuclei, but this field also varies on the timescale of the nuclear precession. This means that we are not able to calculate the value of this effective field and adjust the external field accordingly to compensate for this. Instead, we need to consider methods to suppress this unpredictable precession and this will be discussed in detail below.

We can derive the Hamiltonian for the interaction between an electron with spin $\mathbf{S}$ and a single nucleus with spin $\mathbf{I}$ by considering the Dirac equation of an electron in some potential $V(\mathbf{r})$

$$H_{Dirac} = \mathbf{M} \cdot c(\mathbf{p} + e\mathbf{A}) + \mathbf{P}mc^2 - eV(\mathbf{r}) \tag{2.7}$$

where $\mathbf{A}$ is the vector potential of the electromagnetic field, e is the electron charge, m is the electron rest mass,

$$\mathbf{M} = \begin{pmatrix} 0 & \boldsymbol{\sigma} \\ \boldsymbol{\sigma} & 0 \end{pmatrix} \tag{2.8}$$

where $\boldsymbol{\sigma}$ is the vector of Pauli matrices and $\mathbf{P}$ is the 4×4 identity matrix [115]. Taking a nucleus with magnetic moment μ_N yields

$$\mathbf{A} = \nabla \frac{\mu_N}{r} \tag{2.9}$$

where r is the distance of the nucleus from the electron. This translates to a Hamiltonian of the form (derivation can be found in [115])

$$H_{en} = \frac{16}{3} \pi \mu_b \mu_N \mathbf{S} \otimes \mathbf{I} \delta(\mathbf{r}) \tag{2.10}$$

assuming the non-contact term vanishes for an electron wavefunction with s symmetry. Then H_{en} is equivalent to the Fermi contact hyperfine interaction, given by

$$H_{Fermi} = A \mathbf{S} \otimes \mathbf{I} \tag{2.11}$$

where A represents the position-dependent hyperfine coupling constant and is defined as

$$A = \frac{16}{3} \pi \mu_B \mu_N |\psi(0)|^2 \tag{2.12}$$

with $\psi(0)$ describing the probability of finding the electron at the nucleus, i.e. the overlap. This model describes the interaction between the electron and a single nucleus. To extend this to the many spin case, we consider the electron wavefunction as a superposition of atomic orbitals which occur at every possible atomic site within the QD. We can write the Hamiltonian for the interaction between the electron spin and some number i of nuclei for unspecified values of A_i as

$$H_{int} = \sum_i A_i \mathbf{S} \otimes \mathbf{I}_i. \tag{2.13}$$

with

$$A_i = \frac{16}{3} \pi \mu_B \mu_N |\psi(\mathbf{r}_i)|^2 \tag{2.14}$$

for each nucleus at site $\psi(\mathbf{r}_k)$. For the purposes of this work, we can neglect dipole-dipole couplings between nuclei as these will be suppressed for the fields we are considering [116]. This leaves us with the full Hamiltonian for the system being given by

$$H = H_{elec} + H_{nuc} + H_{int}. \tag{2.15}$$

As a typical nuclear spin bath contains around 10^5 atoms, each of which has a unique position-dependent coupling to the electron spin, we cannot model each of these nuclei individually and so we cannot easily predict the exact behaviour of the system. We therefore look into ways of controlling the dynamics of the bath, such that it will behave in a predictable way. This involves a "calming" of the nuclear spins where we narrow the set of possible states of each nucleus by adding some degree of polarisation along a particular axis due to application of an external field and a train of laser pulses. By controlling this polarisation carefully, we can force the bath into a state that is effectively decoupled from the electron spin precession. There are several proposals that provide potential solutions to this problem by introducing some polarisation of the nuclear spin bath along a magnetic field using a variety of pulse sequences and field strengths [117–122]. We focus on one particular solution proposed by Sophia Economou *et al.* [123] and discuss how this model can be modified to be applicable in an experimental context. The model appears to capture the main processes observed in results obtained by Greilich et al. [93, 124], where the nuclei appear to "remember" the presence of a train of laser pulses applied to an ensemble of QDs and exhibit signs of spin calming along a magnetic field axis. Our application differs from this in that we require single QD nuclear calming and previous results have only been successful in ensembles of QDs. Extending this model to single QDs rather than ensembles is a desired result for the quantum computing world as this would allow for the production of quantum information processing equipment, including single photon sources and quantum memories, both of which require the long spin coherence times we aim to create. The basic premise of the model is detailed below.

First we assume that we have a negatively charged QD which is acted upon by an external field in the plane of the QD (Voigt geometry) and we call the axis of the field the z axis for ease in calculations (see Fig. 2.2). We then apply a train of circularly polarised pulses along the optical axis (we call this axis the x axis). The level diagrams for this system are shown in Fig. 2.3. The first of these diagrams shows us the level structure in terms of the energy eigenstates. The

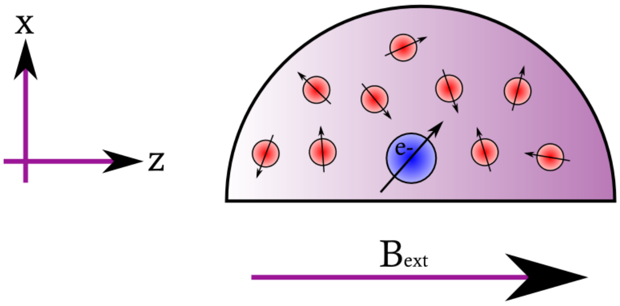

Figure 2.2: Diagram defining the axes used and the direction of the external magnetic field considered throughout this chapter. Note that the shape of the QD will in practice be flat-topped, due to the capping layer added in the growth process.

external field causes a splitting of the electron spin states along the field axis and so when we consider the states in the basis of the optical axis we find that we in fact excite a superposition of the $|\uparrow\rangle_x$ and $|\downarrow\rangle_x$ states. As described in Section 1.4.2 in Chapter 1, a circular pulse will excite only one of two degenerate electron spin states to the trion state. However, as our spin states are non-degenerate in the energy eigenbasis, it is more intuitive to look at the system in terms of the z basis states, where we can define $|\uparrow\rangle_z$ and $|\downarrow\rangle_z$ as basis states. We show the level diagram in terms of both basis states in Fig. 2.3. Then we find that each one of these states will be excited by one of the two circularly polarised pulses only. However, as these states are not eigenstates of the system, there is a mixing between them due to the external field, such that there will be some population transfer between the two ground states of the electron spin. This means that by pumping a single transition with a train of circularly polarised pulses, we are able to transfer some population of the spin state we excite to the opposite spin state. Driving the electron spin in such a way means that the nuclei will see a coherent electron spin precession and will then align into a preferred configuration that allows the electron spin to remain precessing coherently in the absence of the magnetic field and pulse train. We describe this process in detail below.

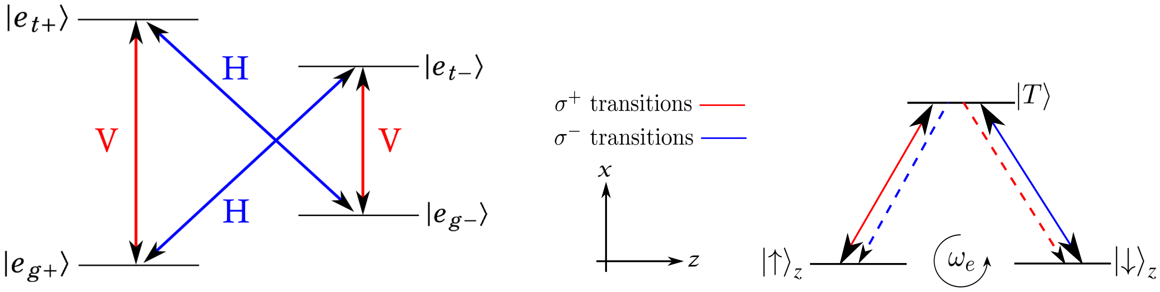

Figure 2.3: The first diagram shows the allowed transitions between the eigenstates $|e_{g\pm}\rangle$ to the trion states $|e_{t\pm}\rangle$. The second diagram is in terms of the optical states for circular pulses. $|T\rangle$ is the trion state (assumed to be a mixture of the two trion states) and ω_e is the total field acting on the electron, causing a mixing of the ground states.

2.1.3 An electron spin acted on by a circularly polarised pulse

The remainder of this section is based on ideas found in [123]. Results from the paper are derived here and we then remodel the results in terms of our experimental parameters. To model this system, we first define the Hamiltonian for an electron spin in a magnetic field in the Voigt geometry acted on by a train of pulses. This is given by [123]

$$H = \omega_e S_z + \epsilon_T |T\rangle\langle T| + \sum_j q(t - jT_R)|\downarrow\rangle_z \langle T| + \text{H.c.} \tag{2.16}$$

where $\omega_e = g\mu_B B_{ext}$ is the precession frequency of the electron due to the external field, B_{ext}, where g is the g-factor of the electron, and μ_B is the Bohr magneton. Note that the S_z term refers to a field in the Voigt geometry, meaning that the ground states are $|\uparrow\rangle \pm |\downarrow\rangle$. The second term gives the population of the trion state ($|T\rangle$ is the trion state with energy ϵ_T). The third term is the pulse term where we have some pulse train of j pulses, each being described by a parameter $q(t)$ which is periodic with period T_R. This excitation acts on the state $|\downarrow\rangle_z$ when we choose $q(t)$ to be a σ^- pulse (or on $|\uparrow\rangle_z$ for a σ^+ pulse). The timescale of a single pulse is of the order of one picosecond whereas the spontaneous emission from the trion state is of the order of 500ps - 1ns. We can therefore use the approximation that the pulses are instantaneous. We can use this Hamiltonian to define Kraus operators representing this system, the full derivation of which can be found in section A.1 of Appendix A.

There are three Kraus operators representing the dynamics of the system:

$$\begin{aligned} E_1 &= \begin{pmatrix} 1 & 0 \\ 0 & q \end{pmatrix} \\ E_2 &= \begin{pmatrix} 0 & a_1 \\ 0 & -a_2 \end{pmatrix} \\ E_3 &= \begin{pmatrix} 0 & 0 \\ 0 & \kappa \end{pmatrix} \end{aligned} \tag{2.17}$$

where E_1 is the Kraus operator describing the pulse and E_2 and E_3 describe the spontaneous emission of the system and we define

$$\begin{aligned} a_1 &= \omega_e \sqrt{\frac{(1-q_0^2)}{2(4\gamma^2+\omega_e^2)}} \\ a_2 &= i\gamma\sqrt{2}\sqrt{\frac{(1-q_0^2)}{4\gamma^2+\omega_e^2}} \\ \kappa &= \sqrt{1-q_0^2-a_1^2-|a_2|^2} \end{aligned} \tag{2.18}$$

for some parameter $q = q_0 e^{i\phi}$ describing the pulse where $0 \le q_0 \le 1$ and $0 \le \phi \le 2\pi$. $\sqrt{1-q_0^2}$ is the population transfer from the ground to the trion state and ϕ is the rotation about the

x axis induced by the pulse. $q = 0$ corresponds to a resonant π pulse and $q = 1$ corresponds to no pulse. A value of q_0 between 0 and 1 will represent some pulse with an area of $< \pi$, getting weaker as $\pi \longrightarrow 1$. Note that the trion component of the final state has been omitted as this has no population after spontaneous emission (i.e. it generates no spin population). Currently, these Kraus operators provide us with a theoretical description of the system, but are difficult to relate to physical parameters that we can vary. Therefore, we want to map these parameters onto experimental values. We can relate these parameters to the power and detuning of the laser pulse if we assume the pulse is a hyperbolic secant (as in [123]) [125]. Then we find

$$\begin{aligned} q &= F(b,-b,c*,1) \\ &= \frac{\Gamma(c)^2}{\Gamma(c-b)\Gamma(c+b)} \end{aligned} \tag{2.19}$$

where F is Gauss's hypergeometric function, Γ is the Γ function, $b \equiv \Omega = \frac{\Omega_0}{\sigma}$, $c = \frac{1}{2}(1 + i\frac{\Delta_0}{\sigma}) \equiv \frac{1}{2}(1 + i\Delta)$ (Δ represents the detuning such that $-1 \leq \Delta \leq 1$ where $\Delta = 0$ represents the resonance condition, $\Delta = \pm 0.5$ is the point where the QD resonance is at the half maximum of the pulse and $\Delta = \pm 1$ is the point at which there is no overlap between the pulse and the resonance), Ω_0 is the Rabi frequency, Δ_0 is the detuning and σ is the bandwidth of the pulse. Then we define

$$\begin{aligned} q_0 &= |F(\Omega,-\Omega,\frac{1}{2}(1+i\Delta),1)| \\ \phi &= \mathrm{Arg}(F(\Omega,-\Omega,\frac{1}{2}(1+i\Delta),1)). \end{aligned} \tag{2.20}$$

We can then use this to determine the relationship between the theoretical parameters q_0 and ϕ and the experimental parameters Δ and Ω. This relationship between q_0 and Δ and Ω is plotted in Fig. 2.4(a) and similarly the relationship between ϕ and Δ and Ω is shown in Fig. 2.1.3. We can see that both q_0 and ϕ are periodic with Rabi frequency, with the period of q_0 being double that of ϕ. Intuitively, it may be useful to think of q_0 as representing the population of the ground state (note that this is not completely accurate, as $\sqrt{1-q_0^2}$ is the population from the ground to the trion state). The value of ϕ represents the angle of the precession of the electron with respect to the optical axis. Fig. 2.4(a) tells us that $q_0 = 0$ (note that this includes the case of the resonant π pulse, $q_0 = 0$, $\phi = 0$) corresponds to a detuning of 0 and that as the pulse becomes more and more detuned, the population transfer to the excited state decreases. This is due to the pulse moving far from the resonance such that the QD experiences only a small effect from the pulse and therefore application of more pulses becomes necessary to successfully drive the electron spin. In terms of ϕ, we find that varying the detuning has only a small effect, whereas the dependence on the Rabi frequency is much more significant and we see switching between the minimum and maximum values for the case of zero detuning as the Rabi frequency increases. Note that the case where $\phi = \pi$ is qualitatively equivalent to the case $\phi = -\pi$, with the only difference being the direction of the rotation from the resonance. We will use these results to relate all further calculations in this chapter to the detuning and Rabi frequency of the pulse, such that we can find experimentally applicable parameters for the protocol.

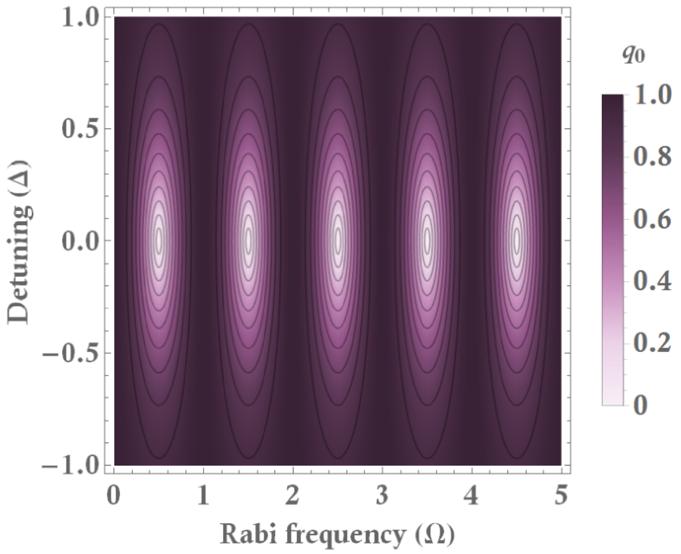

(a) Relationship between q_0 and the Rabi frequency and detuning of the laser pulse.

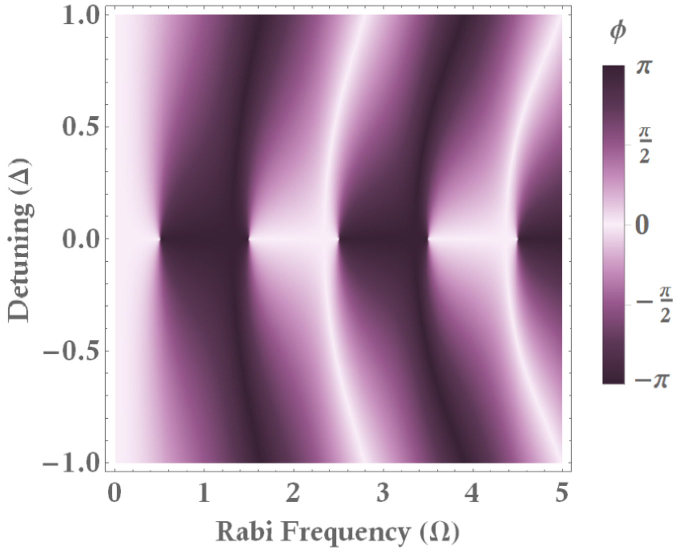

(b) Relationship between ϕ and the Rabi frequency and detuning of the laser pulse.

Figure 2.4: Graphs relating the theoretical parameters q_0 and ϕ to the experimental parameters Ω and Δ.

We will now discuss how the nuclear spin bath can be forced into some predictable and stable configuration. We want to induce some nuclear spin "polarisation" along the axis of the external magnetic field (the z axis as defined in Fig. 2.2, i.e. we want to drive the system in some way that means the nuclei will align such that they have some known population along the z axis. This will allow us to more accurately predict the precession frequency of the electron spin due to the both the external field and the field induced by the nuclei. We consider the amount of polarisation the electron will gain along the optical axis due to this protocol for different parameters. If we define the initial density matrix of a single electron spin to be

$$\rho_{in} = \begin{pmatrix} \rho_{xx} & \rho_{x\bar{x}} \\ \rho_{\bar{x}x} & \rho_{\bar{x}\bar{x}} \end{pmatrix} \tag{2.21}$$

then we can calculate the state of the system after a single application of the laser pulse by acting the Kraus operators defined in Eq. A.14 on ρ_{in}, i.e.

$$\rho_{gen} = \sum_i E_i \rho_{in} E_i^\dagger \tag{2.22}$$

The general state of the system after a single pulse will then be given explicitly by

$$\rho_{gen} = \begin{pmatrix} \rho_{xx} + |a_1|^2 \rho_{\bar{x}\bar{x}} & q^* \rho_{x\bar{x}} - a_1 a_2^* \rho_{\bar{x}\bar{x}} \\ q\rho_{\bar{x}x} - a_1^* a_2 \rho_{\bar{x}\bar{x}} & (|q|^2 + |a_2|^2 + |\kappa|^2)\rho_{\bar{x}\bar{x}} \end{pmatrix}. \tag{2.23}$$

and taking $\mathrm{Tr}(\rho_{gen}\sigma_i)$ tells us the population of the electron spin state along each axis after each pulse, which we define to be the amount of polarisation along that particular axis. The amount of polarisation along the z axis (the axis of the external field) for the initial state (before application of the pulse) is given by

$$\begin{aligned} Pol_{z,in} &= \mathrm{Tr}(\rho_i n \sigma_z) \\ &= 2\mathrm{Re}[\rho_{x\bar{x}}]. \end{aligned} \tag{2.24}$$

and after application of a single pulse is

$$\begin{aligned} Pol_{z,gen} &= \mathrm{Tr}(\rho_{gen}\sigma_z) \\ &= \mathrm{Re}[q^* \rho_{x\bar{x}} + q\rho_{\bar{x}x} - (a_1 a_2^* + a_1^* a_2)\rho_{\bar{x}\bar{x}}] \\ &= 2q_0 \cos\phi \mathrm{Re}[\rho_{x\bar{x}}]. \end{aligned} \tag{2.25}$$

In order to successfully induce polarisation along the z axis, we require the condition

$$Pol_{z,gen} > Pol_{z,in} \tag{2.26}$$

such the action of the pulse increases the amount of population along this axis.

We can see that in the case where $q = 0$ (implying $q_0 = 0$, the condition for a resonant π pulse), $Pol_{z,gen}$ term vanishes, meaning that there can be no polarisation gained along this axis by simply applying resonant π pulses along the x axis to a single electron spin. Then to gain polarisation along this axis, we require the condition $q > 0$ (implying $q_0 > 0$). This enforces the condition $\Delta > 0$ but does not yet put any restrictions on our choice of Ω. If we consider the case where $\phi = 0$, $q_0 \neq 0$, we find

$$Pol_{z,gen} \quad = \quad 2q_0 \mathrm{Re}[\rho_{x\bar{x}}]. \tag{2.27}$$

As $q_0 < 1$, this will always give the condition $Pol_{z,gen} \leq Pol_{z,0}$. Therefore, a non-zero rotation of the electron about the optical axis is required to create polarisation along the z axis. However, we discuss later that this is only true for the single spin case, as one can imagine a scenario in which we could have two polarised nuclei in opposing directions along the z axis and retain this particular electron spin state. Thus, we conclude that to gain polarisation through application of a pulse of this form, we require $q_0 \neq 0$, $\phi \neq 0$, i.e., the pulse must not be a π pulse and must be detuned and rotated from the QD resonance to allow the electron spin to gain polarisation along this axis.

Here, we should also mention what happens when we include the external magnetic field in this model. In the presence of an external magnetic field, B_{ext}, along the z axis (Voigt geometry), when the system is between pulses it will evolve according to Larmor precession

$$U_B = e^{-\omega_e T_R \hat{S}_z} \tag{2.28}$$

where T_R is the repetition rate of the pulse and S_i is the electron spin operator along the i axis with $S_i = \frac{1}{2}\sigma_i$. Then the evolution of some density matrix $\rho_{B,0}$ due to U_B can be calculated using

$$\rho_{B,f} \quad = \quad U_B \rho_{B,0} U_B^{\dagger}. \tag{2.29}$$

To combine this evolution with our pulse evolution, we define a new Kraus operator

$$\mathscr{E}_i \quad = \quad E_i U_B \tag{2.30}$$

such that for some initial state ρ_0, the state after application of a single pulse with $B_{ext} \neq 0$ is given by

$$\rho_f \quad = \quad \sum_i \mathscr{E}_i \rho_0 \mathscr{E}_i^{\dagger}. \tag{2.31}$$

We can use this to find the steady state of the electron spin will be driven to after n periods (where one period is one application of ρ_f). The derivation for this is given in Appendix A.2. This delivers an electron steady state that is of the form $(1, S_x, S_y, S_z)$ (where S_x, S_y and S_z are also given explicity in Appendix A.2). This tells us that in general there will be some population of the electron spin state along each axis, and the direction of the spin is dictated by the values of Δ, Ω and B_{ext}.

2.1.4 The single nuclear spin model

To extend this model to include the nuclear spin bath we first consider the simplest case of a single nuclear spin. Then we replace U_B with

$$U_{hf} \quad = \quad e^{-iH_{hf}t} \tag{2.32}$$

where H_{hf} is the Hamiltonian for the hyperfine interaction between an electron and a single nuclear spin and is given by

$$H_{hf} \quad = \quad \omega_e S_z \otimes \mathbb{I}_n + \omega_n \mathbb{I}_e \otimes I_z + A \sum_{j=x,y,z} S_j \otimes I_j. \tag{2.33}$$

Assuming that the pulse is applied to the electron spin only and the nucleus is unaffected, we can redefine the Kraus operators for this system to be

$$\mathscr{F}_i \quad = \quad U_{hf}(E_i \otimes \mathbb{I}). \tag{2.34}$$

The initial density operator for the system will now be the tensor product of the initial state of the electron with the initial state of the nuclear spin, given by

$$\rho_{en,0} \quad = \quad \rho_{e,0} \otimes \rho_{n,0} \tag{2.35}$$

where we have renamed the initial density operator of the electron spin state to be $\rho_{e,0}$ and $\rho_{n,0}$ is the initial density operator the nucleus. We can then apply the method used above to define an equivalent expression to that given in Appendix A.2 which can be solved as an eigenvalue problem for the two-spin system as for the electron only case. However, we can instead use an approximation to say that on short timescales (i.e. less than the interaction time) this state is in fact separable, i.e. $\rho_{en} = \rho_e \otimes \rho_n$, which leads to the spin operators also being separable:

$$S_{e,n} \quad = \quad S \otimes I. \tag{2.36}$$

For this approximation, we assume that the flip-flop term (the term that induces nuclear spin flips), which is defined as $A(S_+I_- + S_-I_+)$ ($S_\pm = S_x \pm iS_y$ and similarly for $I_\pm$) is taken to second order. This is equivalent to saying that we assume the electron reaches its steady state much quicker than the nuclear spin and that the nuclear spin evolution is much slower than the pulse repetition rate, T_R. I will refer to this approximation as the Markovian approximation for consistency with [123], however, there are some differences between the standard Markov approximation and the approximation we use here. The standard definition of the Markov approximation assumes that the bath correlation quickly goes to zero on the timescale of the change in the evolution of the density operator [126]. There are also similarities between our approximation and the Born approximation, which allows one to take an incident field in place of the total field as the driving field at each point, valid if the scattered field is small compared to the incident field. This means any correlations between the system and bath can be ignored and the density operator of the nuclear spin bath can be assumed to be time-independent. We should note here that making this approximation means that we must also put a restriction on our value of q_0. If we take a value of q_0 that is close to 1, this is equivalent to a weak pulse. This means that it takes many cycles of the pulse to pump the electron into its steady state, lengthening its initialisation time and so we introduce the condition $q_0 \leq 0.5$, chosen using Fig. 2 in [123], which shows the timescale on which the electron spin will reach its steady state for varying values of q_0. Now, it is possible to extract the components of I from $S_{e,n}$, using the equation (see Appendix A.2)

$$(\mathscr{Y}_n)_{\alpha\beta} = \frac{d}{dI_\beta}[\mathscr{Y}_{\rceil\backslash}(S \otimes I)]_\alpha \tag{2.37}$$

and the steady state of the nuclear spin will be given by the eigenstate of $\mathbb{I} - \mathscr{Y}_n$ with zero eigenvalue. This turns out to be of the form (see Appendix A.3)

$$I = (1, 0, 0, I_z) \tag{2.38}$$

such that all polarisation is gained along the axis of the external field. This is due to the strong driving of the electron spin along the optical axis, such that a nucleus will take on the most stable configuration in terms of the electron spin state and the external field. I_z is given explicity in Appendix A.3. The smallest non-zero eigenvalue, λ_1 gives the rate at which the nuclear spin reaches its steady state, which we define as $\gamma_n = \lambda_1/T_R$. The time taken for the steady state to be reached must be sufficiently short to satisfy the Markovian approximation and will affect the T_2 time of the system. Calculations for the steady state and the relaxation rate are given in Appendix A.4.

2.1.5 Including the full nuclear spin bath

To include the full nuclear spin bath in the model, we need to define the nuclear spin flip rate. To do this, we need to consider the nuclear spin state at some time, t, given by

$$\begin{aligned} I_z(t) &= \sum_j \mathbf{v}_j e^{-i\lambda_j t} \\ &\approx I_z^{(0)} e^{-\gamma_n t} + I_z(1 - e^{-\gamma_n t}) \end{aligned} \tag{2.39}$$

where $I_z^{(0)}$ is the zeroth order of the perturbative expansion of I and I_z is the nuclear steady state. We can define the probability for the nucleus to be aligned parallel or anti-parallel to the axis of the magnetic field as

$$\begin{aligned} P_\uparrow &= \frac{1}{2}(1 + I_z(t)) \\ P_\downarrow &= \frac{1}{2}(1 - I_z(t)). \end{aligned} \tag{2.40}$$

This gives

$$I_z(t) = P_\uparrow - P_\downarrow. \tag{2.41}$$

Combining Eqs. 2.40 and 2.41 and differentiating with respect to t gives

$$\begin{aligned} \frac{d(P_\uparrow - P_\downarrow)}{dt} &= -\gamma_n I_z^{(0)} e^{-\gamma_n t} + \gamma_n I_z e^{-\gamma_n t} \\ &= -\gamma_n (I_z(t) - I_z) \end{aligned} \tag{2.42}$$

which rearranges as

$$\frac{dP_\uparrow}{dt} = -\frac{\gamma_n}{2}((P_\uparrow - P_\downarrow) - I_z(P_\uparrow + P_\downarrow). \tag{2.43}$$

By defining

$$l_\pm = \frac{\gamma_n}{2}(1 \pm I_z) \tag{2.44}$$

where l_+ (l_-) is the rate for the spin to flip from down (up) to up (down), we find the rate equation

$$\frac{dP_\uparrow}{dt} = -l_- P_\uparrow + l_+ P_\downarrow. \tag{2.45}$$

This tells us that the nuclear spin flip rate is dependent on the initial nuclear spin state, or more specifically its initial projection on the z axis. If its total initial polarisation along z is zero then the flip rate in each direction will be equal, but the greater the polarisation, the greater the bias to flip in one direction. This is due to the nuclei responding to the angle of the electron spin with respect to the optical axis (given by the value of ϕ), i.e. if the electron is driven to a state with a larger angle of rotation about the optical axis, then the asymmetry in the nuclear spin flip rate will increase, i.e. there will be a larger number of spins in one direction than the other along the external field axis.

To extend this model to the full nuclear spin bath, we introduce a parameter, $m = N_\uparrow - N_\downarrow$, where $N_\uparrow$ ($N_\downarrow$) is the number of spins (anti-)aligned along the axis of the magnetic field. We then assume the initial state of the nuclear spin bath is given by some state $|m\rangle$ and define a new set of nuclear spin flip rates that are dependent on m, by replacing the value of ω_e that appears in the explicit definition of γ_n with $\omega_e + mA$ where A is the average value of the hyperfine coupling constant between the electron spin and a single nucleus. We define these new flip rates as $l_\pm(m)$. Then if the system undergoes a spin flip, we see a change of ± 2 in the value of m, leaving the bath in some state $|m \pm 2\rangle$ and the new rate for a spin to flip will be given by $l_\pm(m \pm 2)$ (see Fig. 2.5). We can then use this to define the probability that m is a particular value, and we call this probability $P(m)$ (see Appendix A.5 for the explicit expression). In general, the value of m for any particular parameter set will not be unique. This means that there will be many possible configurations of the nuclei for an arbitrary choice of Δ, Ω and B_{ext}, such that the precession of the electron spin due to the Overhauser field, which is defined as $\frac{mA}{2}$ will have a number of possible values. The desired outcome of the NFF protocol is to force the system into a single state where we know the size of the Overhauser field, and so having a range of values of m does not satisfy this. However, as we will see below, there are particular parameter sets that will give approximately a single value of m with $P(m) \approx 1$ and it is these parameters that we will focus on in the experimental discussion.

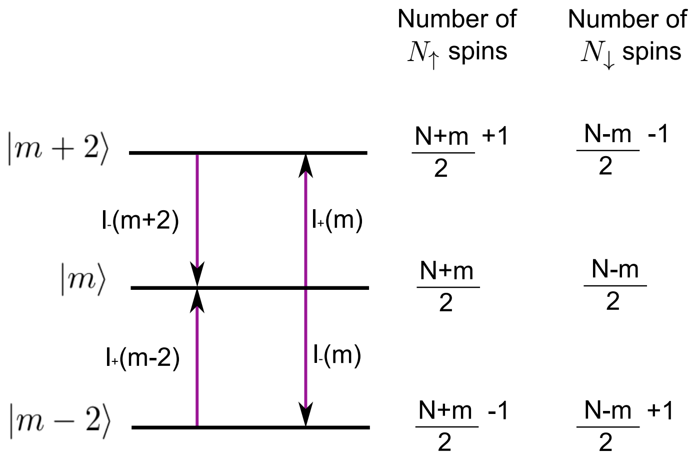

Figure 2.5: Diagram showing how each nuclear spin flip affects the state of the spin bath. We give the flip rates to and from the state $|m\rangle$ and the total number of $N_\uparrow$ and $N_\downarrow$ spins in each of these states.

2.2 Experimental parameters

2.2.1 Restriction of the experimental parameters due to the Markovian approximation

We will now consider how we can experimentally implement this protocol. We need to carefully choose our parameters to control the amount of nuclear polarisation we have, whilst also minimising the number of nuclear spin bath configurations. As discussed above, the length of time taken to reach the electron steady state should be minimised and this leads us to consider the range of values of q_0 to be $q_0 \leq 0.5$. We also know that for $q_0 = 0$, a single nucleus (and therefore the full nuclear spin bath) will not gain any polarisation along the z axis. We therefore choose to consider the range $0.1 \leq q_0 \leq 0.5$. We can then restrict the range of values shown in Fig. 2.4(a) to show the values of Rabi frequency and detuning that both create polarisation along the z axis and are within the valid range of q_0. This is shown in Fig. 2.6. This restricts the values of Δ we consider to be $-0.38 \leq \Delta \leq -0.1$ and $0.1 \leq \Delta \leq 0.38$. A detuning of ± 0.25 corresponds to the QD resonance being found at the half maximum of the pulse. In terms of the Rabi frequency, a value of 0.7 corresponds to the approximate saturation power, i.e., the power required to perform a full π pulse on the electron spin. In the range $0 \leq \Omega \leq 1$, the values of the Rabi frequency that fit the restrictions are $0.25 \leq \Omega \leq 0.5$ and $0.55 \leq \Omega < 0.7$.

It is also useful to note that this restriction on the power of the laser pulse also implies a restriction on the detuning of the pulse, as a far detuned pulse applies little power to the electron spin. We can therefore restrict the values of ϕ to those shown in Fig. 2.7 using the same conditions as for q_0. We should note that the direction of the rotation of the electron spin about the x axis affects the sign of the detuning, i.e. whether the QD resonance is blue or red detuned from the

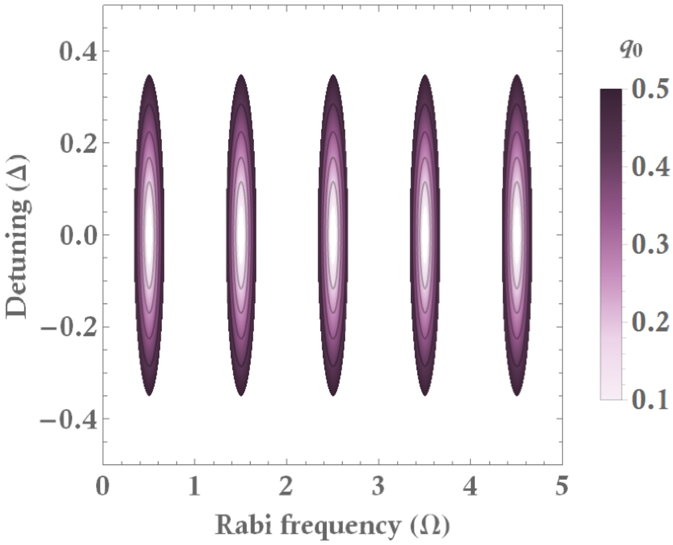

Figure 2.6: Restricted values of q_0 satisfying $0.1 \le q_0 \le 0.5$ in terms of detuning and Rabi frequency.

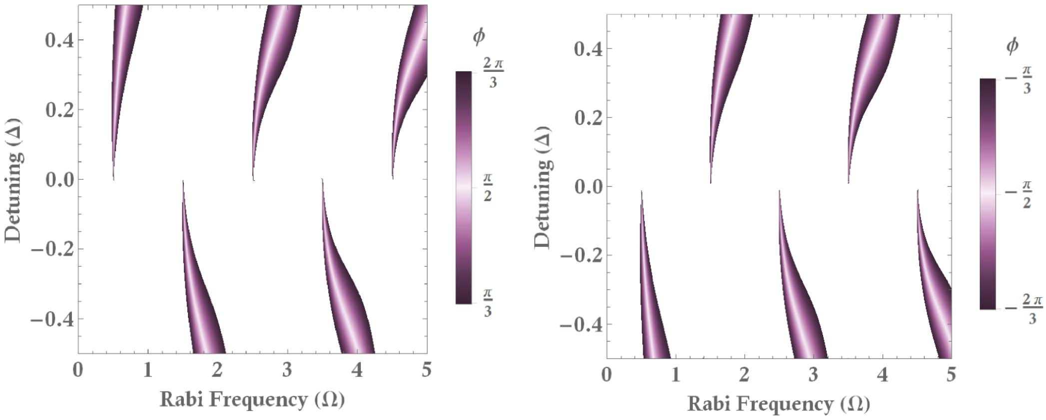

(a)

(b)

Figure 2.7: Restricted values of ϕ giving us the allowed values of the Rabi frequency and detuning.

pulse resonance. This means that if we choose a negative detuning, we require a different laser power to if we choose a positive detuning. This also shows us that larger amounts of detuning are preferable as these give a larger range of values of the laser power, meaning that we require less precision in our choice of power. We can then combine the results of both of these graphs to choose appropriate values of the Rabi frequency and detuning that satisfy these restrictions and are experimentally achievable.

2.2.2 The configuration of the nuclear spin bath

We will now discuss how the full nuclear spin bath will behave in the presence of different Voigt fields and trains of optical pulses. For the single nuclear spin case, we are able to calculate the parameter I_z, which is the population of the nuclear spin that is confined to the z axis and we can model this state. However, we cannot do this for each individual nucleus in the spin bath, due to the size of the Hilbert space the system occupies being too large to model. This leads us to consider the parameter m introduced above. m can be used to calculate the total Overhauser field and is determined by the parameters Δ, Ω and B_{ext}. We make the approximation that each nucleus in the bath has equal coupling and we take this value to be $A = 15$MHz, approximately the average value. In the presence of a Voigt field, we assume that each nucleus within the bath will either align or anti-align with the field direction. Then $m = N_\uparrow - N_\downarrow$, where we choose $N_\uparrow$ to be aligned with B_{ext} and $N_\downarrow$ to be anti-aligned with B_{ext}, can be thought of as the total overall direction of this field and A is used to determine the magnitude of the field. The electron will experience a change in its precession due to the Overhauser field, which is given by

$$\omega_{OH} = \frac{mA}{2}. \tag{2.46}$$

However, as discussed above, the value of ω_{OH} is not unique, leading us to consider the probability distribution $P(m)$ which tells us the likelihood of m being a particular configuration. We should first mention the case where $m = 0$. This corresponds to the point where there are an equal number of spins aligned in each direction. This is a unique configuration with $P(m) = 1$ and gives a total Overhauser shift of 0. This should leave the electron spin precessing with a frequency that is due to the external field only. We should note here that this particular arrangement of nuclei is achieved using a resonant π pulse ($\Delta = 0$), which, when discussed for the single spin case, gave a total overall polarisation of 0. This is simply because if we have a single spin, there is no possible arrangement that is equivalent to two spins in opposing directions and therefore this particular configuration is impossible in the single spin case. In the multiple spin case, this condition occurs when a resonant π pulse is applied in conjunction with an external field B_{ext} that leads to the precession frequency of the electron, ω_e, being synchronised with the repetition rate of the laser pulses, T_R [127], i.e.

$$\omega_e = \frac{2n\pi}{T_R}. \tag{2.47}$$

This is a special case where the system will evolve such that the electron spin is unaffected by the Overhauser shift, however this is difficult to detect experimentally as it will not give a change in the precession frequency of the electron spin and therefore does not allow us to control the size of ω_{eff}. We will therefore consider the general case where B_{ext}, Δ and Ω can all be varied and model the effect on the value of m. We know that for any unique set of parameters, there will in fact be a corresponding set of values of m, each occurring with some probability distribution, $P(m)$. The effect of the system occupying one of these values of m is an Overhauser shift on the precession frequency of the electron with the total effective precession frequency of the electron defined as

$$\omega_{eff} \quad = \quad \omega_e + \frac{mA}{2}. \tag{2.48}$$

Uncertainty in which value of m the system occupies results in ω_{eff} having a range of possible values. This does not solve our initial problem of the value of the effective field acting on the electron not being constant and therefore experimental results would be difficult to quantify and map to a particular configuration. To overcome this, we will search for configurations such that there is a single value of m occurring with high probability ($P(m) \longrightarrow 1$). We therefore need to look into the relationship between the number of possible values of this probability distribution and Ω, Δ and B_{ext}. We are not only interested in the number of possible configurations of m but also the range of values these configurations span, i.e. the difference in the maximum and minimum value of m. We make the assumption that only the values $P(m) > 0.01$ are possible nuclear spin configurations and any configurations with a lower probability of occuring are assumed to be be negligible. We therefore define a parameter $R(m)$ to be the range of m, such that

$$R(m) \quad = \quad m_{max} - m_{min} \tag{2.49}$$

where m_{max} (m_{min}) is the maximum (minimum) value of m for a particular parameter set. This will allow us to quantify variation in the value of ω_{eff}. We also define the number of non-zero values of m for any particular configuration as $N(m)$. Ideally, we want to find parameters such that we have a single value of m occurring with high probability that will give a large value of $\frac{mA}{2}$ so that the change in ω_{eff} is large and thus easier to detect.

The range of B_{ext} we consider is $80 \leq B_{ext} \leq 130$mT due to restrictions in our experimental setup. We believe this to be around the optimum value of the external field, as if we were to move to higher fields, the amount of polarisation gained by the nuclei using this protocol would be insufficient to create an Overhauser field as high as the external field. We initially fix the values of Δ and Ω to be $\Delta = 0.2$ and $\Omega = 0.6$ as these are well within the allowed ranges discussed in Section 2.2.1. We find that the variance in $R(m)$ and $N(m)$ as a function of B_{ext} is extremely large (see Figs. 2.8(e) and 2.8(f)). Fig. 2.8 shows how the parameters $R(m)$ and $N(m)$ vary in relation to each of the experimental parameters. We see that when we vary Δ and Ω there are some stable regions where $N(m) = 1$ and $R(m) = 0$. However, in terms of B_{ext}, these regions, although they do exist, cover a very small range. This tells us that the most difficult parameter to stabilise will be B_{ext}.

The system seems to experience some kind of approximate periodicity, although the pattern is noisy. We see values of $R(m)$ up to 350. If we consider the difference this would make to the value of ω_e, we see that a difference of 350 in the value of m corresponds to a difference in the precession frequency caused by the Overhauser shift of $\omega_{OH} = 2.625$GHz. To put this into context, an external field of $B_{ext} = 100$mT (in the range we are considering) would give a precession frequency of 350MHz if we assume our QD has a g-factor of 0.25 [93, 94]. This means that we will require B_{ext} to be stable on the order of 100μT for $R(m)$ to be stable. $N(m)$ also has a roughly periodic pattern and the sections with a high $N(m)$ correspond to the sections with a high $R(m)$. This is not necessarily obvious but not unexpected as the larger the range of values, the more likely it is that they will span a larger range of values. Selecting the correct value of B_{ext} such that we minimise $N(m)$ and $R(m)$ is achievable, but we should first consider what level of accuracy we require in terms of the Rabi frequency and detuning. The regions of interest in each of the graphs in Fig. 2.8 is the minimum point, i.e. the point where there is only a single possible mode ($N(m) = 1$), which also leads to a span of 0, ($R(m) = 0$). This is needed so that there is a single unique value of ω_{eff}, such that the precession frequency is known.

Using Fig. 2.8, we can choose, for example, $B_{ext} = 102.5$mT as this has $N(m) = 1$, $R(m) = 0$ with $P(m) = 0.9997$, and show that $N(m)$ and $R(m)$ are invariant for $\Delta \gtrapprox 0.05$. Importantly, the positive range of values of Δ given in Section 2.2.1 is within the stable range shown in Figs.2.8(c) and 2.8(d). This means that as long as we correctly choose the sign of Δ, the only restrictions we need to apply are those which satisfy the Markov approximation, i.e. we cannot detune the pulse far enough that it becomes too weak to drive the electron into its steady state sufficiently quickly. This model is valid for a σ^- pulse and we find that switching to a σ^+ pulse simply reverses the sign of the detuning. Choosing the sign of the detuning incorrectly would mean that we could find a span of values of m of up to 1000, corresponding to a difference in precession frequency between different configurations of $\approx$ 15GHz, signifying the need to carefully select the direction of the detuning. We should note that a detuning that causes m to be aligned with B_{ext} (in this case a negative detuning) rather than against it will in general have more than one possible configuration of m whereas when the majority of the spins are anti-aligned with the field, there will in general be a single configuration. There is also a difference in the maximum absolute value of m between the two scenarios. We find that those configurations with the majority of nuclei aligned along the axis will generally have a larger value of $|m|$ than those with the majority of nuclei anti-aligned with the axis. This difference in absolute value is again due to the asymmetry of the system, as the individual nuclei will have a preference to align along the axis of B_{ext} rather than in the opposing direction, meaning that they will find a larger number of configurations that match this scenario.

In terms of Ω, we see that there are some regions where there is a single value of m and some regions with a bigger spread of values (see Fig. 2.8(b)). This happens periodically and shows that there is a switching of the overall direction of m between positive and negative as the laser power is increased. This appears to be due to the precession frequency of the electron spin periodically synchronising with T_R, with the maximal and minima corresponding to even and odd multiples of the repetition rate respectively.

We next consider the values of the parameter m as a function of B_{ext}, Δ and Ω. Ideally, we want $|m|$ to be large, as this will give a more significant difference between ω_e and ω_{eff}, thus

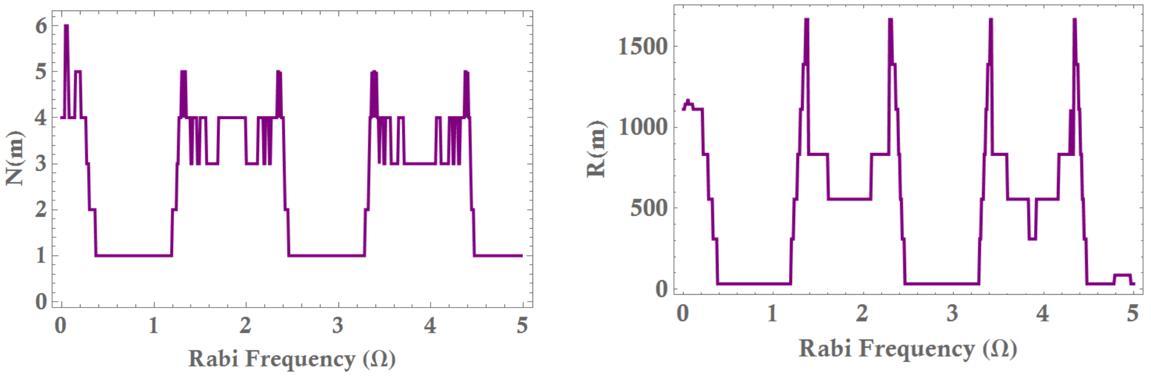

(a) Plot showing how the number of modes, $N(m)$, varies as a function of Ω for B_{ext} = 102.5mT and $\Delta = 0.2$.

(b) Plot showing how the frequency range of the modes, $R(m)$ varies as a function of Ω for B_{ext} = 102.5mT and $\Delta = 0.2$.

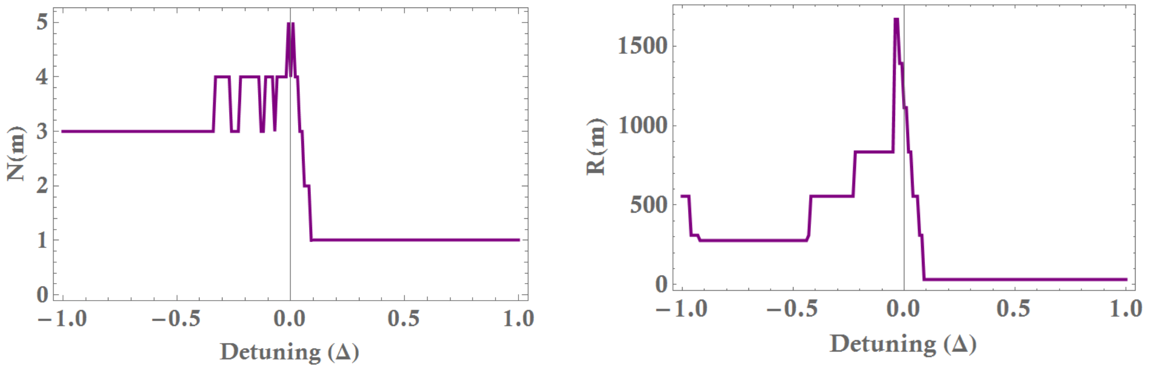

(c) Plot showing how the number of modes, $N(m)$ varies as a function of Δ for B_{ext} = 102.5mT and $\Omega = 0.6$.

(d) Plot showing how the frequency range of the modes, $R(m)$ varies as a function of Δ for B_{ext} = 102.5mT and $\Omega = 0.6$.

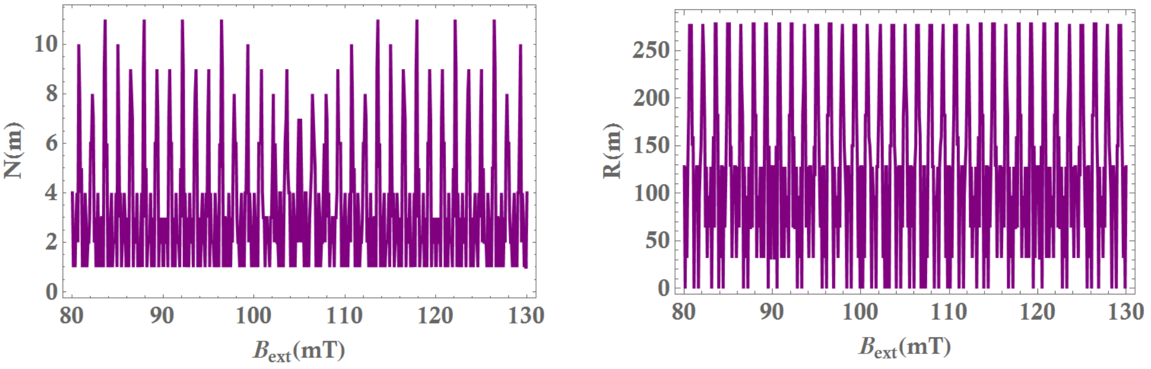

(e) Plot showing how the number of modes, $N(m)$ varies as a function of B_{ext} for $\Omega = 0.6$ and $\Delta = 0.2$.

(f) Plot showing how the frequency range of the modes, $R(m)$ varies as a function of B_{ext} for $\Omega = 0.6$ and $\Delta = 0.2$.

Figure 2.8: Here we show how the number of possible values of m and the range of values these span can vary as a function of B_{ext}, Δ and Ω. The red lines show the span of the values and the blue lines show the number of possible values. We see that there are sections that have single values of m occuring with probability $P(m) = 1$. The optimal regions are the minimal values in each section.

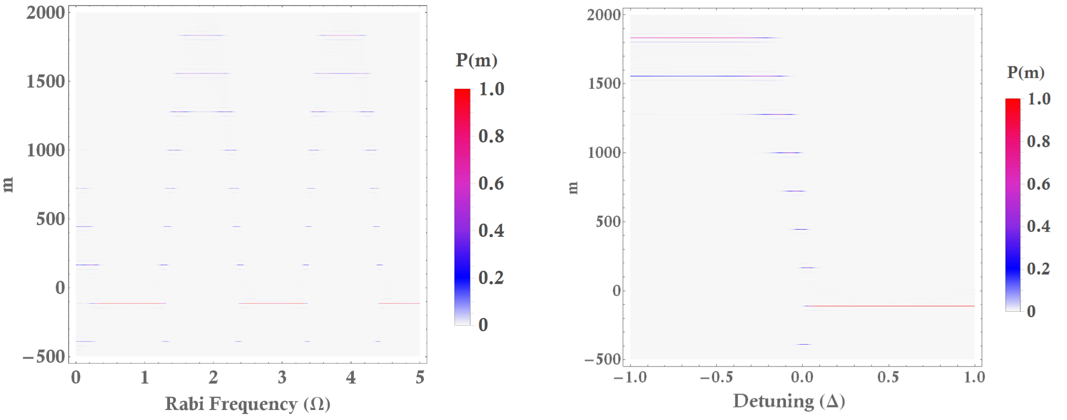

(a) Values of m and $P(m)$ as a function of the Rabi frequency with $\Delta = 0.2$ and $B_{ext} = 102.5$mT.

(b) Values of m and $P(m)$ as a function of the detuning with $\Omega = 0.6$ and $B_{ext} = 102.5$mT.

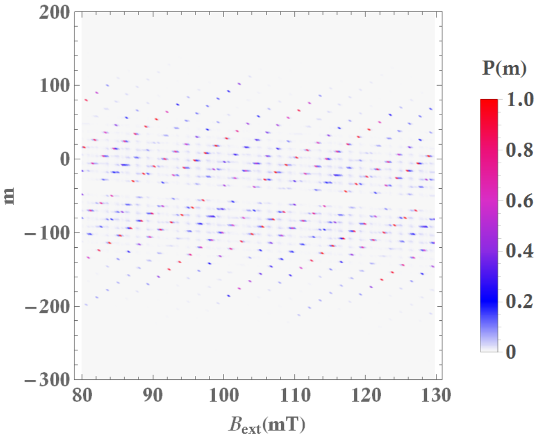

(c) Values of m and $P(m)$ as a function of B_{ext} with $\Delta = 0.2$ and $\Omega = 0.6$.

Figure 2.9: Here we show the stability of m and $P(m)$ as functions of Ω, Δ and B_{ext} respectively. There are clear points where these are invariant with respect to Ω and Δ, but the dependence on B_{ext} is much more sensitive. We choose the g-factor of the QD to be 0.25 and $A = 15$MHz.

changing the precession frequency of the electron spin more significantly and making it easier to detect, although this advantage is negated if $P(m)$ is not close to 1. We plot the values of m and $P(m)$ as functions of Ω, Δ and B_{ext} respectively, as shown in Fig. 2.9. In Fig. 2.9(a), we see the same switching from positive to negative m that was apparent in Fig. 2.8(b), with a negligible variance in the value of $P(m)$ far from these switching points for negative values of m. These stable regions are useful as they do not require a high level of accuracy in our choice of laser power and it is possible to choose values of Ω that are both stable and correspond to regions satisfying the Markovian approximation. Similarly, in Fig. 2.9(b), we see that for positive detuning, the value of m is negative and $P(m) \approx 1$. Ideally, we want a high value of $|m|$, however, we find that $|m|$ is much greater when m is positive (when there is a higher number of nuclei aligned in the same direction as B_{ext}) but that the number of possible values of m is also greater. The condition $P(m) \longrightarrow 1$ holds more importance than maximising the value of $|m|$ and so we choose parameters such that m is negative. This will make the total precession frequency of the electron slower. For example, if $m = -50$, the Overhauser shift will cause a change in the precession frequency of the electron of 375MHz. The precession frequency of an electron spin with a g-factor of 0.25 due to a field of 102.5mT is $\approx$ 357Mhz. Then the precession frequency of the electron will be $\approx$ 18MHz (in the opposite direction) only if we force the nuclei into this particular configuration. This should be easily detectable in measurements of the electron spin.

To implement this protocol we will fix the values of Δ and Ω and perform a scan varying the value of B_{ext}, as this is the parameter that requires the most fine tuning. In practice, the QD will experience spectral jitter, where the resonant frequency of the QD is unstable and will vary on short timescales [128]. This means that the value of Δ will be affected by this moving resonance, however, this is our most stable parameter, giving quite a large range of possible values of Δ over which the protocol will remain stable and this should therefore not play a large role if we choose a value of Δ in the centre of this range. To successfully scan over a region with $P(m) \longrightarrow 1$, we will need to perform a very fine scan, with an increase in B_{ext} of $\approx 50\mu$T per measurement of precession. We must perform a scan over a large enough range of values to be certain of passing through a section where $P(m) \geq 0.8$, and this scan range is $\approx$ 1.5mT. We will choose the values of Δ and Ω to be $\Delta \approx 0.2$ and $\Omega \approx 0.6$ to satisfy the Markovian approximation. $\Delta = 0.25$ corresponds to a pulse that is detuned such that the QD resonance is at the half maximum of the pulse and so we will be slightly closer to the resonance than this. A Rabi frequency of 0.7 corresponds to saturation of the QD, and so we want to be at a power just below the saturation power.

This would require a finer scan of B_{ext}, and would make the change in ω_{eff} more difficult to detect and so we choose to focus on the section $80 \leq B_{ext} \leq 130$mT and consider $P(m) \geq 0.8$. As m is insensitive to reasonably large changes in Δ and Ω, we don't require too much stability in these parameters, although we must remain in the region in which the Markov approximation is valid. Then we can imagine performing an experiment in which we consider two neighbouring regions where $P(m) \geq 0.8$ and take a very fine scan over B_{ext} between these two regions. We expect to see that there are points where the evolution of the electron spin is unpredictable, corresponding to regions where there is a large distribution of values of m, but that as we approach the point where $P(m) = 1$, we will start to find that the state will converge to a particular configuration. This should show an electron spin precession frequency far from that found before application of the laser pulse sequence, such that ω_{eff} will be dictated by the value of m.

2.3 Summary

In this chapter, we discuss the dephasing of the electron spin due to the nuclei in the host material. We describe the NFF protocol in detail and show how it is used to force the nuclei in the spin bath of a QD to align along the axis of an external field in the Voigt geometry, allowing the electron spin confined within the QD to precess in a constant effective field. We adjust the model described in [123] to create a model with variable experimental parameters. We also expand the model further to consider how the parameter m can be controlled and manipulated to allow us to drive our system into a particular configuration. We create a model to show the effect of varying the detuning and Rabi frequency of the laser pulses used to create this configuration and how we can adjust the pulses and external field to control the total effective field on the electron spin, thus controlling its precession frequency. We tailor our model to an experimental setting, defining our parameters to be applicable to our setup. An experimental implementation will be attempted in Chapter 6.

CHAPTER 3

ENTANGLEMENT OF AN ELECTRON AND NUCLEUS

This chapter will discuss isolation and manipulation of single nuclear spins in QDs and how we can transfer the state of an electron spin to these nuclei. This is a theoretical chapter, predominantly consisting of novel research. The chapter begins with a discussion of the strain profile of a QD with reference to the existing strain profile modeling and then moves into novel research, justifying the consideration of single nuclei as qubits by modeling RF pulses. There is also novelty in the study of the interaction between an electron and single nucleus, where we specify suitable parameters for the model to achieve maximal entanglement and refer back to the experimental model of Chapter 2. This will have applications for nuclear spin quantum memories, particularly for use in QKD, as discussed in Chapter 1. We will also consider how these nuclei can be used as spin qubits for quantum information processing [10, 11, 99, 129, 130]. The motivation for using nuclei for quantum information processing is the inherently long coherence times they possess [131–133]. This is an attractive attribute, particularly in QDs, due to the difficulty in satisfying Criterion 5 of DiVincenzo's criteria in this particular platform. However, due to the large number of nuclei ($\approx 10^5$) present in a typical QD environment, manipulation of single nuclei is an extremely complex problem. However, we show that one may use the quadrupolar interaction, induced by strain, to lift the degeneracy of the nuclei. We analyse the strain profile of a QD and how the presence of strain can allow us to find nuclei that are isolated in frequency and therefore address a single nucleus within the QD using radiofrequency (RF) pulses. By modeling the transition energy of different spin species of the QD nuclei as a function of external magnetic field we find parameters that give a high probability of addressing a single nucleus with a RF pulse if we choose the pulse duration and resonant frequency correctly. We then show that if the nuclear spin bath is successfully prepared using the NFF protocol described in Chapter 2, it is possible to apply a RF pulse to a single nucleus such that it is projected into the plane of the electron spin, leaving the remainder of the spin bath aligned along the axis of the external field.

Due to the large number of nuclei in the spin bath, it seems unlikely that it would be possible to address a single nucleus. However, we show that it is not only theoretically possible, but that it can be done with an RF pulse that is broad enough such that the implementation time of the pulse is sufficiently short (≈ 200ns). The reason we choose to focus on addressing single nuclei rather than the full nuclear spin bath is that we would like to produce a method for transferring the electron spin state to a nuclear spin state, thus lengthening the coherence time of the state. This requires entanglement between the electron and any configuration of nuclei we choose. Due to monogamy of entanglement, it is not possible to maximally entangle an electron to more than one distinguishable nucleus. If two or more nuclei are in a maximally entangled state, then it is possible to maximally entangle the electron spin to this entangled state, but in this case the set of indistinguishable nuclei must act as a single particle, and cannot contain more than one quantum state. Hence we must focus on manipulation of single spins. Then the electron and target nucleus will interact and evolve according to the hyperfine interaction independently of the remainder of the spin bath.

We also take into account the effect of the RF pulse on the nuclear spin bath and how this affects our two-spin subsystem of an electron and target nucleus. Next, we show how a two-spin subsystem of an electron and a single nucleus will evolve according to the hyperfine interaction in the presence of magnetic fields in both the Faraday and Voigt geometries. We also discuss how this evolution can be used as a source of entanglement between the electron and nucleus and model the parameters needed and the timescales on which this process happens. This is equivalent to performing a $\sqrt{\text{SWAP}}$ gate on the two-spin subsystem. This is a maximally entangling gate, given by the matrix

$$\sqrt{\text{SWAP}} = \begin{pmatrix} 1 & 0 & 0 & 0 \\ 0 & \frac{1}{2}(1 \pm i) & \frac{1}{2}(1 \mp i) & 0 \\ 0 & \frac{1}{2}(1 \mp i) & \frac{1}{2}(1 \pm i) & 0 \\ 0 & 0 & 0 & 1 \end{pmatrix} \tag{3.1}$$

and the fact that it can be achieved through simple evolution of the system rather than direct external manipulation of the qubits is advantageous as we don't induce any losses other than those inherent in the system (such as decoherence of the spin states) during the application of the gate. Fig. 3.1 summarises the main outcomes of the chapter.

3.1 Strain Distribution in a quantum dot

The growth process used for the InGaAs QDs we consider in this thesis is Stranski-Krastanov growth. As discussed in Chapter 1, by depositing a monolayer of InGaAs onto a substrate of GaAs, one forces a preferential 3-D growth of the InGaAs layer, due to a lattice mismatch between the two materials, creating a large amount of strain in the system. A typical InGaAs QD in a GaAs

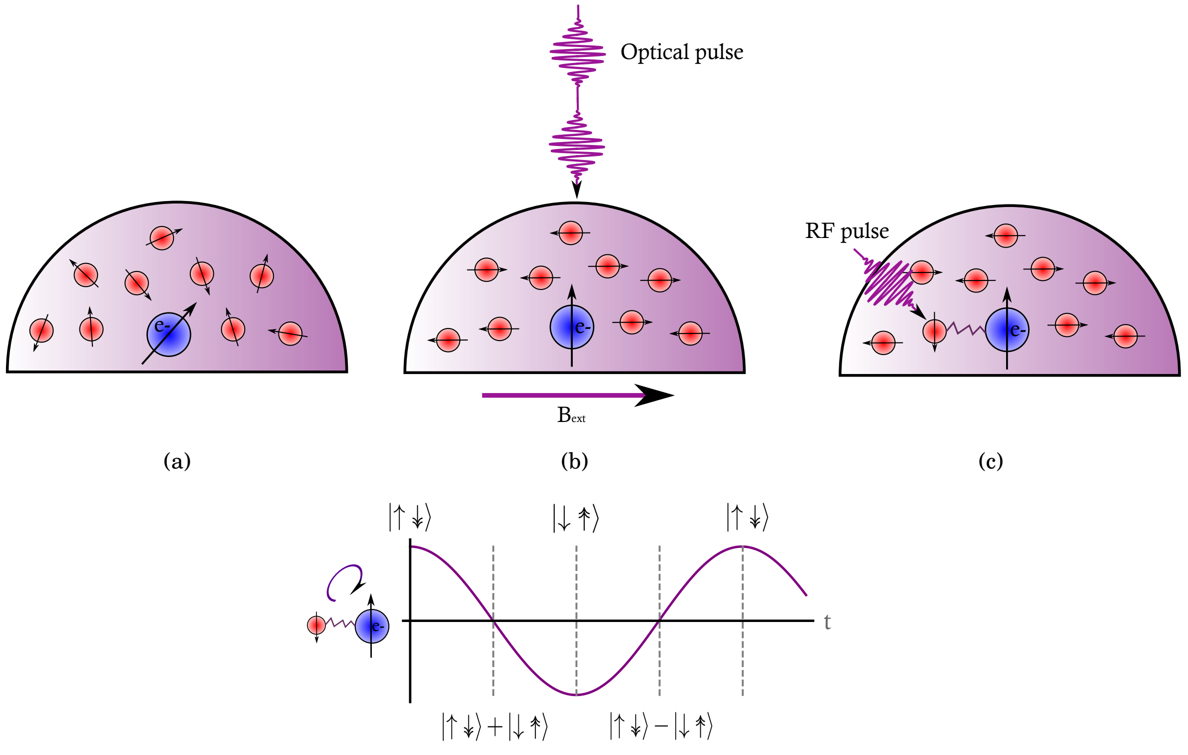

(a) (b) (c)

(d)

Figure 3.1: (a) The structure of a charged QD before any system preparation. The blue circle represents the electron which will be in some unknown spin state shown by the black arrow. The red circles represent the nuclei in the QD, each of which has a different precession frequency, governed by its Zeeman splitting. (b) The protocol we use to perform nuclear frequency focusing. A train of optical pulses addresses the electron spin along the optical axis and an external magnetic field is applied in the Voigt geometry. The nuclei will align along the external field axis whilst the electron is driven by the optical pulse train. The final state of the system is determined by the detuning and Rabi frequency of these pulses and the external field strength. (c) Initialisation of a single nucleus into the plane of the electron spin. A radiofrequency pulse is applied to a target nucleus that is isolated in frequency, rotating it into the plane of the electron spin, such that the two will evolve according to the hyperfine interaction. (d) Evolution of the electron-nuclear subsystem as a function of time due to the hyperfine interaction, assuming no decoherence. The purple line shows the evolution of the two-spin subsystem about the Bloch sphere and the dotted lines tell us the spin state of the system at relevant points in the evolution.

substrate will have a lattice mismatch of 7.8% at 300K, with GaAs having a lattice constant of 5.6533nm and InGaAs 6.0584nm [134]. This strain is unavoidable, as the lattice mismatch is both the reason for QD growth and the reason that there is strain in the system. Strain is often considered to be purely a dephasing mechanism, and there is research into how the strain induced in the fabrication process can be compensated for [135–137], however, we will show in this section that it can in fact be exploited as a means of addressing single nuclei.

QD strain is position-dependent, meaning that each nucleus will experience a different strain profile, although the strain in the plane of the QD is the same in each direction, differing only with the strain along the axis normal to the growth direction [138]. For the QDs we consider, the more highly strained areas will be in the lower half of the QD and close to the centre. The strain causes splitting in the energy levels of the nuclei, and this splitting, together with the position of the nucleus, determines the coupling strength between the electron and each nucleus [139]. In addition to this, the nuclei will experience the quadrupolar interaction, which causes a shift in their magnetic energy (this will be discussed in detail below). For InGaAs QDs, the atomistic strain will typically be around 7-10% [96] and the hyperfine coupling constants are as defined in Eq. 2.12.

3.1.1 Quadrupolar Interaction

Nuclear spins will be also subject to the quadrupolar interaction, an effect which causes a shift in the magnetic energy of each nucleus [115, 140]. In addition to this, there are a range of spin species within the atoms, and a spin species higher than $\frac{1}{2}$ will experience a shift in transition energy due to the quadrupolar interaction. Different atoms have different total spin quantum numbers and we find that in a QD, the Ga/As atoms have a total spin quantum number of $\frac{3}{2}$ and In has a total spin quantum number of $\frac{9}{2}$ (see Fig. 3.2) [96]. The Hamiltonian of the quadrupolar interaction is [96]

$$H_Q = A_Q(3I_x^2 - I^2 + \eta\frac{I_+^2 - I_-^2}{2}) - \omega_n I_z \tag{3.2}$$

where ω_n is the precession frequency of the nucleus due to some external field, B_{ext} in the Voigt geometry, and I_j are the nuclear spin operators for a half-integer spin particle along the j axis and $I = I_x + I_y + I_z$ (note that x is again the optical axis). A_Q is the quadrupolar coupling term and is given by

$$A_Q = \frac{e^2 qQ}{4I(2I+1)}. \tag{3.3}$$

Here, Q is the electric quadrupole moment, e is the electronic charge, I is the spin number of the nucleus ($I = \frac{9}{2}$ for In and $I = \frac{3}{2}$ for Ga and As). q is the field gradient parameter, and is defined as

$$q = \frac{V_{XX}}{e} \tag{3.4}$$

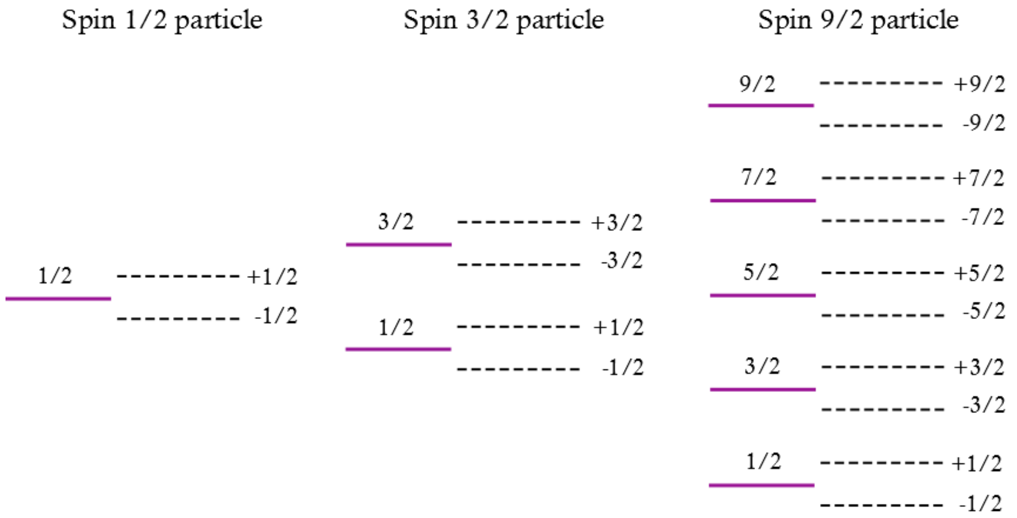

Figure 3.2: Level structure of a spin $\frac{1}{2}$ particle (e.g. an electron), a spin $\frac{3}{2}$ particle (e.g. a Ga atom) and a spin $\frac{9}{2}$ particle (e.g. an In atom) in terms of the total spin quantum number.

where

$$V_{ij} \equiv \frac{\partial^2 V}{\partial x_i \partial x_j} = \sum_{k,l=1}^{3} S_{ijkl}\epsilon_{kl} \tag{3.5}$$

describes the electric field gradient. S is the fourth-rank gradient elastic tensor [141] and ϵ_{ij} is the local strain tensor. η is the dimensional biaxiality, or asymmetry parameter, given by

$$\eta = \frac{V_{XX} - V_{YY}}{V_{ZZ}}. \tag{3.6}$$

In [96], the strain and quadrupolar statistics of InGaAs QDs are given and the distribution of the different strain components is modeled in terms of position within the QD. Values are given for the mean and standard deviation of the different strain components of the QDs. We are interested in the shear strain component, $\epsilon_S \equiv |\epsilon_{xy}| + |\epsilon_{yz}| + |\epsilon_{zx}|$, as this induces the largest range of values of A_Q and is due to As atoms on the QD interface forming heterobonds with In and Ga. We will show that if the particular QD we consider has a particularly high value of ϵ_S (we consider up to 4 standard deviations from the mean value quoted) that the distribution of A_Q will become much wider, which is beneficial when attempting to find a single nucleus that is isolated in frequency. Different spin species will have different energy values due to the transition shift caused by the quadrupolar interaction. We can calculate these energies shifts by plotting the eigenvalues of Eq. 3.2 as a function of external field strength. We consider both the $\frac{3}{2}$ (As) and $\frac{9}{2}$ (In) spin species. Plotting this using the mean value of the shear strain ($\epsilon_S = 0.005$ for As and $\epsilon_S = 0.004$ for In [96, 134]), we see the results in Fig. 3.3.

In Fig. 3.3(a), there is a no initial splitting between the $\frac{\pm 3}{2}$ states and and the $\frac{\pm 1}{2}$ spin levels. This is induced as the value of B_{ext} increases, and at these low fields, we see an asymmetry in

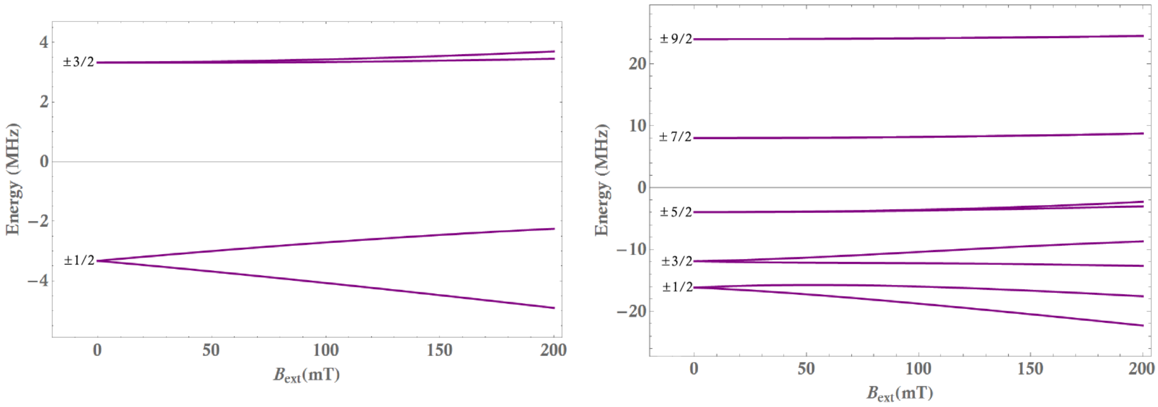

(a) As nucleus with spin $\frac{3}{2}$.

(b) In nucleus with spin $\frac{9}{2}$.

Figure 3.3: Zeeman splitting of the level transitions of (a) a spin $\frac{3}{2}$ nucleus and (b) a spin $\frac{9}{2}$ nucleus with an average strain profile. At $B_{ext} = 0$, there is no splitting between each + and − spin state pair. In (a), the higher energy line at zero field is the $\frac{3}{2}$ spin transition and the lower energy line is the $\frac{1}{2}$ spin transition. These then split for non-zero external fields and we see also the $\frac{-n}{2}$ spin states. Similarly, for (b) the spin transition with the highest energy at zero field is the $\frac{9}{2}$ transition and in order from highest to lowest energy, we have the spin transitions $\frac{9}{2}$, $\frac{7}{2}$, $\frac{5}{2}$, $\frac{3}{2}$ and $\frac{1}{2}$, similarly to those in (a).

the level splittings due to the biaxiality, η, being a dominant part of the system. Fig. 3.3(b) is qualitatively similar, but as there are more energy levels, these energy levels necessarily cover a larger frequency range. The transition energies between the different spin levels are not equal (i.e. the energy of the transition between the $\frac{9}{2}$ spin level and the $\frac{7}{2}$ level is not equal to the energy of the transition between the $\frac{7}{2}$ and $\frac{5}{2}$ transition). This is due to the biaxiality parameter, η, defined above, which is a dimensionless parameter and has a value of $\eta = 0.117$ for As and $\eta = 0.042$ for In [96]. We will now discuss how the values of ϵ_S and η affect the distribution of the energies of the spin transitions and how this can be used to isolate single nuclei by addressing the system with RF pulses.

3.1.2 Isolation of a single nucleus

We can use the fact that the spin transitions are split in energy to our advantage in isolating a single nuclear spin. The greater spread of energy found in the In nuclear spin transitions leads us to focus on these spins over the As spins. We need to design a RF pulse that is able to address a nucleus that is isolated in frequency from the rest of the bath and so we want the energies between the spin transitions to be as large as possible. We have so far only considered how the mean strain profile will behave, and so we instead consider how variation in the value of ϵ_S affects the spread of the energies in this magnetic field range. The mean value of ϵ_S for In is 0.004 and standard deviation is also 0.004. η is also given with both a mean value (0.042)

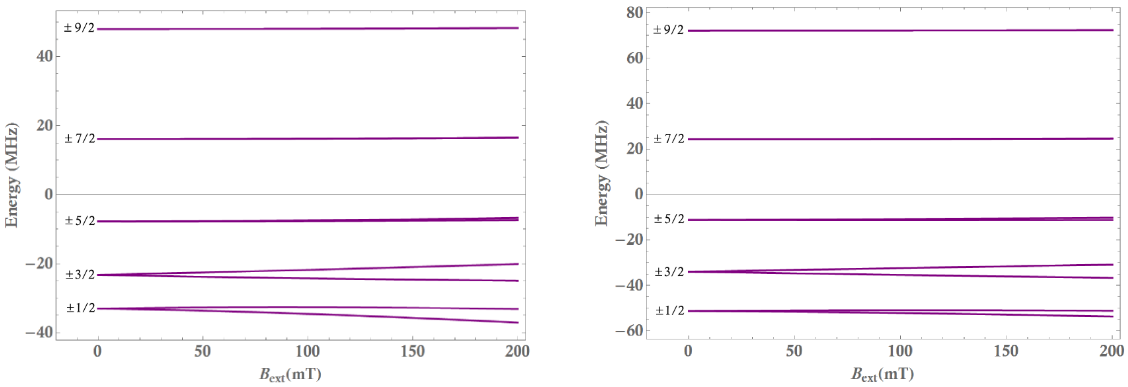

(a) 1 standard deviation (b) 2 standard deviations

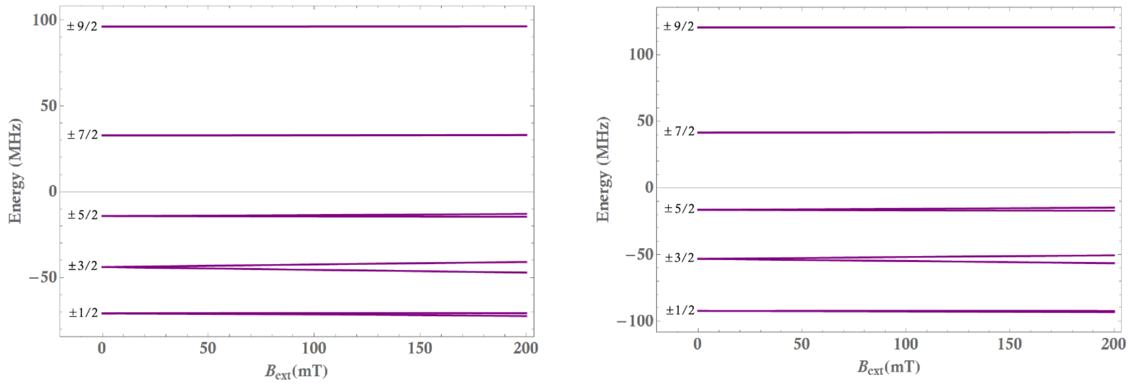

(c) 3 standard deviations (d) 4 standard deviations

Figure 3.4: Variation of the Zeeman splitting of a $\frac{9}{2}$ spin state as a function of magnetic field, taking the first to the fourth standard deviations of ϵ_s and η.

and a standard deviation (0.041) in [96]. Increasing ϵ_S increases the total spread in frequency of the different spin transitions and increasing η means that the difference in the transition energies between the different spin levels is increased. We model the energy splittings up to the 4th standard deviation (see Fig. 3.4). This shows an increase in the widths of the transitions, and a larger asymmetry between the different transitions. The width of the transition we address needs to be sufficiently different to the width of the other transitions, such that we can neglect these transitions. For each of the graphs plotted, the transition between the $\frac{9}{2}$ and $\frac{7}{2}$ spin levels has the largest width. The nuclei within each transition will have a spread of frequencies that obey a Gaussian distribution, therefore, considering the $\frac{9}{2}$ to $\frac{7}{2}$ transition will give the largest spread of values of the nuclear spin frequency, increasing the chance of finding a sufficiently isolated nucleus. The width of each of the transitions is greatest for the 4th standard deviation, with the $\frac{9}{2}$ to $\frac{7}{2}$ increasing from a width of $\approx$ 16MHz for the mean strain profile to $\approx$ 80MHz for the 4th standard deviation. In addition to increasing the nuclear spin frequency range, this also allows us to make the assumption that we can address a single transition, without the other spin

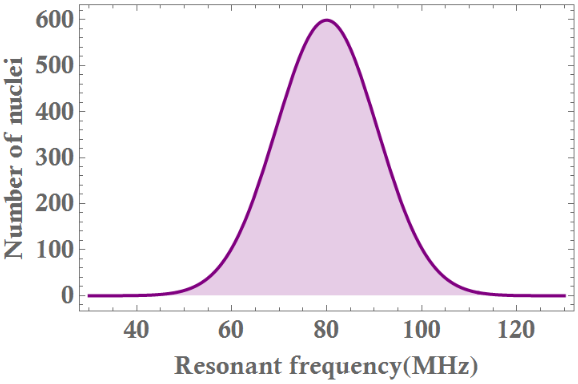

Figure 3.5: Distribution of the resonant frequencies of the In nuclei found in the $\frac{9}{2}$ and $\frac{7}{2}$ transition centred at 80MHz for 16000 spins.

levels experiencing any effects. The width of the $\frac{7}{2}$ to $\frac{5}{2}$ transition is ≈ 55MHz and we claim that this is sufficiently far from the $\frac{9}{2}$ to $\frac{7}{2}$ width that only the wider transition will be addressed. The widths of each transition are shown for each strain profile in the table below.

Transition width	**Average strain**	**1 sd**	**2 sd**	**3 sd**	**4 sd**
$\frac{9}{2}$ **to** $\frac{7}{2}$	16MHz	31.9MHz	47.8MHz	63.4MHz	78.9MHz
$\frac{7}{2}$ **to** $\frac{5}{2}$	12MHz	23.9MHz	35.6MHz	47.0MHz	58.0MHz
$\frac{5}{2}$ **to** $\frac{3}{2}$	8MHz	15.5MHz	22.7MHz	29.8MHz	37.0MHz
$\frac{3}{2}$ **to** $\frac{1}{2}$	4MHz	9.77MHz	17.3MHz	27.0MHz	39.0MHz

We will assume from this point that we are able to find a QD with a strain profile matching the numbers quoted for the fourth standard deviation.

We now need to consider the distribution of the nuclei within the $\frac{9}{2}$ to $\frac{7}{2}$ transition. The energy of this transition has a width of 80MHz. The temperature of our system will be a few Kelvin, which is in the high temperature limit for this type of system. This means that we expect each spin state to be occupied by an approximately equal number of spins, giving 20% of the total number of spins in each of the $\frac{9}{2}$ and $\frac{7}{2}$ transitions. Only the In spins in the QD have spin species $> \frac{3}{2}$ and these make up approximately 40% of the total number of spins in the system. Then if we take the total number of spins in the QD to be 100000, the number of In spins in the $\frac{9}{2}$ and $\frac{7}{2}$ transitions will be ≈ 16000. Then we can model the distribution of values of A_Q of the spins in these transitions according to a Gaussian distribution centred at 80MHz, noting that the natural linewidth of the In transition is ≈ 10kHz [142] (see Fig. 3.5).

We need to design a RF pulse that is able to address a single nucleus. This nucleus then needs to have a value of the quadrupolar coupling, A_Q, that is sufficiently isolated from the values of A_Q of the remainder of the nuclear spin bath. We want to find a section of this distribution with a high probability of containing a single nucleus. The width of the section we choose corresponds to the linewidth of the RF pulse we will use to address the nucleus. A broader frequency range will

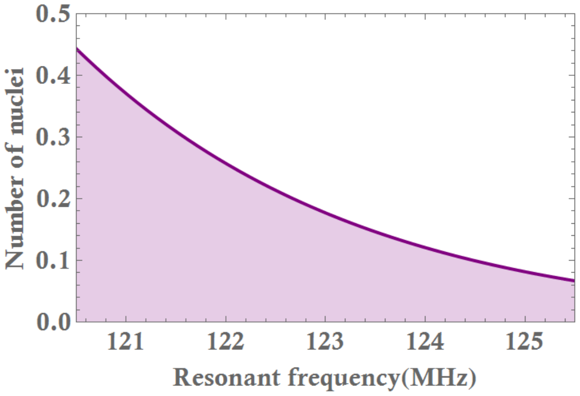

Figure 3.6: A 5MHz section of the Gaussian distribution of A_Q containing a single nucleus isolated in frequency.

correspond to a shorter implementation time for the pulse and so we want to find a reasonably broad section that is likely to contain a single nucleus as this will give a shorter initialisation time for the nucleus. This leads us to consider the frequencies far from the centre of the distribution. We choose to consider the higher energy end of the distribution as spins found in this sections will be far in frequency from any other spin transitions and species.

We must carefully choose the frequency and linewidth of our RF pulse to maximise the chance of addressing a single nucleus. RF pulses act on nuclei by causing a rotation in the angle of the nuclear magnetic moment, corresponding to a rotation of the direction of the spin of the nucleus. Each nucleus will experience some rotation due to the RF pulse which is dependent on its resonant frequency. This leads to the stable configuration of nuclei we have prepared being scrambled, and the precession of the electron spin will revert to its incoherent state. However, if we are able to successfully choose the frequency of our RF pulse such that it will overlap with a single nucleus only, we can use it to rotate this nucleus, whilst leaving the rest of the nuclear spin bath unperturbed.

To find the number of nuclei within a given frequency range of the distribution, we can integrate the area under the curve in Fig. 3.5 for the frequency range we want to consider. The section in Fig. 3.6 shows a 5MHz section (corresponding to a pulse duration of 200ns) which will contain a single nucleus. We choose the linewidth of 5MHz as it is broad enough such that the implementation time (200ns) is shorter than the coherence time of the system but the transition is narrow enough that we are able to select a section of the distribution that will contain a single nucleus that we are able to address resonantly. Then we can imagine applying a RF pulse that is resonant at the centrepoint of this region (123MHz) to address a single nucleus that is resonant at this frequency. We will call this nucleus the target nucleus. We previously gave details of a system that is prepared such that we have an electron spin in the plane perpendicular to the nuclear spin bath. Our eventual application is to interact this electron spin with a target nucleus and therefore we want to rotate this nucleus such that it is in the same plane as the electron spin using the RF pulse we have just described. This will correspond to applying a pulse of area $\frac{\pi}{2}$ about the y axis, given by the rotation matrix

$$R_y(\theta) = \begin{pmatrix} \cos\frac{\theta}{2} & -\sin\frac{\theta}{2} \\ \sin\frac{\theta}{2} & \cos\frac{\theta}{2} \end{pmatrix} \tag{3.7}$$

with $\theta = \frac{\pi}{2}$. However, we will now consider the effect of the RF pulse on nuclei detuned from the pulse resonance but still close enough in frequency that they will experience some small rotation into the plane of the electron and target nucleus.

3.1.3 Effect of the RF pulse on the nuclear spin bath

It is important to note that some of the other nuclei in the spin bath may be affected by this RF pulse. Nuclei that are detuned from the pulse resonance but still sufficiently close in frequency will experience some rotation due to the pulse. This will be a smaller effect than that felt by the resonant target nucleus, but could still produce a significant rotation on a nucleus that may then affect the precession of the two-spin subsystem. To model this, we need to calculate the overlap between the RF pulse and each of the nuclei in the nuclear spin bath. We approximate the lineshape of the RF pulse as a hyperbolic secant pulse, (as in Chapter 2) and represent each nucleus as a rectangular function with linewidth 10kHz at some detuning, δ from the resonance of the RF pulse. This is a valid approximation as the linewidth of the nuclear is orders of magnitude smaller than the linewidth of the pulse. Then the RF pulse, $P(\omega)$, can be represented by the equation

$$P(\omega) = \frac{1}{4}\operatorname{sech}\left(\frac{\omega - \omega_P}{2}\right) \tag{3.8}$$

where ω_P is the central frequency of the pulse and each nucleus by the equation

$$R(\omega,\delta) = \begin{cases} R_0 & \text{if } \omega_R - \frac{\delta}{2} < \omega < \omega_R + \frac{\delta}{2} \\ 0 & \text{otherwise} \end{cases} \tag{3.9}$$

where R_0 is the amplitude, ω_R is the central frequency of the nucleus and δ is the linewidth of the nucleus. We can then calculate the overlap between the pulse and each nuclear spin using the equation

$$\text{Overlap} = \sum_{N=1}^{16000} \int_{A_Q^N - \frac{\delta}{2}}^{A_Q^N + \frac{\delta}{2}} \left| \frac{R_0}{4}\operatorname{sech}\left(\frac{\omega - \omega_P}{2}\right)\right|^2 d\omega \tag{3.10}$$

where each individual nucleus has some resonant frequency A_Q^N, with a detuning from the pulse resonance of $\omega_P - A_Q^N$. We take the linewidth of an Indium nucleus to be $\delta = 10$kHz, as above. Evaluating this integral for each term in the sum gives us the overlap between each of the nuclei and the pulse. Then, a nucleus centred at 123MHz will have maximum overlap with the pulse

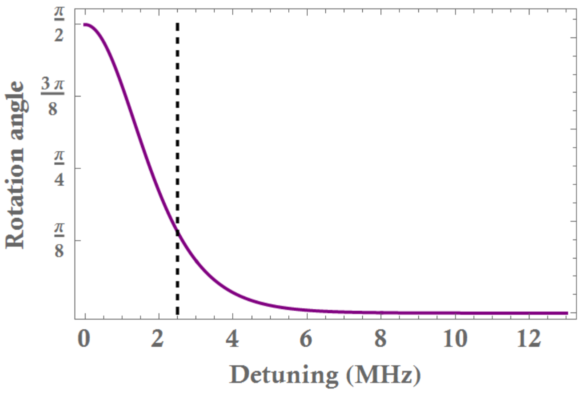

Figure 3.7: Graph showing the angle of rotation of a nucleus as a function of its detuning. The dotted line is at the point that corresponds to $A_Q = 120.5$MHz for reference.

and undergo a rotation of $\frac{\pi}{2}$. As the detuning between the pulse and a nucleus increases, so does the angle of rotation, and we plot this angle as a function of the detuning of the nucleus from the pulse resonance in Fig. 3.7. As the 5MHz region that encompasses the width of the pulse is assumed to contain only a single nucleus, we can neglect the section with a detuning of < 2.5MHz, and consider only those rotations that affect nuclei with $A_Q < 120.5$MHz (the black line in Fig. 3.7 is plotted at the point corresponding to $A_Q = 120.5$MHz for reference). Then we see that the maximum rotation we expect from any nucleus other than the target nucleus is $\approx \frac{\pi}{8}$. We can also calculate the net rotation on the full nuclear spin bath by integrating the area under the curve in Fig. 3.7. This gives a value of 0.15πrad. In Chapter 4, we will examine the effect of the rotation of the nuclei in the remainder of the bath on the system we want to prepare between the electron and nucleus. We will take into account the probability of finding a nucleus at a particular detuning from the pulse resonance and show that there are nuclear spin bath configurations that allow the two-spin subsystem we will discuss to operate with high fidelity, despite these unwanted rotations. We will show both the effect of a single nucleus with the smallest value of detuning we consider and the net effect of the rotation of the full nuclear spin bath.

3.2 Electron-nuclear spin interactions in a quantum dot

3.2.1 Evolution of an electron and single nucleus

Once the nuclear spin has been initialised into the plane of the electron spin, the two spins will begin to evolve according to the hyperfine interaction and external field [143, 144]. The basis states for the nuclear spin are defined as $\{|\Uparrow\rangle, |\Downarrow\rangle\}$ along the optical axis. The Hamiltonian for this system is taken from the full Hamiltonian of the system of an electron spin and a nuclear spin bath defined in Chapter 2, Eq. 2.15. However, in this case, we modify the nuclear term to contain a single nucleus only, ignoring the remainder of the spin bath. We will consider external fields in the Voigt geometry (the in-plane axis). The Hamiltonian of this two-spin subsystem is then defined as

$$H_{en} = \omega_e S_z \otimes \mathbb{1}_n + \omega_n \mathbb{1}_e \otimes I_z + A_t \mathbf{S} \otimes \mathbf{I} \tag{3.11}$$

where $\omega_e = g_e \mu_B B_{ext}$ ($\omega_n = \mu_I \mu_n B_{ext}$) is the precession frequency of the electron (nucleus), g_e (μ_I) is the g-factor of the electron (nucleus), μ_B is the Bohr magneton, μ_n is the nuclear dipole moment, $\mathbf{S}$ is the spin operator of the electron (nucleus), S_z (I_z) is the component of the spin operator of the electron (nucleus) in the external magnetic field direction, and A_t is the hyperfine coupling strength between the electron and the nucleus. We can neglect the second term in H_{en} as the magnetic moment, $\mu_I \mu_N$, of a nucleus is 3 orders of magnitude smaller than that of an electron and therefore has a negligible effect on the system. The temporal evolution of this system is given by a unitary,

$$U_{en}(t) = e^{-iH_{en}t}. \tag{3.12}$$

We can act this operator on the density matrix of the initial state of the electron and nucleus, which we choose to be

$$\rho_i = |\uparrow \twoheaddownarrow\rangle \langle \twoheaddownarrow \uparrow|. \tag{3.13}$$

in the optical axis basis. We should note here that it is also valid to choose the initial state to be $\rho_i = |\downarrow \twoheaduparrow\rangle \langle \twoheaduparrow \downarrow|$. However, we cannot have an initial state where the two spins are in the same state, i.e. $\rho_i = |\uparrow \twoheaduparrow\rangle \langle \twoheaduparrow \uparrow|$ or $\rho_i = |\downarrow \twoheaddownarrow\rangle \langle \twoheaddownarrow \downarrow|$, as there will be no interaction between them and each will decay due to its decoherence time only without experiencing any evolution due to their hyperfine coupling.

We can then model how the system evolves, such that the state after some evolution time, t, the new state is given by

$$\rho_f(t) = U_{en}(t)\rho_i U_{en}^{\dagger}(t). \tag{3.14}$$

We use the partial trace to calculate the reduced density operator of the electron spin state. This is defined as a mapping from a joint density matrix, ρ_{AB}, of two quantum systems, A and B, on some composite space of Hilbert spaces, $\mathscr{H}_A \otimes \mathscr{H}_B$, onto some reduced density matrix, ρ_A, on the Hilbert space, $\mathscr{H}_A$. Then if we define a basis $\{|a_i\rangle\}$ ($\{|b_j\rangle\}$) of the Hilbert space $\mathscr{H}_A$ ($\mathscr{H}_B$), we can say that any density matrix ρ_{AB} on $\mathscr{H}_A \otimes \mathscr{H}_B$ can be described by the decomposition

$$\rho_{AB} = \sum_{i,j,k,l} c_{ijkl} |a_i\rangle \langle a_j| \otimes |b_k\rangle \langle b_l|, \tag{3.15}$$

with coefficients c_{ijkl}. Then the reduced density operator of subsystem A is the partial trace over the subsystem B, given by

$$\rho_A \equiv \mathrm{Tr}_B \rho_{AB} = \sum_{i,j,k,l} c_{ijkl} |a_i\rangle \langle a_j| \langle b_l | b_k\rangle . \tag{3.16}$$

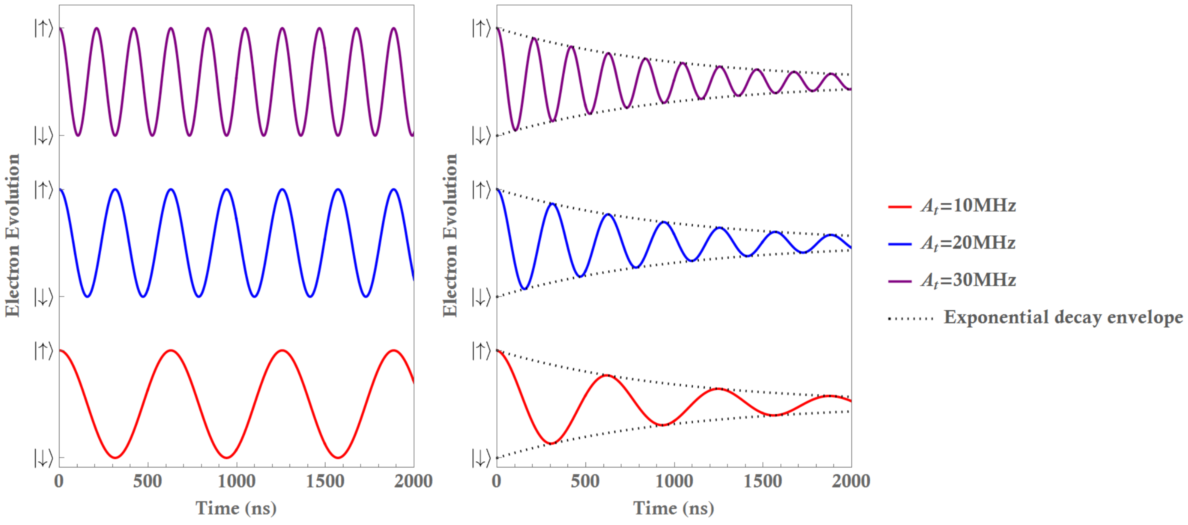

(a) (b)

Figure 3.8: Evolution of the spin state of the electron due to the hyperfine interaction between the electron and target nucleus for varying A_t with $B_{ext} = 0$. The initial state is $|\psi_0\rangle = |\uparrow\twoheaddownarrow\rangle$ in the optical axis basis. The y axis shows the state of the reduced density operator of the electron spin. In (b), we include the inherent exponential decoherence of the electron spin due to $e^{-t/\tau}$ for $\tau = 1\mu$s and show how the evolution changes.

Using this, the initial reduced density operator of the electron is

$$\rho_{i,e} \quad = \quad |\uparrow\rangle\langle\uparrow| \tag{3.17}$$

and the initial reduced density operator of the nucleus is

$$\rho_{i,n} \quad = \quad |\twoheaddownarrow\rangle\langle\twoheaddownarrow| \tag{3.18}$$

as expected. We can then calculate the electron spin reduced density operator as a function of time by considering our system to be of the form $\rho_{en} \equiv \rho_{AB}$ for the electron density operator ρ_e and the nuclear spin density operator ρ_n. Then $\rho_e = \mathrm{Tr}_n \rho_{en}$ will be of the form

$$\rho_e \quad = \quad \frac{1}{2}(\mathbb{I} + \sum_{i=x,y,z} c_i \sigma_i). \tag{3.19}$$

Plotting $c_z(t)$ (we ignore $c_y(t)$ and $c_x(t)$ as they are zero throughout) as a function of time tells us how the electron evolves around the Bloch sphere in the $\{|\uparrow\rangle, |\downarrow\rangle\}$ (optical axis) basis. We can use this to show the dependence of the electron spin evolution on the value of the hyperfine coupling constant of the target nucleus, A_t. Typical values of the hyperfine coupling for In spins will be around 10-30 MHz [116, 145]. We show how varying A_t affects the precession of the electron spin in Fig. 3.8, taking $B_{ext} = 0$ so that we see the evolution due to A_t only. The first of the two plots in Fig. 3.8 does not take into account the decoherence of the electron spin. This allows us to identify which processes are controlled by the value of A_t without considering any forms of decoherence. We can clearly see that an increase in A_t corresponds purely to an increase in the frequency of the rotation of the electron spin. From this graph alone, one would deduce a large A_t is preferable, as any quantum operations we may want to perform will be accessible on a shorter timescale. We can then incorporate decoherence into the model, taking a realistic value for the electron decoherence time to be $\tau = 1\mu$s [124], by simply adding an exponential decay of $e^{-t/\tau}$. Then the evolution of the electron spin will be as shown in the second graph of Fig. 3.8 such that the dashed black line shows the exponential decoherence envelope. We can see that in this case, as the electron spin experiences decoherence, the electron's movement around the Bloch sphere becomes restricted. This makes a larger A_t even more imperative to allow us to access a larger section of the Bloch sphere, and therefore increase the amount of quantum operations that can be performed in the time frame. We therefore choose $A_t = 30$MHz. We should note here that we have already conditioned the nuclear spin in terms of A_Q. Choosing A_Q to be high means that the nucleus is in a highly strained section of the QD. These highly strained sections generally occur in the middle of the QD, where the overlap between the electron spin and each nucleus is large [134]. This corresponds to a large coupling between the electron and nucleus, and therefore we conclude that a large value of A_t is likely for a nucleus with a large value of A_Q.

The next step is to consider how different external fields affect the electron spin precession. As we are assuming that there is no nuclear spin bath in this model, $\omega_e \equiv \omega_{eff}$ (and $B_{ext} \equiv B_{eff}$). The Larmor precession frequency, $\omega_e = g_e \mu_B B_{ext}$, and we expect the value of the g-factor to be $g_e \approx 0.25$ when we apply a magnetic field in the Voigt geometry [93, 94]. The Bohr magneton, $\mu_B \approx 14$GHz/T. Then, for an electron spin precessing in a field in the Voigt geometry, we will consider values $B_{ext} = 0$, ≈ 4.29 and ≈ 8.57 and ≈ 17.1mT, corresponding to $\omega_e = 0$, 15, 30 and 60MHz respectively. We choose these values because we want to make a direct comparison between the value of A_t and ω_e and so we plot ω_e rather than B_{ext} in this case. We should note that the values of B_{ext} are small. This is because for values of $\omega_e > 30$MHz, the precession of the electron spin due to the external field will dominate the system. This will cause some suppression of the effect of the coupling term between the electron and nucleus. We will show later in the chapter, when we reintroduce the nuclear spin bath, that it is possible to control the total size of ω_{eff} by controlling the size and direction of the Overhauser field.

In Fig. 3.9 (a), we plot the electron spin evolution for different values of ω_e in the Voigt geometry in the absence of electron spin decoherence. Here we see that when $\omega_e = 0$MHz (the zero field case), the spins periodically evolve over the full Bloch sphere in the absence of decoherence. As the value of ω_e is increased, we find that the precession frequency increases, but the precession path becomes less coherent, i.e., the oscillations appear to still cover the full Bloch sphere, but there is not a single coherent frequency. The action of ω_e becomes the dominant term in the system, which causes the frequency of the electron spin to increase, such that the driving of the system due to the external field overpowers the interaction term. Both the interaction term and

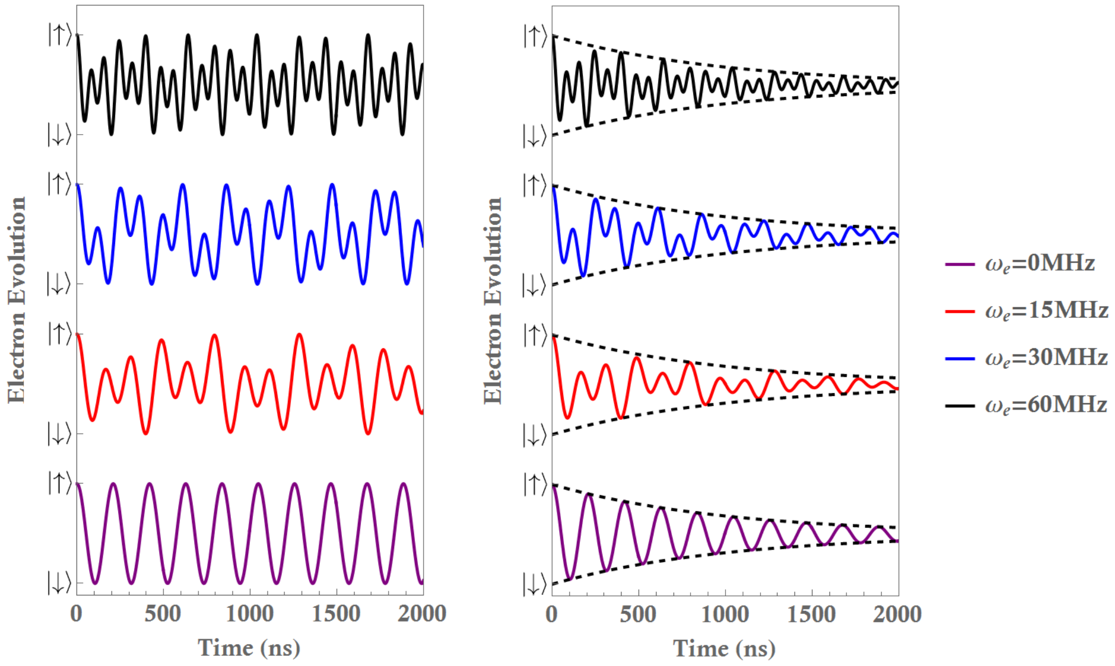

(a) (b)

Figure 3.9: Evolution of the electron spin state as a function of time for increasing external field along the Voigt axis including the inherent exponential decoherence of the electron spin due to $e^{-t/\tau}$ for $\tau = 1\mu$s in (b). The initial state is $|\psi_0\rangle = |\uparrow \Downarrow\rangle$ in the optical axis basis.

the external field term individually induce a coherent precession of the electron spin, but the combination of the two terms acting on the system gives the evolution we see, where the Bloch sphere rotations do not appear to obey a particular pattern. This is due to the external field term acting only on the S_z spin component of the electron spin, whereas the interaction term acts on each of S_i, leading to the two terms becoming out of phase with each other.

Introduction of the electron decoherence term in the second graph in Fig. 3.9 further restricts the evolution of the electron spin about the Bloch sphere, such that its state approaches the the maximally mixed state. This maximally mixed state corresponds to the point at which all of the information contained in the state of the electron spin is lost. We want to maximise the amount of coherent quantum operations that we can perform before the coherence of the electron spin is lost. Full access to the Bloch sphere is only available in the case where $\omega_e = 0$MHz, although the precession frequency is slower. However, we have not yet looked at the points of entanglement in the dynamics between the electron and nucleus.

We now want to know under what conditions the electron and nucleus will become entangled. As the electron and nucleus evolve periodically from the state $|\psi(0)\rangle = |\uparrow \Downarrow\rangle$ to the state $|\psi(\pi)\rangle = |\downarrow \Uparrow\rangle$, assuming that the full Bloch sphere is available to the system (i.e. in the absence of decoherence), at some point in this evolution, the state will reach the configuration $|\psi(t)\rangle = |\uparrow \Downarrow\rangle + |\downarrow \Uparrow\rangle$ and similarly from $|\psi(t)\rangle = |\downarrow \Uparrow\rangle$ to $|\psi(t)\rangle = |\uparrow \Downarrow\rangle$ we will find the maximally entangled state $|\psi(t)\rangle = |\uparrow\Downarrow\rangle - |\downarrow\Uparrow\rangle$. We should note that this is not true in general if B_{ext} is non-zero due to restricted precession of the qubits about the Bloch sphere. A robust method for quantifying the amount of entanglement shared between two particles is to calculate the negativity [146]. This is defined as

$$\mathcal{N}_\rho = \frac{|\lambda_i| - \lambda_i}{2}. \tag{3.20}$$

Here λ_i are the eigenvalues of the partial transpose of ρ_{en} with respect to the nuclear spin subsystem. Using ρ_{en} as defined in Eq. 3.15, this is given by

$$\rho^{T_n} = \sum_{i,j,k,l} c_{ijkl} |a_i\rangle \langle a_j| \otimes (|b_k\rangle \langle b_l|)^T. \tag{3.21}$$

Then the negativity is given by the absolute value of the sum of the negative eigenvalues. This will vary between 0 and $\frac{1}{2}$ with 0 corresponding to no entanglement and $\frac{1}{2}$ corresponding to a maximally entangled state (a Bell state). By plotting the negativity of our two-spin subsystem we can determine the amount of entanglement between the two particles as a function of time. We show how this value varies as a function of ω_e, both with and without the decoherence of the electron spin. This is shown in Fig. 3.10.

Here, we find that in the absence of decoherence, the maximally entangled state is still achievable, however, we see the non-periodic evolution about the Bloch sphere affecting the timescale of these points of maximal entanglement. The increase in precession frequency as the external field increases leads to the maximally entangled state occuring more frequently, but due to the Bloch sphere restrictions, this is no longer periodic. However, when we consider the effect of the electron spin decoherence, we actually find that the decoherence term acts such that in the presence of any non-zero B_{ext}, the maximally entangled state conditions can never be perfectly met. This is due both to the restriction of the available Bloch space due to the decoherence term and the non-periodic evolution due to the phase mismatch between the external field term and the hyperfine coupling term. We therefore conclude that it is necessary to minimise the size of the total field acting on the system. Then, if the total effective field acting on the electron spin, given by

$$B_{eff} = B_{ext} + B_{OH}, \tag{3.22}$$

where B_{OH} is the size of the field induced by the nuclear spin bath, is equal to 0 and $A_t = 30\text{MHz}$, we find that the first point of maximum entanglement will occur after 52.6ns. At this point the state of the electron spin will be mapped onto the state of the nuclear spin. This maximally entangled state between the electron and nucleus is equivalent to acting the quantum gate $\sqrt{\text{SWAP}}$ (defined in Eq. 3.1). The advantage of performing the gate in this way is that the system simply evolves over time to take on this particular state, and no external operations are needed at this stage of the process, decreasing the possibility of losses being introduced to the system from the environment.

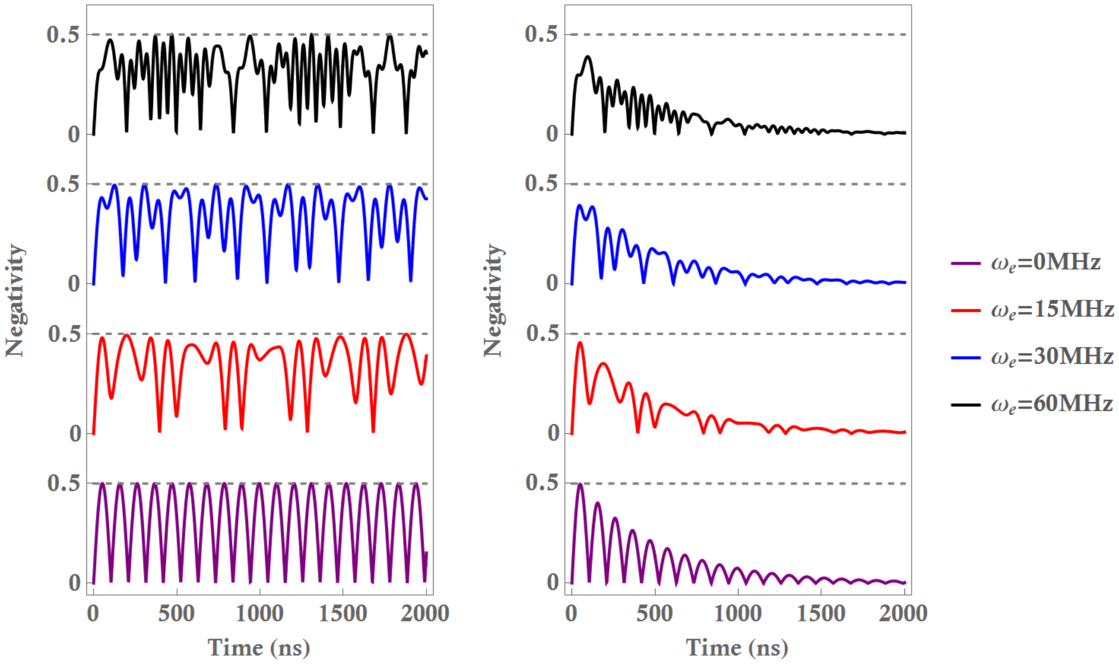

Figure 3.10: Negativity of the two-spin subsystem as a function of time for increasing external field in the Voigt geometry including the inherent exponential decoherence of the electron spin due to $e^{-t/\tau}$ for $\tau = 1\mu$s in (b). The initial state is $|\psi_0\rangle = |\uparrow \Downarrow\rangle$. The dotted lines are references for the points at which the maximally entangled state occurs. We see that as the external field increases in the absence of decoherence, the maximally entangled state can still be achieved for any value of ω_e. In the presence of decoherence, we see the maximum entanglement decreases as the external field increases.

We know that the nuclei, if unpolarised, will induce a fluctuating magnetic field that we need to control and we need an external field applied to the system to achieve this control. This means that we cannot simply apply no external field to achieve the condition $\omega_{eff} = 0$. Hence, we propose to force the system into a configuration such that the field induced by the nuclei is equal in magnitude but in the opposing direction, i.e., $B_{ext} = -B_{OH}$. We will now reintroduce the nuclear spin bath and show that it is possible to achieve this condition.

3.2.2 Creating the ideal nuclear spin environment

We have now shown for an electron and nuclear spin precessing according to an external field in the Voigt geometry and a hyperfine coupling between them that to achieve the maximally entangled state between the two, we require the condition $B_{ext} \approx 0$. We now want to show that it is possible to achieve this condition in the presence of the nuclear spin bath, in the QD, by controlling the size and direction of the Overhauser field. In Chapter 2, we describe the NFF protocol. We now want to use this model to determine the parameters needed to achieve the condition $B_{eff} = 0$. This can be calculated using the total effective precession frequency of the electron spin due to both B_{ext} and the polarised nuclear field, B_{OH}, given by

$$\omega_{eff} = \omega_e + \frac{mA}{2}, \tag{3.23}$$

assuming the box model, where ω_e is the precession frequency of the electron spin due to B_{ext} only, $m = N_\uparrow - N_\downarrow$ is the number of nuclei (anti-)aligned to the external field, hence determining the overall direction of the state of the nuclear spin bath and A is the average value of the hyperfine coupling constants which we choose to be $A = 15$MHz. However, this condition alone is not sufficient - as discussed in Chapter 2, we also require $P(m) \longrightarrow 1$, such that the solution giving $\omega_{eff} = 0$ is approximately the only possible nuclear spin configuration for the particular parameter set.

To find such a parameter set, we need to simultaneously satisfy the equations

$$\omega_e = -\frac{mA}{2} \tag{3.24}$$

and

$$P(m) \geq 0.8. \tag{3.25}$$

The parameters are plotted in a similar graph to that shown in Fig. 2.9(c), however, we replace B_{ext} with ω_e, the precession frequency of the electron due to B_{ext} only and m with $\frac{mA}{2}$, the Overhauser shift. This allows us to determine at which points the conditions given in Eqs. 3.24 and 3.25 above are satisfied. In Fig. 3.11 we plot this relationship between ω_e and ω_{OH}. Additionally, we plot a black dashed line that indicates all of the points at which the first condition, $\omega_e = -\omega_{OH}$ is satisfied. Then, any point on this line will force the system into a configuration where $\omega_{eff} = 0$, as required. However, many of these points have a very low probability of occurring. We must therefore consider our second condition, $P(m) \geq 0.8$. We need to find the points at which the high values of $P(m)$ overlap with the dotted line, such that we have a configuration that will satisfy Eq. 3.24 and also have a high probability of occurring. In the range of ω_e that we are considering, we find that there is a single point where this is satisfied. This point is located at $\omega_e \approx 0.325$GHz (corresponding to an external field of $B_{ext} \approx 92.9$mT) with $P(m) \approx 0.91$ (see Fig. 3.12).

Although we find only a single point that satisfies both of our conditions, increasing the range of B_{ext} we consider should result in more of these points being accessible. The value of the g-factor will also affect these results, and so it may be necessary to measure the g-factor of a particular QD and then adjust the parameters accordingly to find the value of B_{ext} required to correctly drive the system into this state. The values of Δ and Ω should not affect the result, unless they deviate far from the values we choose. We have now shown that the system will reach a maximally entangled state, or $\sqrt{\text{SWAP}}$ gate configuration most stably when $\omega_{eff} = 0$ and that this condition is achievable for a particular parameter set we choose. In addition to this, we have shown that single spin manipulation in a QD is possible, provided the nucleus is chosen carefully such that it will be isolated in terms of its quadrupolar coupling, A_Q from the other nuclei in the

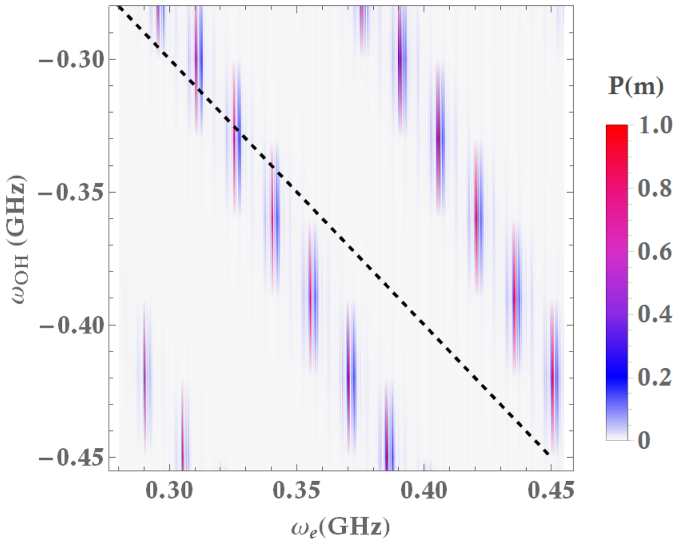

Figure 3.11: Graph showing the relationship between the precession frequency of the electron spin (ω_e), the Overhauser shift ($\omega_{OH} = \frac{mA}{2}$) and the value of $P(m)$. We use $\Delta = 0.2$, $\Omega = 0.6$, $g = 0.25$ and $A = 15$MHz as in Chapter 2. The dotted line shows the points at which the total effective field on the electron, $\omega_{eff} = \omega_e - \frac{mA}{2} = 0$.

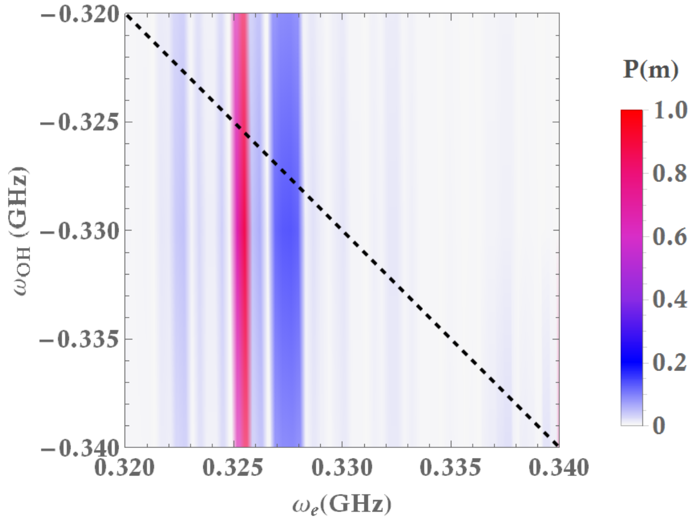

Figure 3.12: This figure shows the location of the point in Fig. 3.11 that satisfies the two conditions we require. The parameters are $\Delta = 0.2$, $\Omega = 0.6$, $g = 0.25$ and $A = 15$MHz as given above.

spin bath. The following chapter will now show that combining these two processes allows us to construct a protocol for a nuclear spin quantum memory.

3.3 Summary

To summarise, we have analysed the strain profile of InGaAs QDs with a view to identifying a nuclear spin within the QD that is isolated in frequency from the rest of the nuclear spin bath. We conclude that the chances of finding an isolated nucleus are high if we choose the frequency range carefully. We have shown that it is possible to design a RF pulse that will rotate this nucleus into the plane of the excess electron spin found within the QD and shown how this RF pulse will affect the remainder of the nuclei in the spin bath. We then analysed the evolution of the electron spin and target nucleus in the absence of a nuclear spin bath due to the hyperfine interaction and precess frequency of the electron spin in an external magnetic field, and showed that if we choose the parameters $B_{ext} = 0$ and $A_t = 30$MHz, it is possible to create a maximally entangled state between the electron spin and the nucleus. Finally, we reintroduced the nuclear spin bath and showed that it is possible to drive the full system into a configuration such that $\omega_e = -\omega_{OH}$, i.e. the Overhauser field induced by the nuclear spins cancels out the external field acting on the electron, leaving $\omega_{eff} = 0$, as we require to achieve the maximally entangled state between the electron and nucleus. The following chapter will show how this information transfer can be used to construct a quantum memory protocol for quantum communications applications.

CHAPTER 4

A NUCLEAR SPIN QUANTUM MEMORY PROTOCOL

In this chapter, we exploit the entangling evolution described in Chapter 3 to construct a protocol for a nuclear spin quantum memory using the two-spin system, such that an initial electron spin state can be mapped onto a nucleus and retained on long timescales. This is a theoretical chapter and all material discussed in the chapter is novel. We show that through use of an ancilla photon, we can read out this nuclear spin state, meaning that it can be used as a robust store for a quantum state [147]. Next, we discuss how unwanted coupling between the electron-nuclear subsystem and outlying nuclei in the spin bath that may be close in frequency to the isolated spin affects the precession of the two-spin subsystem. Finally, we discuss the possibility of extending this system to implement the ancilla-driven quantum computation (ADQC) protocol proposed by Janet Anders *et al.* in 2010 [148, 149] and show promising preliminary data for such a model.

4.1 A quantum memory protocol

A quantum memory is an interface between light and matter that allows a quantum state of light to be mapped onto one or an ensemble of particles that is able to retain this state such that it can be retrieved in its original form via some measurement process [70, 71]. By definition, a quantum memory will store a given quantum state for a particular time interval, such that the state is retrievable. Quantum memories are an important component of quantum information processing and can be used for such things as synchronisation of quantum computing processes, converting heralded photons to on-demand photons and implementing long-distance communication protocols [63, 64]. A spin in a QD is a promising example of a store for quantum information, however, the relatively short relaxation time ($T_1 \approx$ms) [30] and coherence time ($T_2 \approx \mu$s) [124] of the electron spin leads us to consider nuclear spins as alternatives. Indeed, the motivation for using the nuclear spin as the memory over the electron spin itself (as proposed in

[30]) is that the coherence time of a nuclear spin is much longer than that of an electron spin and has the potential to last for times on the order of hours if prepared correctly [131–133, 147]. We should note here that none of the previous references refer to a QD platform and discuss the more general cases of nuclear spins, and there are currently no publications of successful measurements of T_2 times for single nuclear spins in QDs. However, there are several demonstrations of long T_2^* times for the nuclei in QDs, with the state of the art being on the order of one hour [150, 151]. The nuclear spin quantum memory protocol can be achieved if we imagine using the $\sqrt{\text{SWAP}}$ gate (defined in Eq. 3.1 in Chapter 3) as a transfer of the electron spin state to the nuclear spin state.

However, there are several considerations we must take into account. First, we must think about how we can stop the evolution of the system at the point of maximal entanglement, as currently, the electron and nucleus will continue to precess until the decoherence of the electron dominates the system. We must also consider how we can read out the state of the nucleus after it is decoupled from the electron spin without destroying its state. To address the first of these points, we can perform a disentangling operation on the electron at the point of maximal entanglement. This can be done by applying a $\frac{\pi}{2}$ pulse to the electron spin at this point, which performs a 90° rotation about the Bloch sphere to project the electron onto the axis perpendicular to the nucleus using the rotation matrix given in Eq. 3.7. Then the nucleus will retain the state it had acquired at the point of entanglement for as long as its coherence time allows.

Readout of the nuclear spin state is more complex. To achieve this, we propose a quantum non-demolition measurement similar to those described in [152, 153]. This is a measurement designed to preserve the state of the physical system upon detection. This involves use of an ancilla, which, in this case, will be a photon. This photon, if polarised correctly, can be entangled to the electron-nuclear subsystem; this will be derived in Section 4.1.1. The photon will then experience an optical Faraday rotation, with each of its circularly polarised components experiencing a different phase shift, dependent on the spin state of the electron. This is possible due to the spin selection rules of a QD as described in Chapter 1. It has been shown that an electron spin in a cavity will induce different phase shifts for the different circular polarisations of light, i.e. the phase shift induced onto a photon interacting with an electron spin in a QD by left circularly polarised light will be different to the phase shift induced onto the same electron spin by right circularly polarised light due to the Pauli exclusion principle (the available transitions in a QD are as shown in Fig. 4.1) [31, 152]. Then, if the initial polarisation of the photon is linear, say $|H\rangle$, the state of this photon ($|\psi\rangle$) can be represented as a combination of two circular components:

$$|\psi\rangle \quad = \quad \frac{1}{\sqrt{2}}(|R\rangle + |L\rangle). \tag{4.1}$$

Then, for an electron in the state $|\uparrow\rangle$, the photon reflected from the cavity will be in the state

$$|\psi\rangle \quad = \quad e^{i\phi_0}|R\rangle + e^{i\phi_1}|L\rangle, \tag{4.2}$$

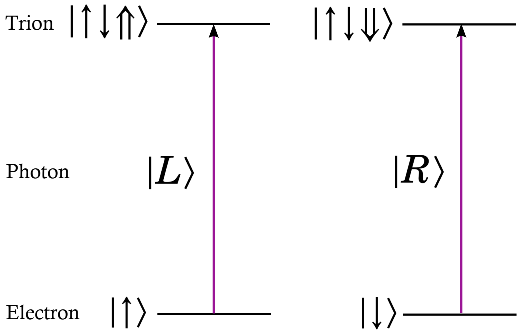

Figure 4.1: Available transitions for an excess electron in a QD that is exposed to circularly polarised light. The Pauli exclusion principle tells us that each circular polarisation will excite only one of the electron spin states.

where ϕ_0 is the phase shift of the component of the photon that has not interacted with the cavity and ϕ_1 is the phase shift of the component of the photon that has interacted with the cavity. The total Faraday rotation angle, θ_F of the photon is then given by

$$\theta_F = \frac{\phi_0 - \phi_1}{2}. \tag{4.3}$$

This corresponds, in a perfect system, to a switch of the photon polarisation from $|H\rangle$ to $|V\rangle$, which we can then, in theory, measure using single photon detectors.

If we extend this to spin-photon interactions (e.g. a photon interacting with the electron spin), we find that there will be a phase shift applied to the photon dependent on the state of the electron it interacts with. For example, if the state of the photon is originally $|H\rangle$ and it interacts with an electron in the spin state $|\uparrow\rangle + |\downarrow\rangle$, there will be an induced phase shift. If the rotation angle $\theta_F = \frac{\pi}{2}$, this induced phase shift will give the transformation

$$|H\rangle(|\uparrow\rangle + |\downarrow\rangle) \implies |D\uparrow\rangle + |A\downarrow\rangle, \tag{4.4}$$

where $|D\rangle = \frac{1}{\sqrt{2}}(|H\rangle + |V\rangle)$ and $|A\rangle = \frac{1}{\sqrt{2}}(|H\rangle - |V\rangle)$, i.e. each of the spin states of the electron will induce a different phase shift on each of the circular components of the photon. This process is called photon-spin entanglement.

We should note that this assumes that our QD is symmetrical both in shape and strain distribution, such that there will be no splitting or mixing between the states at zero field [154]. Here, we extend this model to show that we can use a similar protocol to perform a non-demolition measurement on a nuclear spin that is entangled to the electron spin. The process we use to model this is to take the electron-nuclear state at the point of maximal entanglement and introduce a polarised photon into the system. We then disentangle the electron from this system using a projective measurement in the orthogonal basis. When the electron is decoupled from the system, we will maintain the photon-nuclear entanglement and by measuring the photon in the correct basis, we can determine the state of the nuclear spin.

4.1.1 Photon entanglement

The first step is to entangle the photon to the subsystem. At the point of maximal entanglement between the electron and nucleus, the state of the two-spin subsystem will be

$$|\psi_{en}\rangle \quad = \quad \frac{1}{\sqrt{2}}(|\uparrow\twoheaddownarrow\rangle + |\downarrow\twoheaduparrow\rangle). \tag{4.5}$$

We choose the photon to be in the state

$$|\psi_{ph}\rangle \quad = \quad \alpha|H\rangle + \beta|V\rangle, \tag{4.6}$$

where α and β represent an arbitrary quantum state we encode in the electron spin, $|H\rangle$ and $|V\rangle$ are the horizontal and vertical components of the photon polarisation and $|\alpha|^2$ and $|\beta|^2$ are the probabilities of the photon being in the $|H\rangle$ and $|V\rangle$ states respectively with $|\alpha|^2 + |\beta|^2 = 1$. We then send the photon into the cavity where it interacts with the electron spin. Due to the spin selection rules described in Chapter 1, the state of the three-spin subsystem will become

$$|\psi\rangle = |\psi_{ph}\rangle \otimes |\psi_{en}\rangle \quad \Rightarrow \quad \frac{1}{\sqrt{2}}(\alpha(|D\rangle|\uparrow\twoheaddownarrow\rangle + |A\rangle|\downarrow\twoheaduparrow\rangle) + \beta(|D\rangle|\downarrow\twoheaduparrow\rangle - |A\rangle|\uparrow\twoheaddownarrow\rangle)) \tag{4.7}$$

(if $\theta_F = \frac{\pi}{2}$). This is an entangled state between the three particles. To verify that the photon has become entangled with the nucleus, we need to show that the photon state has been encoded on the nuclear spin. In order for the nucleus to retain this state, we must suppress the evolution between the electron and nucleus. This can be done using an optical pulse of area $\frac{\pi}{2}$ about the y axis (defined in Eq. 3.7) to rotate the electron into the plane perpendicular to the nucleus, a process which will disentangle the two spins. We can represent the effect of the disentangling pulse as

$$|\psi\rangle \quad \Rightarrow \quad \frac{1}{2}(\alpha(|D\rangle(|\uparrow\rangle + |\downarrow\rangle)|\twoheaddownarrow\rangle + |A\rangle(|\uparrow\rangle - |\downarrow\rangle)|\twoheaduparrow\rangle) + \beta(|D\rangle(|\uparrow\rangle - |\downarrow\rangle)|\twoheaduparrow\rangle - |A\rangle(|\uparrow\rangle + |\downarrow\rangle)|\twoheaddownarrow\rangle)). \tag{4.8}$$

Then we can measure the state of the electron spin along $|\uparrow\rangle$ (or similarly $|\downarrow\rangle$) to retrieve the state of the photon-nuclear subsystem. This gives

$$\begin{aligned} |\psi_{phn}\rangle &= \frac{\langle\uparrow|\psi\rangle}{\sqrt{\langle\psi|\uparrow\rangle\langle\uparrow|\psi\rangle}} \\ &= \frac{1}{2}(\alpha(|D\twoheaddownarrow\rangle + |A\twoheaduparrow\rangle) + \beta(|D\twoheaduparrow\rangle - |A\twoheaddownarrow\rangle)). \end{aligned} \tag{4.9}$$

To verify that there is entanglement between the photon and nucleus at this point, we perform a projective measurement on the photon in the $\{|D\rangle, |A\rangle\}$ basis. If the photon is detected in the $|D\rangle$ state, then the state of the nuclear spin is

$$\begin{aligned} |\psi_n\rangle &= \frac{\langle D|\psi_{phn}\rangle}{\sqrt{\langle D|\psi_{phn}\rangle\langle\psi_{phn}|D\rangle}} \\ &= \frac{1}{\sqrt{2}}(\alpha|\twoheaddownarrow\rangle + \beta|\twoheaduparrow\rangle) \end{aligned} \tag{4.10}$$

and if we measure the photon in $|A\rangle$, the state of the nuclear spin is

$$\begin{aligned} |\psi_n\rangle &= \frac{\langle A|\psi_{phn}\rangle}{\sqrt{\langle A|\psi_{phn}\rangle\langle\psi_{phn}|A\rangle}} \\ &= \frac{1}{\sqrt{2}}(\alpha\,|↟\rangle - \beta\,|↡\rangle). \end{aligned} \tag{4.11}$$

Comparing this to the initial photon state in Eq. 4.7, we can see that the state of the photon has been mapped onto the nuclear spin and measuring the photon in this basis confirms that the nucleus has retained the spin information of the photon (although detecting the photon in $|A\rangle$ gives a π phase shift of the $|↡\rangle$ component), thus confirming the entanglement between the two. We can conclude using this method that the photon and nucleus have undergone maximal entanglement and that we can recover the original photon state from the nuclear spin state.

4.1.2 Readout of the nuclear spin state

The fact that we are able to successfully entangle a photon spin to this system means that we can use this photon to give us information about the nuclear spin state. To show that the nucleus retains the information transferred by the electron spin, we need to re-entangle the electron to the nucleus, using, as before, a rotation pulse (this time with angle $-\frac{\pi}{2}$ to rotate in the opposite direction) to rotate the electron back into the plane of the QD. We then redefine the initial state of the electron-nuclear subsystem to be

$$|\psi_{en}\rangle = a\,|\uparrow ↡\rangle + b\,|\downarrow ↟\rangle \tag{4.12}$$

such that we can show that the values a and b can be encoded in the nuclear spin. We again require the photon to have linear polarisation, however, in this case we choose the photon state to be simply

$$|\psi_{ph}\rangle = |H\rangle. \tag{4.13}$$

Entangling this photon with the electron-nuclear state will give us

$$\begin{aligned} |\psi\rangle &= |H\rangle\otimes|\psi_{en}\rangle \\ &\implies a\,|D\uparrow ↡\rangle + b\,|A\downarrow ↟\rangle. \end{aligned} \tag{4.14}$$

As before, it is necessary at this point to disentangle the electron spin from the system to create a two-spin subsystem between the photon and the nucleus. Again, a $\frac{\pi}{2}$ will rotate the electron spin onto the axis orthogonal to the nuclear spin state. After this electron spin rotation, we have the state

$$|\psi\rangle \implies \frac{1}{\sqrt{2}}(a\,|D\rangle(|\uparrow\rangle + |\downarrow\rangle)|↡\rangle + b\,|A\rangle(|\uparrow\rangle - |\downarrow\rangle)|↟\rangle). \tag{4.15}$$

We then need to perform a projective measurement on the electron spin. We measure along $|\uparrow\rangle$, which gives the photon-nuclear subsystem:

$$\begin{aligned} |\psi_{phn}\rangle &= \frac{\langle\uparrow|\psi_{phn}\rangle}{\langle\psi_{phn}|\uparrow\rangle\langle\uparrow|\psi_{phn}\rangle} \\ &= \frac{1}{\sqrt{2}}(a\,|D\Downarrow\rangle + b\,|A\Uparrow\rangle). \end{aligned} \tag{4.16}$$

To read out the state of the nuclear spin non-destructively we now need to disentangle the nucleus from the photon. This can be done by applying the RF pulse described above when we first projected the nucleus into the plane of the electron (with opposite sign to reverse the direction). This will give the state

$$|\psi_{ph}\rangle = \frac{1}{2}(a\,|D\rangle(|\Uparrow\rangle - |\Downarrow\rangle) + b\,|A\rangle(|\Uparrow\rangle + |\Downarrow\rangle)) \tag{4.17}$$

and by projecting the nucleus along $|\Uparrow\rangle$ using

$$|\psi_{ph}\rangle = \frac{\langle\Uparrow|\psi_{phn}\rangle}{\sqrt{\langle\psi_{phn}|\Uparrow\rangle\langle\Uparrow|\psi_{phn}\rangle}} \tag{4.18}$$

we can retrieve the photon state, given by

$$|\psi_{ph}\rangle = \frac{1}{\sqrt{2}}(a\,|D\rangle + b\,|A\rangle), \tag{4.19}$$

which now contains the information originally stored in the nuclear spin state. Then we have a protocol that allows us to retain the state of the electron spin in the nuclear spin, thus allowing for a quantum memory on a longer timescale. Next, we will discuss how the nuclei within the nuclear spin bath can affect the ability of the system to achieve maximal entanglement and investigate how the RF pulse we apply instigates some rotation of additional spins within the bath into the plane of the electron and nucleus due to the off-resonant Rabi oscillations introduced above.

4.2 Effect of the rotation of additional bath nuclei into the plane of the two-spin subsystem

In Chapter 3, we discuss the effect of a RF pulse on nuclei that are detuned from the pulse resonance. We find that the RF pulse will induce some rotation of the nuclei that are close in frequency to the target nucleus (see Fig. 3.7). We now want to quantify the effect these small rotations have on the electron-nuclear spin subsystem we have modeled. The initial state of a nucleus in the prepared spin bath will be

$$|\psi_{n\pm}\rangle = \frac{1}{\sqrt{2}}(|\uparrow\rangle \pm |\downarrow\rangle) \tag{4.20}$$

in the optical axis basis where $|\psi_{n+}\rangle$ ($|\psi_{n-}\rangle$) represents a nucleus that is (anti-)aligned with B_{ext}. Then, acting the rotation matrix given in Eq. 3.7 in Chapter 3 on this nuclear spin state, we can calculate the component of $|\psi_{n\pm}\rangle$ that is in the same plane as the electron-nuclear subsystem. Then, we can model a subsystem that includes nearby additional nuclei, and show how these nuclei affect the precession of the electron-nuclear subsystem. We will consider how these rotations affect the evolution of the two-spin subsystem and whether maximal entanglement between the electron and target nucleus is still achievable in the presence of these effects. We have shown that the effect of the pulse on spins far detuned from the pulse resonance is negligible and only consider those nuclei that are close in frequency to the target nucleus. It is also true that the nuclei far detuned from the pulse are likely to have a small value of A_i, as the most highly strained region of the QD is the middle, and will therefore have a much smaller coupling to the electron, meaning that they are unlikely to have a significant effect on the entangled state in the time frame we are considering. We will therefore consider the effect of a nucleus close to the frequency of the target nucleus. The values of A_Q will follow a Gaussian distribution, as shown in Fig. 3.5 in Chapter 3. Using the distribution of values of A_Q, we now consider the range of frequencies $118 \le \omega_n \le 120.5$ as this section has high probability of containing a single nucleus only and covers the most significant portion of the action of the pulse outside of the pulse width.

We will now combine this additional nucleus into the model of the electron-nuclear subsystem to see how the evolution of the two-spin subsystem is affected by this additional parameter. Because a nucleus with a value of A_Q that is close to the target nucleus's value of A_Q will experience some rotation due to the RF pulse (as discussed in Chapter 3), it will then have some population in the plane of the electron and target nucleus, meaning we can no longer assume it is decoupled from the electron. This requires us to include any rotated nuclei in our two-spin model. To do this, we must make an assumption about the value of the hyperfine coupling of the additional nucleus. We expect, as previously discussed, that the value of the hyperfine coupling, A_i will be large for a nucleus with a high value of A_Q, and so we first take the case where the value of A_i is the same for the target nucleus as an additional nucleus, i.e. $A_i = A_t = 30$MHz [116, 145]. As the target nucleus has a higher value of A_Q, it is unlikely that the value of A_i of the additional nucleus will be greater than A_t. We then model the evolution of this three-spin subsystem. From this, we can model the negativity of the subsystem of the electron and target nucleus, retrieving this two-spin subsystem using the partial trace, as given in Eq. 3.16 (similarly to the negativity measurements in Chapter 3). We plot this in Fig. 4.2 for an additional nucleus with $A_Q = 120.5$MHz (this will experience a rotation of $\frac{\pi}{8}$) and a hyperfine coupling of $A_i = A_t = 30$MHz. The state of the additional nucleus is calculated by assuming an initial nuclear state of $\frac{1}{\sqrt{2}}(|\uparrow\rangle + |\downarrow\rangle)$ and applying the rotation operator defined in Eq. 3.7 with $\theta = \frac{\pi}{8}$. Here the total entanglement between the electron and nucleus is reduced due to the additional nucleus. We describe the total entanglement, F by the ratio of the negativity over the maximum possible value of the negativity, i.e.

$$F = \frac{\mathcal{N}_\rho}{\mathcal{N}_{max}} \tag{4.21}$$

where $\mathcal{N}_{max}$ is the highest possible value of the negativity, corresponding to a maximally entan-

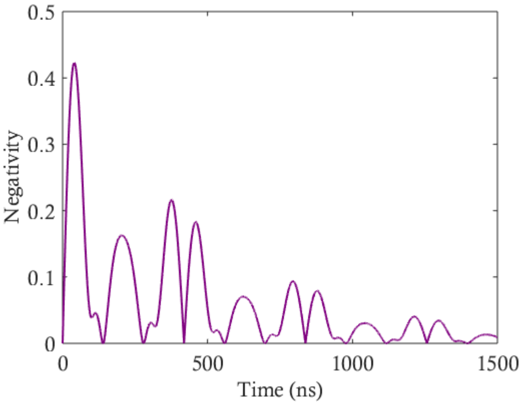

Figure 4.2: Values of the negativity for the two-spin subsystem of electron and nucleus with the addition of a second nucleus that has been partially rotated into the same plane.

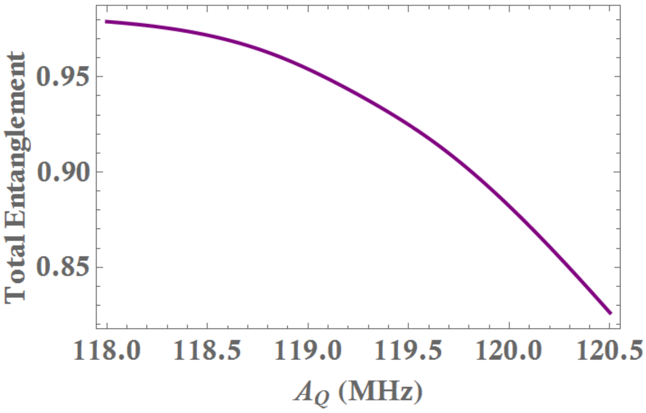

Figure 4.3: Graph showing the relationship between the detuning of an additional nucleus with $A_i = A_t = 30$MHz coupling to the system and the total entanglement between the electron and target nucleus. The range of detuning used is 118-120.5MHz as this section will, by probability, contain one single nuclear spin.

gled state (0.5) and $\mathcal{N}_\rho$ is defined in Eq. 3.20. The total entanglement with an additional nucleus centred at 120.5MHz is ≈ 0.82. This degree of entanglement is not sufficient to successfully transfer the full state of the electron spin to the nucleus. However, we will now consider how the total entanglement varies as a function of the detuning of the additional nucleus.

We will first show the total entanglement between the electron and nucleus when $A_i = 30$MHz and A_Q is in the range $118 \leq A_Q \leq 120.5$. This gives the plot in Fig. 4.3. We find that as the detuning of the additional nucleus increases, the total entanglement between the electron and target nucleus increases, as expected. In this case, the maximum value of the total entanglement is ≈ 0.978, assuming that the additional nucleus has a frequency $A_Q = 118$MHz. This can be improved upon if the value of A_i of the additional nucleus is lower than A_t (in the above graph

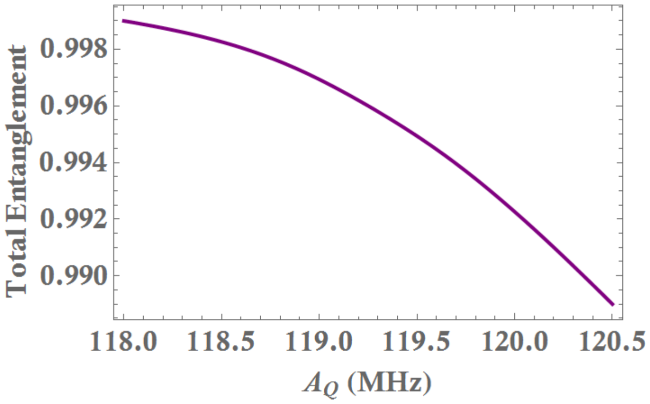

Figure 4.4: Graph showing the relationship between the detuning of an additional nucleus with $A_i = 28$MHz coupling to the system and the total entanglement between the electron and target nucleus. The range of detuning used is 118-120.5MHz as this section will, by probability contain one single nuclear spin.

we assumed $A_i = A_t$). We find that decreasing the value of A_i improves the total entanglement very quickly, for example, when we decrease the value of A_i to $A_i = 28$MHz, we get a maximum total entanglement of $F = 0.999$ (see Fig. 4.4). It is also possible to calculate the net rotation caused to the nuclear spin bath by the pulse by integrating the area under the curve in Fig. 3.7. We find that this overall rotation of the spin bath is 0.15πrad, up to a detuning of 85MHz (this covers all of the frequencies in the nuclear spin bath). Because there are approximately an even number of nuclei pointing in each direction along the external field axis, we assume that the total value of A will be approximately the average value. If we then take the average value of A_i to be $A = 15$MHz (as used previously) we can represent the spin bath as a single spin that has been rotated by 0.15πrad with a hyperfine coupling of 15MHz. We then calculate the total entanglement of the electron and target nucleus to be $F \approx 0.99$.

This shows that although we cannot assume the entangled state of the electron and target nucleus will not be affected by an additional nucleus being rotated by the RF pulse, there are possible nuclear spin configurations that will allow the maximally entangled state to be achievable. We should note that the effect of additional nuclei that are not within this range of detuning induces a maximum loss in total entanglement of 0.1% if $A_i \leq 28$MHz and so we neglect the effect of any of these nuclei. Satisfying this condition is dependent on finding a QD with a nuclear spin distribution that follows these particular parameters, which is currently difficult and would have to be done by trying many QDs. If we were to think of scaling up a protocol such as this, it would be impractical to test multiple QDs to find one that satisfied these conditions. However, control of the strain profile of a QD is currently being researched, with the aim of producing site-controlled QDs with identical strain profiles [155, 156]. Then we can imagine designing a QD that will give the distribution of A_Q we require such that its production is repeatable.

We have now shown that it is possible to construct a protocol for a nuclear spin quantum memory within a QD and given details of how the environment of the QD could be controlled to allow this protocol to be successfully implemented. This will have extensive applications in the field of quantum computing and in particular quantum communications. Another possible application for these electron-nuclear interactions is quantum repeaters for long-distance communications [65, 66]. A particularly applicable approach is that proposed by Vinay and Kok using NV centres in diamond [157]. This combines existing successful processes for creation of long-range Bell pairs, connection of such pairs via repeater stations and distillation of states in a single system of NV centres with nuclear spin and electron spin qubits connected via double-heralded entanglement in a graph state structure. One could also imagine the protocol being extended to a full QC model, which we will now discuss in more detail.

4.3 Ancilla-driven quantum computation

We will now consider how this quantum memory could be extended to a full QC protocol and show some preliminary data giving a proof of concept and incentive for further research into this area. Rather than considering one of the standard QC models, i.e. gate-based (GBQC) or measurement-based quantum computation (MBQC) [6, 7, 158], we will instead study ancilla-driven quantum computation (ADQC), a quantum computing model proposed by Janet Anders in 2010 [148, 149]. This model lends itself to our application much more readily than the others. The basic premise of the model is to create a quantum register of qubits that can be manipulated indirectly via a single ancilla. An obvious advantage to this model over GBQC is that it is not necessary to directly address the register qubits and these will therefore be granted an additional layer of protection from the environment. The ancilla will be entangled to one or more register qubits sequentially, such that direct manipulation of the ancilla leads to indirect manipulation of the register qubits. For example, if we have an ancilla entangled to a single register qubit via some fixed entangling operation, we can imagine measuring the ancilla in some basis that will cause the state of the register qubit to be decided. Both single- and two-qubit operations can be implemented via this method and this is proven to be sufficient to create a universal gate set, giving an advantage over MBQC, for which there is currently no quantification of the classes of entangled state needed to achieve universal QC. We propose that this system would map to our scheme if we consider the electron spin as the ancilla and the target nucleus as the register qubit.

Finer details of the model given in [148] show that arbitrary single-qubit operations on register qubits are not required. The only requirements for the protocol to perform universal QC are that it is possible to measure the ancilla qubit in a suitable basis and that we can construct a suitable entangling gate. This alone is sufficient to create a universal set of quantum gates assuming that they satisfy specific conditions outlined (two entangling gates are shown to fit these criteria). One universal interaction that acts to entangle an ancilla to a register qubit is the controlled-Z (CZ) operation

$$CZ = \begin{pmatrix} 1 & 0 & 0 & 0 \\ 0 & 1 & 0 & 0 \\ 0 & 0 & 1 & 0 \\ 0 & 0 & 0 & -1 \end{pmatrix} \tag{4.22}$$

accompanied by local Hadamard gates

$$H = \frac{1}{\sqrt{2}}\begin{pmatrix} 1 & 1 \\ 1 & -1 \end{pmatrix} \tag{4.23}$$

such that the full entangling operation is defined as

$$E_{AR} = H_A H_R CZ_{AR} \tag{4.24}$$

where A and R refer to the ancilla and register respectively. The second universal entangling interaction is the $CZ+SWAP$ gate,

$$CZ+SWAP = \begin{pmatrix} 1 & 0 & 0 & 0 \\ 0 & 0 & 1 & 0 \\ 0 & 1 & 0 & 0 \\ 0 & 0 & 0 & -1 \end{pmatrix} \tag{4.25}$$

and the entangling operation in this case does not require any additional local operations and is simply given by

$$E_{AR} = (CZ+SWAP)_{AR}. \tag{4.26}$$

Both of these are maximally entangling Clifford operations [159–161]. The ADQC protocol allows for direct manipulation of the register qubits in the entangling process, however, we propose that our model may allow entanglement preparation to be achieved in the absence of any direct manipulation through evolution due to the hyperfine interaction as described for the nuclear spin quantum memory protocol outlined above. We therefore need to find a point in the evolution of the electron and nucleus that matches the configuration of either the CZ or the $CZ+SWAP$ gate. To calculate this, we take a measurement of the overlap between the gate we require and the configuration of the two spin subsystem as it evolves. The overlap we calculate is defined as

$$OL = \mathrm{Tr}(CZ^{\dagger}.U_{en}(B_{ext},t)) \tag{4.27}$$

for the CZ operation and

$$OL = (CZ+SWAP)^{\dagger}.U_{en}(B_{ext},t) \tag{4.28}$$

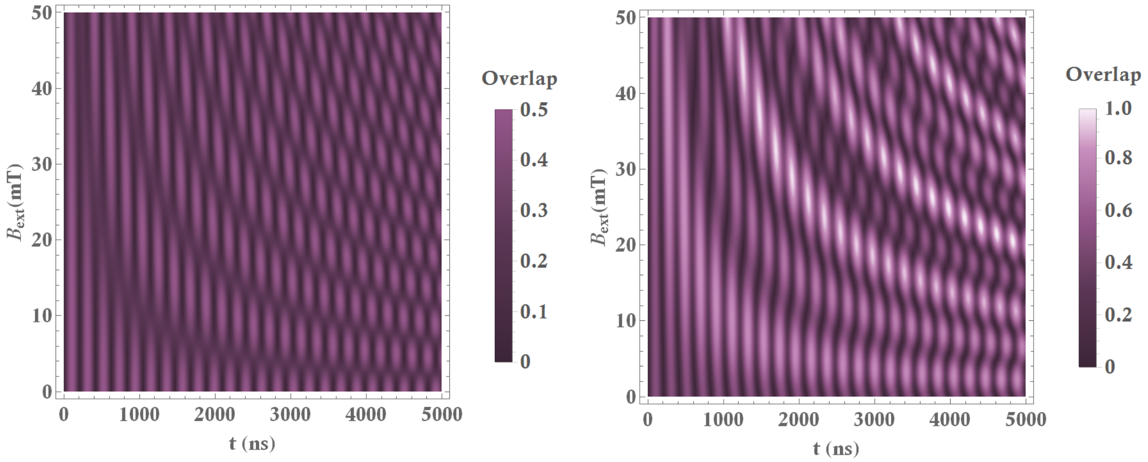

(a) CZ gate

(b) $CZ + SWAP$ gate

Figure 4.5: Here we see the overlap between the output matrix of the electron-nuclear evolution as a function of time and external field and the (a) CZ and (b) $CZ + SWAP$ gate. In (a), we find that the total overlap will never exceed 0.5 and so the configuration required for this gate to be implemented cannot be found due to simple time evolution. In (b), we see that a maximum overlap of 1 can be reached.

for the $CZ + SWAP$ operation where we vary both the size of B_{ext} and the evolution time. The results for the CZ and $CZ + SWAP$ gates are shown in Fig. 4.5.

The evolution shows a similar pattern for each of the gates, with the main differences being in the size of the overlap. We see some oscillating behaviour as the system evolves, and the system appears to become more unstable over time, with the high overlap regions becoming smaller and more frequent. We find that our system will never undergo the correct evolution to form the configuration of the CZ gate. This is due to all of the matrix components of the CZ gate being on the diagonals, and the Hamiltonian is such that the output matrix will never evolve to include non-zero entries on the second and third diagonals. This means that if we were to implement this gate we would need to consider additional quantum operations that could be applied to the electron spin to force the system to obey this configuration. However, when we consider the $CZ + SWAP$ gate, we find that there are parameters where the system will evolve to the point where there is maximum overlap with the output matrix of the evolution of the electron-nuclear subsystem, i.e. there are points where the electron-nuclear subsystem evolves to be in this particular configuration independently, allowing for simpler and therefore less lossy implementation of the protocol. In contrast to the $\sqrt{\text{SWAP}}$ gate, this particular operation would require non-zero values of the external field, and as such would require different pulse parameters in the NFF protocol that would need to be calculated similarly to the calculations given in Section 3.2.2.

Another requirement for the ADQC model is to be able to address multiple register qubits.

This would require more extensive research into the initialisation of nuclei using RF pulses such that we could have multiple register qubits. Consideration of how a single ancilla could address multiple nuclei independently is also necessary, including how the interactions between electron and nucleus can be turned on and off. Eventually, scaling up this model would probably require use of multiple QDs such that each will have an electron to be used as an ancilla. This would lead to research into how these electron spins would interact with each other and also how the individual register qubits could be made to interact with register qubits in other QDs. Then interactions between the QDs would also need to be addressed. Despite the topic requiring extensive additional research, we have shown that the ADQC model appears to be mappable to our protocol, and there is potential to successfully construct a full model for this system.

4.4 Summary

In this chapter we constructed a nuclear spin quantum memory protocol using the evolution of the electron and target nucleus due to the hyperfine interaction and showed that we can read out the state of this nucleus using an ancilla photon to perform a quantum non-demolition measurement. We calculated the total entanglement of this model in the presence of an additional nucleus that has been perturbed into the plane of the electron and nucleus and showed that it is still possible to achieve the maximally entangled state, depending on the Rabi frequency of the additional nucleus. Finally, we considered how this could be extended into a full model of QC and showed preliminary data suggesting that it may be possible to implement the ADQC protocol.

CHAPTER 5

SAMPLE CHARACTERISATION AND EXPERIMENTAL SETUP DETAILS

This chapter will discuss the experimental setups used in this thesis. We detail the process for the characterisation of QD samples and show results using these processes. This is an experimental methods chapter, with the novelty being the setup rather than the results. In the description of the experimental setups, we outline the design of an interferometer. This is a novel design that is used to measure the precession of a single electron spin in a QD. After a discussion of each of the experimental setups used in the two experimental chapters, we give the structure of the samples used and how the QDs are confined within them. We then give details of how these structures can be fabricated to maximise the efficiency of the emitted light. The optical setups used for the characterisation processes use photoluminescence spectroscopy and resonant scattering to study QD samples. We show these characterisation processes, focusing on some particular QDs with interesting properties.

5.1 Experimental setups

In this section, we describe the setups used for each of the different techniques discussed in the next two chapters.

5.1.1 Photoluminescence setup

The first setup, shown in Fig. 5.1 is the setup we use to carry out photoluminescence (PL) measurements (explained in detail in Section 5.3). We begin with a Ti:S tunable laser, resonant at 780nm. This is transferred to our optical setup via a single mode polarisation-maintaining fibre to filter out any unwanted modes and a collimating lens. There is a linear polariser that transmits vertically polarised light and helps to improve the extinction (signal to background)

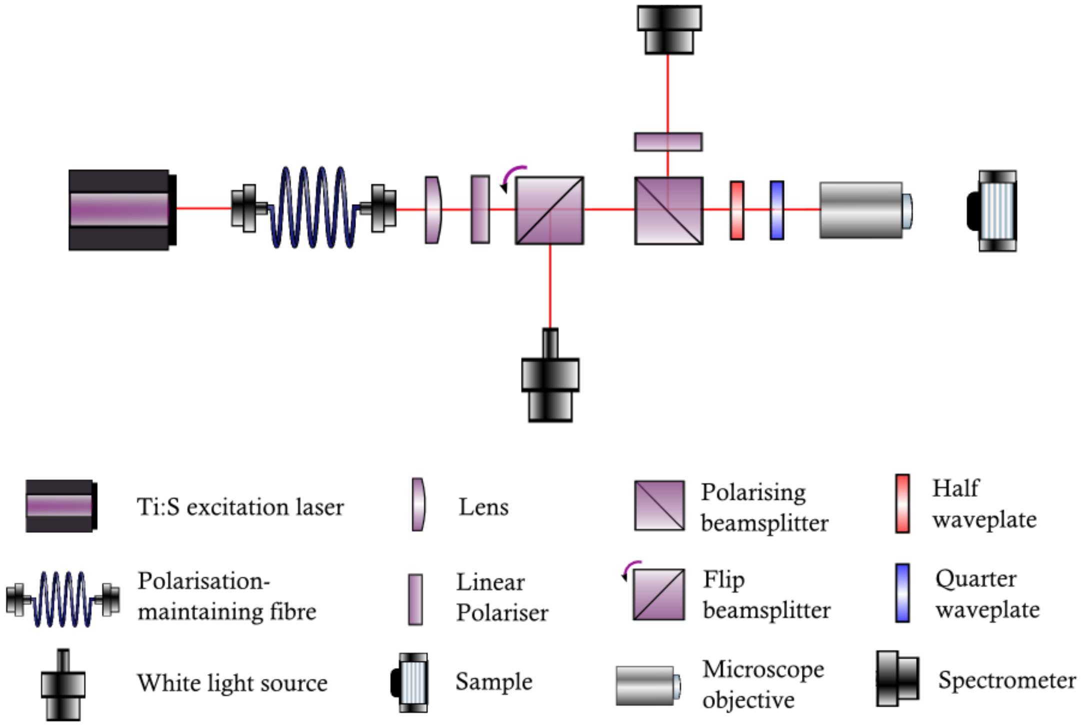

Figure 5.1: Optical setup used to perform the photoluminescence measurements discussed in this chapter. The Tsunami Spectra-Physics Ti:S excitation laser is used to send light to the sample. It is first sent through a polarisation-maintaining fibre, lens and linear polariser (colorPol VISIR10mm×10mm). The light then travels through the microscope objective and is focused onto the sample, which is contained in a Janis ST-500 flow cryostat. After interacting with the sample, the light will be reflected and sent to the TriVista Princeton Instruments spectrometer via a polarising beamsplitter and linear polariser.

ratio of the setup. The sample is mounted in a Janis ST-500 flow cryostat cooled to ≈ 12K and accessed through a window using a microscope objective. We use an 11mm focal length objective to focus the light onto the sample, chosen to optimise the amount of emission collected from the micropillar. The emitted light is directed through the spectrometer grating via a polarising beamsplitter and linear polariser, which allow us to be able to perform polarisation selective PL, although in this case, the laser light is filtered spectrally. The emitted light will have experienced some polarisation rotation due to its interaction with the QD, and we can perform polarisation filtering to detect only the light that has interacted with the QD. Careful alignment of the fast and slow axes of the half waveplate (HWP), quarter waveplate (QWP) and other optics also helps with increasing the extinction ratio. We have a white light source that can be sent into the setup via a flip beamsplitter, so that the sample can be viewed on a camera to aid alignment.

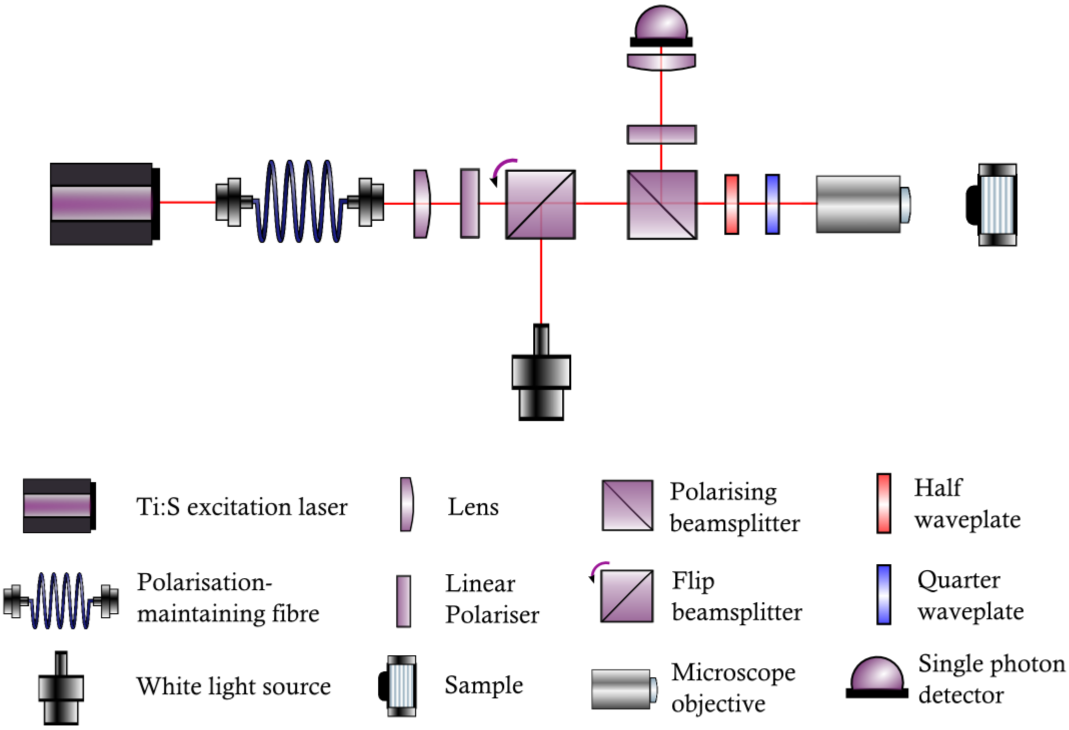

Figure 5.2: Optical setup used to perform the resonant scattering measurements discussed in this chapter. The Tsunami Spectra-Physics Ti:S excitation laser is used to send light to the sample. It is first sent through a polarisation-maintaining fibre, lens and linear polariser (colorPol VISIR10mm×10mm). The polarisation of this light can be controlled using the half and quarter waveplate. The light then travels through the microscope objective and is focused onto the sample, which is contained in a Janis ST-500 flow cryostat. After interacting with the sample, the light will be reflected and sent to the avalanche photodiode via a polarising beamsplitter and linear polariser.

5.1.2 Resonant scattering measurement setup

When measuring the resonant scattering profile and lifetime of the QDs, we modify the setup such that instead of the emitted light being directed into the spectrometer, it is instead sent to an avalanche photodiode (APD), as shown in Fig. 5.2. For both of these techniques, we require resonant excitation of the QD resonance and so we must carefully tune the laser resonance such that it is at the same wavelength as the QD emission. The tuning process can be difficult due to the spectral jitter of the QD resonance; this is an effect where the QD resonance is not stable, but instead fluctuates over a range of wavelengths. This is thought to be due to trapped charges in the QD environment. However, in general, the accuracy we are able to achieve is sufficient to provide a reasonable estimate for the techniques we use [162]. Resonant scattering involves exciting the QD with a resonant laser, driving it into a higher energy state. This higher energy

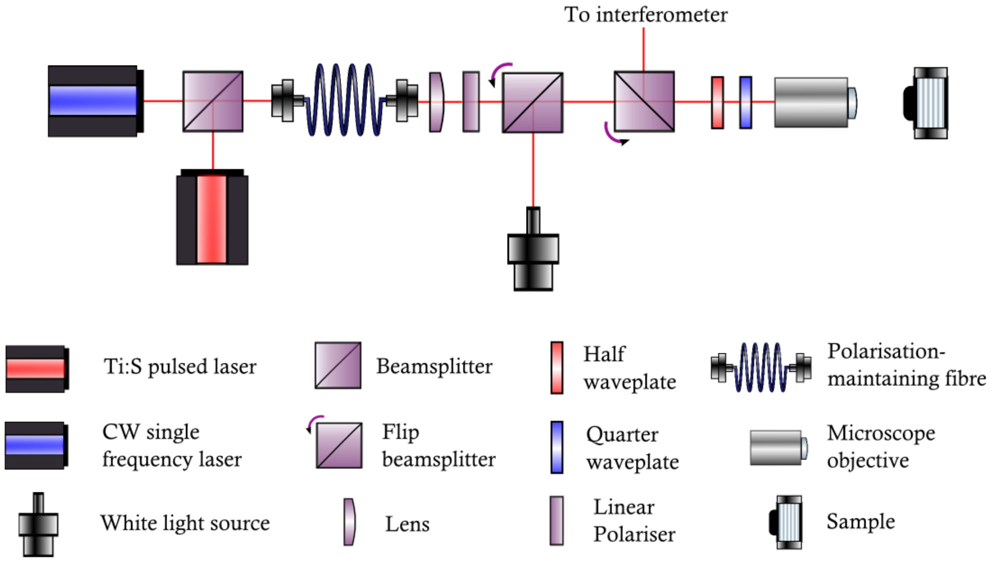

Figure 5.3: Optical setup used for the NFF results obtained in this chapter. The input is a Ti:S pulsed laser or a CW MSquared SolsTiS single frequency laser (these will not be used simultaneously). The laser is directed through a polarisation-maintaining fibre, collimating lens, linear polariser, HWP, QWP and microscope objective to the sample. The light reflected from the sample is directed to the interferometer setup via a beamsplitter. The sample is cooled in a vacuum chamber inside an Attocube dewar.

state then decays, emitting a photon, which we detect. In practice for this system, the QD may not be transferred to the excited state, but virtual excitation causes some interaction between the ground state of the QD and the photons and this is why we use the term resonant scattering [163].

5.1.3 Study of nuclear effects setup

For the setup we use to study the effects of nuclear spins in QDs, we require an altered version of the setup given in Fig. 5.2. We have an additional laser input such that we can address the sample with either pulsed or continuous wave (CW) light. This setup uses an Attocube dewar with a microscope objective that is inside a vacuum tube in the dewar along with the sample. This requires a different microscope objective to that used in the previous measurements, in this case we choose an objective with a focal length of 2.75mm and a numerical aperture (NA) of 0.64. The lens tube has been redesigned to be made from an alloy of Titanium, Aluminium and Vanadium (Ti90/Al6/V4). This is because we found that the original lens tube was slightly ferromagnetic at low temperatures and so we were experiencing some drift in the position of the lens tube. There are two lasers used in this setup - the Ti:S pulsed laser, which is used to drive the electron spin into the state we require and the CW single frequency laser, which is used as a probe laser to measure the state of the system through the interferometer. These are

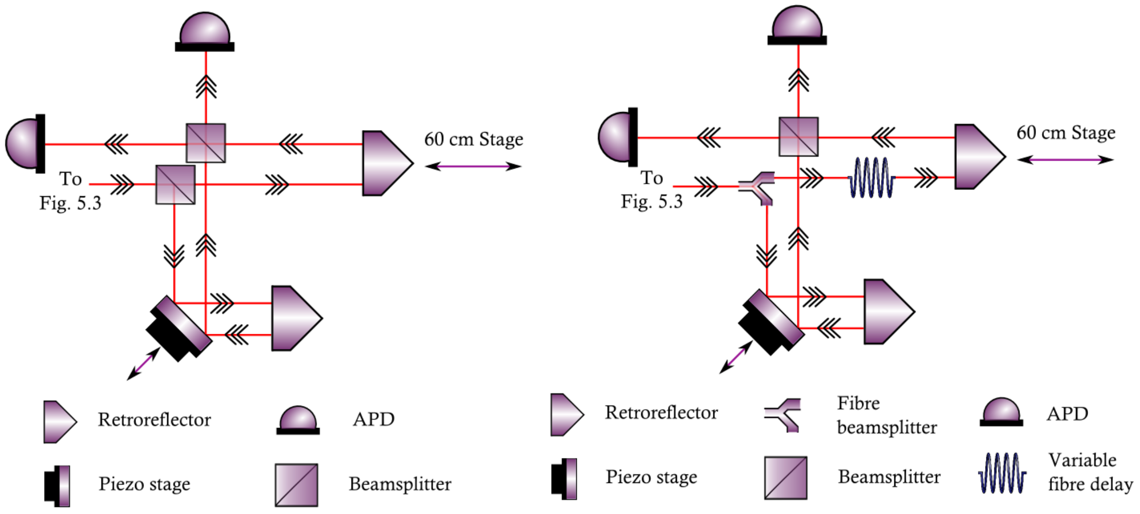

(a) Interferometer with beamsplitter (b) Interferometer with fibre beamsplitter and fibre delay

Figure 5.4: Novel optical setup used to detect the electron spin precession. Both setups show a Mach-Zender interferometer with a piezo actuator (Noliac, NAC2125-A01, piezo multilayer ring actuator, maximum displacement 3.3μm, $dl/dV \approx 17$ nm/V) and translation stage (Owis, LIMES 170 − 600-HSM, 600mm travel, resolution 0.8μm) used to vary the time delay between the interfering photons. The section labeled 'stage' refers to the translation stage and the retroreflector (Edmund optics, 63.5 mm Clear Aperture, 1 Arcsec, Gold Retroreflector) sits on this. The black arrows show the direction of the light beam (this is the light emitted from the CW probe laser).

introduced into the setup via a single mode polarisation-maintaining fibre (SMF, 780HP) with a collimating lens. The light then passes through a linear polariser, which filters out light which is not vertically polarised. The HWP and QWP can be used to rotate the polarisation of the light to any polarisation state ($|H\rangle$, $|V\rangle$, $|D\rangle$, $|A\rangle$, $|L\rangle$ or $|R\rangle$). The Ti:S will be circularly polarised and the CW probe laser will be linearly polarised. The microscope objective focuses the beam onto the sample. The sample itself is contained within a vacuum chamber inside a liquid helium dewar cooled to ≈ 4K. We are able to apply a magnetic field in the Voigt geometry onto the QDs in the sample using a superconducting coil. The beam interacts with the QD and is reflected back along the same path. The light will then be sent to the interferometer setup via a beamsplitter. The white light source is used for alignment such that the sample can be illuminated on a camera.

In this case, the light that is reflected from the sample is directed to one of the two interferometer setups shown in Fig. 5.4. This is used to measure the interference fringes of the emitted photons over a range of time delays. This interferometer design is unique to this experiment and allows us to achieve the results given in chapter 6. Fig. 5.4(a) uses a standard 50 : 50 beamsplitter to split the incoming beam between the two arms of the interferometer. The difference in Fig. 5.4(b) is that we instead use a fibre beamsplitter to split the incoming beam. Then one output of the beamsplitter is directed into a variable fibre delay (we use 1m, 2m and 5m fibres, and any combination of these, corresponding to 4.6ns, 9.7ns, 14.8ns and 25ns time delay respectively) for one arm and the other output is unchanged from the path it takes in Fig. 5.4(a). This second version of the interferometer is used when we require the length of the delay between the two arms to be extended to show longer time delays.

5.2 Sample details

The two samples used in this thesis contain InGaAs QDs in a GaAs substrate and were fabricated through MBE growth as described in Chapter 1. Evenly spaced over the sample are micropillars [164]. To create these micropillars, alternating layers of AlAs and GaAs are grown which each have a thickness of $\lambda/4$ [165]. The pillars are then etched into this planar structure using electron beam lithography. These alternating layers form a distributed Bragg reflector (DBR). Within these alternating layers, there will be a single layer of thickness λ, and this layer forms a cavity between the two sets of DBRs. It is in this layer that the QDs are contained. Fig. 5.5(a) gives an example of how the structure of a micropillar will look, with the vertical dots showing that the number of mirror pairs can be chosen to fit the particular application. The bottom DBR stack will always contain an odd number of layers, to ensure that the layers adjacent to both the substrate and the cavity are AlAs.

If we want to control the direction of the light emission from the cavity, we can vary the amount of DBR pairs above and below the cavity. The asymmetry in the number of pairs of layers in the DBRs of the micropillar is significant as this enforces the single-sided nature of the cavity, i.e. the direction of light emission will preferentially be reflected out of the top of the micropillar due to the lower reflectivity of the smaller DBR stack [166]. It is within the cavity layer itself that the QD layer is grown - these are modulation doped low density ($1.8 \times 10^9 \text{cm}^{-2}$) QDs (samples grown at the University of Würzburg). Below this QD layer is a layer of Si, used as an electron donor, giving an average of one excess electron per QD. An image of a micropillar sample (note that this is not an image of the sample studied in this thesis) is shown in Fig. 5.5(b). This shows the section where we find the cavity containing the QDs, and a zoomed in image of a QD that is found in that particular cavity. This particular micropillar has a diameter of 1.5μm and has the same number of DBRs above and below the cavity mode. The fabrication process for these micropillars consists of depositing the layers of AlAs and GaAs across the sample using electron beam lithography and etching the micropillars afterwards using focused ion beam etching.

The height of the micropillar will be dependent on the number of pairs of AlAs and GaAs layers that have been fabricated and will be on the order of a few microns. Each sample contains various diameters of micropillar, ranging from 1μm to 5μm in steps of 0.5μm. The structure of the particular sample we use can be seen in Fig. 5.6. We can see that the layout of this sample is such that the micropillars are evenly distributed across the sample. However, the QDs are self-assembled (as outlined in Chapter 1) and are therefore randomly distributed across the

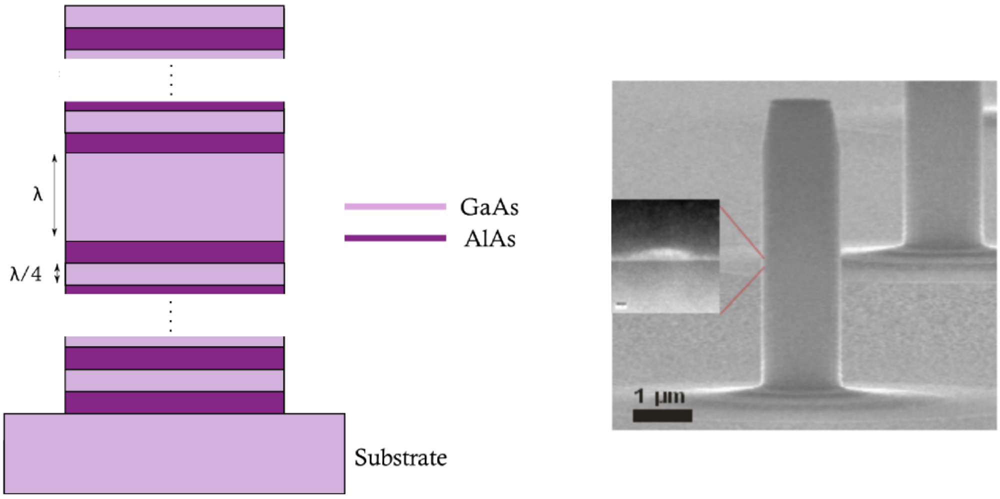

(a) (b)

Figure 5.5: (a) Image showing the structure of a micropillar. There are two sets of DBR stacks of alternating layers of AlAs and GaAs $\lambda/4$ separated by a larger section of GaAs of thickness λ that forms a cavity. The GaAs substrate extends across the sample. The vertical dots represent extra DBR layers. The bottom stack has an odd number of layers, and the layer adjacent to the substrate is an AlAs layer. (b) Image of a micropillar sample. The zoomed in section is showing a QD contained within the cavity. Image courtesy of University of Würzburg.

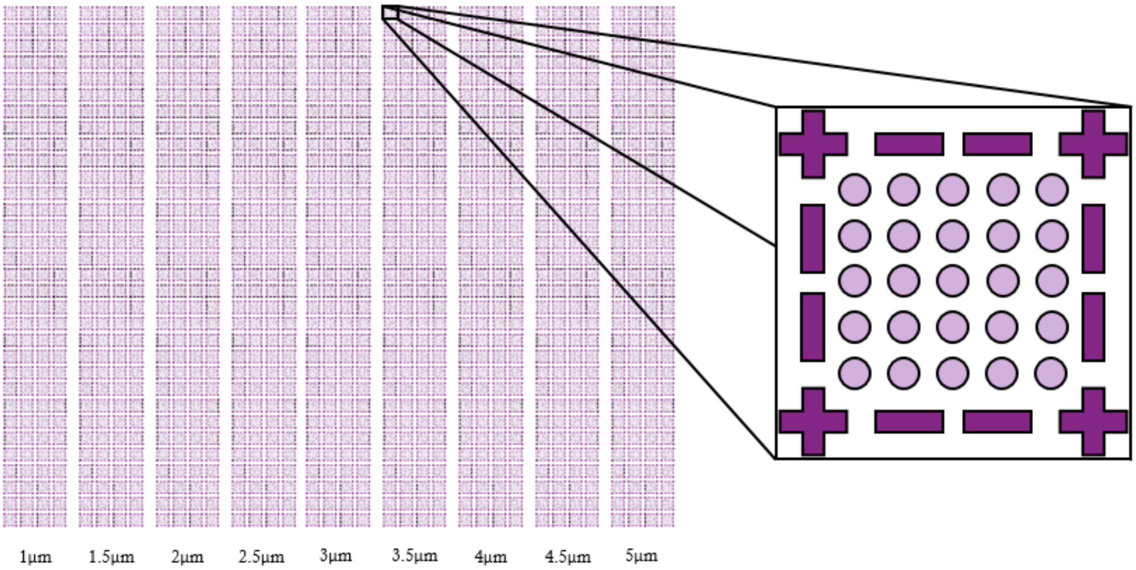

Figure 5.6: Sample map showing the layout of the micropillars. In the zoomed in section, each circle represents a single micropillar. The crosses and dashes are used as markers to allow us to reference particular micropillars. There are 9 columns of micropillars, each of a different diameter and each column contains 128 sections identical to that shown in the zoomed in section, giving a total of 28800 micropillars contained in the sample.

sample. The result of this is that the micropillars do not target specific QDs, i.e. the position of the micropillar is independent of the position of the QDs. This means that we cannot assume that there will be an isolated QD in the centre of any particular micropillar at the same wavelength as the cavity mode. This can result in a large part of the QD emission not being directed into the cavity mode. This is due to difficulties in the fabrication process. It is possible to do some site-controlling of QDs, however, this is an area of research in itself [167–169]. Here, we choose to use a sample that is more easily fabricated, but has the disadvantage that we may have to search many micropillars to find a QD that is correctly positioned and with the correct wavelength, such that there is a large amount of emission from the QD into the cavity mode. However, this introduces difficulties in terms of scaling up our systems to use multiple QDs, as the size of the sample is extremely large compared to the number of usable micropillars. This particular sample contains 9 columns of micropillars, each with a different diameter. Each of these columns contains a total of 3200 micropillars, arranged in the boxes shown in Fig. 5.6. We expect that in such a big sample size we will be able to find several QDs with the correct properties to achieve a relatively high percentage of emission into the desired mode.

5.2.1 Quality factor and β factor

An important aspect of the QD micropillar is its quality factor (Q factor). This is a dimensionless parameter that is used to characterise a resonator's bandwidth with respect to its central frequency and is defined as [164]

$$Q = \frac{f_c}{\Delta f} \tag{5.1}$$

where f_c is the central frequency of the resonator and Δf is its bandwidth. We can think of this as the rate at which the energy dissipates from the cavity, with a quicker dissipation representing a low Q factor and a slower dissipation representing a high Q factor. In terms of a micropillar, the Q factor is controlled by altering the number of pairs of mirrors in each DBR stack to optimise the reflectivity of the DBR stacks [170]. By designing a micropillar with a smaller number of DBR pairs above the cavity than below it, one can ensure that the majority of the light emitted will be through the top of the micropillar, as this DBR will have a lower reflectivity. It is usually assumed that a high Q factor will correspond to a highly efficient cavity, however in a micropillar this is not the case, as a higher Q factor will also contribute to a higher percentage of light dissipated through the side walls of the micropillar [171]. This is due to the photons from the laser being confined within the cavity mode for a longer period of time, and thus the probability of any particular photon being lost through the side walls of the micropillar is increased. Then, a more meaningful parameter that we can consider is the β factor. This is the ratio of the rate of decay into the mode we require and the sum of all possible modes, given by

$$\beta = \frac{\Gamma}{\Gamma + \gamma}, \tag{5.2}$$

where Γ is the cavity mode rate and γ is the total emission into any other mode, such that $\Gamma + \gamma$ is the total emission into any possible mode and the β factor is a quantity between 0 and 1. Then a high β factor corresponds to the majority of the emitted light being found in the desired mode. For the QDs we consider, the micropillars are designed such that there are fewer DBR layers on the top than on the bottom, meaning that the light will predominantly be emitted through the top of the micropillar.

The micropillars characterised in this thesis come from two different samples. One will be in the medium Q factor regime, with the Q factors of the cavity modes being in the region of 1000-10000 and the other in the low Q factor regime, in the region of a few hundred. The data taken from the medium Q factor sample is primarily characterisation data and is contained in this chapter. The experimental data taken in Chapter 6 will use the low Q factor sample as it is easier to find QDs that are bright and centred in a micropillar for low Q factor samples. The full characterisation is not shown below for the low Q factor micropillars as this was completed before the work shown this thesis, however, we will show some previous characterisation results for the particular QDs used to obtain the data found in Chapter 6.

5.2.2 Phase shift of a photon due to a quantum dot

Another attribute of the QDs that we exploit in this chapter is their ability to induce phase shifts in the photons that interact with them. This is due to the spin selection rules discussed in Section 1.4.2, where we state that when a circularly polarised photon interacts with an electron in a QD, it will interact with only one of the spin states of the electron, dependent on the direction of circular polarisation. From this, we can calculate the phase shift a photon will pick up on interaction with the electron in the QD. The light reflected from the cavity will experience some phase shift that is a function of frequency detuning. If we assume this detuning is 0, the phase shift can reach a maximum of $\pm\pi$. If a horizontally polarised photon enters the cavity in which the electron spin is confined, we need to consider the interaction in terms of its circular components ($|H\rangle = \frac{1}{\sqrt{2}}(|R\rangle + |L\rangle)$). Then, depending on the state of the electron spin, one of the components will interact with the electron spin state and the other will not. We can say that if the component interacts with the electron spin it will induce a phase shift of ϕ_1 on the photon and if it does not interact, the phase shift will be defined as ϕ_0 [152]. The light reflected from the cavity, $|\psi_{ref}\rangle$, can then be defined by

$$|\psi_{ref}\rangle \quad = \quad e^{i\phi_0}|R\rangle + e^{i\phi_1}|L\rangle . \tag{5.3}$$

Then, for a perfect system, where $\phi_0 = 0$ and $\phi_1 = \pm\pi$, we get the output state

$$|\psi_{ref}\rangle \quad = \quad |R\rangle - |L\rangle , \tag{5.4}$$

(ignoring normalisation) which is equivalent to a photon in the $|V\rangle$ state. This allows us to switch the polarisation of photons in a cavity [31]. This technique also has many uses in photon-cavity interactions, as it allows us to measure phase shifts between photons interacting with QDs in the cavity, as will be demonstrated in Chapter 6.

5.3 Photoluminescence spectroscopy

In order to perform characterisation of the QD samples, it is necessary to use photoluminescence spectroscopy (PL) of single QDs within micropillars. This involves pumping the QD sample (cooled to $\approx$ 12K) with a titanium sapphire (Ti:S) laser resonant at a wavelength above the bandgap of the GaAs wetting layer. For the results shown in this chapter, we set the wavelength of this laser to be 780nm. The light from this laser will be absorbed into the GaAs and forms electron-hole pairs (excitons). These excitons will relax into the QDs and subsequently recombine. This recombination will result in the emission of a photon. If the QD has an emission energy that is close to the energy of the cavity mode, the emitted photons can be coupled into this mode, such that detection is possible using a high resolution triple spectrometer cooled to $\approx$ 153K (-120°C).

We find that pumping the sample with a laser power on the order of μW allows us to detect the cavity mode of the micropillar. At these powers, the QDs cannot usually be seen individually and instead contribute to the signal we see from the cavity mode, which will be the dominant feature. As we lower the laser power, we begin to see the features of individual QDs appearing, whereas the cavity mode itself is suppressed. This characterisation will focus on micropillars with a diameter of 2μm, as these have, in general, given the best emission into the cavity mode. We do not consider smaller diameters than 2μm as coupling into these micropillars becomes increasingly difficult due to mechanical instabilities. An additional problem is that for a micropillar with a small diameter, the chance of the photon being lost through the side wall of the cavity becomes increasingly likely. This contributes to a loss in efficiency and a loss in β factor. The QDs that are most useful for quantum information processing applications will have a narrow linewidth and be isolated in wavelength from nearby QDs, in order to make them easy to optically address without introducing emission from other QDs. We also require the QD to be situated close to the centre of the micropillar to increase both the brightness and signal to background ratio of the emission. We have identified some QDs that will potentially be suitable candidates for quantum information processing applications below and will show the spectra of the QDs chosen from each sample in this section. The experimental setup we use for these measurements is shown in Fig. 5.1.

5.3.1 Medium Q factor sample PL

For the medium Q factor sample, we show results from two micropillars that contain QDs that exhibit interesting properties. The spectrum in Fig. 5.7 is taken from a 2μm micropillar with a continuous wave (CW) excitation power of 8μW. This power is high enough that we see the cavity mode but not the spectra of the individual QDs. This PL spectrum is measured through the triple

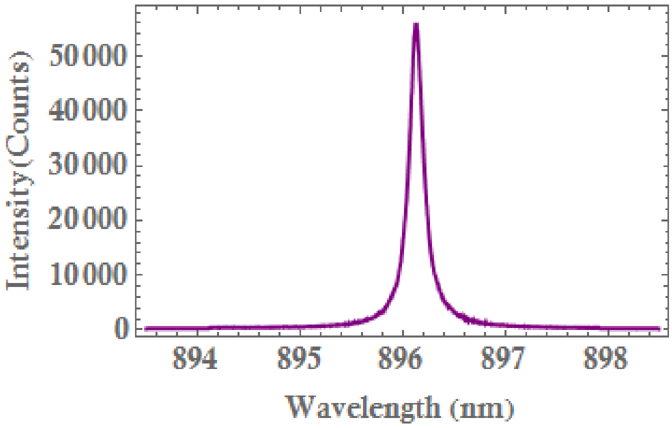

Figure 5.7: An example of the PL spectrum of a micropillar cavity mode in a 2μm micropillar at 11K, excited by an 8μW continuous wave laser with a spectrometer integration time of 0.25s.

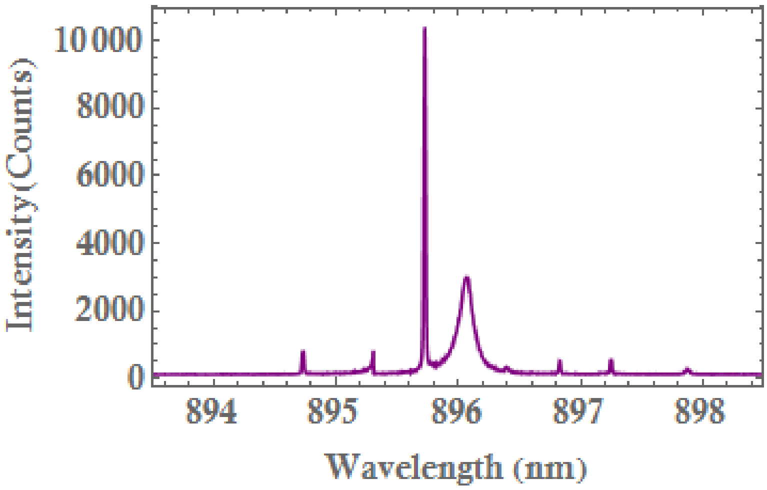

Figure 5.8: An example of the PL spectrum of the previous micropillar excited by a 100nW CW laser with a spectrometer integration time of 1s.

spectrometer with an integration time of 0.25s at 11K. The resonance of this particular QD is $\approx$ 896.2nm, which is typical of InGaAs QDs fabricated in this way.

When we reduce the laser power, we start to see the individual QD features inside the micropillar. Fig. 5.8 shows the same micropillar as Fig. 5.7, this time subject to a CW laser with 100nW power and 1s integration. Here we can clearly see the separation of the QDs and the cavity mode. The cavity mode is the broader feature appearing at around 896nm. The measured Q factor for this cavity mode is $\approx 5641 \pm 5$, using a Lorentz fit as shown in Fig. 5.9. The large spike in intensity shown at $\approx$ 895.8nm is a single QD. This is close to the cavity mode, contributing to it being brighter in comparison to the smaller QD spikes shown in the spectrum. To successfully couple the light emitted from the QD into the cavity mode with high efficiency, the QD ideally

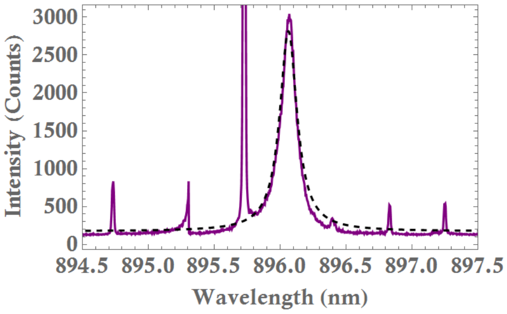

Figure 5.9: Theoretical fit using a Lorentz equation of the cavity mode found in a 2μm micropillar at 11K, excited by an 8μW continuous wave laser with a spectrometer integration time of 0.25s. The measured Q factor is = 5641 ± 5.

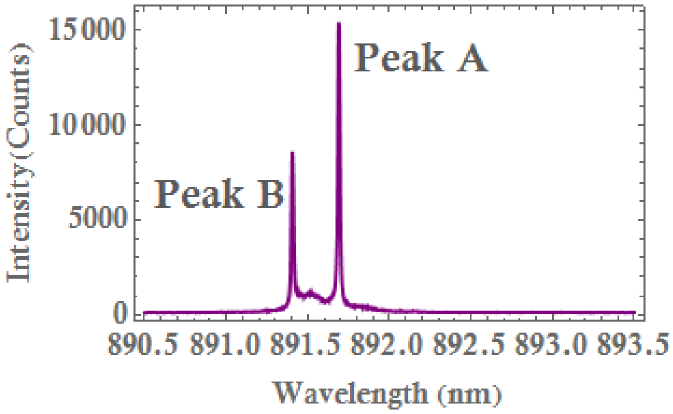

Figure 5.10: Spectrum taken from a micropillar with two emission peaks that each have a very different power dependence. The laser power in this case is 2μW and this is chosen arbitrarily as this spectrum shows both peaks clearly.

needs to be overlapping with this mode. We will look into ways to achieve this later in the chapter.

We also show spectra from one other 2μm micropillar in the medium Q factor sample. The emission peaks found in this micropillar are shown in Fig. 5.10. This spectrum is taken at 2μW with the CW Ti:S laser and we see individual QD features at this power. This time we see 2 peaks that are either side of the cavity mode of the QD. The spectrum shown is arbitrarily chosen to use a laser power of 2μW because at this power both emission peaks are clearly visible at this power. Later in the chapter, we will show characterisation results using QDs in this micropillar.

5.3.2 Low Q factor sample PL

The sample we use for the measurement results below is a sample of low Q factor micropillars (Q factor ≈ 300) with 5 top mirror pairs and 18.5 bottom mirror pairs. The layout of the sample is the same as that shown in Fig. 5.6 and we again choose to use 2μm micropillars. These results are focused on five QDs, one of which is neutral and four of which are negatively charged (note

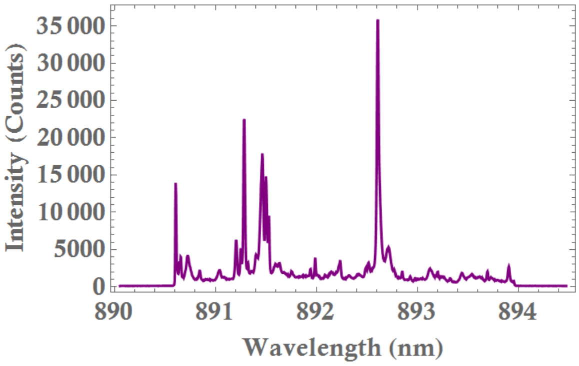

Figure 5.11: PL spectrum taken from a 2μW micropillar with the CW Ti:S laser at a power of ≈ 2μW. The identified QD is shown by the large spike in intensity at ≈ 892.6nm.

that the charge of the QDs is not identifiable from the PL measurements and will be justified later). First, we show the PL spectrum of the QD that we believe to be neutral in Fig. 5.11. The QD identified in this spectrum is the spike with the highest counts, at ≈ 892.6nm.

The QDs we measure that exhibit properties of a negatively charged QD are shown using PL in Fig. 5.12. In Fig. 5.12, we use a variety of different laser powers to excite the QDs. We will show later in the chapter that different QDs have different power dependences and so for each we use a power that clearly shows the particular QD we are interested in (in each case the highest peak in the spectrum is the QD we are considering). We find that there are some differences in the spectra, for example, some micropillars have QDs that are more isolated than others, some have a higher density of QDs and the QDs themselves have a variety of intensities and linewidths. To determine whether these QDs have the charge that we claim in this section, we use resonant scattering techniques.

5.4 Resonant scattering

Resonant scattering is the process of scattering light from the QD at its resonant frequency - i.e. the wavelength of the input photons is equal to the wavelength of the QD. The QD will then emit a photon at the frequency of the photon that was absorbed. Then, despite its frequency being the same as the input excitation light, this photon can be distinguished by polarisation filtering, as the scattered light will have experienced a phase shift due to the selection rules described in Section 1.4.2. Using the setup shown in Fig. 5.2 with the resonant laser power set to be ≈ 0.5nW at a temperature of ≈ 4.3K we can measure the spectrum of the QD (we do not yet introduce external fields). We show the initial measurement of the resonant scattering spectrum of the neutral QD in Fig. 5.13. This is a higher resolution resonant measurement of the peak that we identified in Fig. 5.11 and we no longer see the QD as a single spike. The curve is broadened and the resonance appears unstable, as we expect to be able to see some kind of single or double

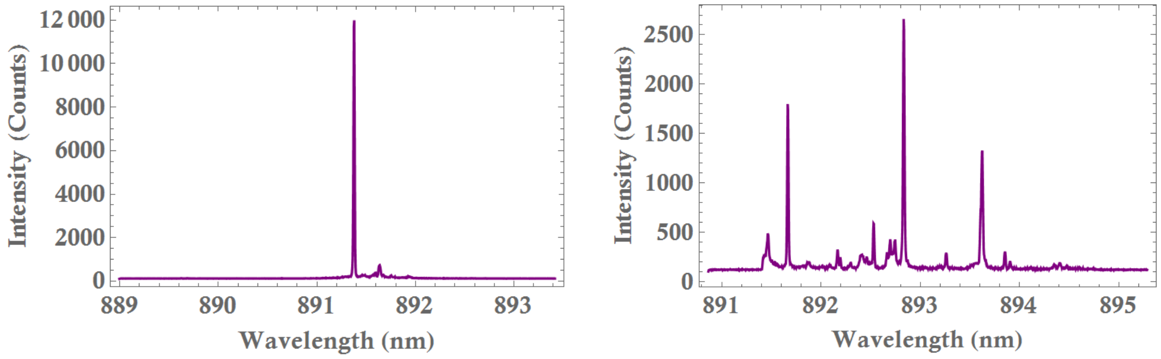

(a) Charged QD 1 excited with a laser power of 750nW.

(b) Charged QD 2 excited with a laser power of 1μW

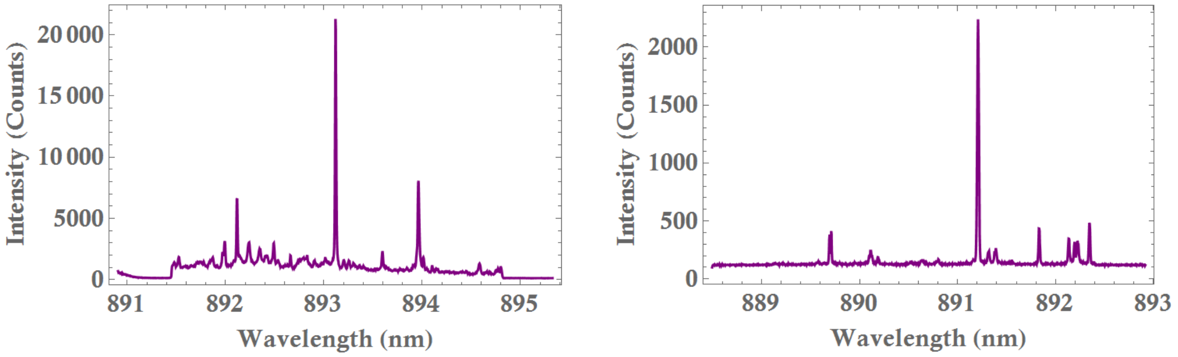

(c) Charged QD 3 excited with a laser power of 1.7μW

(d) Charged QD 4 excited with a laser power of 500nW.

Figure 5.12: PL spectrum of the four charged QDs at ≈ 4.3K.

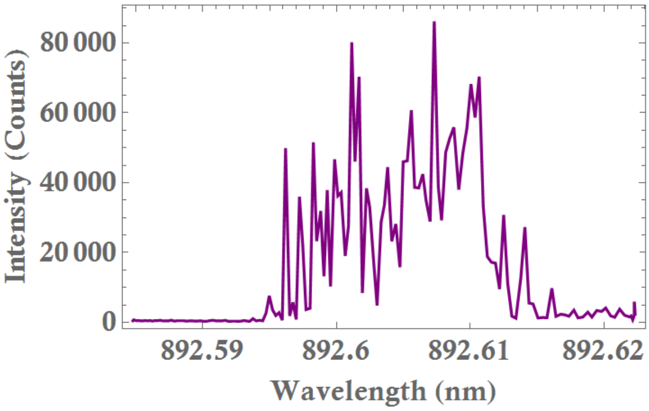

Figure 5.13: Resonant scattering spectrum of a QD in the sample with a resonant excitation laser at ≈ 0.5nW power at ≈ 4.3K.

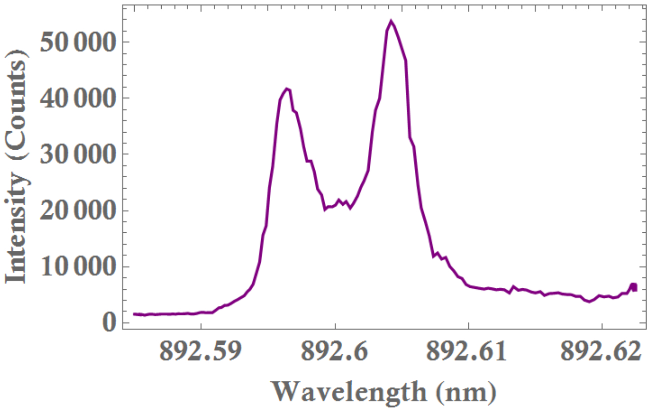

Figure 5.14: Resonant scattering spectrum of the same QD as that shown in Fig. 5.13 but using an additional laser at higher energy to suppress charge noise.

peak in counts as the laser scans over the resonance. This is a result of charge noise in the QD. To compensate for this, we introduce another laser into the setup at 820nm at very low power (≈ 2nW). This laser appears to control the effect of this charge noise, and repeating the measurement with the only change being the addition of this laser, we find the spectrum shown in Fig. 5.14. We can now clearly see that there are two peaks in the spectrum of the QD, which were not visible without the addition of the "calming" laser. These two peaks show the characteristic fine structure splitting we expect from a neutral QD due to the symmetric electron-hole exchange interaction [172]. This spectrum alone is not sufficient to conclude that this is a neutral QD, as there could be other things that would give this spectrum, for example, two charged QDs situated very close to each other, but it is a strong indication. We will later confirm that the QD is neutral using data obtained from measurements through the interferometer. For the following measurements, for each of the QDs shown, we include only the measurements with the "calming" laser turned on.

In Fig. 5.15, we show the resonant scattering spectra for each of the charged QDs shown in the PL measurements in Fig. 5.12. Importantly, in these results, we see the characteristic single peak of a charged QD in the spectra. Again, we see variations in the intensity and linewidth and in this case, we also see the lineshape varying between QDs. We should note that the laser is realigned for each QD as it must excite the QD on resonance and so some of the variation in intensity between the QDs could be due to alignment.

Charged QD 3 looks as though it might have a small second peak, but has a very high number of counts. This second peak could be due to poor alignment leading to a lower extinction ratio, or to other effects such as charge noise or spectral jitter and does not look separated from the other peak enough to be showing the fine structure splitting that we expect from a neutral QD. However, it is also possible that the small second peak is actually a second QD that has an overlapping spectrum with the first. To determine whether or not this is the case, we can perform a second

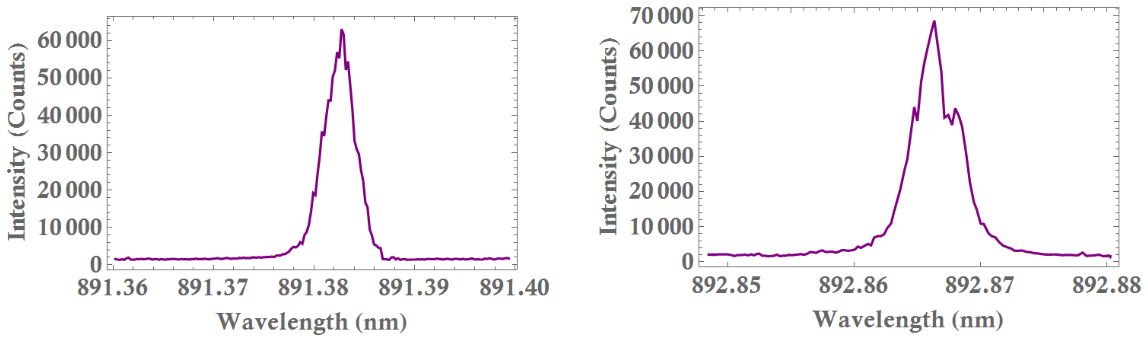

(a) Charged QD 1

(b) Charged QD 2

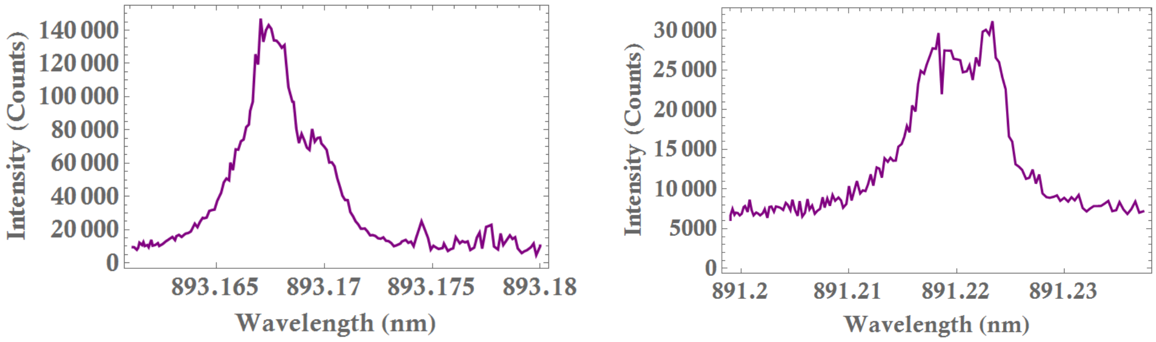

(c) Charged QD 3

(d) Charged QD 4

Figure 5.15: Resonant scattering spectrum of the four charged QDs with a resonant excitation laser at ≈ 0.5nW (for QD 4 the laser power was ≈ 0.8nW) at ≈ 4.3K.

order temporal correlation ($g^{(2)}(\tau)$) measurement. Physically, this describes the probability of a photon being detected at a time $t+\tau$ given that a photon has already been detected at time t and determines whether the emitted photons are bunched or anti-bunched. Using a CW excitation laser, we expect to see a dip in the value of $g^{(2)}(\tau)$ at $\tau = 0$, signifying the fact that a single QD is able to emit only a single photon at any one time ($g^{(2)}(0)$ tells us how often we can detect two photons simultaneously). If $g^{(2)}(0) < 0.5$, the emitted photons are antibunched, i.e. there is only one photon emitted at one time [173]. If multiple QDs were being excited, we would expect to see bunching in the photon emission and this dip would either be significantly reduced or lost altogether. In Fig. 5.16 we see that this is not the case, and there is a large dip, meaning that the emission peak we are considering is very likely to be a single QD. It is noteworthy here, that this a very respectable $g^{(2)}(\tau)$ for a QD system. However, in terms of applications in QC, this dip is not close to 0 and this suggests that the anti-bunching of the emitted photons is a long way from the requirements needed, for example, for a source of single photons [174].

Each of the QDs measured in this section will be analysed in relation to implementation of the NFF protocol. We will compare how each responds to different pulse trains and external fields. This will allow us to see how much variation there is between the behaviours of different

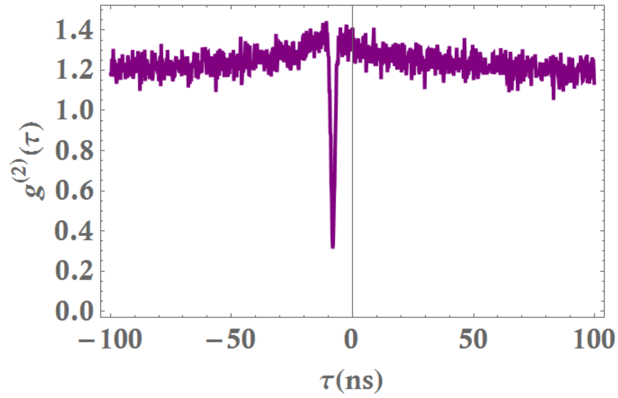

Figure 5.16: $g^{(2)}(\tau)$ correlation function for charged QD 3, showing a dip in the number of coincidences close to $g^{(2)}(0)$.

QDs under the same conditions. The next section will return to the QDs identified in the medium Q factor sample, and we will show some characterisation measurements we have performed on these QDs.

5.5 Additional characterisation measurements

All of the following measurements are characterisation measurements and will be taken using the QDs identified in the medium Q factor sample in Section 5.3.1.

5.5.1 Micropillar 1

This section gives some useful properties of the QD found in micropillar 1 in the medium Q factor sample using PL spectroscopy. First, we will show how the temperature of the system can affect the wavelength of the QD resonance. A potential alternative to searching multiple micropillars for a QD which is overlapping with this mode is temperature tuning. The cavity mode is made from GaAs, whereas the QD is made from InGaAs, and these two materials have different temperature dependences due to their differing bandgaps. This means that if we vary the temperature, it is possible to tune the resonance of the QD such that it moves to be overlapping with the cavity mode. This effect is small, but can be effective when the QD is close to the wavelength of the cavity mode.

Fig. 5.17 shows how the spectrum of the QD changes with temperature. We can clearly see that as the temperature is increased, both the cavity mode and the QD that we see in the spectrum shift to higher wavelengths. However, the shift of the QD is larger than the shift of the cavity mode. This means that when the temperature reaches 26.5K, the QD and the cavity mode are overlapping and the emission from the QD into this mode is maximised. Beyond this point, the intensity decreases and as the temperature is increased further we will see the QD

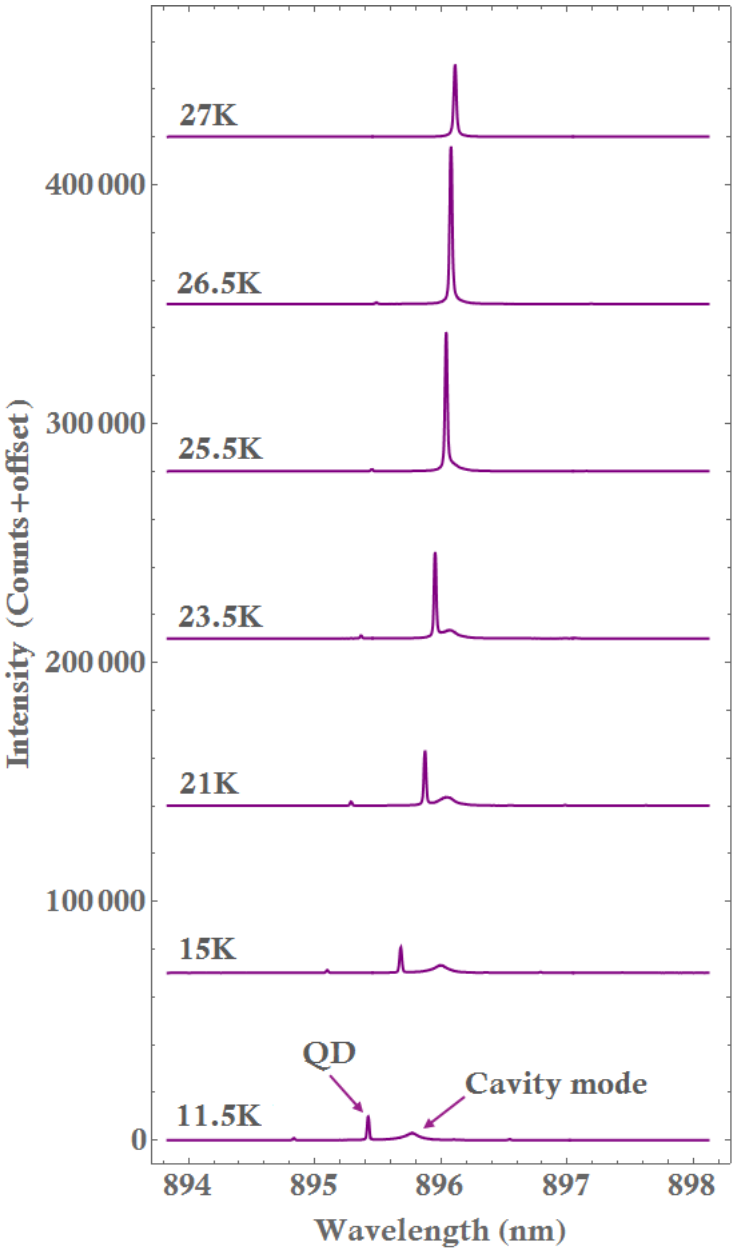

Figure 5.17: Spectrum of a 2μm micropillar excited by a 100nW CW Ti:S laser at various temperatures. The QD and cavity mode are labelled in the 11.5K spectrum and can be seen to shift in wavelength as the temperature increases.

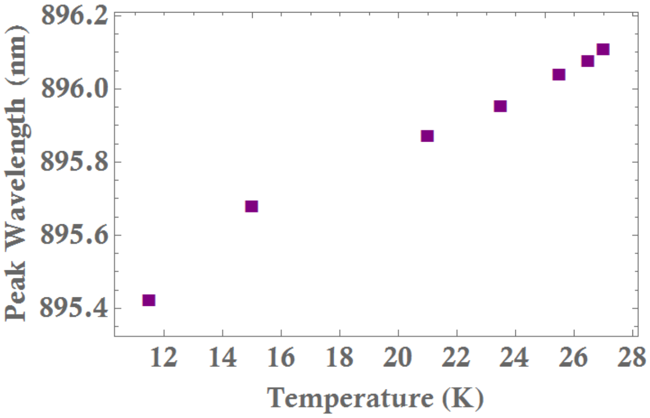

Figure 5.18: Dependence of the peak wavelength of the QD emission on the temperature.

emerging on the higher wavelength side of the cavity mode. Note that the increments in the temperature increase are not equal, due to the difficulty in stabilising the temperature of the setup. This method can be used to tune the emission of the QD into the cavity mode, such that we see a higher efficiency from the system. We should note that as the temperature of the system increases, we start to see additional dephasing effects, including phonon dephasing and so at higher temperatures, the intensity will drop considerably due to thermal activation of carriers in the material. It is therefore necessary to take care when using this technique not to increase the temperature beyond the limit where the phonon dephasing becomes significant [175–177].

We can also analyse the dependence of the position of the peak wavelength and the linewidth of the QD on the temperature. These are shown in Figs. 5.18 and 5.19 respectively. It may be beneficial to minimise the linewidth of the QD for applications such as single photon sources that require indistinguishable photons. A typical QD will have a bandwidth in the MHz region whereas the narrowest linewidths are of the order of 100s of kHz using spontaneous parametric down conversion sources [178]. This gives motivation for tuning the QD linewidth to be minimal such that the QD platform can be more competitive with other single photon sources. Another reason why narrow linewidth QDs are desirable is for QD lasers [179, 180]. Quantum well lasers allowed for exciting developments in terms of laser performance many years ago and it is believed that there is potential for QD lasers to bring further improvements due to the 3-D confinement that QDs provide. In Fig. 5.17, we saw that the emission peaks shifted as a function of temperature. Fig. 5.18 shows that increasing the temperature causes a linear red-shift in the peak wavelength. This is not unexpected - similar results to these have been observed before in the literature (see for example [181]) and are due to the bandgap of the material shrinking with increasing temperature. The linewidth of the QD is also strongly influenced by the temperature, as we see in Fig. 5.19. This can be attributed to phonon scattering which becomes more significant at higher temperatures and obeys the equation given in [182].

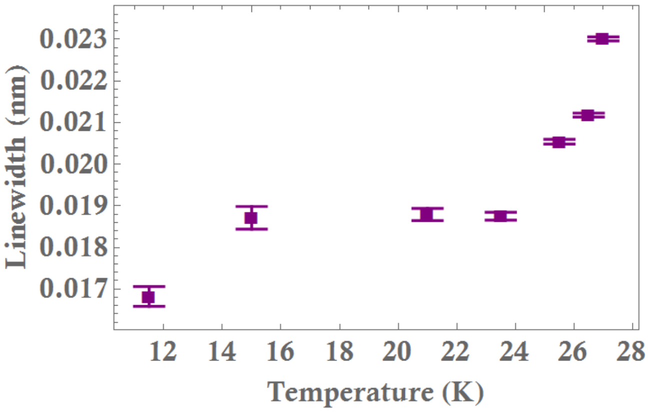

Figure 5.19: Dependence of the linewidth of the QD emission on the temperature.

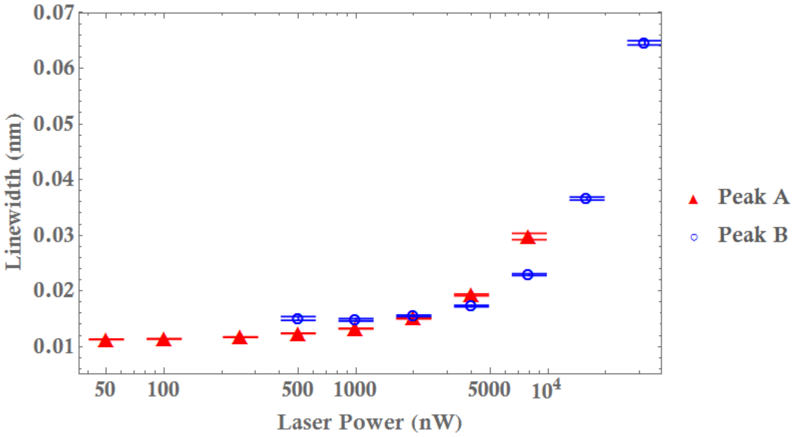

Figure 5.20: Dependence of the linewidth of the emission peaks on the laser power.

5.5.2 Micropillar 2

This section will show a range of other characterisation measurements we are able to perform on QDs, which will be taken on two emission peaks found in a second micropillar in the medium Q factor sample. For these emission peaks, we consider how the laser power affects some of the QD properties. First, in Fig. 5.20 we consider the dependence of the linewidth of the QD on the laser power, and compare how the two emission peaks differ. In this case the linewidth dependence on the power for the two peaks is qualitatively similar and also shows a similar trend to the dependence of the linewidth on the temperature. We would expect the linewidth to increase with power in general due to extra carriers being introduced into the environment of the QD and so this result is intuitive and reaffirms the need to use lower powers [183].

Another thing we consider is the dependence of the position of the peak wavelength on the laser power. This will experience some shift in position as the power is increased due to the extra charge carriers that are introduced at higher powers. This is most commonly found to be a

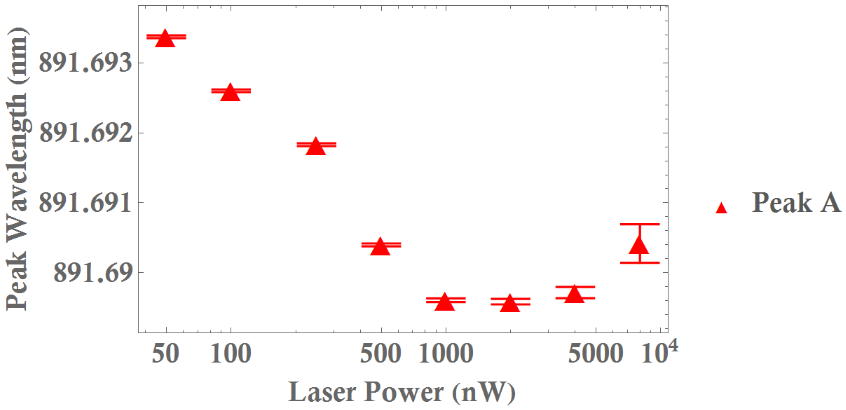

(a) Dependence of the wavelength of peak A on the excitation power.

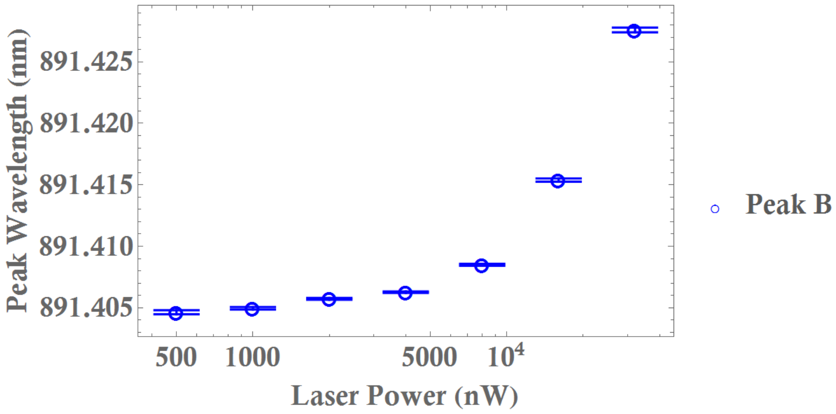

(b) Dependence of the wavelength of peak B on the excitation power.

Figure 5.21: This figure shows how the two peaks shown in Fig. 5.10 each vary in wavelength as the excitation power is increased. We see that peak A experiences a red shift whereas peak B experiences a blue shift.

red-shift, however, although we see a shift in the peak wavelength for each emission peak, peak A is blue-shifted, whereas peak B is red-shifted from their respective resonances (see Fig. 5.21). The fact that one of these peaks experiences a blue-shift while the other experiences a red-shift may be due to the distribution of charges in the material. The environment of a QD is complex and it is often difficult to determine the origin of such effects, however, charge noise within the structure is certainly a possible cause. In general, analysis of many QDs in this sample showed an overall likelihood of an emission peak being red-shifted as the excitation power is increased and it is not obvious why this particular peak would experience a blue-shift. This method can be used to some extent to tune the wavelength of the QD resonance, however, the variation is small and the temperature dependence is in general more effective. Then, the motivation for tuning the resonance using the laser is the fact that some QDs will experience a blue-shift in wavelength, whereas the temperature tuning will always introduce a red-shift, meaning that a QD found at

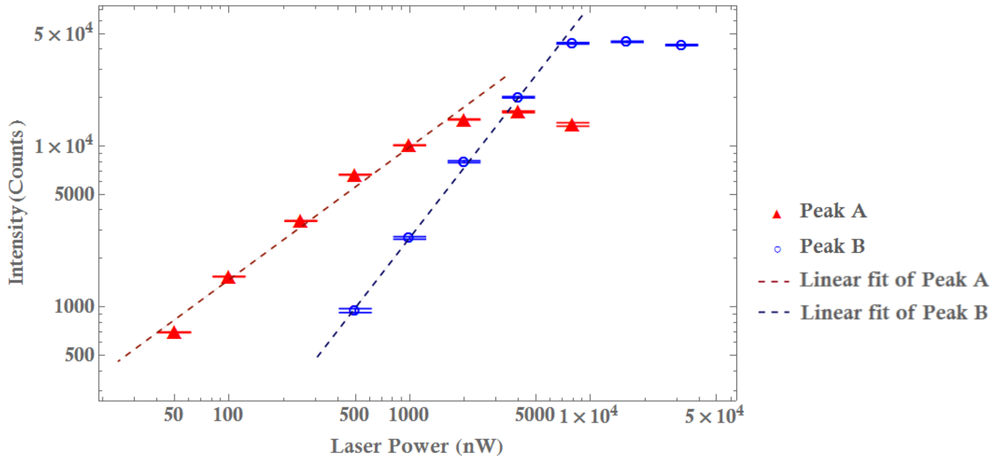

Figure 5.22: Power dependence of the two peaks shown in Fig. 5.10. We see both of the emission peaks saturate as the power increases. The fit used ignores the points where we assume saturation has occured and concentrates on a fit that is linear with respect to the log scale.

a lower wavelength than the cavity mode cannot be temperature tuned to be on resonance, but may be tuned using the laser power in some cases.

Single QD PL also allows us to study the properties of both excitons and biexcitons in neutral and negatively charged QDs. An exciton is defined as a bound electron and hole and in a QD these are formed between a confined electron that has been promoted to the CB and the hole it leaves behind [184]. The Coulomb force between the electron and hole binds them to each other and upon recombination a photon will be emitted. A biexciton is two excitons bound together and will decay into a single exciton and a photon. We can study the difference between the excitation properties of an exciton and a biexciton using PL spectroscopy by considering the dependence of the intensity of the emission peak resonance on the laser power; an exciton will have a linear power dependence, whereas for a biexciton the dependence will be quadratic [185]. For this particular measurement, we will characterise the emission peaks of the spectrum shown in Fig. 5.10.

Studying these two emission peaks in terms of power dependence, we see that one of the peaks behaves as we would expect from a biexciton and the other as we would expect from an exciton [186]. This is shown in Fig. 5.22 where we see that the power dependence of peak A shown has a slope of ≈ 1 which corresponds to a linear dependence on the laser power, whereas peak B has a slope of ≈ 2 which corresponds to a quadratic power dependence. It is likely that these two peaks correspond to an exciton and biexciton emission in a single QD, due to their close proximity in wavelength.

When fitting these points, we should note that there is a point at which the emission peak of the QD will no longer increase - the saturation point. We therefore neglect the points where we believe this saturation point has occurred when fitting the data (in both cases the three

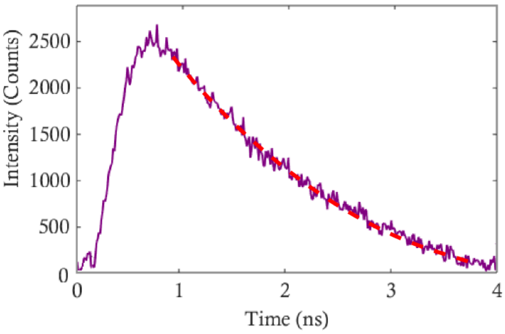

Figure 5.23: Lifetime data taken using the Picoharp for Peak A in micropillar 2 excited by a resonant laser at a power of 2μW. The measured lifetime is $T_1 = 1.29 \pm 0.03$ns.

data points that correspond to the highest powers have been neglected). This power dependence measurement is therefore also useful in finding the point at which the QD is saturated; equivalent to the point at which a π pulse is applied to the QD when using pulsed light. At this point, we will no longer see an increase in the intensity as the power is increased. It is necessary to determine the position of this point when considering the NFF protocol, as we require the Rabi frequency to be such that the QD is subject to a laser pulse that is close to the saturation power. We will use this technique in Chapter 6 to determine the pulse power that should be used for the NFF protocol to work successfully.

Using the resonant scattering setup described in Section 5.4, we can measure the lifetime of the QDs. Each of the lifetime measurements was taken at 11.5K at a laser power of 2μW. The counts from the APD are recorded using a Picoharp. We can use this to perform a lifetime measurement on each of the QD emission peaks discussed above. We calculate the lifetime from this by fitting the exponential decay. The lifetime measurements for peak A and peak B are shown in Figs. 5.23 and 5.24 respectively. The dotted red line shows the exponential fit. From this we find that peak A has a lifetime of $T_1 = 1.29 \pm 0.03$ns and peak B has a lifetime of $T_1 = 1.24 \pm 0.02$ns These lifetimes are on the order of what would be expected in an InGaAs QD. In general, for applications where we will use pulsed light, it is preferable to have a shorter QD lifetime so that there is no overlap between each pulse and the previous initialisation of the QD lifetime.

5.6 Summary

Finding a QD that has the ideal spectrum is difficult, but searching through different QDs and different samples can allow us to find one that is sufficient for the application we are considering. We showed that we can use PL spectroscopy to identify single QD emission peaks and showed how these are dependent on temperature and excitation power. The techniques outlined can be used to tune the linewidth, peak wavelength and emission intensity of the QD wavelength to a certain extent. We also showed how it is possible to use the excitation power dependence on the

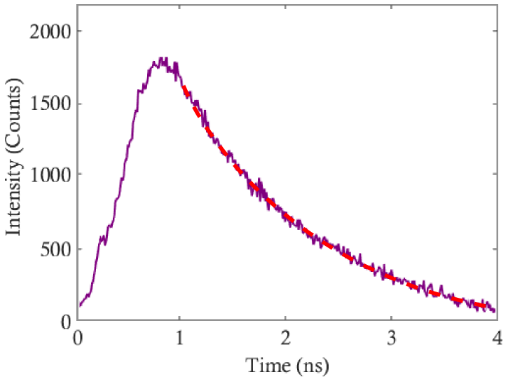

Figure 5.24: Lifetime data taken using the Picoharp for Peak B in micropillar 2 excited by a resonant laser at a power of 2μW. The measured lifetime is $T_1 = 1.24 \pm 0.02$ns.

emission intensity to identify whether an emission peak comes from an exciton or a biexciton. Our characterisation shows several promising emission peaks for QC applications. The results shown in Chapter 6 will be measured using the QDs identified on the low Q factor QD sample. This is because it is much easier to identify QDs with the required properties on the low Q factor sample, due to the cavity mode being broader, making the chances of finding a QD overlapping with the mode much higher. Previously characterised QDs identified in low Q samples are better suited to the applications we require.

CHAPTER 6

AN EXPERIMENTAL STUDY OF NUCLEAR EFFECTS IN InGaAs QUANTUM DOTS

In this chapter we attempt an experimental implementation of the NFF protocol discussed in Chapter 2. This is an experimental chapter - the results shown are novel and the interferometer setup used to measure these results is also novel, as discussed in Chapter 5. We will show exploratory data using a complex optical setup designed to control and manipulate the electron and surrounding nuclear spin bath of a negatively charged InGaAs QD. We will first describe how the experimental setup can be used to measure the visibility of the photons emitted from the QD. We show how this allows us to identify whether a QD is neutral or charged. We then show that altering the pulses we apply to the system can allow us to control and manipulate an electron spin in the QD and measure the resulting spin state. We analyse the results of these measurements, including identifying differences in the electron spin precession before and after implementation of the NFF protocol. We will discuss these results and how they could be improved to give a more predictable change in the electron spin precession.

6.1 Experimental Setup

The experimental setups used for the measurements in this chapter are shown in Figs. 5.3 and 5.4. The first part of the setup (Fig. 5.3) shows how each laser inputs light onto the sample. The pulsed laser is used to drive the electron in an attempt to align the nuclear spin bath along an external field and the single frequency laser is used to measure the electron spin, with the reflected light being sent to the interferometer setup shown in Fig. 5.4. The external field is applied using a superconducting coil, where we apply a current in the range of $20-30$A, corresponding to an external field range of $\approx 80-130$mT. This interferometer setup is used to measure the interference

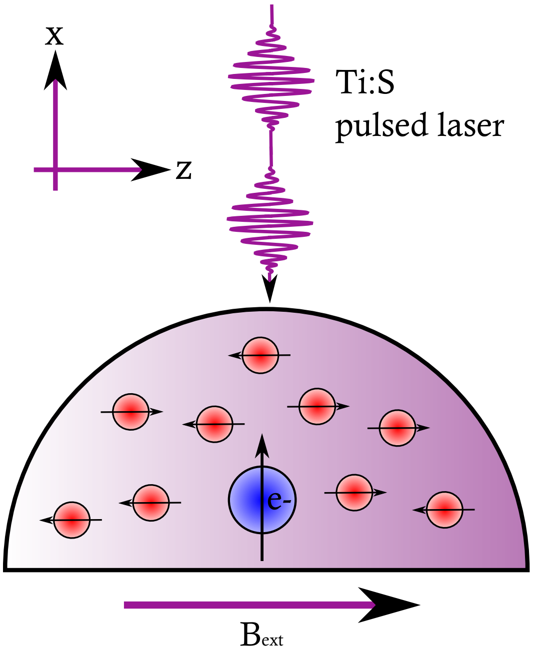

Figure 6.1: Diagram showing the geometry of the setup, with the direction of the pulse sequence in relation to the external field direction.

fringes of the emitted photons. Importantly, when we apply an external field, the probe laser is in the orthogonal plane to the direction of the external field (see Fig. 6.1). This is significant when measuring the output of the probe laser through the interferometer. Assuming the QD we measure is charged, the electron spin will be precessing about the axis of the external field. This means that when the probe laser interacts with the electron, it will see a different electron spin state at different times, as the electron will be effectively switching between the $|\uparrow\rangle$ and $|\downarrow\rangle$ state in the optical axis plane. This means that each photon that interacts with the electron spin will experience a different phase shift corresponding to the phase of the electron spin at that point. We can use this to measure the precession of the electron spin using a time delay interferometer. In Fig. 6.2, we see the interaction of a linearly polarised photon with the precessing electron spin. Each photon entering the cavity and interacting with the electron spin will be linearly polarised (assuming perfect optics). The electron begins in the state $|\uparrow\rangle$ and will precess about the z (in-plane) axis according to the external field and laser pulse sequence. Then, in the optical axis plane the electron is rotating between the state $|\uparrow\rangle$ and the state $|\downarrow\rangle$. Each interacting photon will therefore see a time-dependent electron spin state. This means that these photons will pick up a phase after the interaction, as described in Chapter 5. This allows us to determine the spin state of the electron at any point in time by interacting each photon with a time delayed version of itself. The detection of these photons is done using the interferometer, and the process will be explained below.

The photons entering the interferometer will be split along its two arms. One of these arms

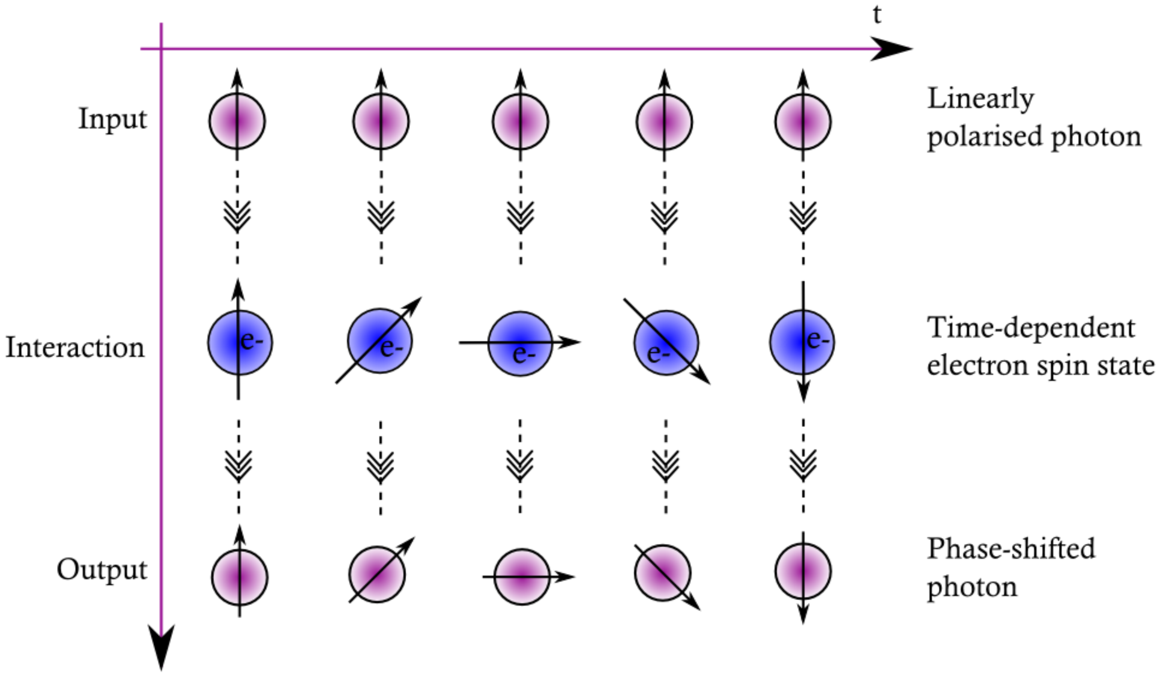

Figure 6.2: Diagram to illustrate the effect of a linearly polarised photon that is input along the optical axis interacting with an electron spin precessing due to a field in the Voigt geometry. As the time increases, we see how the electron rotates in the optical axis plane and its influence on the phase of the interacting photon.

has a retroreflector and a piezo stage which has tens of nm position precision and can be used to perform a scan over the position of the incoming photons. The second arm of the interferometer has a retroreflector positioned on a translation stage. This stage will move in larger increments ($\approx 10\mu$m). To measure interference fringes, we move the translation stage one step, let the piezo stage do a full scan, then move the translation stage another step and let the piezo stage scan again and so on. This will give interference fringes between each photon and its delayed self at a range of different time delays, determined by the length of the stage. The photons are then recombined at the second beamsplitter and sent to the two APDs. We can measure the output counts in each detector to give us the $g^{(1)}$ (first-order correlation) function, which quantifies the fluctuation of the electric field in time and therefore determines the visibility of the interference fringes. The visibility, V, can then be calculated according to the relation

$$V = \frac{I_{max} - I_{min}}{I_{max} + I_{min}} \tag{6.1}$$

where I_{max} (I_{min}) is the maximum (minimum) value of the intensity over one stage step and V is the absolute value of the $g^{(1)}$ function.

The output data we receive from the interferometer scan is in the form of two channels of counts, one from each APD. We can convert these counts to a relative intensity, RI, calculated at

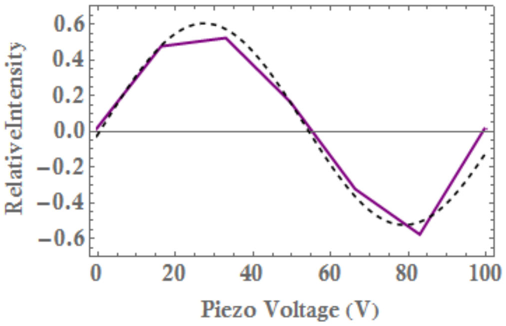

Figure 6.3: An example of a sinusoidal fit for one translation stage step.

each data point using the relation

$$RI = \frac{C_1(t) - C_2(t)}{C_1(t) + C_2(t)} \tag{6.2}$$

where $C_1(t)$ ($C_2(t)$) is the number of counts at a particular point, t, in the interferometer scan on the first (second) detector. The output data will have a form similar to that shown in Fig. 6.4(a) (this shows a charged QD in an external field of $B_{ext} \approx 84.9$mT). Note that we will not discuss this result in this section, and will just give details of the data analysis procedure. The data itself will be analysed below. From this relative intensity, we can find the visibility of the output. For each stage step of the course translation stage, there are 11 piezo steps, increasing from 0 to 10V. These 11 data steps will give a sinusoidal data set, with a frequency corresponding to the wavelength of the measured photons. The period of each sinusoid will be on the order of 3fs. However, we find that each time the translation stage moves, there is a jump in the data of $\approx$ 80ps. We therefore cannot fit the data as a full set, and must fit each translation stage step to a sinusoid independently, as shown in Fig. 6.3. We extract the amplitude from each of these small fits and use this to create an envelope for the data. This envelope represents the visibility and is shown in Fig. 6.4(b).

To perform the NFF protocol, we first use the Ti:S pulsed laser to drive the electron spin and apply a magnetic field in the Voigt geometry. We set this external field and also the detuning and Rabi frequency of the pulsed laser according to the parameters discussed in Chapter 2 and introduce the Ti:S laser without the CW single frequency laser. We orient the HWP and QWP such that the polarisation of the pulsed light will be circular, to allow us to address only one of the electron spin states, thus driving it using the method described in Chapter 2. We leave this pulsing for $\approx$ 2 minutes. We expect that the electron and nuclei will reach their stable configuration in a few ns, [123], however, we leave the pulses on for much longer timescales to ensure the driving is successful. We do not perform detection at this point and so we do not send the emitted light to the interferometer setup. The pulsed laser is then turned off for the detection part of the experiment (the external field is still turned on). Here, we introduce the CW single frequency laser as a probe laser. For this measurement, we require the probe to be linearly

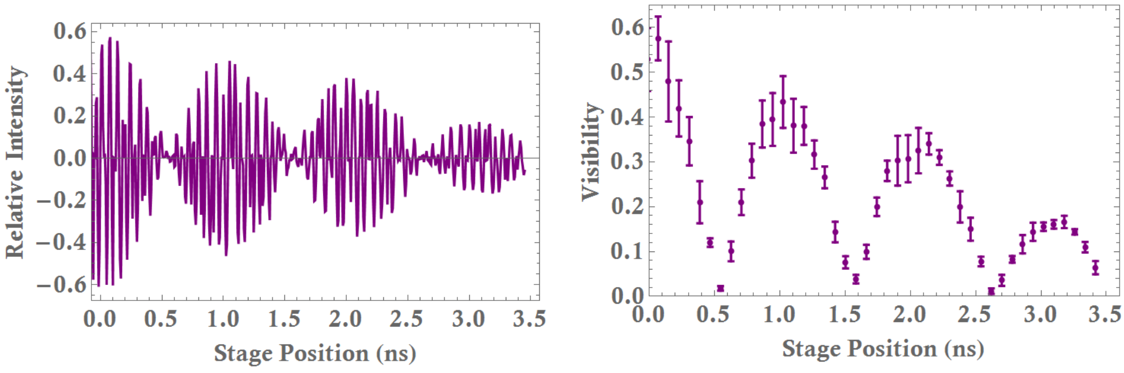

(a) Raw data

(b) Fitted visibility

Figure 6.4: (a) Relative intensity plot for a charged QD in an external field of $B_{ext} \approx 84.9$mT. (b) Fitted visibility from the relative intensity plot.

polarised (we choose the input polarisation to be $|V\rangle$) to perform the measurement described above. The CW light is sent to the interferometer setup and we calculate the visibility from the output data.

6.2 Preliminary interferometer measurements

This section will discuss results found using the interferometer setup described in Section 6.1. We will first show how we can identify neutral and charged QDs using the setup. We will then calculate the precession frequency and g-factor of the 4 charged QDs analysed in Section 5.3.2. The length of the translation stage used is 60cm, giving a total scanning distance of ≈ 4ns. We find that in some cases this is not sufficiently long enough to see all of the nuclear spin effects and so we also show how the time delay can be lengthened using fibre delays to allow us to analyse the systems over longer timescales. For all of these measurements, the CW probe laser power was set to be ≈ 0.5nW with linear polarisation and the temperature of the setup was ≈ 4.3K.

6.2.1 Identifying neutral and charged QDs

In Section 5.4, we showed the resonant scattering scans of 4 QDs. We are able to give an indication of whether the QD is charged or neutral by considering these spectra. However, using the interferometer setup, we can introduce a more reliable method for quantifying whether a QD is charged or not. We showed in Section 6.1 that the interferometer can be used to measure the visibility of the interference fringes of the photons emitted from the QD. Then, assuming no external field is applied to the system, the exponential decay of the envelope of the visibility (calculated using Eq. 6.1) gives the coherence time of the electron. In the case where we apply some external field to the system, we expect to see the visibility oscillating as the electron spin

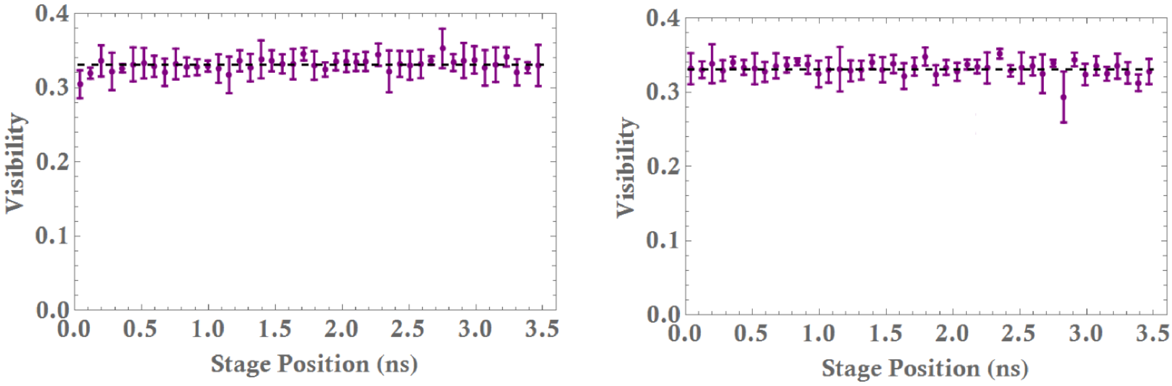

(a)

(b)

Figure 6.5: Interferometer output for a neutral QD in zero field and ≈ 72.18mT external field. The laser power is ≈ 0.5nW and the temperature is ≈ 4.3K.

precesses, and by fitting a sine wave to the envelope function, using the fitting procedure detailed in Section 6.2.2 below, we can calculate the electron spin precession frequency. If there is no excess electron in the system, we will see no change in the visibility and we can infer from this that the QD we are measuring is neutral.

First, we consider the interferometer output of the QD we have assumed to be neutral. Here, we expect that there will be no electron spin to detect and so we will not see any change in visibility due to the precession of the electron. This is confirmed by Fig. 6.5. Here we see that the envelope of the visibility fringes is constant (excluding slight changes due to noise), such that there is no decay, both in zero external field and a field of $B_{ext} \approx 72.18$mT. This means that we are not measuring an electron spin as we see no exponential decay and no change in the visibility when we introduce an external field. These measurements were taken using the fibre beamsplitter, which is why the visibility we see is quite low. This result fits with our assumption that the QD is in fact neutral, however, we must first verify this by measuring the visibility of a charged QD in both a zero and non-zero external field, thus confirming that the interferometer is working correctly.

First, we will consider how each of the QDs we believe to be charged behaves when measured through the interferometer setup at zero magnetic field. The visibility of charged QD 1 is shown in Fig. 6.6(a). These results show very clear exponential decays in the visibility of the oscillations for each of the charged QDs and are significantly different to the graphs shown in Fig. 6.5. From this, we can state with confidence that we are now measuring an electron spin within a QD. For QD 1 and QD 4, the interferometer setup has been realigned, and we estimate that there is an offset of ≈ 0.4ns, such that the time delay of 0 will actually occur at ≈ 0.4ns rather than 0, due to alignment of the interferometer stage. Taking this into account, by fitting the exponential decay for the four charged QDs, we get the following coherence times:

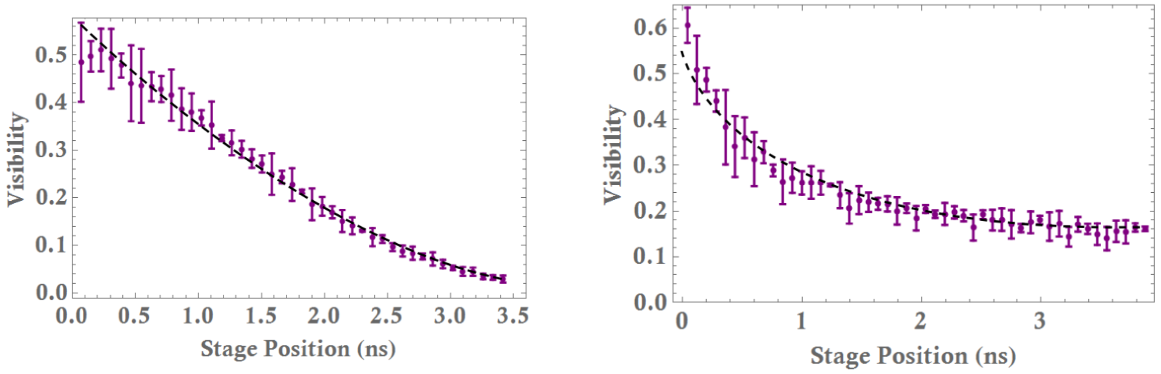

(a) Charged QD 1

(b) Charged QD 2

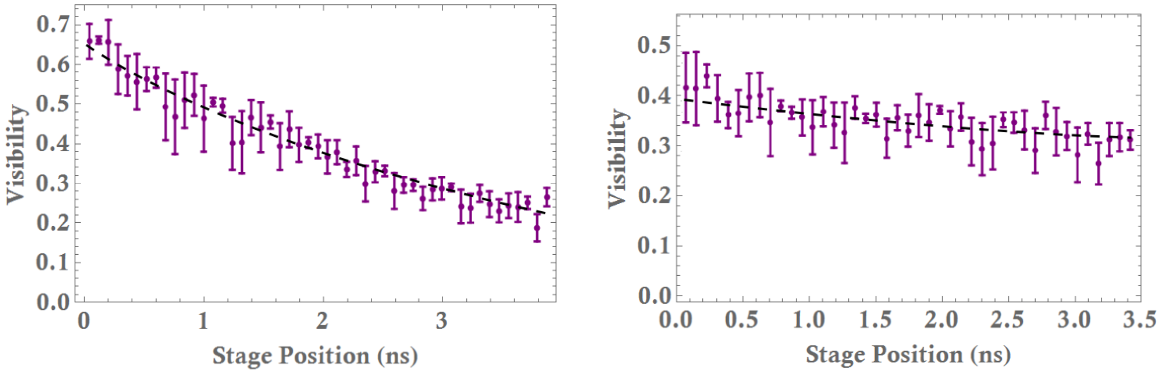

(c) Charged QD 3

(d) Charged QD 4

Figure 6.6: Visibility of the charged QD in zero external field with laser power of ≈ 0.5nW and a temperature of ≈ 4.3K.

- **Charged QD 1**
  $T_1 = 1.68 \pm 0.07$ns
- **Charged QD 2**
  $T_1 = 1.26 \pm 0.04$ns
- **Charged QD 3**
  $T_1 = 2.77 \pm 0.05$ns
- **Charged QD 4**
  $T_1 = 18.41 \pm 0.65$ns.

These coherence times vary quite considerably between the four QDs. Charged QDs 1 to 3, although different, all have values of T_1 that are within the normal range. However, when we consider charged QD 4, we see that there is only a very small amount of decay in the time frame we consider and that its coherence time is much longer than the others. QDs with long coherence times can be extremely desirable for many quantum information processing applications as this allows for more operations to be performed on the quantum state within its coherence time. However, to be able to take more useful measurements with this QD, we need to be able to see the visibility fringes of the electron spin on longer timescales. The obvious way to do this would be to extend the length of the interferometer stage, however, the setup is limited by space. Because of this, we choose to insert additional fibre delays into the setup. We have three possible fibres that can be diverted through the setup in any combination - a 1m, a 2m and a 5m single mode fibre. We can then take measurements for different time delays and stitch together the results, allowing us to effectively lengthen the translation stage. Due to the length of the fibres, there are values of the time delay that we cannot access, and so there are gaps in the data sets, however, these gaps are small enough that the shape of the data in the gaps can be sufficiently well inferred. When we use the fibre delay setup, we are using fibre beamsplitters rather than standard beamsplitters, which are polarisation maintaining and this means that there will be some loss of visibility due to the polarisation being less well preserved through the fibre beamsplitters in comparison to the polarising beamsplitter. We will use these time delays for several of the measurements discussed in the following sections.

6.2.2 Measuring the precession frequency of the electron spin in an external magnetic field

In this section, we show how applying an external magnetic field in the Voigt geometry to this system allows us to calculate the precession frequency of the electron spin. In Section 6.1, we described how the interferometer can be used to measure the visibility of the interfering photons as a function of the time delay. Here, we will measure the four charged QDs we have selected and show the precession frequency of each of these due to a particular external magnetic field value. The setup we are using is able to produce external fields in the Voigt geometry of up to ≈ 200mT and so we are limited to these low fields. However, we show in Chapter 2 that it is possible to implement the NFF protocol in this field range. We will first show the electron spin precession of each of the four charged QDs due to some external field, B_{ext} without applying the pulse sequences outlined in Chapter 2 and describe the fitting procedure we use to determine the electron precession frequency. The precession of charged QDs 1, 2 and 4 according to $B_{ext} \approx 84.9$mT and charged QD 3 according to $B_{ext} \approx 106.2$mT is shown in Fig. 6.7.

We see that all of the visibility measurements have changed from the zero field case, showing that the application of B_{ext} is effective. Each of the QDs shows a recurring peak in visibility, where the visibility increases after reaching a minimum, showing that there is some precession of the electron spin. The peaks in visibility correspond to times when the photons are in phase with each other, i.e. where the electron has rotated by either π or 2π from the initial state $|\uparrow\rangle$. The minima occur when the electron has rotated by $\frac{\pi}{2}$ or $\frac{3\pi}{2}$ from the initial state. As before, QDs 1 and 4 have a timing offset of ≈ 0.4ns. Charged QD 1 has a very clean precession, showing an exponential decay in the maximum of each peak, corresponding approximately to the coherence time measured above. Charged QD 3 has quite a clean precession, but in this case a large proportion of the visibility has been lost between the first and second peaks. Charged QD 2 appears to have a small second peak between the larger first and third peaks. This looks as though it could be another effect that is oscillating at a different frequency to the electron spin, but it isn't clear at this point what this is caused by. Charged QD 4 looks qualitatively more similar to charged QD 1, but over a much longer timescale. The gaps in the visibility measurements correspond to the mismatch between the fibre length and the interferometer stage length as described above. The visibility decreases but we very clearly see that oscillations occur up to at least 13ns, and the visibility has only decreased by $\approx 25\%$ by this point in some cases.

We fit a sine wave to the data points in each piezo stage step independently and plot the amplitudes of each of these fits to create an accurate envelope for the data. These envelope fits are shown in Fig. 6.7. We can then fit these data points to extract the precession frequency of the electron spin. The fitting for charged QD 1 is shown in Fig. 6.8. In this case, the envelope of the visibility fits well to the absolute sine function, $|a\sin(bx+c)|+d$, with an exponential decay. The exponential decay gives a new coherence time of 3.71 ± 0.03. Taking the position of the minima from this fit allows us to make an accurate estimate for the precession frequency of the electron spin. We fit the data from each interferometer measurement in this way to model the change in precession frequency of the electron spin as a function of B_{ext}, however, this function is not always accurate for the visibility of different QDs. For charged QDs 2 and 4, we fit each of the minima individually using the parabolic function $a(x+b)^2+c$. We should note here that the envelope decay of each QD is altered by the external field. For some of the QDs, the decay becomes longer, and for others it becomes shorter. The cause of this is likely to be the configuration of the nuclei, such that the action of the external field will either make the nuclei gain or lose polarisation in a particular direction.

The precession frequency of an electron spin measured in this way is given by

$$\omega_{eff} = \frac{1}{t_{min2} - t_{min1}} \tag{6.3}$$

where t_{min1} (t_{min2}) is the time delay at which the first (third) minimum occurs, i.e. a full 2π rotation. The first minimum represents a rotation of $\frac{\pi}{2}$, the first returning peak a rotation of π etc., with the full Bloch sphere rotation occuring at the maximum of the second returning peak. We calculate the precession frequency using the minima as this gives a higher accuracy (we see this in the size of the error bars at the minima compared to the maxima). For some of these measurements, we are not able to access the position of t_{min2} as some data was taken without the fibre delays and so the third minimum is obscured and for charged QD 4, we cannot see the third minimum due to the fibre mismatch and so we estimate the precession frequency from the first and second minima. In the case of charged QD 2, we ignore the first small peak and assume this is not part of the electron spin's coherent precession. We call the electron spin precession

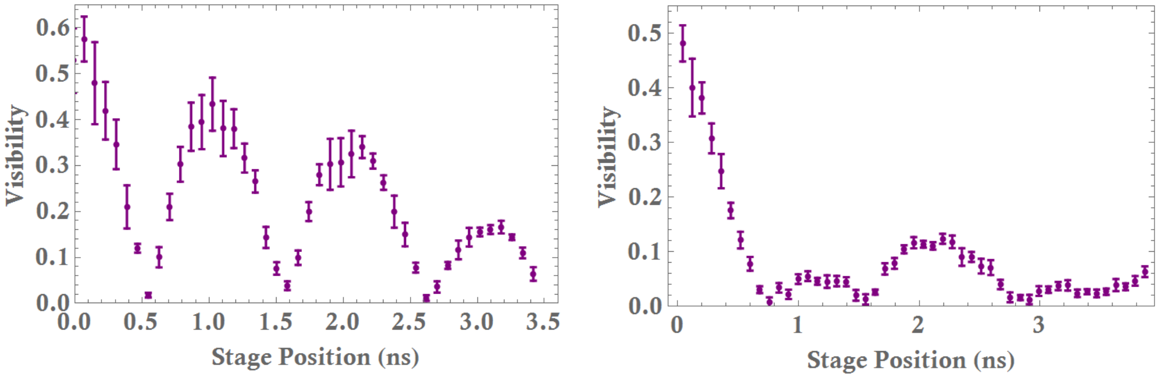

(a) Charged QD 1

(b) Charged QD 2

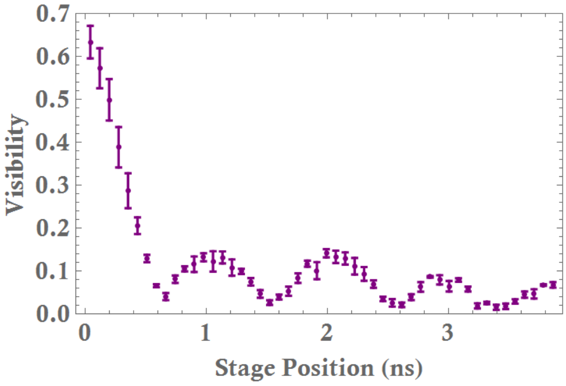

(c) Charged QD 3

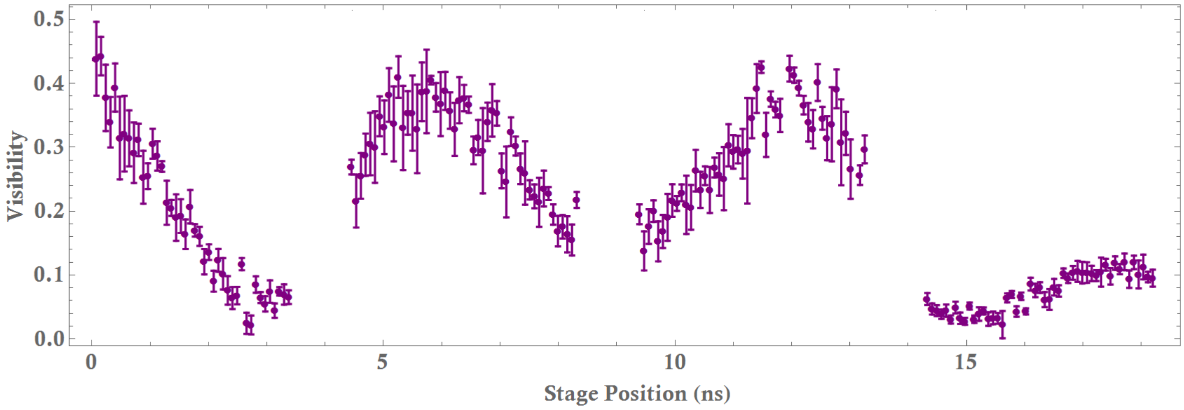

(d) Charged QD 4

Figure 6.7: Electron spin precession from the 4 charged QDs we consider. Charged QD 4 includes a range of fibre delays, up to a 3m delay. Charged QDs 1, 2 and 4 are measured at a value of $B_{ext} \approx 84.9$mT and charged QD 3 was measured at a value of $B_{ext} \approx 106.2$mT. The CW laser was at a power of ≈ 0.5nW and the temperature was ≈ 4.3K.

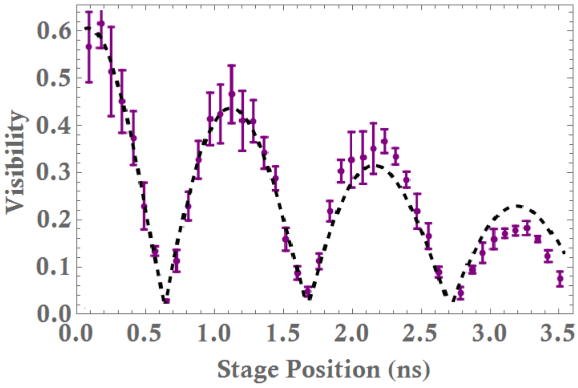

Figure 6.8: Theoretical fit of the envelope of the data taken from charged QD 1 with $B_{ext} \approx 84.9\text{mT}$. The fitting function used is $|a\sin(bx+c)|+d$ accompanied by an exponential decay.

ω_{eff} as this is the total precession frequency the electron experiences and we do not assume that this is a result of B_{ext} only.

The precession frequencies for each QD are calculated to be

- **Charged QD 1**
  $\omega_{eff} = 0.519 \pm 0.009\text{GHz}$ ($B_{ext} \approx 84.9\text{mT}$)
- **Charged QD 2**
  $\omega_{eff} = 0.268 \pm 0.006\text{GHz}$ ($B_{ext} \approx 84.9\text{mT}$)
- **Charged QD 3**
  $\omega_{eff} = 0.576 \pm 0.007\text{GHz}$ ($B_{ext} \approx 106.2\text{mT}$)
- **Charged QD 4**
  $\omega_{eff} = 0.0835 \pm 0.009\text{GHz}$ ($B_{ext} \approx 84.9\text{mT}$).

From this, we find that the precession frequency can vary considerably between QDs, even when the value of B_{ext} is the same. This is due to the variation in g-factors between QDs. We can calculate what the g-factor will be for each of the QDs using the equation

$$g = \frac{\omega_{eff}}{\mu_B B_{ext}} \tag{6.4}$$

where ω_{eff} is the precession frequency, $B_{ext} \approx 84.9\text{mT}$, the Bohr magneton $\mu_B \approx 14\text{GHz}$ and g is the g-factor of the electron. Then we calculate the g-factors of each QD to be

- **Charged QD 1**
  $g = 0.437 \pm 0.009$
- **Charged QD 2**
  $g = 0.225 \pm 0.006$

- **Charged QD 3**
  $g = 0.388 \pm 0.007$
- **Charged QD 4**
  $g = 0.0702 \pm 0.009$.

We find that charged QDs 2 is close to the $g \approx 0.25$ that we expect [93, 94], whereas charged QDs 1 and 3 are higher than we expect and charged QD 4 is considerably lower. However, this number is known to vary between QDs and it is not unusual to find a variety of different g-factors within a sample of QDs [187].

We have now shown that we have a setup capable of detecting whether there is an electron spin precessing in a particular QD and that we can calculate the precession frequency and g-factor of this electron accurately. We have also discussed how we can use fibre delays to effectively extend the length of the time delay in the interferometer so that QDs with longer coherence times can also be studied. We will now attempt an implementation of the NFF protocol.

6.3 Implementation of the NFF protocol

This section will show the results of our experimental implementation of the NFF protocol outlined in Chapter 2. We will show how each of the charged QDs responds to being acted on by trains of circularly polarised pulses and how varying the value of B_{ext} affects the system. The pulse sequence is applied to the system using the Ti:S pulsed laser. During this pulsing period, the light from the CW probe laser is blocked and the QWP is rotated such that the pulsed light is rotated from linear to circular. It is important to correctly choose the direction of the circularly polarised light in relation to the direction of the detuning of the QD resonance from the laser pulses, as if we choose incorrectly, we will not be able to find a single stable nuclear spin configuration for any given parameter set (see Chapter 2). A positive (negative) detuning corresponds to the laser pulse being on the red (blue) side of the QD resonance. Then for a positive (negative) detuning we need to apply σ^- (σ^+) polarised pulses to achieve the correct nuclear spin bath configuration. Due to difficulties in stabilising the pulsed laser at the correct wavelength, some of the QDs will have blue-detuned pulses and some will have red-detuned pulses, so we choose the direction of the circular polarisation accordingly. We set the detuning and Rabi frequency of the pulses to match the parameters in Chapter 2 ($\Delta = 0.2$, $\Omega = 0.6$) as accurately as we can. The detuning is set by taking PL spectra of the QD resonance and Ti:S pulse and tuning the wavelength of the laser pulse by eye until the QD resonance is at the half maximum of the pulse. This is inaccurate but sufficient for the low level of stability in detuning we show is needed. For the Rabi frequency, we use PL measurements to determine the laser power needed to saturate the QD (as shown in Chapter 5). We require the condition $\Omega \approx 0.6$ and we know that the saturation power corresponds to $\Omega \approx 0.7$ and so we can adjust the power accordingly to achieve this ratio. Again, this level of accuracy should be sufficient for the Rabi frequency to be within

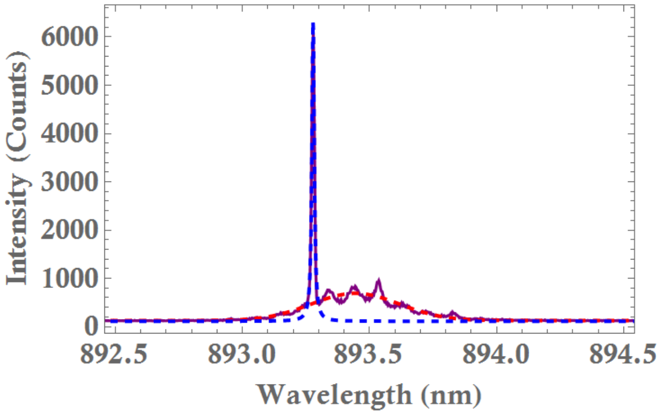

Figure 6.9: PL spectrum of charged QD 1 showing the detuning of the pulse acting on the QD. The power of the Ti:S laser pulse is ≈ 250nW and the CW single frequency laser is at a power of 250nW. The red dotted line shows a hyperbolic secant fit to the pulse and the blue dotted line shows a Lorentzian fit to the QD. We measure $\Delta = 0.203 \pm 0.004$.

the stable range. The laser pulse sequence is applied to each of the charged QDs for ≈ 2 minutes. After application of these pulses, the light from the Ti:S laser is blocked, the QWP is rotated such that the input light will be linearly polarised and the CW probe laser is introduced. We then measure the precession frequency of the electron spin using the method described above.

6.3.1 Charged QD 1

In this section, we will focus on results obtained from charged QD 1. We will show the dependence of the QD precession frequency on B_{ext} after application of pulses. Using PL spectroscopy, we align the laser pulse such that the QD is positioned at approximately the half maximum of the laser pulse on the blue side and apply σ^- pulses (the aligned spectrum is shown in Fig. 6.9). The QD is the large spike at ≈ 891.38nm and the wide feature is the Ti:S pulse. The pulse is fitted to a hyperbolic secant and the QD to a Lorentzian, shown by the red and blue dotted lines in Fig. 6.9 respectively. From these, we can extract the value of the detuning - in this case $\Delta = 0.203 \pm 0.004$. We measure the pulse power required to saturate the QD to be ≈ 300nW and so we set the power to be ≈ 250nW. We should note here that this power is ≈ 10× the real power applied to the QD, as the beamsplitter is a $90:10$ beamsplitter, with the power meter in the arm that contains 90% of the light. This will be true of all of the Ti:S powers quoted. After applying these pulses for ≈ 2 minutes with $B_{ext} \approx 84.9$mT as before, we rotate the QWP back to linear and measure the visibility using the CW probe laser. In Fig. 6.10 we show the visibility measurements for charged QD 1 before (this is the result shown in Fig. 6.7 and is included again for easier comparison) and after application of the pulses.

There is no obvious difference between the outputs of these two measurements despite the application of circularly polarised pulses. However, we see in Fig. 2.9(c) that the value of B_{ext}

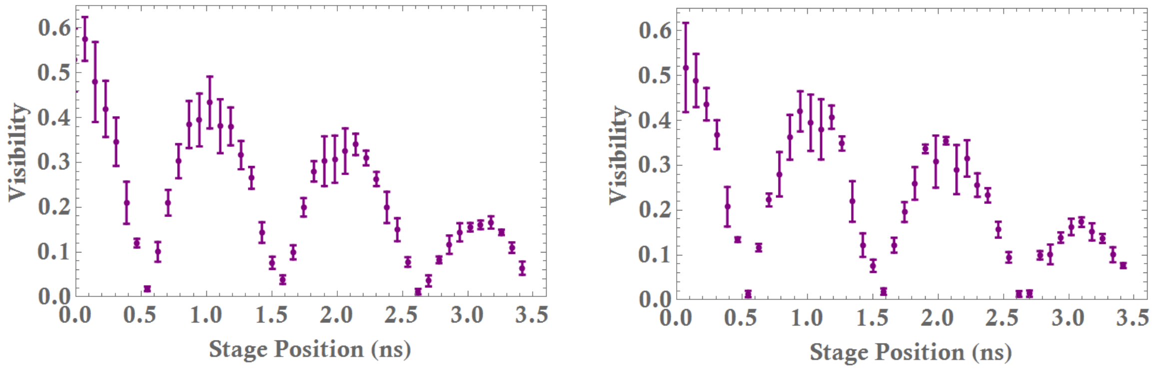

(a) Charged QD 1 before application of circularly polarised pulses

(b) Charged QD 1 after application of σ^- circularly polarised pulses

Figure 6.10: Visibility from charged QD 1 before and after application of a train of circularly polarised pulses.

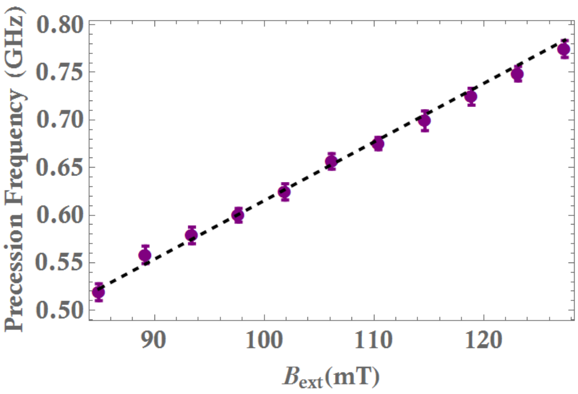

Figure 6.11: Relationship between B_{ext} and the precession frequency of the electron spin of charged QD 1 (course scan). The purple circles show the experimental data and the black data shows the theoretical precession frequency of an electron spin with a g-factor of 0.437 with increasing B_{ext}.

must be chosen very accurately to give a stable configuration for the nuclear spin bath, so it is not necessarily surprising that we do not see an immediate change after applying pulses. We will now take a set of measurements where we increase the value of B_{ext} in increments of ≈ 4.25mT up to ≈ 127.4mT (this is chosen because it corresponds to an increase in current in steps of 1A through the superconducting coil). We reapply the same pulses after each change in B_{ext}.

In Fig. 6.11, we plot both the measured precession frequency of the electron spin as a function of B_{ext} and also the theoretical model of an electron spin with a g-factor of 0.437 (as measured for QD 1) to precess with increasing B_{ext}. To calculate the precession frequency of the electron spin, we use the fitting procedure described in Section 6.2.2 to create an envelope for the data and then fit this envelope as described. This theoretical model matches the trend of the experimental

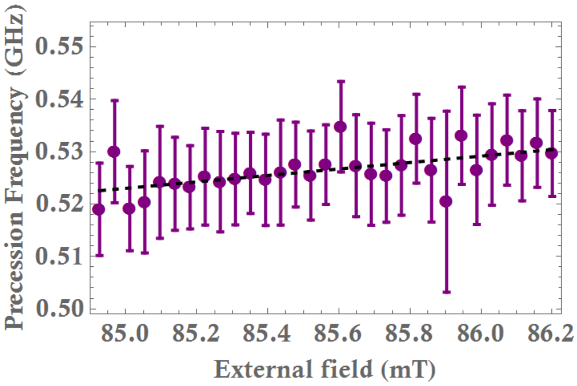

Figure 6.12: Relationship between B_{ext} and the precession frequency of the electron spin of charged QD 1 (fine scan). The purple circles show the experimental data and the black data shows the theoretical precession frequency of an electron spin with a g-factor of 0.437 with increasing B_{ext}.

data very well, despite the fact that we have attempted to change the precession frequency of the electron spin using the laser pulse train. This suggest that the pulse train has been ineffective. However, because the effect is so sensitive to changes in B_{ext}, we try implementing a very fine scan over a much smaller range of B_{ext}.

In this fine scan, we increase the value of B_{ext} from 84.9mT to 86.2mT in increments of 42.4μT, again applying σ^- pulses after each iteration of B_{ext}. This range is such that according to the model given in Chapter 2, we should scan through at least one point where the nuclear spin bath takes on a single configuration, meaning that we would hope to see some change in the electron spin precession. The output of this measurement is shown in Fig. 6.12. However, we find that, although the data is noisy, there don't seem to be any obvious points at which the precession frequency is changed by increasing B_{ext} after pulsing the system with σ^- pulses. Examining the visibility graphs does not show any unusual behaviour and we conclude that for this QD, we cannot see any nuclear spin polarisation effects. The precession frequency of charged QD 1 looks very clean and stable, and it is possible that once in a stable configuration, it is difficult to perturb the system, due to the nuclei being in a preferred state. We also tried turning off the external field and turning it back on to the same value, however, this still did not give any change (see Fig. 6.13). If the stability were due to nuclear spin effects, we would expect that resetting B_{ext} would result in a changed precession of the electron spin, which we have not observed. We will assume that the protocol was ineffective for this particular QD and move onto charged QD 2. It is possible that the evolution of this electron spin is non-Markovian because the short envelope coherence (T_2^*) leads to a short T_2 time, meaning that the time it takes for the electron spin to reach its stable state becomes longer. As we saw in Chapter 2, if the electron spin takes too long to reach its steady state, the Markovian approximation is no longer valid, and in that case we wouldn't necessarily expect the protocol to be effective.

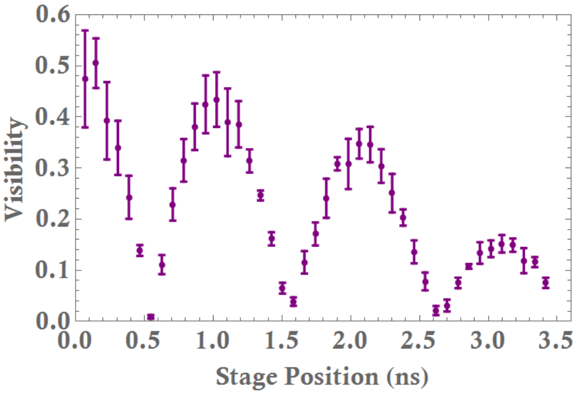

Figure 6.13: Visibility of charged QD 2 after turning off the external field and then turning it on again to the same value ($B_{ext} \approx 84.9$mT).

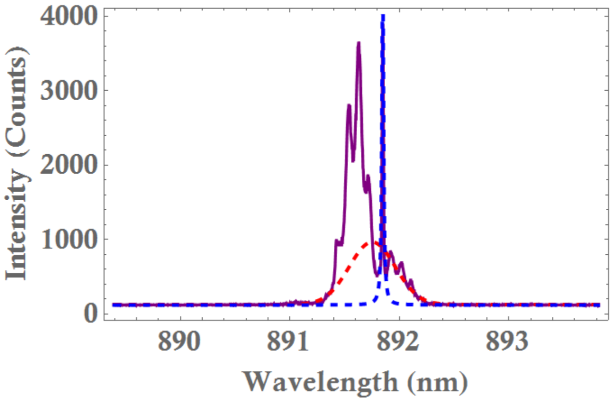

Figure 6.14: PL spectrum of charged QD 2 showing the detuning of the pulse acting on the QD. The power of the Ti:S laser is ≈ 1μW and the CW single frequency laser is at a power of 250nW. The red dotted line shows a hyperbolic secant fit to the pulse and the blue dotted line shows a Lorentzian fit to the QD. We measure $\Delta = 0.113 \pm 0.007$.

6.3.2 Charged QD 2

This section will focus on results obtained from charged QD 2. We focus on the result of a fine scan over B_{ext} (again from 84.9mT to 86.2mT in steps of 42.4μT). For this measurement, we have detuned the pulse such that it is on the blue side of the QD, with the QD at approximately the half maximum and we apply σ^+ pulses at a power of 1.2μW (just below saturation power). The PL spectrum of charged QD 2 acted on by these pulses is shown in Fig. 6.14. The QD can be seen clearly as the sharp spike at ≈ 891.85nm. As before, we fit the pulse and QD with a hyperbolic secant and Lorentzian respectively. We should note here that this pulse cannot be accurately fitted due to the distortion of its shape where it overlaps with the QD, but the important measures are the central position and width, which can still be extracted with reasonable accuracy from this

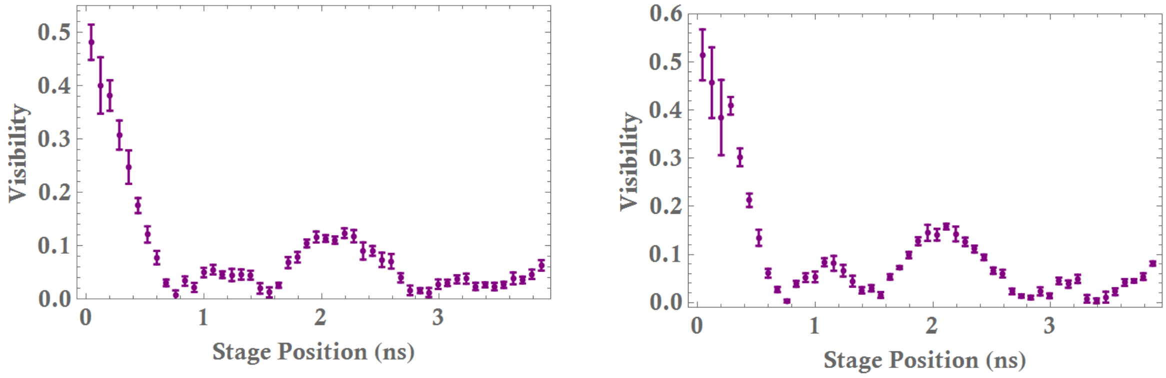

(a) Charged QD 2 before application of circularly polarised pulses with $B_{ext} \approx 84.9$mT at ≈ 4.3K.

(b) Charged QD 2 after application of σ^+ circularly polarised pulses with $B_{ext} \approx 84.9$mT at ≈ 4.3K.

Figure 6.15: Visibility from charged QD 2 (a) before and (b) after application of a train of circularly polarised pulses.

fit. Here, we calculate $\Delta = 0.113 \pm 0.007$. We first show, as for charged QD 1, how the application of σ^+ pulses gives variation in the visibility output for a fixed value of $B_{ext} \approx 84.9$mT. This is shown in Fig. 6.15. Here we do see some small differences between the two graphs. The most noticeable is that the small peak between the two larger peaks is much more pronounced after the pulses have been applied than before. We also measure a small change in the precession frequency, from $\omega_{eff} = 0.268 \pm 0.006$ before application of the pulses to $\omega_{eff} = 0.271 \pm 0.007$ after application of the pulses, but these are equal within the error of the measurements. These changes are not significant enough on their own to draw any conclusions about the application of the pulses, however, it is more promising than the results seen for charged QD 1. We will now show the results we find when increasing the value of B_{ext} in increments of 42.4μT. In this case, the data does not fit to an absolute sine graph, and we instead fit each of the minima using the parabolic function $a(x+b)^2 + c$. The power of the Ti:S laser was set to be $\approx 1.2\mu$W (just below saturation as before) with the pulse detuned so that the QD resonance is approximately at the half maximum of the pulse on the blue side.

These results show a definite deviation from the theoretical trend we expect to see. We find that initially the trend of the experimental data matches the theoretical model quite closely, however at $B_{ext} \approx 85.4$mT, there is a clear drop in the precession frequency away from this theoretical model (see Fig. 6.16). Towards the end of the scan, the data begins to return to the expected trend. We analyse the area in which the drop in precession frequency first begins. We find that between $B_{ext} \approx 85.39$mT and $B_{ext} \approx 85.44$mT (neighbouring data points) there is a clear difference in the visibility measurements. This is shown in Fig. 6.17. We can see that the small second peak in Fig. 6.17(a) has been completely suppressed, the total visibility has increased and the precession frequency has altered in Fig. 6.17(b). The origin of the small second peak is unclear, however, it doesn't seem to be part of the coherent precession we expect to see from the

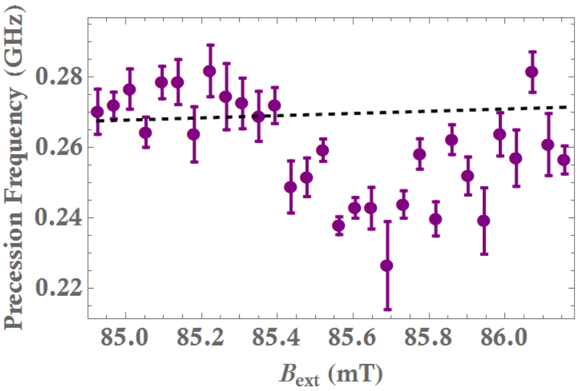

Figure 6.16: Relationship between B_{ext} and the precession frequency of the electron spin of charged QD 2 (fine scan). The purple circles show the experimental data and the black line shows the theoretical precession frequency of an electron spin with a g-factor of 0.225 with increasing B_{ext}.

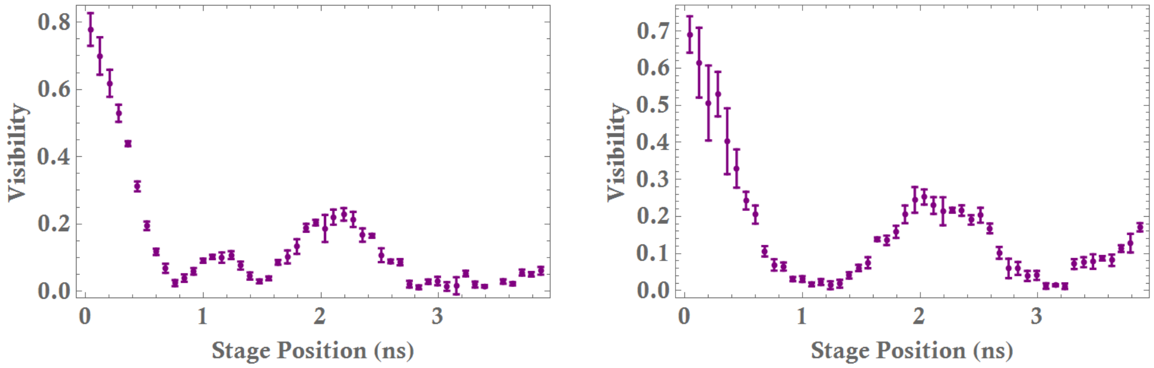

(a) $B_{ext} \approx 85.39$mT

(b) $B_{ext} \approx 85.44$mT

Figure 6.17: Visibility measured from charged QD 2 at (a) $B_{ext} \approx 85.39$mT and (b) $B_{ext} \approx 85.44$mT after application of σ^+ pulses. The Ti:S power is $\approx 1.2\mu$W, the CW single frequency laser power is ≈ 0.5nW and the temperature is ≈ 4.3K.

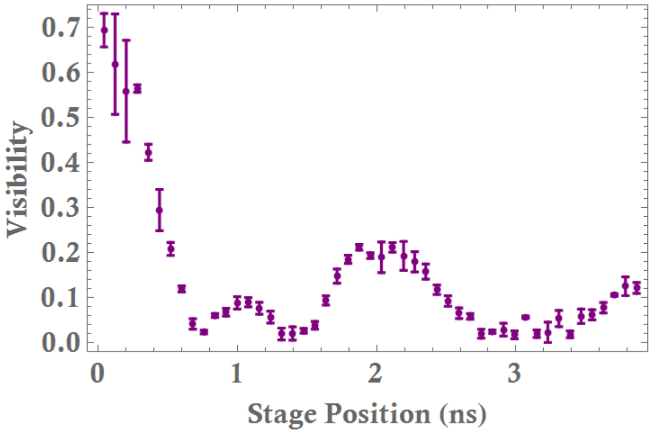

Figure 6.18: Visibility measured from charged QD 2 at $B_{ext} \approx 85.44$mT before application of σ^+ pulses. The CW single frequency laser power is ≈ 0.5nW and the temperature is ≈ 4.3K.

electron spin. Suppressing this peak gives a precession that is cleaner and looks more coherent. It is important at this point to compare these results to results obtained when no pulses have been applied to the system. Due to time constraints, we do not have a full data scan before application of pulses, however, Fig. 6.18 shows the visibility measurement taken for charged QD 2 before application of the σ^+ pulses at a field of $B_{ext} \approx 85.44$mT (the field where we see a change after application of the pulses). Here, we see that the second peak observed in the lower field measurements is visible in this measurement and has not been suppressed, as we see after application of the pulses. One possible reason that we see a small second peak in the data is that there are two nuclear spin configurations that the system is oscillating between and this manifests as a beating between two frequencies. In this case, the two frequencies would be the two lines seen in Fig. 6.21, which will be discussed later.

Using techniques described in Chapter 2, we can model the possible values of m that these parameters should induce into the system and this is plotted in Fig. 6.19. The value of B_{ext} where we observe a change in precession frequency is $B_{ext} \approx 85.44$mT and the minimum precession frequency (0.226 ± 0.01GHz) is measured at 85.68mT. At this point, in Fig. 6.19, we find 4 possible nuclear spin bath configurations satisfying $P(m) \geq 0.001$. The values of m these correspond to are 28, −4, −68 and −100 and these have values $P(m) = 0.07$, 0.29, 0.51 and 0.09 respectively. We can then work out the precession frequency of the electron induced by the Overhauser field for each of these values of m using the equation

$$\omega_{OH} = \frac{mA}{2} \tag{6.5}$$

where ω_{OH} is the Overhauser precession frequency and we choose $A = 15$MHz as in Chapter 2. We find that these values are $\omega_{OH} = 0.21$, −0.03, −0.51 and −0.75GHz respectively (note that the negative sign corresponds to the direction of the field, such that the Overhauser field is in the

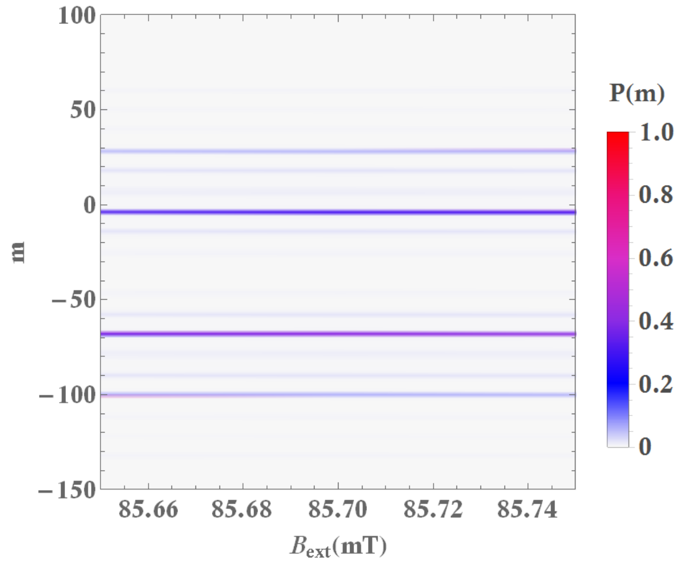

Figure 6.19: Theoretical prediction of the nuclear spin bath configuration found for a QD acted on by σ^- pulses with $g = 0.225$ with $\Delta = 0.2$, $\Omega = 0.6$ and $T_R = 12.47$ns.

opposite direction to the external field for a negative ω_{eff}). We can then use the equation

$$\omega_{eff} \quad = \quad \omega_e + \omega_{OH} \tag{6.6}$$

to determine the altered precession frequency that each of these values of m would induce. These values are $\omega_{eff} = 0.478$, 0.238, −0.257 and −0.482GHz respectively. One might expect that the altered precession frequency would correspond to a weighting of these precession frequencies. This weighted precession, W, can be calculated using

$$W = \sum_{i=1}^{N(m)} P(m_i)\omega_{eff,i} \tag{6.7}$$

where $N(m)$ is the number of modes as defined in Chapter 2 and $P(m_i)$ and $\omega_{eff,i}$ are the probabilities of particular modes occurring and the effective precession frequencies given by each of these possible modes. Plotting this as a function of B_{ext} gives the plot shown in Fig. 6.20. The range of B_{ext} between the black dotted lines is the range over which we take the data shown in Fig. 6.16. This does not match the values that we measure, however, the trend of the curve shown in Fig. 6.20 is similar to the trend of the curve we measure in Fig. 6.16. This could be showing that the effect we want is working, but on a smaller scale than predicted by the theory. However, we also consider the possibility that the nuclear spin bath could be shifting to the value of a single one of the available values of m, rather than a weighted maximum of them.

When we consider each of the precession frequencies individually, we find that the second of these, 0.238GHz, is equal, within error, to the minimum measured precession frequency of 0.226 ± 0.01GHz. This means that it is possible that the system has entered this stable

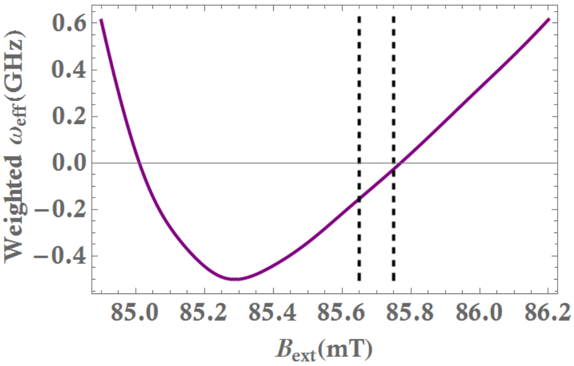

Figure 6.20: Variation in the theoretical weighted precession frequency as a function of B_{ext}. The black dashed lines show the range of B_{ext} over which we perform the NFF protocol. Here, we have $g = 0.225$, $\Delta = 0.113$ and $\Omega = 0.6$.

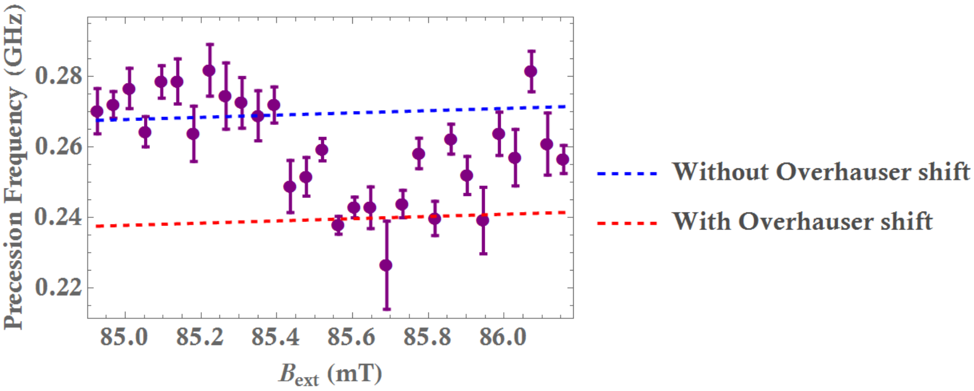

Figure 6.21: Relationship between B_{ext} and the precession frequency of the electron spin of charged QD 2 (fine scan). The purple circles show the experimental data, the blue line shows the theoretical precession frequency of an electron spin with a g-factor of 0.225 and the red line shows the theoretical precession frequency of an electron spin with a g-factor of 0.225 and an Overhauser shift of −0.03MHz.

configuration. Despite this not being the highest probability state, it still has $P(m) = 0.29$ and the fact that the system is closer to this state initially may play a role in this being the state that the system is forced into. In Fig. 6.21, we show the precession frequency as a function of B_{ext} as before, but this time we include the theoretical precession frequency of the electron spin if it were experiencing an Overhauser shift of $\omega_{OH} = -0.03$GHz (corresponding to $m = -4$), assuming a hyperfine coupling of $A = 15$MHz. We find that the data points that deviate from the expected theoretical precession frequency with no Overhauser shift appear to be shifted such that they follow the theoretical precession frequency due to the Overhauser shift induced by a nuclear spin configuration with $m = -4$.

We need to be able to show that this effect is repeatable, however, we find that when attempt-

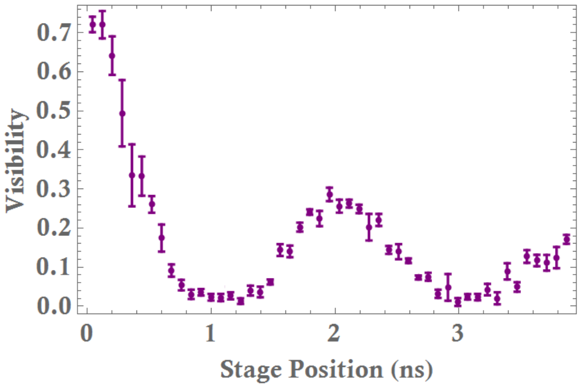

Figure 6.22: Visibility measured from charged QD 2 at $B_{ext} \approx 84.9$mT after we see a change and attempt to repeat the measurement. The CW single frequency laser power is ≈ 0.5nW and the temperature is ≈ 4.3K and we do not apply any σ^+ pulses.

ing to repeat the measurements without application of the σ^+ pulses, the precession does not change back to the visibility measurements we saw before any pulses had been applied to the system, i.e. the second peak remains suppressed. The second peak is now also suppressed at lower fields, i.e. if we return to the first measurement, $B_{ext} \approx 84.9$mT, this also has a precession where the small second peak is suppressed (see Fig. 6.22). This is possibly due to the system finding a stable configuration and perturbation from this configuration becomes difficult. We therefore need to find a way to "reset" the electron spin precession to its original state. We expect that application of linear pulses to the system will destroy any polarisation effects we have created, as this will drive both of the spin states of the electron simultaneously. However, we find that after applying linear pulses, the system maintains the configuration shown in Fig. 6.17(b) with the small peak still suppressed. We also try changing the value of B_{ext} significantly - we increase the value of the field up to $B_{ext} \approx 127$mT, turn the field to 0 and finally back to ≈ 84.92mT. However, even after all of these processes, we do not manage to change the electron precession back to its original state (see Fig. 6.23). Finally, we leave the CW single frequency laser on low power for ≈ 10 hours (overnight) and measure the precession frequency of the electron again. This time, we see a significant difference, with the visibility shown in Fig. 6.24 for $B_{ext} \approx 84.92$mT before application of any pulses.

This graph shows that the precession frequency is now much slower (we estimate the g-factor to be $g = 0.149 \pm 0.003$, an $\approx 50\%$ decrease) for the same value of B_{ext}. There is no clear explanation for why this is the case, as we have not tried to force the nuclei into any particular configuration and the external field is the same as the previous measurements, so it seems like this effect must be caused by the action of the CW laser. The other possibility is that the instability of the magnetic field (this is stable on the order of μT) is allowing the system to choose a different nuclear configuration when B_{ext} changes slightly, but this seems unlikely, as we do not see this changing dramatically when changing the field in small increments. It is possible

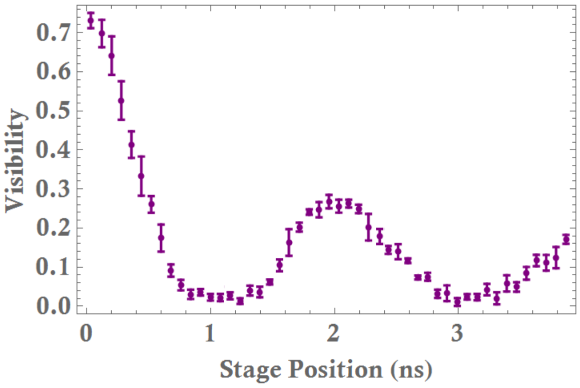

Figure 6.23: Visibility measured from charged QD 2 at $B_{ext} \approx 84.9$mT after an attempt to reset the nuclear spin configuration. The CW single frequency laser power is ≈ 0.5nW, the temperature is ≈ 4.3K and we do not apply any σ^+ pulses.

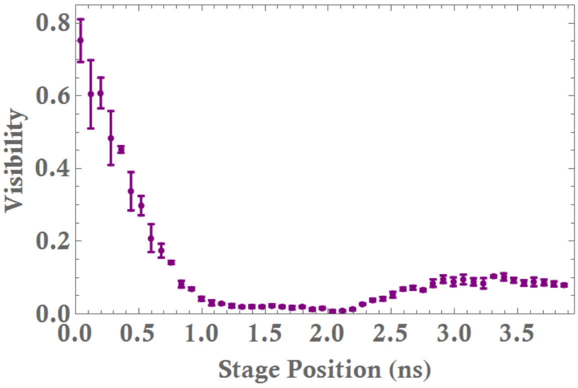

Figure 6.24: Visibility measured from charged QD 2 at $B_{ext} \approx 84.9$mT after leaving a CW probe laser at ≈ 0.5nW for ≈ 10 hours. The temperature is ≈ 4.3K and we do not apply any σ^+ pulses.

that the electron spin that we have measured previously has been in some configuration with a non-zero value of B_{OH}, and the application of linear CW light over such a long timescale has disturbed the nuclear stability such that the precession we see is due to B_{ext} only. The new precession frequency of the electron spin is $\omega_{eff} = 0.229 \pm 0.007$, which corresponds to a change in the electron g-factor of ≈ 0.135, (close to half of the original g-factor). We are not sure of the origin of this effect, however, it is unlikely that the g-factor of the QD could change by this amount without some external factor, which we assume to be the action of the CW linearly polarised single frequency laser that was exposed to the system for ≈ 10 hours. It is possible that the laser destroyed some polarisation of the nuclei that was present in the initial state we measured for this particular QD, meaning that the measurements shown in Fig. 6.24 give the g-factor of the QD with an overall nuclear polarisation of 0. However, we address this new precession with σ^+ pulses but now find no changes (see Fig. 6.25).

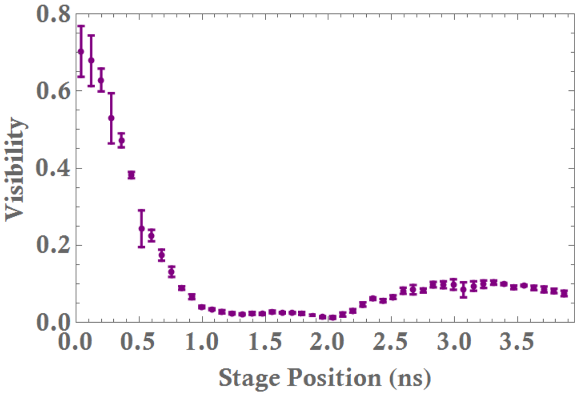

Figure 6.25: Visibility measured from charged QD 2 at $B_{ext} \approx 84.92$mT after leaving a CW probe laser at ≈ 0.5nW for ≈ 10 hours and then applying σ^+ pulses for ≈ 2 minutes. The temperature is ≈ 4.3K and we do not apply any σ^+ pulses.

We can conclude that for charged QD 2, by acting some external field B_{ext} on the system, we can produce a g-factor that differs from what we expect, and corresponds to the theoretical predictions for the nuclear spin configurations in the NFF protocol. However, we cannot show that this measurement is repeatable or return to the original conditions before the measurement was performed. We believe that some nuclear spin effects are happening, but these are unpredictable and hard to quantify in this particular QD.

6.3.3 Charged QD 3

For charged QD 3, we consider other ways to change the precession of the electron spin, rather than changing the value of B_{ext}. We show measurements where we apply both σ^+ and σ^- pulses and vary the power of these pulses whilst keeping a fixed detuning. We would expect to see a large variation in the outputs of the visibility measurements if we change from σ^+ pulses to σ^- pulses, as one of these should give a single stable nuclear spin configuration, while the other should give more than one stable configuration, depending on the direction of the detuning. We also vary the direction of the detuning by realigning the pulse between measurements. A PL spectrum is shown for the detuning of the pulse to both the blue and red side of the pulse in Fig. 6.26. Here, we show the hyperbolic secant fit to the pulses with a red dashed line, however, in this case, we are not able to fit the QD, due to the low intensity of the QD, and therefore we plot a blue dashed line to indicate the position of the QD. We measure the detuning of the pulses to be $\Delta = 0.22 \pm 0.009$ and $\Delta = 0.27 \pm 0.008$ for blue and red detuning respectively. This particular QD requires a Ti:S power of $\approx 1.7\mu$W to be just below the saturation power and all of the measurements shown will be at $B_{ext} \approx 106.2$mT. The visibility measurement for charged QD 3 before application of any pulses is shown in Fig. 6.7. We show this measurement again in Fig. 6.27(a) and Fig. 6.27(b) shows the same measurement after application of σ^+ pulses that are

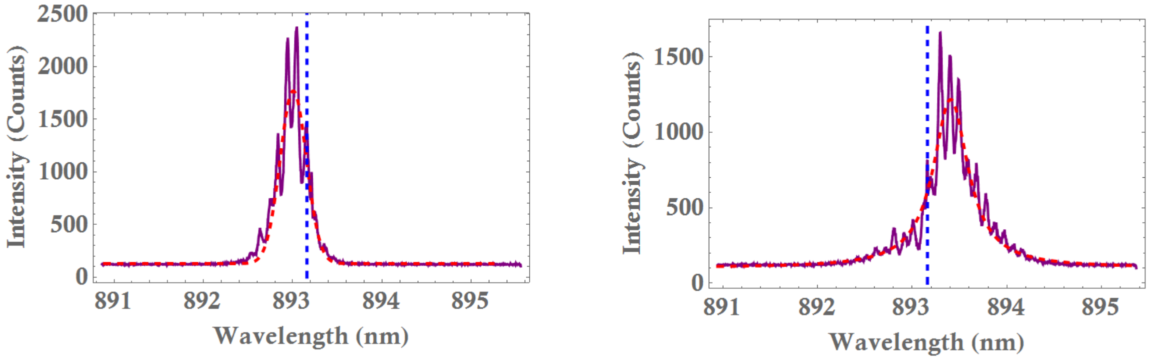

(a) PL spectrum of charged QD 3 with the pulse on the blue side of the QD with $B_{ext} \approx 106.2$mT. The red dotted line shows a hyperbolic secant fit to the pulse and the blue dotted line shows the position of the QD. We measure $\Delta = 0.22 \pm 0.006$.

(b) PL spectrum of charged QD 3 with the pulse on the red side of the QD with $B_{ext} \approx 106.2$mT. The red dotted line shows a hyperbolic secant fit to the pulse and the blue dotted line shows the position of the QD. We measure $\Delta = 0.27 \pm 0.008$.

Figure 6.26: PL spectra of charged QD 3 with the pulse at approximately the half maximum on (a) the blue side of the QD and (b) the red side of the QD. The power of the Ti:S laser is $\approx 1.7\mu$W. The temperature of the system is ≈ 4.3K. The black dashed line shows the position of the QD.

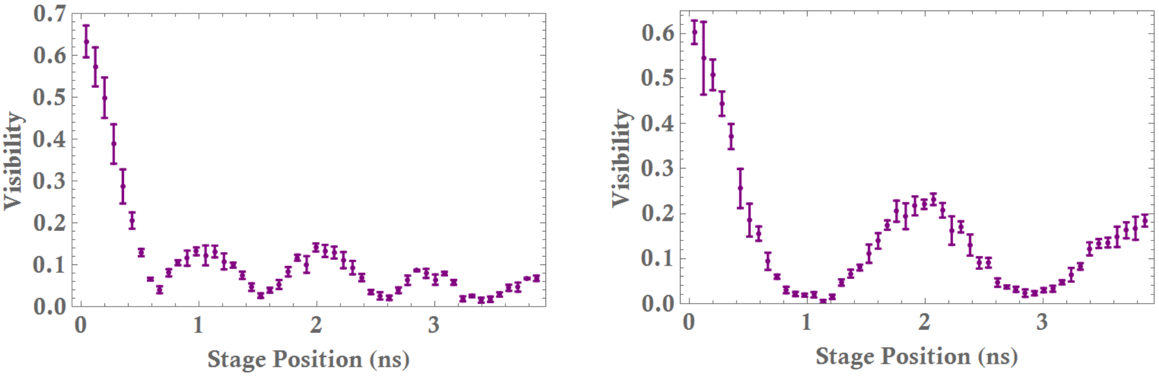

(a) Charged QD 3 before application of circularly polarised pulses. The parameters used are $B_{ext} \approx 106.2$mT and the power of the CW laser is 0.5nW.

(b) Charged QD 3 after application of σ^+ circularly polarised pulses detuned to the blue side of the QD resonance. The parameters used are $B_{ext} = 106.2$mT and the power of the CW laser, 0.5nW.

Figure 6.27: Visibility measurements (a) before and (b) after application of σ^+ pulses with $B_{ext} \approx 106.2$mT, Ti:S power of $\approx 1\mu$W, CW probe laser power of ≈ 0.5nW and temperature of ≈ 4.3K.

detuned to the half maximum on the blue side of charged QD 3 for ≈ 2 minutes. In this case, we again fit each of the minima using the parabolic function $a(x+b)^2 + c$ as described above.

We see a dramatic change in the precession frequency of the electron spin between these two measurements. Before application of the pulses, we estimated the precession frequency to be $\omega_{eff} = 0.576 \pm 0.007$GHz, whereas after the application of σ^+ pulses, the new precession

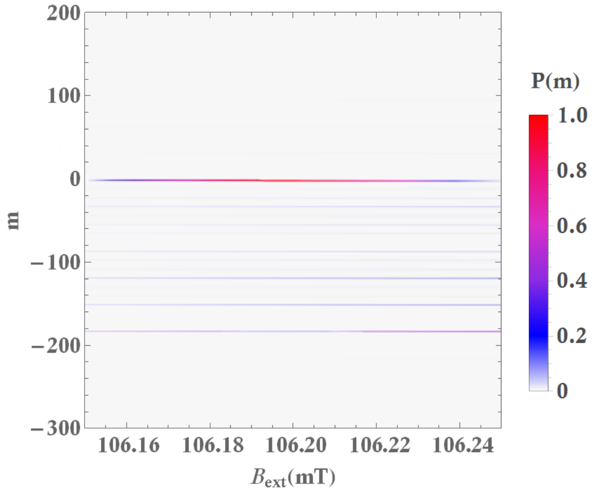

Figure 6.28: Theoretical prediction of the nuclear spin bath configuration found for a QD acted on by σ^+ pulses with $g = 0.338$, $\Delta = 0.2$, $\Omega = 0.6$, $A = 15$MHz and $T_R = 12.47$ns.

frequency is calculated to be $\omega_{eff} = 0.290 \pm 0.005$GHz, close to half of the original precession frequency. This is equivalent to a change in field of ≈ 60.8mT. This is the type of effect we hope to see when attempting to polarise the nuclear spin bath, as we appear to have successfully slowed down the precession of the electron spin. We also see a small peak between the first and second peaks, showing that again we might have two beating modes for the nuclear configuration. We now want to compare this to the theoretical prediction to see whether the result we find is the expected nuclear spin configuration. The theoretical model is shown in Fig. 6.28. If we assume the change in precession frequency between the results taken before and after the application of the pulses is ω_{OH}, we can calculate the value of m that would give this value of ω_{OH} using the equation

$$m = \frac{2\omega_{OH}}{A}. \tag{6.8}$$

For $\omega_{OH} = 0.286$GHz (the difference between the two precession frequencies measured), we calculate $m = -38$, using as always $A = 15$MHz. However, this does not correspond to any of the regions where $P(m)$ is high (see Fig. 6.30). It is, however, close to one of the low probability modes we see, with $m = -42$. It may be the case that the value of A we have chosen is not correct, and we find that if we instead choose $A = 13.6$MHz, we get the plot shown in Fig. 6.29. This has a mode with the correct value of m, although this mode should happen with very low probability ($P \approx 0.0022$). We can't therefore say for sure whether the protocol has worked effectively, but it seems as though the spin bath may have taken on this configuration. We also plot the weighted precession frequency in Fig. 6.30. We find again that this does not correspond to the precession frequency we measure. There are many reasons that the measurements we see would not match the theoretical predictions exactly, for example, we choose the total number of nuclei to be 100000

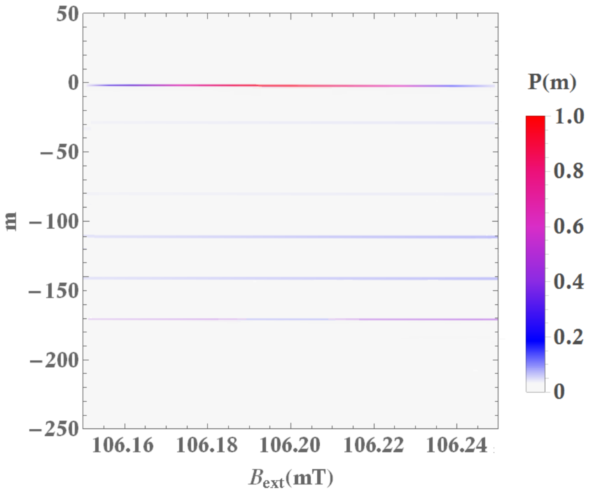

Figure 6.29: Theoretical prediction of the nuclear spin bath configuration found for a QD acted on by σ^+ pulses with $g = 0.338$, $\Delta = 0.2$, $\Omega = 0.6$, $A = 13.6$MHz and $T_R = 12.47$ns.

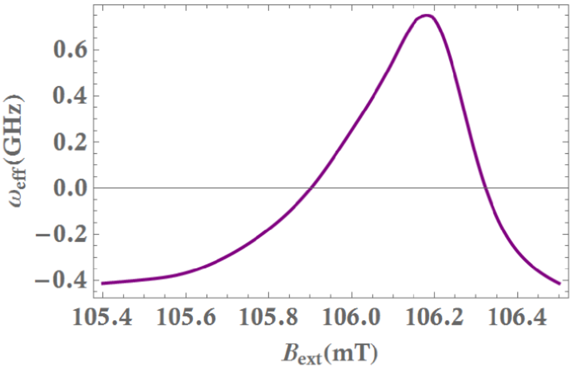

Figure 6.30: Change in weighted precession frequency of charged QD 3 as a function of B_{ext}. Here, $g = 0.338$, $\Delta = 0.274$, $\Omega = 0.6$ and $A = 13.6$MHz.

and $A = 13.6$ or 15MHz, meaning that if this particular QD has parameters that are not close to these, it could show significantly different results. It is also possible that the original g-factor measured is not the true g-factor if the precession frequency of the electron spin is altered by the nuclei in the state we measure before application of the pulses. This could mean that the change in precession frequency we measure is not entirely accurate, as we would be modeling the incorrect g-factor.

However, if we are able to show repeatability in these measurements, it seems clear that there is an effect induced by applying a certain type of pulse to the system. We therefore pulse the system again, but this time with σ^- pulses, which we expect to induce a significant change in the precession. We also realign the pulses to be on the red side of charged QD 3 and pulse the system with σ^+ pulses (this should have the same effect as pulsing with σ^- pulses with the pulse on the

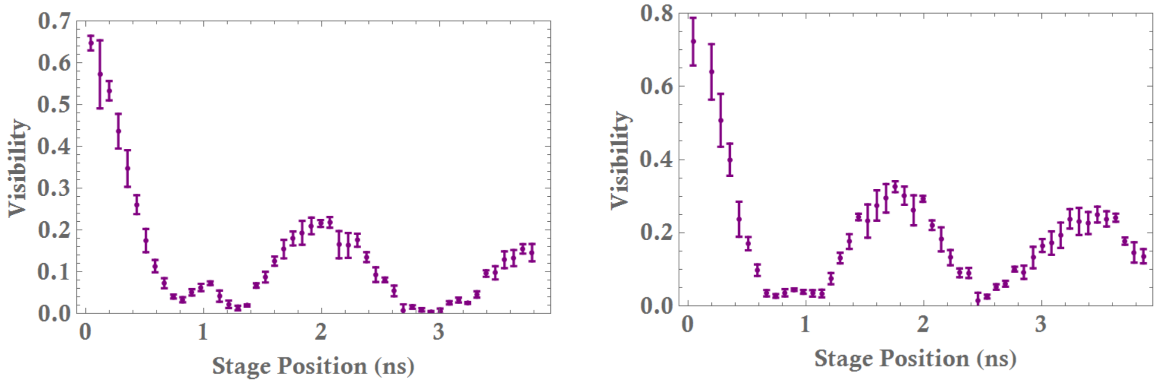

(a) Charged QD 3 after application of σ^- circularly polarised pulses detuned to the blue side of the QD resonance.

(b) Charged QD 3 after application of σ^+ circularly polarised pulses detuned to the red side of the QD resonance.

Figure 6.31: Visibility measurements (a) after application of blue-detuned σ^- pulses and (b) after application of red-detuned σ^+ pulses with $B_{ext} \approx 106.2$mT, Ti:S power of $\approx 1\mu$W, CW probe laser power of ≈ 0.5nW and temperature of ≈ 4.3K

blue side). We hope to see further changes to the electron spin precession by performing these measurements. The output of each of these measurements is shown in Fig. 6.31. The precession frequency of the measurement shown in Fig. 6.31(a) is given by $\omega_{eff} = 0.293 \pm 0.007$GHz and that of the measurement shown in Fig. 6.31(b) is $\omega_{eff} = 0.332 \pm 0.007$GHz. The first of these is within the error of the precession frequency of the measurement shown in Fig. 6.27(b) and so we conclude that there is no change, however, the second shows an increase in precession frequency of $\approx 15\%$. However, we find that, as with the previous measurement, this does not correspond to the theoretical model for this particular parameter set (see Fig. 6.32) and so we are unable to conclude that the NFF protocol is being successfully implemented.

Next, we try again to reverse the effect of the pulses. This time, we apply red-detuned σ^+ pulses but at a much higher power of $\approx 10\mu$W and leave these pulses pumping the system for ≈ 15 minutes, compared to the usual ≈ 2 minutes. The result of this is shown in Fig. 6.33. We can see that the precession frequency has again decreased and is now $\omega_{eff} = 0.280 \pm 0.07$GHz. This is now back to being (within error) the same precession frequency as the precession frequency of the measurements given in Figs. 6.27(b) and 6.31(a). It is difficult to see why this is, but it is possible that this is the precession frequency of the QD when there is no polarisation of the nuclei, i.e. the total Overhauser field is 0. This would mean that there was an initial nuclear polarisation before we applied any pulses to the system, increasing the precession frequency of the electron spin. This is possible as we do not know the initial state of the nuclear spin bath and are not able to measure this. However, we are still not able to reset the electron spin back to the original state we find in Fig. 6.27(a). This means that we are not able to perform the same measurements again to assess the repeatability of the process. We are not then able to confirm

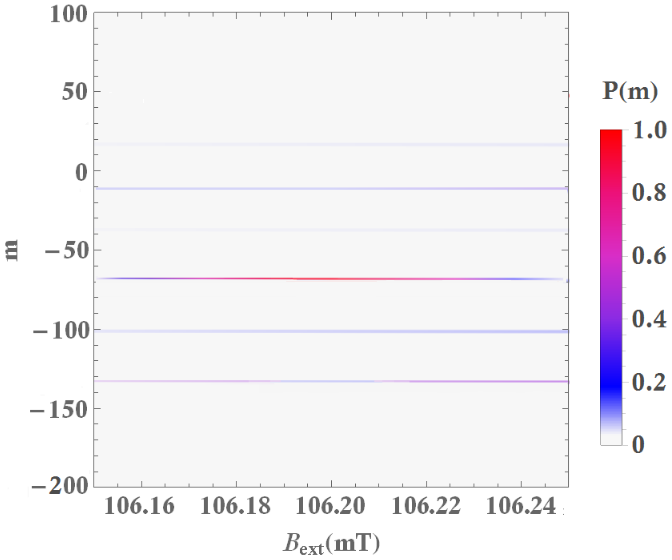

Figure 6.32: Theoretical prediction of the nuclear spin bath configuration found for a QD acted on by σ^+ pulses with $g = 0.338$, $\Delta = -0.2$, $\Omega = 0.6$ and $T_R = 12.47$ns.

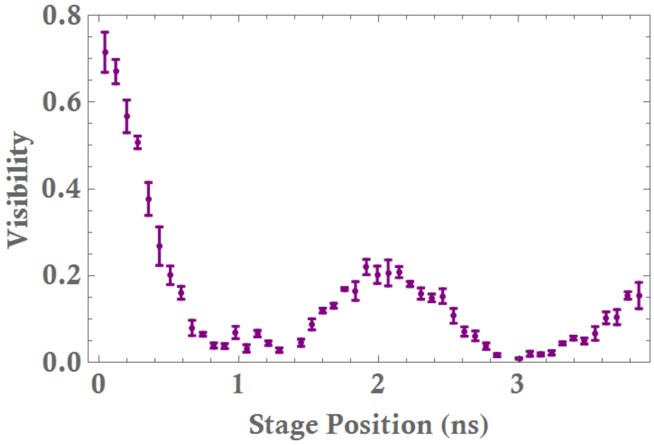

Figure 6.33: Charged QD 3 after application of σ^+ circularly polarised pulses for ≈ 15 minutes detuned to the red side of the QD resonance.

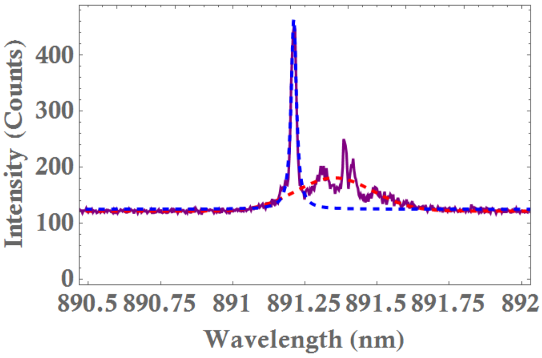

Figure 6.34: PL spectrum of charged QD 4 showing the detuning of the pulse acting on the QD. The power of the Ti:S laser is ≈ 170nW. The red dotted line shows the hyperbolic secant fit to the pulse and the blue dotted line shows the Lorentzian fit of the QD. The detuning is measured to be $\Delta = 0.225 \pm 0.005$.

whether the change in precession frequency is moving the electron spin into a stable state or not. It is also possible that application of several different pulses has reduced the amount of polarisation of the nuclei, rather than increasing it, such that the precession has become less coherent. However, we do show that this particular electron seems to have a preference for a particular precession frequency of ≈ 0.290GHz, despite this not being the original state of the system when it was measured before application of any laser pulses. This is possibly a stable configuration of nuclei but we are not able to confirm this with the theoretical predictions.

6.3.4 Charged QD 4

The final QD we consider is charged QD 4. As discussed above, this QD has a much longer coherence time than the other QDs we consider and we therefore use the fibre delays to show the recurring visibility fringes. The PL spectrum of charged QD 4 acted on by a pulse is shown in Fig. 6.34 and we can see the QD resonance at ≈ 891.2nm at approximately the half maximum of the pulse. Fig. 6.34 shows the fitting of the pulse to a hyperbolic secant and the Lorentzian fit of the QD. From this, the detuning, Δ, is measured to be $\Delta = 0.225 \pm 0.005$. In Fig. 6.35, we show the precession of charged QD 4 before and after application of laser pulses. In this case, we use σ^- pulses as these pulses are on the red side of charged QD 4 with a laser power of ≈ 170nW and apply them to the QD system for 2 minutes. In this case, the data is fitted using the parabolic function $a(x+b)^2+c$, however, in this case, we use the maxima rather than the minima, as the minima fall in the gaps caused by the fibre mismatch. We see that the most pronounced difference between these two measurements is in the visibility, i.e. the minimum value of the visibility is much lower and the oscillations are clearer. There also appears to be a small peak between the first two large peaks that has appeared upon application of the laser pulses, possibly again showing a beating between two nuclear spin configurations, although the fibre mismatch is

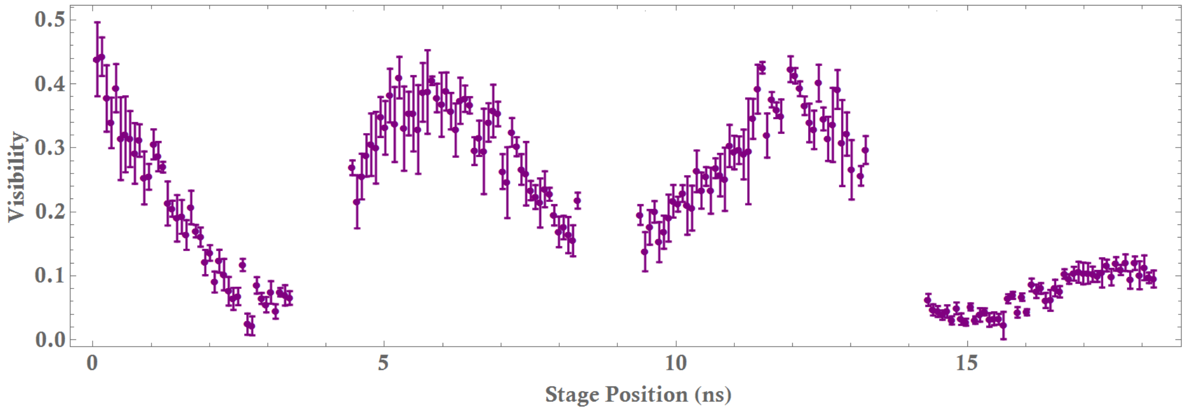

(a) Charged QD 4 before application of laser pulses.

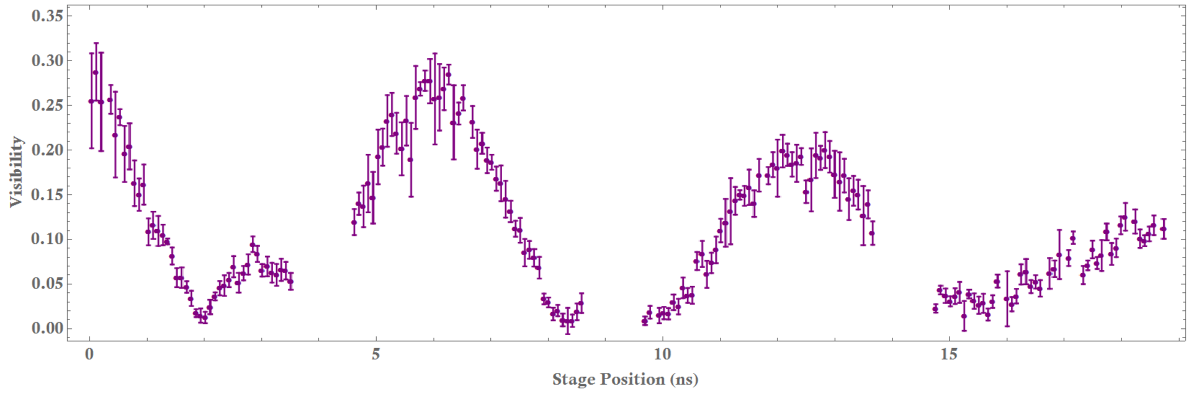

(b) Charged QD 4 after application of σ^- laser pulses.

Figure 6.35: Visibility measurements (a) before and (b) after application of red-detuned σ^- pulses with $B_{ext} \approx 84.9$mT, Ti:S power of $\approx 1\mu$W, CW probe laser power of ≈ 0.5nW and temperature of ≈ 4.3K

positioned such that this is ambiguous.

Most interestingly, when we calculate the distance between the first and third peak (i.e. the time taken to perform a precession about the full Bloch sphere), we find that after application of the laser this gives a stage position of 12.47 ± 0.01ns compared to the 12.39 ± 0.01ns we calculate before application of the laser pulses. This is significant because 12.47ns is the repetition rate of the laser pulses. This means that the precession frequency of the electron spin appears to have synchronised with the repetition rate of the laser pulse, i.e. $\omega_{eff} = \frac{2n\pi}{T_R}$. This is not a large change in precession frequency, but it may be a result of the natural precession frequency of charged QD 4 being close to the repetition rate of the laser that makes it possible to synchronise the electron spin with this repetition rate, i.e., we do not have to change the precession frequency very significantly and so this change is more easily implementable. We calculate in Chapter 2 that synchronisation of the precession frequency with the laser repetition rate requires laser pulses

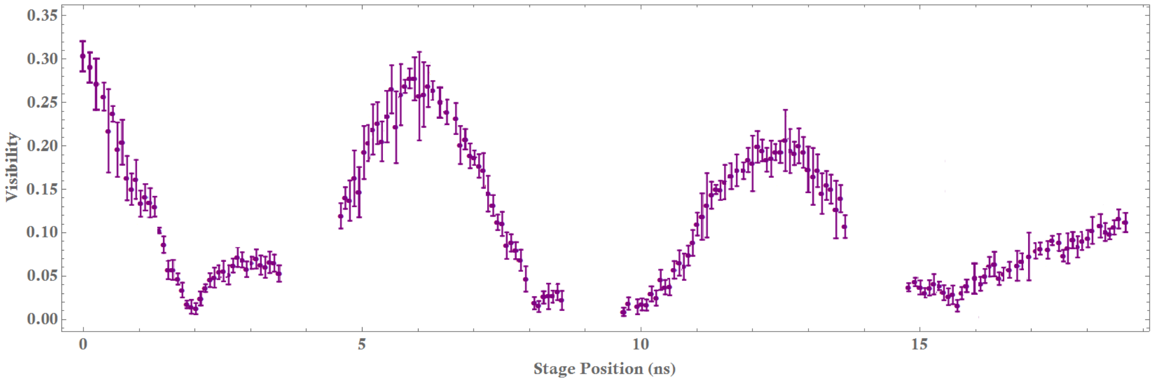

Figure 6.36: Charged QD 4 after application of σ^+ pulses and attempting to reverse the effect of the pulses by applying different sizes of B_{ext}.

that are on resonance with the QD, however, we show that the pulses we use are detuned to approximately the half maximum. Once again, we find that attempting to change this precession after the first implementation of pulses by applying linear pulses and changing the value of the external field from $B_{ext} \approx 84.9$mT to $B_{ext} \approx 42.5$mT and back to $B_{ext} \approx 84.9$mT is not possible and the precession remains the same to within error after implementation of the additional pulses and changes in B_{ext} (see Fig. 6.36). From this, we are unable to conclude what the effect of the pulses is and whether the nuclear spin effects we believe could be occurring are repeatable.

6.4 Summary

In this chapter, we have discussed a range of results taken using a time delay interferometer for different charged QDs. We have given a reliable method for confirming whether a particular QD is neutral or charged and measured the coherence time of the excess electron contained within four charged QDs. For each of these charged QDs, we have also shown implementations of the NFF protocol that have worked with varying success. Charged QD 1 did not show any changes that could be attributed to nuclear spin effects and was extremely stable. However, charged QD 2 showed some interesting changes in precession frequency after application of driving pulses with some correspondence to the theoretical predictions. However, we were unable to reverse these effects and therefore couldn't repeat the measurement, as the electron spin precession seemed to become "stuck" in the altered state. Similarly, charged QD 3 showed some changes in precession due to changes in the detuning and power of the driving pulses applied to the system, but once again this seemed to be an irreversible effect. Charged QD 4 showed that pulsing the system with detuned pulses seemed to induce the synchronisation condition between the repetition rate of the laser and the electron spin precession ($\omega_{eff} = \frac{2n\pi}{T_R}$).

It is possible that the reason we do not see the nuclear spin effects reliably between QDs is due to the instability of the nuclear spin configuration. In Chapter 2, we gave an expression

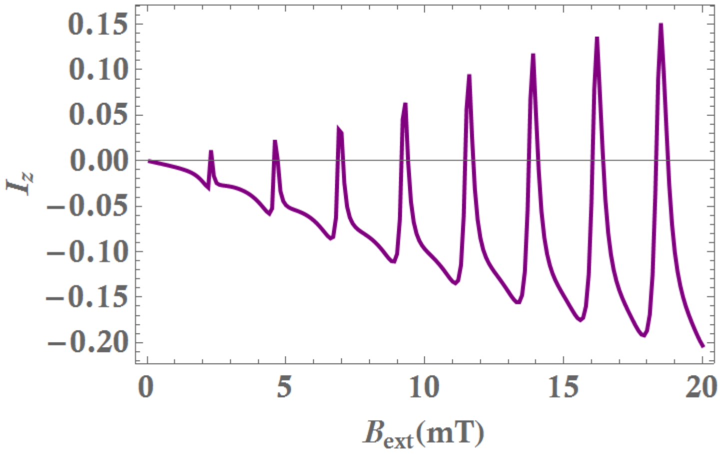

Figure 6.37: Plot of the nuclear polarisation, I_z, as a function of B_{ext}, with a g factor of $g = 0.25$, detuning, $\Delta = 0.2$ and Rabi frequency $\Omega = 0.6$.

for the steady state of a single nuclear spin coupled to an electron spin after application of the NFF protocol. This was of the form $I = (1, 0, 0, I_z)$ and we gave the explicit expression for I_z in the appendix. If we plot I_z as a function of B_{ext} for the detuning and Rabi frequency that we have used throughout the modeling in this thesis, we find the plot in Fig. 6.37. Here, we see that there are sharp peaks in the values of I_z in relation to B_{ext}. This shows that the nuclear spin configuration is inherently unstable and to achieve a high amount of nuclear polarisation, we require high accuracy in our value of B_{ext}.

We conclude that charged QD 1 exhibits no nuclear spin polarisation effects, whereas charged QDs 2-4 all show effects that could be a result of nuclear spin polarisation, although only charged QD 2 exhibits results that correspond to the theoretical predictions. A common problem between the results is that we are unable to reverse the effect of the pulses we apply. The electron spins appear to be driven into a particular stable state which we are not able to reset. To reach any meaningful conclusions, we would need to establish a method of resetting the electron precession to its original state, however, it is not clear why application of linear pulses does not achieve this. In addition to this, some of the results found show unexpected deviations from the theoretical model, for example the synchronisation of the precession frequency of the excess electron in charged QD 4 with the repetition rate of the laser pulses. It is also possible that, particularly for charged QD 1, the effect might be working on shorter timescales than we expect, meaning that in the time that we switch between the pulse setup and the probe setup, the change in precession frequency is lost and the results we see are no longer the fully polarised states we expect. We are not able to probe the system whilst pumping, due to the high power of the pulses compared to the probe and the fact that we need to rotate the QWP between the pumping and the measurement. Currently, it appears that the necessary next step is to solve the problem of resetting the electron precession frequency back to its original state, such that we can test whether the results are repeatable.

CHAPTER 7

CONCLUSIONS AND FURTHER WORK

This chapter will summarise the results obtained from each of the previous chapters, and discuss further research into the topics discussed. The focus of this work is on control and manipulation of the complex environment of an InGaAs QD for quantum information processing applications. We discuss the NFF protocol at length - this is a protocol that forces nuclear spins in the environment of the QD into alignment along the axis of a magnetic field, thus suppressing the hyperfine interaction and allowing the electron spin to precess coherently. We transform this from a theoretical model into an experimental proposal and outline the experimental parameters we need to control, showing that the requirements on these parameters are within practical constraints. In addition to this, we discuss the isolation and manipulation of single nuclei within the environment of an InGaAs QD. We show that the quadrupolar Hamiltonian dictates the spread of values of the nuclear frequencies, and that by considering various strain distributions in a QD, we can locate a nucleus that is sufficiently far in frequency from its neighbours that we may address it independently with a RF pulse. We design the RF pulse such that the target nucleus is rotated into the perpendicular plane to the remainder of nuclear spin bath, into the same plane as the electron spin. The small rotations that the neighbouring nuclei will experience due to the RF pulse are shown to be insignificant in most cases and we show that the effect of those nuclei that experience a significant rotation on the two-spin subsystem decreases with increasing detunings. We follow on from this by modeling the behaviour of the two-spin subsystem of electron and target nucleus, first in the absence of the prepared nuclear spin bath. We show that the hyperfine coupling between the electron and nucleus induces an evolution that periodically creates maximal entanglement between the electron and nucleus in the form of a $\sqrt{\text{SWAP}}$ gate and show how the decoherence of the electron spin affects the fidelity of this entanglement. We discuss the applications of this system, and in particular, we outline a protocol for a nuclear spin quantum memory. This protocol details how one might encode the state of the electron in the state of the nucleus, which has a longer coherence time, and outlines how a photon can be used as an ancilla to perform a measurement to retrieve the state stored in the nucleus. The protocol requires an effective precession frequency of 0, which requires exploitation of the stable nuclear configuration we propose to create using NFF. We establish control over the size and direction of the Overhauser field, such that we are able to create a system in which the Overhauser field and external field effectively cancel each other out and the system behaves as if in zero field but with the nuclear spin bath in a controlled state. We also show that this model has the potential to be extended to a full quantum computation platform and give preliminary data motivating research in this area.

The experimental section of this thesis focuses on an implementation of the NFF protocol. We first show in Chapter 5 how we can use PL spectroscopy to perform a range of characterisation measurements on QDs to determine properties such as Q factor and lifetime. We show how adjusting the temperature of the QD can tune its resonant wavelength and give details of how this can be used to create maximum overlap between the cavity mode and the QD emission peak, thus improving the efficiency of the system. We also show how the power dependence of the QD emission peak on the intensity of the emission allows us to identify whether an emission peak represents an exciton or a biexciton. In Chapter 6, we design an interferometer that is able to measure the visibility of photons that have interacted with an electron spin in a negatively-charged QD. We use this to measure the precession frequency and g-factor of a range of QDs. We use this setup to measure the change in precession frequency of the electron spin both before and after attempting to implement the NFF protocol. We see a variety of different results for different QDs, with some showing potential success in the implementation of the NFF protocol. A clear problem with all of the data is the inability to reverse the effects of the protocol we implement, thus eliminating the possibility of repeating the measurements. Any effects we do see consist of small changes that are difficult to justify, however, charged QD 2 in particular shows a shift in precession frequency consistent with the nuclei aligning into a configuration predicted by the theoretical model. We conclude that there are nuclear spin effects present in the measurements we perform, but that these effects are inconsistent and do not always match the predictions. This could be due to the environment of different QDs varying significantly, such that our model is not representative of some of the QDs we discuss, i.e. the total number of nuclei could be far from the number we have chosen, or the average hyperfine coupling constant could be significantly different for the QD we are measuring.

The subject of this thesis could lead to several areas of research. From a theoretical perspective, we have given motivation for the model we use to be extended to a full QC model. There are many things to consider in the context of this model, including how the electron spin could be entangled to several nuclei in turn, how this electron-nuclear interaction could be turned on and off and how we could apply external quantum operations to the electron spin to alter the precession of the electron-nuclear subsystem in order to perform different quantum operations indirectly on the nuclear spins. Experimentally, the first hurdle is the difficulty in reversing the effects of the NFF protocol, in order to confirm that the nuclear spin bath can be repeatedly configured in the same way. It would also be beneficial to be able to force the nuclei into a configuration that induces a more drastic change in the precession frequency, particularly for the end goal of constructing a system where the Overhauser field is as strong as the external field. Currently, the only successful implementation of NFF we have observed (the results taken on charged QD 2) has been such that the stable configuration achieved only requires a very small change in precession frequency. It seems clear that the system is more likely to take on the configuration that requires the least change to its original behaviour, however, we need to find a way of achieving other configurations that give a larger deviation from the expected value. It could be possible to achieve this by pumping the QD with higher laser powers or for longer timescales. It is also worth considering whether it is possible to modify the experimental setup such that we can measure the precession frequency of the electron spin whilst simultaneously applying the driving laser pulses to the system. We have shown that the effect has a strong dependence on the QD we choose and its individual properties. This further motivates current research into designing QDs that have identical environmental properties. In summary, this work has motivated several areas of research expanding on the results already obtained. There is potential for QDs to be used as a full platform for QC and we show progress in controlling the environment of InGaAs QDs - a major difficulty that needs to be overcome if QDs are to become the platform of choice for quantum information processing applications.

APPENDIX A

APPENDIX A

The appendix will include all derivations required for the model used to described the NFF protocol.

A.1 Derivation of the Kraus operators of the system

This section gives the derivation of the Kraus operators for a system acted on by a circularly polarised laser pulse, including the effects of spontaneous emission. We take the most general form of a spin density matrix in the basis $|\uparrow\rangle_z$, $|\downarrow\rangle_z$, $|T\rangle$:

$$\rho_{in} = \begin{pmatrix} \rho_{\uparrow\uparrow} & \rho_{\uparrow\downarrow} & 0 \\ \rho_{\downarrow\uparrow} & \rho_{\downarrow\downarrow} & 0 \\ 0 & 0 & 0 \end{pmatrix} \tag{A.1}$$

with $\rho_{\uparrow\uparrow} + \rho_{\downarrow\downarrow} = 1$. We assume that the action of the σ^- pulse does not affect the $|\uparrow\rangle$ state and so we can model the action of the pulse by some general evolution operator

$$U_p = \begin{pmatrix} 1 & 0 & 0 \\ 0 & u_{\downarrow\downarrow} & u_{\downarrow T} \\ 0 & u_{T\downarrow} & u_{TT} \end{pmatrix} \tag{A.2}$$

where the elements of the matrix will be dependent on the Rabi frequency, detuning, bandwidth and shape of the pulse. We can use Eqs. A.1 and A.2 to construct a density matrix $\rho = U_p \rho_0 U_p^\dagger$ to represent the state of the system after application of a single pulse. This will be given by

$$\rho = \begin{pmatrix} \rho_{\uparrow\uparrow} & u^*_{\downarrow\downarrow}\rho_{\uparrow\downarrow} & u^*_{T\downarrow}\rho_{\uparrow\downarrow} \\ u_{\downarrow\downarrow}\rho_{\downarrow\uparrow} & |u_{\downarrow\downarrow}|^2\rho_{\downarrow\downarrow} & u_{\downarrow\downarrow}u^*_{T\downarrow}\rho_{\downarrow\downarrow} \\ u_{T\downarrow}\rho_{\downarrow\uparrow} & u_{T\downarrow}u^*_{\downarrow\downarrow}\rho_{\downarrow\downarrow} & |u_{T\downarrow}|^2\rho_{\downarrow\downarrow} \end{pmatrix} \tag{A.3}$$

assuming $u_{\downarrow T} = u_{T\downarrow}$. The system is now in an excited state and will experience spontaneous emission. The Lindblad master equation, given by

$$\frac{d\rho_s(t)}{dt} = -i[H,\rho_s(t)] + \sum_k \left(L_k \rho_s(t) L_k^\dagger - \frac{1}{2}\{L_k^\dagger L_k, \rho_s(t)\}_+ \right) \tag{A.4}$$

where $\rho_s(t)$ is the time-dependent density matrix of some system, s, H is the system Hamiltonian, L_k are the Lindblad operators and $\{\cdot\}_+$ is and anti-commutator, describes the dynamics of a system between its initial and final state (i.e. the microscopic dynamics that the Kraus operators misses). Our system is experiencing spontaneous emission and a rotation between the two ground states of the system. The Lindblad operator for spontaneous emission can be deduced as

$$L_1 = \sqrt{\Gamma} \left| \rho_{\bar{x}\bar{x}} \right\rangle \left\langle \rho_{TT} \right|, \tag{A.5}$$

where Γ is the spontaneous decay rate, assuming that we initially excited the system using a σ^- pulse. The second Lindblad operator we need is the operator describing the rotation between the two ground states. The ground states each initially have some population, and the rotation takes us between the two states, such that the population in each is equal. Then we find

$$L_2 = \frac{\omega_e}{2} \left(\left| \rho_{xx} \right\rangle \left\langle \rho_{\bar{x}\bar{x}} \right| + \left| \rho_{\bar{x}\bar{x}} \right\rangle \left\langle \rho_{xx} \right| \right), \tag{A.6}$$

where ω_e is the frequency induced by the external field. These Lindblad operators describe the dynamics on a shorter timescale between the start and end points of the interaction, whereas the Kraus operators describe the transition between the initial and final state without considering how the system gets to the end state. The Kraus operators come from solving the Liouville equations, given by

$$\frac{d\rho_0}{dt} = -i[H,\rho_0] \tag{A.7}$$

where in this case, ρ_0 is the state before spontaneous emission, i.e. where the full population is in the trion state. Then, the rate of change of the density operator for each component of the density matrix from the point where the state is fully excited (the full population is in the trion state, call this ρ_0) is given by

$$\begin{aligned} \dot{\rho}_{\uparrow\uparrow} &= \frac{\gamma}{2}\rho_{TT} \\ \dot{\rho}_{\downarrow\downarrow} &= \frac{\gamma}{2}\rho_{TT} \\ \dot{\rho}_{TT} &= -\gamma\rho_{TT} \end{aligned} \tag{A.8}$$

where γ is the relaxation rate and we consider the regime $1/T_R \ll \gamma \ll \omega_e$. Note that these equations do not include the optical coherences as these do not have any effect on the emission dynamics. The fact that $\dot{\rho}_{\uparrow\uparrow} = \dot{\rho}_{\downarrow\downarrow}$ tells us that the decay is incoherent and the $\rho_{\uparrow\downarrow}$ and $\rho\downarrow\uparrow$ are coherent and unaffected by spontaneous emission. The solutions to Eqs. A.8 are

$$\begin{aligned}
\rho_{\uparrow\uparrow} &= \rho_{0,\uparrow\uparrow} + \frac{1}{2}(1-e^{-\gamma t})\rho_{0,TT} \\
\rho_{\downarrow\downarrow} &= \rho_{0,\downarrow\downarrow} + \frac{1}{2}(1-e^{-\gamma t})\rho_{0,TT} \\
\rho_{TT} &= \rho_{0,TT}e^{-\gamma t}
\end{aligned} \tag{A.9}$$

and in the limit $t \gg \frac{1}{\gamma}$ we have

$$\begin{aligned}
\rho_{\uparrow\uparrow} &= \rho_{0,\uparrow\uparrow} + \frac{1}{2}\rho_{0,TT} \\
\rho_{\downarrow\downarrow} &= \rho_{0,\downarrow\downarrow} + \frac{1}{2}\rho_{0,TT} \\
\rho_{TT} &= 0.
\end{aligned} \tag{A.10}$$

Combining the density operators of the pulse and the spontaneous emission, we get a set of total expressions given by

$$\begin{aligned}
\rho_{tot,\uparrow\uparrow} &= \rho_{\uparrow\uparrow} + \frac{1}{2}|u_{T\downarrow}|^2\rho_{\downarrow\downarrow} \\
\rho_{tot,\downarrow\downarrow} &= |u_{\downarrow\downarrow}|^2\rho_{\downarrow\downarrow} + \frac{1}{2}|u_{T\downarrow}|^2\rho_{\downarrow\downarrow} \\
\rho_{tot,\uparrow\downarrow} &= u^*_{\downarrow\downarrow}\rho_{\uparrow\downarrow}.
\end{aligned} \tag{A.11}$$

As U_p is unitary, it must satisfy the condition $U_pU_p^\dagger = \mathbb{I}$. This implies that $|u_{T\downarrow}|^2 = 1-|u_{\downarrow\downarrow}|^2$, meaning that Eqs. A.11 transform to be

$$\begin{aligned}
\rho_{tot,\uparrow\uparrow} &= \rho_{\uparrow\uparrow} + \frac{1}{2}(1-|u_{\downarrow\downarrow}|^2)\rho_{\downarrow\downarrow} \\
\rho_{tot,\downarrow\downarrow} &= \frac{1}{2}(1+|u_{\downarrow\downarrow}|^2)\rho_{\downarrow\downarrow} \\
\rho_{tot,\uparrow\downarrow} &= u^*_{\downarrow\downarrow}\rho_{\uparrow\downarrow}.
\end{aligned} \tag{A.12}$$

Then ρ_{tot} is of the form

$$\rho_{tot} = \sum_i E_i\rho E_i^\dagger \tag{A.13}$$

where E_i are the Kraus operators describing the system, such that

$$\begin{aligned}
E_1 &= \begin{pmatrix} 1 & 0 \\ 0 & q \end{pmatrix} \\
E_2 &= \begin{pmatrix} 0 & a_1 \\ 0 & -a_2 \end{pmatrix} \\
E_3 &= \begin{pmatrix} 0 & 0 \\ 0 & \kappa \end{pmatrix}
\end{aligned} \tag{A.14}$$

where E_1 is the Kraus operator describing the pulse and E_2 and E_3 describe the spontaneous emission of the system and we define

$$\begin{aligned} a_1 &= \omega_e\sqrt{\frac{(1-q_0^2)}{2(4\gamma^2+\omega_e^2)}} \\ a_2 &= i\gamma\sqrt{2}\sqrt{\frac{(1-q_0^2)}{4\gamma^2+\omega_e^2}} \\ \kappa &= \sqrt{1-q_0^2-a_1^2-|a_2|^2} \end{aligned} \tag{A.15}$$

such that $u_{\downarrow\downarrow} = q$ for some parameter $q = q_0 e^{i\phi}$ describing the pulse where $0 \le q_0 \le 1$ and $0 \le \phi \le 2\pi$.

A.2 Derivation of the electron steady state in the absence of a nuclear spin bath

We will derive the expression for the steady state of the electron spin in the presence of a Voigt field after a train of pulses as defined in Section 3.1.1 in Chapter 2. Here we use the spin vector representation of the state by defining

$$\begin{aligned} S_m &= \mathrm{Tr}(\rho_0\sigma_m) \\ S'_m &= \mathrm{Tr}(\rho\sigma_m) \end{aligned} \tag{A.16}$$

with general evolution of the form

$$S'_m = PS_m + K. \tag{A.17}$$

Then we can express ρ_0 in the form

$$\rho_0 = \frac{1}{2}+\frac{1}{2}\sum_m \sigma_m S_m. \tag{A.18}$$

and define

$$\begin{aligned} S'_m &= \mathrm{Tr}\Big(\sum_i \sigma_1 \mathscr{E}_i\Big(\frac{1}{2}+\frac{1}{2}\sum_m \sigma_m S_m\Big)\mathscr{E}_i^\dagger\Big) \\ &= \frac{1}{2}\mathrm{Tr}\Big(\sum_l E_i E_i^\dagger\Big)+\frac{1}{2}\mathrm{Tr}\Big(\sum_i \sigma_l \mathscr{E}_i\Big(\sum_m \sigma_m S_m\Big)\mathscr{E}_i^\dagger\Big) \end{aligned} \tag{A.19}$$

which is of the form given in Eq. $A.17$. We can then extend this to define the state S_n which occurs after n driving periods. If we start with an initially unpolarised spin, then we have $S_0 = 0$ and

$$\begin{aligned} S_1 &= PS_0 + K \\ &= K \\ S_2 &= PS_1 + K \\ &= PK + K \end{aligned} \tag{A.20}$$

which allows us to define the recursion relation

$$\begin{aligned} S_n &= PS_{n-1} + K \\ S_n &= (P^{n-1} + P^{n-2} + \cdots + P + \mathbb{I})K. \end{aligned} \tag{A.21}$$

Then the infinite term in this sequence is given by

$$S^{\infty} = (\mathbb{I} - P)^{-1}K, \tag{A.22}$$

which can be represented by the 4-D matrix

$$\mathscr{C} = \begin{pmatrix} 1 & 0 & 0 & 0 \\ K_x & P_{xx} & P_{xy} & P_{xz} \\ K_y & P_{yx} & P_{yy} & P_{yz} \\ K_z & P_{zx} & P_{zy} & P_{zz} \end{pmatrix}. \tag{A.23}$$

We can then define the eigenvalue equation

$$\lambda S = \mathscr{C} S \tag{A.24}$$

and can extract the steady state from this by solving for $\lambda = 0$. This will be of the form $(1, S_x^{\infty}, S_y^{\infty}, S_z^{\infty})$ with

$$\begin{aligned} S_x &= \frac{a_1(a_1 q_0(q_0 - \cos\phi)\cos(\omega_e T_R) - i a_2(q_0\cos\phi - 1)\sin(\omega_e T_R) - a_1 q_0 \cos\phi + a_1)}{\xi} \\ S_y &= \frac{a_1(a_1 q_0(\cos\phi - q_0)\sin(\omega_e T_R) - i a_2(q_0\cos\phi - 1)(\cos(\omega_e T_R) - 1))}{\xi} \\ S_z &= \frac{a_1 q_0 \sin\phi(a_1 \sin(\omega_e T_R) - i a_2(\cos(\omega_e T_R) - 1))}{\xi} \end{aligned} \tag{A.25}$$

where $\xi = (a_1^2 + q_0^2 - 1)\cos(\omega_e T_R) - a_1 q_0 \cos\phi(i a_2 \sin(\omega_e T_R) + a_1\cos(\omega_e T_R) + 1) + i a_1 a_2 \sin(\omega_e T_R) + (a_1^2 - 1)q_0^2 + 1$.

A.3 Explicit expression for the z component of the nuclear spin steady state

$$I_z = \frac{-2e^{iAT_R}(S_z(-(S^2 - 1)\cos(AT_R) - 4\cos(\frac{AT_R}{2}) + S^2 + 3))}{(e^{iAT_R/2} + e^{3iAT_R/2})(4 + S_z^2 - S^2) + 2e^{iAT_R}(-2S_z^2 + S^2 - 3) + (e^{2iAT_R} + 1)(S^2 - 1)} \tag{A.26}$$

A.4 Derivation of the nuclear steady state and relaxation rate

To derive the nuclear relaxation rate, we need to consider the evolution of the 4D nuclear spin vector

$$I(t+T_R) = \mathscr{Y}_n I(t). \tag{A.27}$$

We know that the nuclear evolution is much slower than T_R which means that we can transform this into a differential equation for the nuclear spin vector in the following way:

$$\begin{aligned} I(t+T_R) &= \mathscr{Y}_n I(t) \\ I(t+T_R)-I(t) &= (\mathscr{Y}_n-\mathbb{I})I(t) \\ \Delta I(t) &= (\mathscr{Y}_n-\mathbb{I})I(t) \\ \frac{\Delta I(t)}{T_R} &= \frac{1}{T_R}(\mathscr{Y}_n-\mathbb{I})I(t) \\ \frac{d}{dt}I(t) &= \frac{1}{T_R}(\mathscr{Y}_n-\mathbb{I})I(t). \end{aligned} \tag{A.28}$$

The solution to this will be

$$I(t) = e^{(\mathscr{Y}_n-\mathbb{I})t/T_R} I(0) \tag{A.29}$$

This tells us that the nuclear spin steady state can be found by solving the eigenvalue equation

$$(\mathbb{I}-\mathscr{Y}_n)I = \lambda_n I, \tag{A.30}$$

with the case where $\lambda_0 = 0$ referring to the steady state and the smallest non-zero eigenvalue giving the nuclear relaxation rate $\gamma_n = \lambda_1/T_R$. We will take the flip-flop term to second order, so we need the perturbative expansion

$$\mathscr{Y}_n = \mathscr{Y}_n^{(0)} + \mathscr{Y}_n^{(1)} + \mathscr{Y}_n^{(2)}(+\cdots) \tag{A.31}$$

and similarly for the 4D spin vector of the nucleus

$$I = I^{(0)} + I^{(1)} + I^{(2)}(+\cdots). \tag{A.32}$$

We can use this to get the zeroth, first, and second order terms as such:

$$(\mathbb{I}-(\mathscr{Y}_0+\mathscr{Y}_1+\mathscr{Y}_2))(I^{(0)}+I^{(1)}+I^{(2)}) \quad = \quad (\lambda_0+\lambda_1+\lambda_2)(I^{(0)}+I^{(1)}+I^{(2)}) \tag{A.33}$$

and equating the terms of the same order we find three equations:

$$\begin{aligned}
I^{(0)}-\mathscr{Y}_n^{(0)}I^{(0)} &= \lambda_0 I^{(0)} \\
I^{(1)}-\mathscr{Y}_n^{(0)}I^{(1)}-\mathscr{Y}_n^{(1)}I^{(0)} &= \lambda_0 I^{(1)}+\lambda_1 I^{(0)} \\
I^{(2)}-\mathscr{Y}_n^{(0)}I^{(2)}-\mathscr{Y}_n^{(1)}I^{(1)}-\mathscr{Y}_n^{(2)}I^{(0)} &= \lambda_0 I^{(2)}+\lambda_1 I^{(1)}+\lambda_2 I^{(0)}
\end{aligned} \tag{A.34}$$

and setting $\lambda_0 = 0$, these simplify to

$$\begin{aligned}
(\mathbb{I}-\mathscr{Y}_n^{(0)})I^{(0)} &= 0, \\
(\mathbb{I}-\mathscr{Y}_n^{(0)})I^{(1)} &= (\mathscr{Y}_n^{(1)}+\lambda_1)I^{(0)}, \\
(\mathbb{I}-\mathscr{Y}_n^{(0)})I^{(2)} &= (\mathscr{Y}_n^{(2)}+\lambda_2)I^{(0)}+(\mathscr{Y}_n^{(1)}+\lambda_1)I^{(1)}.
\end{aligned} \tag{A.35}$$

We know at this point that the zeroth order term will only evolve according to precession and the Knight field, which means no polarisation will be generated. This means we know its form as a 4D spin vector will be

$$\mathscr{Y}_n^{(0)} \quad = \quad \begin{pmatrix} 1 & 0 & 0 & 0 \\ 0 & \mathscr{Y}_{n,xx}^{(0)} & \mathscr{Y}_{n,xy}^{(0)} & 0 \\ 0 & \mathscr{Y}_{n,yx}^{(0)} & \mathscr{Y}_{n,yy}^{(0)} & 0 \\ 0 & 0 & 0 & 1 \end{pmatrix}. \tag{A.36}$$

where the first column shows that there is no polarisation generated. Now the first step is to solve the first equation of Eq. A.35 (the zeroth order), where we have $\lambda_0 = 0$, i.e.

$$(\mathbb{I}-\mathscr{Y}_n^{(0)}))I^{(0)} \quad = \quad 0. \tag{A.37}$$

From looking at Eq. A.36 we can tell that there will be two zero eigenvalues. One of these will be zero at all orders, and this is the one that corresponds to the steady state. The other will get some non-zero components at higher orders, and this will be the smallest non-zero eigenvalue of the system. The eigenvectors of $\mathbb{I}-\mathscr{Y}_n^{(0)}$ corresponding to the zero eigenvalues can be easily calculated as $v_0 = (1,0,0,0)$ and $v_1 = (0,0,0,1)$ and these span the null space. This tells us that if we were to take just the first order component of $\mathscr{Y}_n$ to define the steady state, we would have something of the form $I_{ss}^{(0)} = (1,0,0,\zeta)$ where ζ is a constant. The fact that this is constant means that the steady state is not unique and depends on the initial state when in the zeroth order. This tells us that we need to go to higher orders to get a realistic value for the nuclear steady state.

Looking at the first order equation with $\lambda_1 = 0$

$$(\mathbb{I} - \mathcal{Y}_n^{(0)})I^{(1)} = \mathcal{Y}_n^{(1)}I^{(0)} \tag{A.38}$$

we can act v_0 and v_1 on both sides of the equation. Looking at the LHS we see that $\mathbb{I} - \mathcal{Y}_n^{(0)}$ will be of the form

$$\mathbb{I} - \mathcal{Y}_n^{(0)} = \begin{pmatrix} 0 & 0 & 0 & 0 \\ 0 & 1 - \mathcal{Y}_{n,xx}^{(0)} & -\mathcal{Y}_{n,xy} & 0 \\ 0 & -\mathcal{Y}_{n,yx} & 1 - \mathcal{Y}_{n,yy}^{(0)} & 0 \\ 0 & 0 & 0 & 0 \end{pmatrix} \tag{A.39}$$

It is clear from looking at this form that if we act either of the eigenvectors $v_0 = (1,0,0,0)$, $v_1 = (0,0,0,1)$ on Eq. A.39, we will be left with zero on the LHS. We also know that in the first order expansion $\lambda_1 = 0$, giving us an equation for each eigenvalue:

$$\begin{aligned} v_0\mathcal{Y}_n^{(1)}v_0 &= 0 \\ v_1\mathcal{Y}_n^{(1)}v_1 &= 0. \end{aligned} \tag{A.40}$$

It is easy to see that this is correct by looking at the form of $\mathcal{Y}_n^{(1)}$. As we know the steady state is of the form $I_{ss} = (1,0,0,\zeta)$ and we know that the total form of $\mathcal{Y}_n$ will be equivalent to that for the electron spin given in Eq. A.23. This means that because the element $\mathcal{Y}_{n,00} = 1$ and the same element for the zeroth order $\mathcal{Y}_{n,00}^{(0)} = 1$, the higher order components must all have this element equal to zero. It is also the case that in first order perturbation theory that we have no change in population which means that $\mathcal{Y}_{n,zz}^{(1)} = 0$. This leaves us with $\mathcal{Y}_n^{(1)}$ of the form

$$\mathcal{Y}_n^{(1)} = \begin{pmatrix} 0 & 0 & 0 & 0 \\ 0 & \cdot & \cdot & \cdot \\ 0 & \cdot & \cdot & \cdot \\ 0 & \cdot & \cdot & 0 \end{pmatrix} \tag{A.41}$$

confirming that Eq. $A.40$ is correct. We can then solve the first order equation to find $I^{(1)}$ with $\lambda_1 = 0$ as follows

$$\begin{aligned} (\mathbb{I} - \mathcal{Y}_n^{(0)})I^{(1)} &= \mathcal{Y}_n^{(1)}I^{(0)} \\ \Rightarrow I^{(1)} &= (\mathbb{I} - \mathcal{Y}_n^{(0)})^{-1}\mathcal{Y}_n^{(1)}I^{(0)} + bv_1 \\ &\equiv p_1 + bv_1 \end{aligned} \tag{A.42}$$

where b is an arbitrary constant. As $\lambda_1 = 0$ we now need to go to second order to find the relaxation rate. We multiply both sides of the second order equation by v_1, giving

$$v_1(\mathbb{I} - \mathscr{Y}_n^{(0)})I^{(2)} = v_1(\mathscr{Y}_n^{(2)} + \lambda_2)I^{(0)} + v_1(\mathscr{Y}_n^{(1)} + \lambda_1)I^{(1)} \tag{A.43}$$

and as before the LHS is equal to zero and substituting in the value of $I^{(1)}$ given in Eq. A.42 we have

$$v_1(\mathscr{Y}_n^{(2)} + \lambda_2)I^{(0)} + v_1\mathscr{Y}_n^{(1)}p_1 = 0. \tag{A.44}$$

This can be transformed into an eigenvalue equation and has two possible solutions:

$$\begin{aligned} I^{(0)} &= (1,0,0,\zeta^*) \quad \text{when } \lambda_2 = 0, \\ I^{(0)} &= (0,0,0,1) \quad \text{when } \lambda_2 = \lambda_2^*. \end{aligned} \tag{A.45}$$

The first of these corresponds to the nuclear steady state, such that

$$\begin{aligned} I_x^{(0)} &= 0 \\ I_y^{(0)} &= 0 \\ I_z^{(0)} &= \zeta^* \end{aligned} \tag{A.46}$$

where ζ^* is determined by the control sequence chosen, and the second to the relaxation rate (the rate at which the nuclear spin reaches its steady state) with

$$\gamma_n = \frac{\lambda_2^*}{T_R} \tag{A.47}$$

which vanishes when T_R is a multiple of the electron precession period (and $\frac{A^2}{w_e^2}$). The electron is now being driven so strongly that the nuclei have no effect, but a nucleus is still able to feel the effective field caused by the steady state of the electron (Knight field).

We can then calculate the nuclear spin flip rate, which is defined as

$$\omega_{\pm}^{1} = \frac{\gamma_n}{2}(1 \pm I_z) \tag{A.48}$$

where $w_+^1(w_-^1)$ is the rate to flip from down (up) to up (down). This tells us that the nuclear spin flip rate changes depending on the initial nuclear spin state, i.e. if the initial state has no z polarisation ($I_z = 0$) then the spin flip rate is just $\frac{\gamma_n}{2}$. This can also be written as

$$\frac{dP_\uparrow}{dt} = -\omega_- P_\uparrow + \omega_+ P_\downarrow \tag{A.49}$$

where $P_\uparrow$ is the probability that the nucleus is aligned on the same axis as the magnetic field and $P_\downarrow = 1 - P_\uparrow$ is the probability that it is aligned anti-parallel to this axis. In terms of $\mathscr{S}_{n,z}$, we have

$$\begin{aligned} P_\uparrow &= \frac{1}{2}(1+I_z) \\ P_\downarrow &= \frac{1}{2}(1-I_z) \end{aligned} \tag{A.50}$$

To derive this equation we need to consider the nuclear spin state at some time, t which is defined by

$$\begin{aligned} I(t) &= \sum_j \mathbf{v}_j e^{-i\lambda_j t} \\ &\approx I^{(0)} e^{-\gamma_n t} + I^{(\infty)}(1-e^{-\gamma_n t}). \end{aligned} \tag{A.51}$$

Note that the nuclear steady state is now being written as $I_z^{(\infty)}$. This leads to

$$I_z(t) = I_z^{(0)} e^{-\gamma_n t} + I_z^{(\infty)}(1-e^{-\gamma_n t}) \tag{A.52}$$

and also

$$I_z(t) = P_\uparrow - P_\downarrow. \tag{A.53}$$

Combining Eqs. A.52 and A.53 and differentiating with respect to t gives

$$\begin{aligned} \frac{d(P_\uparrow - P_\downarrow)}{dt} &= -\gamma_n I_z^{(0)} e^{-\gamma_n t} + \gamma_n I_z^{(\infty)} e^{-\gamma_n t} \\ &= -\gamma_n (I_z(t) - I_z^{(\infty)}). \end{aligned} \tag{A.54}$$

We can then rearrange this in terms of $P_\uparrow$ and $P_\downarrow$ as follows:

$$\begin{aligned} \frac{d(2P_\uparrow - 1)}{dt} &= -\gamma_n((P_\uparrow - P_\downarrow) - I_z^{(\infty)}) \\ \frac{d(P_\uparrow)}{dt} &= -\frac{\gamma_n}{2}((P_\uparrow - P_\downarrow) - I_z^{(\infty)}(P_\uparrow + P_\downarrow)) \end{aligned} \tag{A.55}$$

which leads directly to Eqs. A.48 and A.49.

A.5 Derivation of the probability distribution of values of m

We can define the probability that $N_\uparrow - N_\downarrow = m$ to be

$$P(m) \quad = \quad P_\uparrow^{\frac{N+m}{2}} P_\downarrow^{\frac{N-m}{2}} \begin{pmatrix} N \\ \frac{N+m}{2} \end{pmatrix} \tag{A.56}$$

where $P_\uparrow^{\frac{N+m}{2}}$ ($P_\downarrow^{\frac{N-m}{2}}$) is the probability that $N_\uparrow = \frac{N+m}{2}$ ($N_\downarrow = \frac{N-m}{2}$) and $\begin{pmatrix} N \\ \frac{N+m}{2} \end{pmatrix}$ are the binomial coefficients representing how many spins are in the state $N_\uparrow$ compared to the total number of spins $N = N_\uparrow + N_\downarrow$. $P(m \pm 2)$ can be defined similarly. We can then define the available transitions to and from the state $|m\rangle$. For example, we can define the transition from the state $|m\rangle$ to the state $|m+2\rangle$ as

$$T_{|m\rangle \to |m+2\rangle} \quad = \quad -l_+(m)\frac{N-m}{2}P(m) \tag{A.57}$$

where the sign of the transmission is defined by the direction if the flip in relation to the starting state $|m\rangle$ (i.e. if the spin flips away from $|m\rangle$ the sign is negative and if the spin flips towards the state m, the sign is positive). This allows us to define a probability distribution for m as

$$\frac{dP(m)}{dt} \quad = \quad \sum_{\pm} P(m \pm 2) l_\mp(m \pm 2)\Big(\frac{N \pm m}{2} + 1\Big) - \sum_{\pm} P(m) l_\pm(m) \frac{N \mp m}{2}. \tag{A.58}$$

The steady state occurs when $\frac{dP(m)}{dt} = 0$. Then

$$\begin{aligned} & P(m) l_+(m) \frac{N-m}{2} - P(m+2) w_-(m+2)\Big(\frac{N+m}{2} + 1\Big) \\ = \quad & P(m-2) l_+(m-2)\Big(\frac{N-m}{2} + 1\Big) - P(m) l_-(m) \frac{N+m}{2} \end{aligned} \tag{A.59}$$

implying that both sides are constant. As the full equation is invariant as $P(m)$ is rescaled, this constant must be zero. Then, taking the right hand side of Eq. A.59 we can define a recursion relation for $P(m)$ in terms of $P(m-2)$, given by

$$P(m) \quad = \quad \frac{N-m+2}{N+m} \frac{l_+(m-2)}{l_-(m)} P(m-2). \tag{A.60}$$

This tells us all of the possible nuclear spin bath configurations for given Δ, Ω, B_{ext} and A.

BIBLIOGRAPHY

[1] Á. Rivas and S. F. Huelga, *Open quantum systems: An introduction*. Springer-Verlag Berlin Heidelberg, 2012.

[2] S. Attal, A. Joye, and C.-A. Pillet, *Open quantum systems I*. Springer-Verlag Berlin Heidelberg, 2006.

[3] T. D. Ladd, F. Jelezko, R. Laflamme, Y. Nakamura, C. Monroe, and J. L. O'Brien, "Quantum computers," *Nature*, vol. 464, pp. 45–53, 2010.

[4] D. P. DiVincenzo, "The physical implementation of quantum computation," *Fortchritte der Physik*, vol. 48, pp. 771–783, 2000.

[5] M. A. Nielsen and I. L. Chuang, *Quantum computation and quantum information*. Cambridge University Press, 2000.

[6] R. Raussendorf and H. J. Briegel, "A one-way quantum computer," *Phys. Rev. Lett.*, vol. 86, p. 5188, 2001.

[7] H. J. Briegel, D. E. Browne, W. Dür, R. Raussendorf, and M. V. den Nest, "Measurement-based quantum computation," *Nature Physics*, vol. 5, pp. 19–26, 2009.

[8] C. Deng and X. Hu, "Electron-spin dephasing via hyperfine interaction in a quantum dot: An equation-of-motion calculation of electron-spin correlation functions," *Phys. Rev. B*, vol. 78, p. 245301, 2008.

[9] Ł. Cywiński, "Dephasing of electron spin qubits due to their interaction with nuclei in quantum dots," *Acta physica polonica A*, vol. 119, pp. 576–587, 2011.

[10] D. Loss and D. P. DiVincenzo, "Quantum computation with quantum dots," *Phys. Rev. A*, vol. 57, pp. 120–126, 1998.

[11] C. Kloeffel and D. Loss, "Prospects for spin-based quantum computing in quantum dots," *Annu. Rev. Condens. Matter Phys.*, vol. 4, pp. 51–81, 2013.

[12] Y.-X. Gong, X.-B. Zou, T. C. Ralph, S.-N. Zhu, and G.-C. Guo, "Linear optical quantum computation with imperfect entangled photon-pair sources and inefficient non - photon-number-resolving detectors," *Phys. Rev. A*, vol. 81, p. 052303, 2010.

[13] T. Rudolph, “Why i am optimistic about the silicon-photonic route to quantum computing,” *APL Photonics*, vol. 2, p. 030901, 2017.

[14] L. Childress and R. Hanson, “Diamond nv centers for quantum computing and quantum networks,” *MRS Bulletin*, vol. 38, 2, pp. 134–138, 2013.

[15] R. Hanson and D. D. Awschalom, “Coherent manipulation of single spins in semiconductors,” *Nature*, vol. 453, pp. 1043–1049, 2008.

[16] B. E. Kane, “A silicon-based nuclear spin quantum computer,” *Nature*, vol. 393, pp. 133–137, 1998.

[17] Y. M. He, G. Clark, J. R. Schaibley, Y. He, M. C. Chen, Y. J. Wei, X. Ding, Q. Zhang, W. Yao, X. Xu, C. Y. Lu, and J. W. Pan, “Single quantum emitters in monolayer semiconductors,” *Nature Nanotechnologies*, vol. 10, 6, pp. 497–502, 2015.

[18] A. M. Steane, “The ion trap quantum information processor,” *Appl. Phys. B*, vol. 64, p. 623, 1997.

[19] K. R. Brown, J. Kim, and C. Monroe, “Co-designing a scalable quantum computer with trapped atomic ion,” *npj Quantum Information*, vol. 2, p. 16034, 2016.

[20] M. H. Devoret and R. J. Schoelkopf, “Superconducting circuits for quantum information: An outlook,” *Science*, vol. 339, 6124, pp. 1169–1174, 2013.

[21] E. Knill, R. Laflamme, and G. J. Milburn, “A scheme for efficient quantum computation with linear optics,” *Nature*, vol. 409, pp. 46–52, 2001.

[22] J. Carolan, C. Harrold, C. Sparrow, E. Martin-Lópex, N. J. Russell, J. W. Silverstone, P. J. Shadbolt, N. Matsuda, M. Oguma, M. Itoh, G. D. Marshall, M. G. Thompson, J. C. F. Matthews, T. Hashimoto, J. L. O’Brien, and A. Laing, “Universal linear optics,” *Science*, vol. 349, 6249, pp. 711–716, 2015.

[23] G. Wendin, “Quantum information processing with superconducting circuits: a review,” *Rep. Prog. Phys.*, vol. 80, p. 106001, 2017.

[24] B. K. (announcer), “Intel keynote,” *Presented at CES*, 2018.

[25] D. G. (announcer), “Ibm announcement - 50 qubit processor,” *Yorktown Heights, NY*, 2017.

[26] J. Kelly, “Engineering superconducting qubit arrays for quantum supremacy,” *APS March Meeting*, 2018.

[27] E. Gibney, “D-wave upgrade: How scientists are using the world’s most controversial quantum computer,” *Nature*, vol. 541, pp. 447–448, 2017.

[28] J. Yoneda, K. Takeda, T. Otsuka, T. Nakajima, M. R. Delbecq, G. Allison, T. Honda, T. Kodera, S. Oda, Y. Hoshi, N. Usami, K. M. Itoh, and S. Tarucha, “A quantum-dot spin qubit with coherence limited by charge noise and fidelity higher than 99.9%,” *Nature Nanotechnology*, vol. 13, pp. 102–106, 2018.

[29] P. Senellart, G. Soloman, and A. White, “High-performance semiconductor single photon sources,” *Nature Nanotechnology*, vol. 12, pp. 1026–1039, 2017.

[30] M. Kroutvar, Y. Ducommun, D. Heiss, M. Bichler, D. Schuh, G. Abstreiter, and J. J. Finley, “Optically programmable electron spin memory using semiconductor quantum dots,” *Nature*, vol. 432, pp. 81–84, 2004.

[31] P. Androvitsaneas, A. B. Young, J. M. Lennon, C. Schneider, S. Maier, J. J. Hinchliff, G. S. Atkinson, E. Harbord, M. Kamp, S. Höfling, J. G. Rarity, and R. Oulton, “Efficient deterministic giant photon phase shift from a single charged quantum dot,” *arxiv*, vol. 1609.02851v2, 2017.

[32] M. Davanco, J. Liu, L. Sapienza, C.-Z. Zhang, J. V. D. M. Cardoso, V. Verma, R. Mirin, S. W. Nam, L. Liu, and K. Srinivasan, “Heterogeneous integration for on-chip quantum photonic circuits with single quantum dot devices,” *Nat. Comms.*, vol. 8, 889, pp. 1–12, 2017.

[33] M. Blencowe, “Quantum ram,” *Nature*, vol. 468, pp. 44–45, 2010.

[34] S. Khasminskaya, F. Pyatkov, K. Słowik, S. Ferrari, O. Kahl, V. Kovalyuk, P. Rath, A. Vetter, F. Hennrich, M. M. Kappes, G. Gol’tsman, A. Korneev, C. Rockstuhl, R. Krupke, and W. H. P. Pernice, “Fully integrated quantum photonic circuit with an electrically driven light source,” *Nature Photonics*, vol. 10, pp. 727–732, 2016.

[35] A. W. Elshaari, I. E. Zadeh, A. Fognini, M. E. Reimer, D. Dalacu, P. J. Poole, V. Zwiller, and K. D. Jöns, “On-chip single photon filtering and multiplexing in hybrid quantum photonic circuits,” *Nat. Comms.*, vol. 8, 379, pp. 1–8, 2017.

[36] J. Adcock, E. Allen, M. Day, S. Frick, J. Hinchliff, M. Johnson, S. Morley-Short, S. Pallister, A. Price, and S. Stanisic, “Advances in quantum machine learning,” *arXiv*, vol. 1512.02900v1, 2015.

[37] A. Perdomo-Ortiz, N. Dickson, M. Drew-Brook, G. Rose, and A. Aspuru-Guzik, “Finding low-energy conformations of lattice protein models by quantum annealing,” *Scientific Reports*, vol. 2, 571, pp. 1–7, 2012.

[38] D. K. Thapa and A. Pandey, “Evidence for superconductivity at ambient temperature and pressure in nanostructures,” *arXiv*, vol. 1807.08572, 2018.

[39] J. Biamonte, P. Wittek, N. Pancotti, P. Rebentrost, N. Wiebe, and S. Lloyd, “Quantum machine learning,” *Nature*, vol. 549, pp. 195–202, 2017.

[40] D. J. Moylett, N. Linden, and A. Montanaro, “Quantum speedup of the traveling-salesman problem for bounded-degree graphs,” *Phys. Rev. A*, vol. 95, p. 032323, 2017.

[41] R. Orus, S. Mugel, and E. Lizaso, “Quantum computing for finance: overview and prospects,” *arXiv*, vol. 1807.03890, 2018.

[42] S. Boixo, S. V. Isakov, V. N. Smelyanskiy, R. Babbush, N. Ding, Z. Jiang, M. J. Bremner, J. M. Martinis, and H. Neven, “Characterizing quantum supremacy in near-term devices,” *Nature Physics*, vol. 14, pp. 595–600, 2018.

[43] W. Diffie and M. E. Hellman, “New directions in cryptography,” *IEEE Transactions for information theory*, vol. 22, 6, pp. 644–654, 1976.

[44] R. M. Needham and M. D. Schroeder, “Using encryption for authentication in large networks of computers,” *Communications of the ACM*, vol. 21, 12, pp. 993–999, 1978.

[45] R. L. Rivest, A. Shamir, and L. Adleman, “A method for obtainng digital signatures and public-key cryptosystems,” *Communications of the ACM*, vol. 21, 2, pp. 120–126, 1978.

[46] B. Lu, “A review of modern cryptography: From the world war ii era to the big-data era. In: T. M. Choi, J. Gao, J. Lambert, C. K. Ng, J. Wang (eds) optimization and control for system in the big-data era.,” *International series in operations research and management science*, vol. 252, Springer, Cham, 2017.

[47] P. W. Shor, “Algorithms for quantum computation: discrete logarithms and factoring,” *Proceedings 35th annual symposium on foundations of computer science*, vol. Santa Fe, NM, USA, pp. 124–134, 1994.

[48] P. W. Shor, “Polynomial-time algorithms for prime factorization and discrete logarithms on a quantum computer,” *Siam J. Comp. Sci.*, vol. 26, 5, pp. 1484–1509, 1997.

[49] C. H. Bennett and G. Brassard, “Quantum cryptography: Public key distribution and coin tossing,” *Proceedings of IEEE internation conference on computers, systems and signal processing, Bangalore*, vol. 125, pp. 175–179, 1984.

[50] C. H. Bennett and G. Brassard, “Quantum cryptography: public key distribution and coin tossing,” *Theoretical computer science*, vol. 560 part 1, pp. 7–11, 2014.

[51] V. Scarani, A. Acín, G. Ribordy, and N. Gisin, “Quantum cryptography protocols robust against photon number splitting attacks for weak laser pulse implementations,” *Phys. Rev. Lett.*, vol. 92, p. 057901, 2004.

[52] M. M. Khan, M. Murphy, and A. Beige, “High error-rate quantum key distribution for long-distance communication,” *New Journal of Physics*, vol. 11, p. 063043, 2009.

[53] H.-K. Lo, X. Ma, and K. Chen, “Decoy state quantum key distribution,” *Phys. Rev. Lett.*, vol. 94, p. 230504, 2005.

[54] D. Stucki, C. Barreiro, S. Fasel, J.-D. Gautier, O. Gay, N. Gisin, R. Thew, Y. Thoma, P. Trinkler, F. Vannel, and H. Zbinden, “Continuous high speed coherent one-way quantum key distribution,” *Optics Express*, vol. 17, 16, pp. 13326–13334, 2009.

[55] A. K. Ekert, “Quantum cryptography based on bell’s theorem,” *Phys. Rev. Lett.*, vol. 67, p. 661, 1991.

[56] T. C. Ralph, “Continuous variable quantum cryptography,” *Phys. Rev. A*, vol. 61, p. 010303(R), 1999.

[57] C. H. Bennett and G. Brassard, “Experimental quantum cryptography: the dawn of a new era for quantum cryptography: the experimental prototype is working,” *ACM SIGACT*, vol. 20, 4, pp. 78–80, 1989.

[58] C. H. Bennett, F. Bessette, G. Brassard, L. Salvail, and J. Smolin, “Experimental quantum cryptography,” *Journal of Cryptology*, vol. 5, 1, pp. 3–28, 1991.

[59] D. Bouwmeester, J.-W. Pan, K. Mattle, M. Eibl, H. Weinfurter, and A. Zeilinger, “Experimental quantum teleportation,” *Nature*, vol. 390, pp. 575–579, 1997.

[60] D. L. Moehring, P. Maunz, S. Olmschenk, K. C. Younge, D. N. Matsukevich, L.-M. Duan, and C. Monroe, “Entanglement of single-atom quantum bits at a distance,” *Nature*, vol. 449, pp. 68–71, 2007.

[61] B. Hensen, H. Bernien, A. E. Dréau, A. Reiserer, N. Kalb, M. S. Blok, J. Ruitenberg, R. F. L. Vermeulen, R. N. Schouten, C. Abellán, W. Amaya, V. Pruneri, M. W. Mitchell, M. Markham, D. J. Twitchen, D. Elkouss, S. Wehner, T. H. Tainiau, and R. Hanson, “Loophole-free Bell inequality violation using elecrton spins separated by 1.3 kilometres,” *Nature*, vol. 526, pp. 682–686, 2015.

[62] S. Wang, Z.-Q. Yin, W. Chen, D.-Y. He, X.-T. Song, H. W. Li, L.-J. Zhang, Z. Zhou, G.-C. Guo, and Z.-F. Han, “Experimental demonstration of a quantum key distribution without signal disturbance monitoring,” *Nature Photonics*, vol. 9, pp. 832–836, 2015.

[63] A. Boaron, G. Boso, D. Rusca, C. Vulliez, C. Autebert, M. Caloz, M. Perrenoud, G. Gras, F. Brussières, M.-J. Li, D. Nolan, A. Martin, and H. Zbinden, “Secure quantum key distribution over 421km of optical fibre,” *arXiv*, vol. 1807.03222, 2018.

[64] T. Schmitt-Manderbach, H. Weier, M. Fürst, R. Ursin, F. Tiefenbacher, T. Scheidl, J. Perdigues, Z. Sodnik, C. Kurtseifer, J. G. Rarity, A. Zeilinger, and H. Weinfurter, "Experimental demonstration of free-space decoy-state quantum key distribution over 144km," *Phys. Rev. Lett.*, vol. 98, p. 010504, 2007.

[65] W. Dür, H. J. Briegel, J. I. Cirac, and P. Zoller, "Quantum repeaters based on entanglement purification," *Phys. Rev. A*, vol. 60, p. 725, 1999.

[66] H. J. Briegel, W. Dür, J. I. Dirac, and P. Zoller, "Quantum repeaters: the role of imperfect local operations in quantum communication," *Phys. Rev. Lett.*, p. 5932, 1998.

[67] L. M. Duan, M. D. Lukin, J. I. Cirac, and P. Zoller, "Long-distance quantum communication with atomic ensembles and linear optics," *Nature*, vol. 414, pp. 413–418, 2001.

[68] H.-K. Lo, M. Curty, and B. Qi, "Measurement-device-independent quantum key distribution," *Phys. Rev. Lett.*, vol. 108, p. 130503, 2012.

[69] H.-L. Yin, T.-Y. Chen, Z.-W. Yu, H. Liu, L.-X. You, Y.-H. Zhou, S.-J. Chen, Y. Mao, M.-Q. Huang, W.-J. Zhang, H. Chen, M. J. Li, D. Nolan, F. Zhou, X. Jiang, Z. Wang, Q. Zhang, X.-B. Wang, and J.-W. Pan, "Measurement-device-independent quantum key distribution over a 404km optical fiber," *Phys. Rev. Lett.*, vol. 117, p. 190501, 2016.

[70] A. I. Lvovsky, B. C. Sanders, and W. Tittel, "Optical quantum memory," *Nature Photonics*, vol. 3, pp. 706–714, 2009.

[71] K. Heshami, D. G. England, P. C. Humphreys, P. J. Bustard, V. M. Acosta, J. Nunn, and B. J. Sussman, "Quantum memories: emerging applications and recent advances," *Journal of Modern Optics*, vol. 63 (20), pp. 2005–2028, 2016.

[72] C. Liu, Z. Dutton, C. H. Behroozi, and L. V. Hau, "Observation of coherent optical information storage in an atomic medium using halted light pulses," *Nature*, vol. 409, pp. 490–493, 2001.

[73] S. J. Yang, X. J. Wang, X. H. Bao, and J. W. Pan, "Efficient quantum light-matter interface with sub-second lifetime," *Nat. Photon.*, vol. 10, pp. 381–384, 2016.

[74] M. Afzelius, C. Simon, H. de Riedmatten, and N. Gisin, "Multimode quantum memory based on atomic frequency combs," *Phys. Rev. A*, vol. 79, p. 052329, 2009.

[75] G. Burkard and D. Loss, *Electron spins in quantum dots as qubits for quantum information processing. In: D. D. Awschalom and D. Loss and N. Samarth (eds) Semiconductor spintronics and quantum computation*.
NanoScience and Technology. Springer, Berlin, Heidelberg, 2002.

[76] A. Imamoglu, D. D. Awschalom, G. Burkard, D. P. DiVincenzo, D. Loss, M. Sherwin, and A. Small, “Quantum information processing using quantum dot spins and cavity qed,” *Phys. Rev. Lett.*, vol. 83, p. 4204, 1999.

[77] Y. Masumoto and T. Takagahara, *Semiconductor quantum dots: Physics, spectroscopy and applications*.
NanoScience and Technology. Springer-Verlag Berlin Heidelberg, 2002.

[78] L. Goldstein, F. Glas, J. Y. Marzin, M. N. Charasse, and G. L. Roux, “Growth by molecular beam epitaxy and characterization of InAs/GaAs strained-layer superlattices,” *Appl. Phys. Lett.*, vol. 47, p. 1099, 1985.

[79] H. J. Carmichael, “Statistical methods in quantum optics 2: Non-classical fields,” 2008.

[80] R. Loudon, *The quantum theory of light (Third edition)*.
Oxford Science Publications, 2000.

[81] D. Bimberg, M. Grundman, and N. N. Ledentsov, *Quantum dot heterostructures*.
Wiley, 1998.

[82] I. N. Stranski and L. Krastanov, “Abhandlungen der mathematisch-naturwissenschaftlichen klasse iib.,” *Akademie der Wissenschaften Wien*, vol. 146, pp. 797–810, 1938.

[83] E. H. C. Parker, *The technology and physics of molecular beam epitaxy*.
Plenum Press, 1985.

[84] J. J. Harris, “Delta-doping of semiconductors,” *Journal of Materials Science: Materials in Electronics*, vol. 4, 2, pp. 93–105, 1993.

[85] A. M. Smith and S. Nie, “Semiconductor nanocrystals: Structure, properties and band gap engineering,” *Acc. Chem. Res.*, vol. 43, 2, pp. 190–200, 2010.

[86] G. T. Einevoll, “Confinement of excitons in quantum dots,” *Phys. Rev. B*, vol. 45, p. 3410, 1992.

[87] N. H. Bonadeo, J. Erland, D. Gammon, D. Park, D. S. Katzer, and D. G. Steel, “Coherent optical control of the quantum state of a single quantum dot,” *Science*, vol. 282, pp. 1473–1476, 1998.

[88] R. J. Warburton, C. S. Dürr, K. Karrai, J. P. Kotthaus, G. Medeiros-Ribeiro, and P. M. Petroff, “Charged excitons in self-assembled semiconductor quantum dots,” *Phys. Rev. Lett.*, vol. 79, p. 5282, 1997.

[89] I. M. Tsidilkovski, *Band structure of semiconductors*.
Elsevier Ltd, 1982.

[90] P. Yu and M. Cardona, *Fundamentals of Semiconductors*.
Springer-Verlag Berlin Heidelberg, 2010.

[91] A. S. Bracker, D. Gammon, and V. L. Korenev, "Fine structure and optical pumping of spins in individual semiconductor quantum dots," *Semicond. Sci. Technol.*, vol. 23, p. 114004, 2008.

[92] H. Haug and S. W. Koch, *Quantum theory of the optical and electron properties of semiconductors*.
World Scientific Publishing Co. Pte. Ltd., 2009.

[93] V. Belykh, A. Greilich, D. Yakovlev, M. Yacob, J. Reithmaier, M. Benyoucef, and M. Bayer, "Electron and hole g factors in inas/inasgaas self-assembled quantum dots emitting at telecom wavelengths," *Phys. Rev. B*, p. 165307, 2015.

[94] W. Sheng, S. Xu, and P. Hawrylak, "Electron g-factor distribution in self-assembled quantum dots," *Phys. Rev. B*, vol. 77, p. 241307, 2008.

[95] M. I. Dyakonov, *Spin physics in semiconductors*.
Springer-Verlag Berlin Heidelberg, 2008.

[96] C. Bulutay, "Quadrupolar spectra of nuclear spins in strained $in_xga_{1-x}as$ quantum dots," *Phys. Rev. B*, vol. 85, p. 115313, 2012.

[97] C. Kammerer, C. Voisin, G. Cassabois, C. Delalande, P. Roussignol, F. Klopf, J. P. Reithmaier, A. Forchel, and J. M. Gérard, "Line narrowing in single semiconductor quantum dots: Toward the control of environment effects," *Phys. Rev. B*, vol. 66, 2002.

[98] C. F. Fong, Y. Ota, S. Iwamoto, and Y. Arakawa, "Manipulation of dynamic nuclear spin polarization in single quantum dots by photonic environment engineering," *Phys. Rev. B*, vol. 95, 2017.

[99] E. A. Chekhovich, M. N. Makhonin, A. I. Tartakovskii, A. Yacoby, H. Bluhm, K. C. Nowack, and L. M. K. Vandersypen, "Nuclear spin effects in semiconductor quantum dots," *Nat. Materials*, vol. 12, pp. 494–504, 2012.

[100] X. R. Wang, Y. S. Zheng, and S. Yin, "Spin relaxation and decoherence of two-level systems," *Phys. Rev. B*, vol. 72, p. 121303, 2005.

[101] I. Žutić, "Spintronics: Fundamentals and applications," *Rev. Mod. Phys.*, vol. 76, pp. 323–410, 2004.

[102] A. V. Khaetskii, D. Loss, and L. Glazman, “Electron spin decoherence in quantum dots due to interaction with nuclei,” *Phys. Rev. Lett.*, vol. 88, p. 186802, 2002.

[103] T. D. Ladd, F. Jelezko, R. Laflamme, Y. Nakamura, C. Monroe, and J. L. O’Brien, “Quantum computers,” *Nature*, vol. 464, pp. 45–53, 2010.

[104] S. Bandyopadhyay, *Introduction to spintronics*.
CRC Press, 2015.

[105] A. V. Khaetskii and Y. V. Nazarov, “Spin relaxation in semiconductor quantum dots,” *Phys. Rev. B*, vol. 61, p. 12639, 2000.

[106] V. N. Golovach, A. Khaetskii, and D. Loss, “Phonon-induced decay of the electron spin in quantum dots,” *Phys. Rev. Lett.*, vol. 93, p. 016601, 2004.

[107] A. V. Khaetskii and Y. V. Nazarov, “Spin-flip transitions between zeeman sublevels in semiconductor quantum dots,” *Phys. Rev. B*, vol. 64, p. 125316, 2001.

[108] M. Kroutvar, T. Ducommun, D. Heiss, M. Bichler, D. Schuh, G. Abstreiter, and J. J. Finley, “Optically programmable electron spin memory using semiconductor quantum dots,” *Nature*, vol. 432, pp. 81–84, 2004.

[109] X. M. Dou, B. Q. Sum, D. S. Jiang, H. Q. Ni, and Z. C. Niu, “Temperature dependence of electron-spin relaxation in a single inas quantum dot at zero applied magnetic field,” *Journal of Applied Physics*, vol. 111, p. 053524, 2012.

[110] I. A. Merkulov, A. L. Efros, and M. Rosen, “Electron spin relaxation by nuclei in semiconductor quantum dots,” *Phys. Rev. B*, vol. 65, p. 205309, 2002.

[111] V. N. Golovach, A. Khaetskii, and D. Loss, “Phonon-induced decay of the electron spin in quantum dots,” *Phys. Rev. Lett.*, vol. 93, p. 016601, 2004.

[112] J. R. Petta, A. C. Johnson, J. M. Taylor, E. A. Laird, A. Yacoby, M. D. Lukin, C. M. Marcus, M. P. Hanson, and A. C. Gossard, “Coherent manipulation of coupled electron spins in semiconductor quantum dots,” *Science*, vol. 309, 5744, pp. 2180–2184, 2005.

[113] J. M. Kikkawa and D. D. Awschalom, “All optical magnetic resonance in semiconductors,” *Science*, vol. 21;287(5452), pp. 473–6.

[114] J. M. Kikkawa and D. D. Awschalom, “Resonant spin amplification in n-type gaas,” *Phys. Rev. Lett.*, vol. 80, p. 4313, 1998.

[115] A. Abragam, *The principles of nuclear magnetism*.
Oxford University Press, 1961.

[116] W. Coish and J. Baugh, “Nuclear spins in nanostructures,” *Phys. Status Solidi*, vol. 246, no. 10, pp. 2203–2215, 2009.

[117] P. Schering, J. Hüdepohl, and G. S. Uhrig, “Nuclear frequency focusing in periodically pulsed semiconductor quantum dots described by infinite classical spin models,” *Phys. Rev. B*, vol. 98, p. 024305, 2018.

[118] R. Matsusaki, R. Kaji, S. Yamamoto, H. Sasakura, and S. Adachi, “Dynamic nuclear spin polarization in self-assembled quantum dots under zero magnetic field,” *arxiv*, vol. 1703.06046, 2017.

[119] R. Stockill, C. L. Gall, C. Matthiesen, L. Huthmacher, E. Clarke, M. Hugues, and M. Atatüre, “Quantum dot spin coherence governe by a strained nuclear environment,” *Nat. Comms.*, vol. 7, p. 12745, 2016.

[120] G. Éthier-Majcher, D. Gangloff, R. Stockill, E. Clarke, M. Hugues, C. L. Gall, and M. Atatüre, “Improving a solid-state qubit through an engineered mesoscopic environment,” *Phys. Rev. Lett.*, vol. 119, p. 130503, 2017.

[121] N. Jäschke, A. Fischer, E. Evers, V. V. Belykh, A. Greilich, M. Bayer, and F. B. Anders, “Nonequilibrium nuclear spin distribution function in quantum dots subject to periodic pulses,” *Phys. Rev. B*, vol. 96, p. 205419, 2017.

[122] J. Scheuer, I. Schwartz, Q. Chen, D. Schulze-Sünninghausen, P. Carl, P. Höfer, A. Retzker, H. Sumiya, J. Isoya, B. Luy, M. B. Plenio, B. Naydenov, and F. Jelezko, “Optically induced dynamic nuclear spin polarisation in diamond,” *New J. Phys.*, vol. 18, p. 013040, 2016.

[123] S. E. Economou and E. Barnes, “Theory of dynamic nuclear polarization and feedback in quantum dots,” *Phys. Rev. B*, vol. 89, p. 165301, 2014.

[124] A. Greilich, D. R. Yakovlev, A. Shabaev, A. L. Efros, I. A. Yugova, R. Oulton, V. Stavarache, D. Reuter, A. Wieck, and M. Bayer, “Mode locking of electron spin coherences in singly charged quantum dots,” *Science*, vol. 313, p. 341, 2006.

[125] S. E. Economou, L. J. Sham, Y. Wu, and D. G. Steel, “Proposal for optical u(1) rotations of electron spin trapped in a quantum dot,” *Phys. Rev. B*, vol. 74, p. 205415, 2006.

[126] G. M. Moy, J. J. Hope, and C. M. Savage, “Born and markov approximation for atom lasers,” *Phys. Rev. A*, vol. 59, pp. 667–675, 1999.

[127] S. G. Carter, A. Shabaev, S. E. Economou, T. A. Kennedy, A. S. Bracker, and T. L. Reinecke, “Directing nuclear spin flips in in as quantum dots using detuned optical pulse trains,” *Phys. Rev. Lett.*, vol. 102, p. 167403, 2009.

[128] C. Y. Lin, F. Grillot, Y. Li, R. Rangunathan, and L. F. Lester, "Characterization of timing jitter in a quantum dot passively mode-locked laser at low offset frequency," *Optics Express*, vol. 18, 21, 2010.

[129] B. Urbaszek, X. Marie, T. Amand, O. Krebs, P. Voisin, P. Malentinsky, A. Högele, and A. Imamoglu, "Nuclear spin physics in quantum dots: An optical investigation," *Rev. Mod. Phys.*, vol. 85, p. 79(55), 2013.

[130] V. Privman, D. Mozyrsky, and I. D. Vagner, "Quantum computing with spin qubits in semiconductor structures," *Elsevier Computer Phys. Comms.*, vol. 146, pp. 331–338, 2002.

[131] M. Steger, K. Saeedi, M. L. W. Thewalt, J. J. L. Morton, H. Riemann, N. V. Abrosimov, P. Becker, and H.-J. Pohl, "Quantum information storage for over 180s using donor spins in a 28si 'semiconductor vacuum'," *Science*, vol. 336, 6086, pp. 1280–1283, 2012.

[132] P. Maurer, G. Kucsko, C. Latta, L. Jiang, N. Y. Yao, S. D. Bennett, F. Pastawski, D. Hunger, N. Chisholm, M. Markham, D. J. Twitchen, J. I. Cirac, and M. D. Lukin, "Room-temperature quantum bit memory exceeding one second," *Science*, vol. 336, 6086, pp. 1283–1286, 2012.

[133] J. Longdell, E. Fraval, M. Sellars, and N. Manson, "Stopped light with storage times greater than one second using electromagnetically induced transparency in a solid," *Phys. Rev. Lett.*, vol. 95, p. 063601, 2005.

[134] P. S. Sokolov, M. Y. Petrov, T. Mehrtens, K. Müller-Caspary, A. Rosenauer, D. Reuter, and A. D. Wieck, "Reconstruction of nuclear quadrupole interaction in (In,Ga)As/GaAs quantum dots observed by transmission electron microscopy," *Phys. Rev. B*, vol. 93, p. 045301, 2016.

[135] O. Kojima, R. Izumi, and T. Kita, "Effect of lattice-mismatched strain on electron dynamics in InAs/GaAs quantum dots as seen by time-domain terahertz spectroscopy," *J. Phys. D: Appl. Phys.*, vol. 51, p. 305102, 2018.

[136] X. Q. Zhang, S. Ganapathy, I. Suemune, H. Kumano, K. Uesugi, Y. Nabetani, and T. Matsumoto, "Improvement of InAs quantum-dot optical properties by strain compensation with GaNAs capping layers,"

[137] J. Tatebayashi, N. Nuntawong, P. S. Wong, Y.-C. Xin, L. F. Lester, and D. L. Huffaker, "Strain compensation technique in self-assembled InAs/GaAs,"

[138] P. E. Vullum, M. Nord, M. Vatanparast, S. F. Thomassen, C. Boothroyd, R. Holmestad, B.-O. Fimland, and T. W. Reenaas, "Quantitative strain analysis of InAs/GaAs quantum dot materials," *Nature Scientific Reports*, vol. 7, p. 45376, 2017.

[139] F. Meier and B. P. Zakharchenya, *Modern problems in condensed matter sciences: Optical orientation*.
Elsevier, 1984.

[140] U. Haeberlen, *High resolution NMR in solids*.
Academic Press, 1976.

[141] B. J. W. R. G. Shulman and P. W. Anderson, "Nuclear magnetic resonance in semiconductors. ii. quadrupole broadening of nuclear magnetic resonance lines by elastic axial deformation," *Phys. Rev.*, vol. 107, p. 953, 1957.

[142] D. Mao and P. Taylor, "Nuclear spin echoes in gaas:zn and gaas:in," *Phys Rev B*, vol. 52, p. 5665, 1995.

[143] D. Klauser, *Hyperfine interaction and spin decoherence in quantum dots*.
Dissertation, University of Basel, 2008.

[144] W. Coish and D. Loss, "Hyperfine interaction in a quantum dot: Non-markovian electron spin dynamics," *Phys. Rev. B*, vol. 70, p. 195340, 2004.

[145] B. Uzbaszek, X. Marie, T. Amand, O. Krebs, P. Voisin, P. Malentinsky, A. Högele, and A. Imamoglu, "Nuclear spin physics in quantum dots: An optical investigation," *Rev. Mod. Phys.*, vol. 85, p. 79, 2013.

[146] G. Vidal and R. Werner, "Computable measure of entanglement," *Phys. Rev. A*, vol. 65, p. 032314, 2002.

[147] C. Boehme and D. R. McCamey, "Nuclear-spin quantum memory poised to take the lead," *Science*, pp. 1239–1240, 2012.

[148] J. Anders, D. K. L. Oi, E. Kashefi, D. E. Browne, and E. Andersson, "Ancilla-driven universal quantum computation," *Phys. Rev. A*, vol. 82, p. 020301, 2010.

[149] E. Kashefi, D. K. L. Oi, D. Browne, J. Anders, and E. Andersson, "Ancilla-driven quantum computation with twisted graph states," *Theoretical Computer Science*, vol. 430, pp. 51–72, 2012.

[150] A. Greilich, A. Shabaev, D. Yakovlev, A. Efros, I. Yugova, and D. Reuter, "Nuclei-induced frequency focusing of electron spin coherence," *Science*, vol. 317, pp. 1896–1899, 2007.

[151] P. Maletinsky, A. Badolato, and A. Imamoglu, "Dynamics of quantum dot nuclear spin polarization controlled by a single electron," *Phys. Rev. Lett.*, vol. 99, p. 056804, 2007.

[152] C. Hu, A. Young, J. L. O'Brien, W. J. Munro, and J. G. Rarity, "Giant optical faraday rotation induced by a single-electron spin in a quantum dot: Applications to entangling remote spins via a single photon," *Phys. Rev. B*, vol. 78, p. 085307, 2008.

[153] C. Y. Hu, W. J. Munro, J. L. O'Brien, and J. G. Rarity, "Proposed entanglement beam splitter using a quantum-dot spin in a double-sided optical microcavity," *Phys. Rev. B*, vol. 80, p. 205326, 2009.

[154] R. M. Stevenson, R. J. Young, P. See, D. G. Gevaux, K. Cooper, P. Atkinson, I. Farrer, D. A. Ritchie, and A. J. Shields, "Magnetic-field-induced reduction of the exciton polarization splitting in inas quantum dots," *Phys. Rev. B*, vol. 73, p. 033306, 2006.

[155] V. Haxha, I. Drouzas, J. Ulloa, M. Bozkurt, P. Koenraad, D. Mowbray, H. Liu, M. Steer, M. Hopkinson, and M. Migliorato, "Control of strain in gasbas/inas/gaas quantum dots," *J. Phys. Conf Ser.*, vol. 245, p. 012065, 2010.

[156] M. K. Yakes, C. D. Cress, J. G. Tischler, and A. S. Bracker, "Three-dimensional control of self-assembled quantum dot configurations," *American Chemical Society Nano*, vol. 4 (7), pp. 3877–3882, 2010.

[157] S. E. Vinay and P. Kok, "Practical repeaters for ultralong-distance quantum communication," *Phys. Rev. B*, vol. 95, p. 052336, 2017.

[158] P. Walther, K. Resch, T. Rudolph, E. Schenk, H. Weinfurter, V. Vedral, M. Aspelmeyer, and A. Zeilinger, "Experimental one-way quantum computing," *Nature*, vol. 434, pp. 169–176, 2005.

[159] B. Kraus and J. Cirac, "Optimal creation of entanglement using a two-qubit gate," *Phys. Rev. A*, vol. 63, p. 062309, 2001.

[160] L. H. M.S. Leifer and N. Linden, "Optimal entanglement generation from quantum operations," *Phys. Rev. A*, vol. 67, p. 012306, 2003.

[161] S. Aaronson and D. Gottesman, "Improved simulation of stabilizer circuits," *Phys. Rev. A*, vol. 70, p. 052328, 2004.

[162] J. Houel, A. V. Kuhlmann, L. Greuter, F. Xue, M. Poggio, B. D. Gerardot, P. A. Dalgarno, A. Badolato, P. M. Petroff, A. Ludwig, D. Reuter, A. D. Wieck, and R. J. Warburton, "Probing single-charge fluctuations at a GaAs/AlAs interface using laser spectroscopy on a nearby InGaAs quantum dot," *Phys. Rev. Lett.*, vol. 108, p. 107401, 2012.

[163] A. Moelbjerg, P. Kaer, M. Lorke, and J. Mørk, "Resonance fluorescence from semiconductor quantum dots: Beyond the mollow triplet," *Phys. Rev. Lett.*, vol. 108, p. 017401, 2012.

[164] S. Reitzenstein and A. Forchel, “Quantum dot micropillars,” *J. Phys. D: Appl. Phys.*, vol. 43, p. 033001, 2010.

[165] S. Maier, P. Gold, A. Forchel, N. Gregersen, J. Mørk, S. Höfling, C. Schneider, and M. Kamp, “Bright single photon source based on self-aligned quantum dot-cavity systems,” *Optics Express*, vol. 22(7), pp. 8136–8142, 2014.

[166] N. Gregersen, P. Kaer, and J. Mørk, “Modeling and design of high-efficiency single photon sources,” *IEEE Journal of selected topics in quantum electronics*, vol. 19(5), pp. 1–16, 2013.

[167] C. Schneider, T. Heindel, A. Huggenberger, P. Weinmann, C. Kistner, M. Kamp, S. Reitzenstein, S. Höfling, and A. Forchel, “Single photon emission from a site-controlled quantum dot-micropillar cavity system,” *Appl. Phys. Lett.*, vol. 94, p. 111111, 2009.

[168] T. J. Pfau, A. Gushterov, J. P. Reithmaier, I. Cestier, and G. Eisenstein, “High optical quality site-controlled quantum dots,” *Microelectronic engineering*, vol. 87, pp. 1357–1359, 2010.

[169] M. Strauß, A. Kaganskiy, R. Voigt, P. Schnauber, J.-H. Schulze, S. Rodt, A. Strittmatter, and S. Reitzenstein, “Resonance fluorescence of a site-controlled quantum dot realized by the buried stressor growth technique,” *Appl. Phys. Lett.*, vol. 110, p. 111101, 2017.

[170] C. Schneider, P. Gold, S. Reitzenstein, S. Höfling, and M. Kamp, “Quantum dot micropillar cavities with quality factors exceeding 250000,” *Appl. Phys. B*, vol. 122, p. 19, 2016.

[171] P. Androvitsaneas, A. B. Young, C. Schneider, S. Maier, M. Kamp, S. Höfling, S. Knauer, E. Harbord, C. Y. Hu, J. G. Rarity, and R. Oulton, “Charged quantum dot micropillar system for deterministic light-matter interactions,” *Phys. Rev. B*, vol. 93, p. 241409, 2016.

[172] M. Bayer, G. Ortner, O. Stern, A. Kuther, A. A. Gorbunov, and A. Forchel, “Fine structure of neutral and charged excitons in self-assembled In(Ga)As/(Al)GaAs quantum dots,” *Phys. Rev. B*, vol. 65, p. 195315, 2002.

[173] L. Mandel and E. Wolf, *Optical coherene and quantum optics*.
Cambridge University Press, 1995.

[174] T. Jennewein, M. Barbieri, and A. G. White, “Single-photon device requirements for operating linear optics quantum computing outside the post-selection basis,” *Journal of Modern Optics*, vol. 58, pp. 276–287.

[175] F. Grosse, E. A. Muljarov, and R. Zimmermann, *Phonons in quantum dots and their role in exciton dephasing. In: Bomberg D. (eds) Semiconductor nanostructures*.
NanoScience and technology. Springer, Berlin, Heidelberg, 2008.

[176] H. Benisty, C. M. Sotomayor-Torrès, and C. Weisbuch, “Intrinsic mechanism for the poor luminescence properties of quantum-box systems,” *Phys. Rev. B*, vol. 44, p. 19, 1991.

[177] L. C. Camenzind, L. Yu, P. Stano, J. D. Zimmerman, A. C. Gossard, D. Loss, and D. M. Zumbühl, “Hyperfine-phonon spin relaxation in a single-electron gaas quantum dot,” *Nat. Comms.*, vol. 9, p. 3454, 2018.

[178] M. Rambach, A. Nikolova, T. J. Weinhold, and A. G. White, “Sub-megahertz linewidth single photon source,” *APL Photonics*, vol. 1, p. 096101, 2016.

[179] J. P. Reithmaier and A. Forchel, “Recent advances in semiconductor quantum-dot lasers,” *Elsevier: C. R. Physique*, vol. 4, pp. 611–619, 2003.

[180] J. J. Coleman, J. D. Young, and A. Garg, “Semiconductor quantum dot lasers: A tutorial,” *Journal of Lightwave Technology*, vol. 29 (4), pp. 499–510, 2011.

[181] S. Sutts, S. N. Elliott, P. M. Smowton, and A. B. Krysa, “Exploring the wavelength range of InP/AlGaInP qds and applications to dual state lasing,” *Semiconductor Science and Technology*, vol. 30, p. 044002, 2015.

[182] T. Braun, C. Schneider, S. Maier, R. Igusa, S. Iwamoto, A. Forchel, S. Höfling, Y. Arakawa, and M. Kamp, “Temperature dependency of the emission properties from positioned In(Ga)As/GaAs quantum dots,” *AIP Advances*, vol. 4, p. 097128, 2014.

[183] S. Münch, S. Reitzenstein, P. Franeck, A. Löffler, T. Heindel, S. Höfling, L. Worschech, and A. Forchel, “The role of optical excitation power on the emission spectra of a strongly coupled quantum dot-micropillar system,” *Optics express*, vol. 17, 15, pp. 12821–12828, 2009.

[184] M. Boero, J. R. Rorison, G. Duggan, and J. C. Inkson, “A detailed theory of excitons in quantum dots,” *Elsevier Surface Science*, vol. 377-379, pp. 371–375, 1997.

[185] J. Renard, R. Songmuang, C. Bougerol, B. Daudin, and B. Gayral, “Exciton and biexciton luminescence from single gan/aln quantum dots in nanowires,” *Nano Letters*, vol. 8, 7, pp. 2092–2096, 2008.

[186] D. Sarkar, H. P. van der Meulen, J. M. Calleja, J. M. Becker, R. J. Haug, and K. Pierz, “Exciton fine structure and biexciton binding energy in single self-assembled InAs/AlAs quantum dots,” *Journal of Applied Physics*, vol. 100, p. 023109, 2006.

[187] A. J. Bennett, M. A. Pooley, Y. Cao, N. Sköld, I. Farrer, D. A. Ritchie, and S. Andrew J, “Voltage tunability of single-spin states in a quantum dot,” *Nat Comms*, vol. 4, p. 1522, 2013.